Constraining the Formation and Fate of Hydroperoxides in the Remote Atmosphere

Thesis by
Hannah Marie Allen

In Partial Fulfillment of the Requirements for the
Degree of
Doctor of Philosophy

CALIFORNIA INSTITUTE OF TECHNOLOGY
Pasadena, California

2021
Defended May 19, 2021

Hannah Marie Allen
ORCID: 0000-0002-4218-5133

ACKNOWLEDGEMENTS

Though I may have authored this dissertation, I could not have done so without the support, advice, time, and energy of the people around me. I can't express enough my gratitude for all those that have helped me in the lab, in the field, in data analysis, and in sharing memories during my time at Caltech. There have been too many people who have touched my life to thank them all by name, but I would like to acknowledge those who have contributed to supporting me as a scientist: I would not have made it this far without you.

First and foremost, Paul Wennberg has been an incredible advisor throughout these past many years at Caltech. The projects presented in this dissertation span a dizzying array of instrument development, operating multiple instruments, several field deployments, laboratory investigations, and model coding — if I am a well-rounded scientist, it is only because Paul has given me so many amazing opportunities to learn and to challenge myself. Thank you for the chance to learn atmospheric chemistry through an adventure that, quite literally, took me around the world. Thank you for the continuous support and guidance throughout the years. And thank you for always pushing me to become a better scientist.

If there's one person who is the keystone to ensuring that our instruments work, our lab continues to function, and we're ready for field deployments, it's John Crounse. None of the measurements collected in this dissertation would have happened without his immense knowledge and support. John is by far our first and best resource when an instrument malfunctions or when data looks strange. Thank you for your endless patience in explaining how instruments work, the steps to take when something breaks, and why error analysis is important. And thank you for always taking the time to thoughtfully answer my questions, no matter how big or small.

I have had the privilege of finding mentorship in many places in my life, but most especially in Jenn Weaver at Caltech and Julie Fry at Reed College. Jenn has been my guide and support throughout my professional and personal development at Caltech. I am continuously amazed by how much the pedagogy skills she taught me have transcended teaching and helped me in all areas of life; I have become an infinitely better presenter, communicator, teacher, and mentor because of her example. Thank you for always being so generous in giving me your time and

attention, for always being willing to workshop problems with me, for all of your incredibly helpful advice, and for the unwavering encouragement whenever I needed it. As my undergraduate mentor at Reed College, Julie was the one who started me down the path that led to this dissertation. Her support, guidance, and infectious excitement for teaching, mentoring, and atmospheric chemistry have stayed with me on my journey through grad school. Thanks also to my thesis committee, Mitchio Okumura, John Seinfeld, and Brian Stoltz, who have provided me with their time, support, and advice.

The Wennberg group has been a richly collaborative and supportive environment in which to work and grow as a scientist. All of the people who have been a part of the group over the years have supported me in some way, even when our projects did not directly overlap. I especially have to thank Alex Teng for mentoring me when I first arrived in graduate school, coaching me through lab experiments, and giving me ways to think more deeply about my data. Thanks also to Krystal Vasquez, Eric Praske, and Anke Noelscher for their hard work in making the PROPHET campaign happen despite all the evidence to the contrary. To Michelle Kim for her support and dedication during the ATom campaign. To Kelvin Bates for always being ready to test my ideas in GEOS-Chem and decode the results. And to Lu Xu, Josh Laughner, and Kat Saad for invaluable discussions over the years.

There have been numerous people who have provided me with the technical, administrative, and logistical support that has made this dissertation possible. Nora Oshima, Kathy Young, Kathy Bravo, Bronagh Glaser, and Leilani Rivera-Dotson deserve a great many thanks for keeping everything in Linde-Robinson running smoothly. Steve Bertman spearheaded the PROPHET campaign and Steve Wolfsy and Tom Ryerson did the same for the ATom; their motivation and organization enabled scientists from so many different institutions to collaborate and share data. Thanks also to the folks at ESPO who moved mountains to get us the ground support to keep our instruments running in some of the most remote regions of the world. And finally thanks to the pilots and crew of the NASA DC-8 who enable the aircraft to keep flying.

My friends have been a foundational source of support in keeping me grounded during tough times, in exploring California, and in creating the wonderful memories that I have gathered alongside my scientific work.
Elizabeth Lunny has been an amazing person to not only share an office with, but also to commiserate with over grad school woes, share life updates, create snowflakes

(and Christmas decorations) for the windows, and analyze human behavior.
Sara Murphy brings so much joy and laughter to everything we do together, including office shenanigans, movie nights, quesarito eating, linguistics discussions, and so much more, while at the same time being so present and supportive during the times when I need a friend to listen.
Lily Dove is one of the most caring and nurturing people I know, whose presence I have definitely benefited from; thank you for all the cookies, dinners, social organizing, and for all of your work to ensure that the people around you feel welcome and supported.
Zach Erickson has been a support throughout all of the ups and downs of grad school from the beginning, and has introduced me to so many wonderful things including contra dancing, backpacking trips, classical music, and downtown LA.
Sophia Charan, Anna Ho, and Heidi Klumpe have engaged me in so many stimulating conversations that have broadened my perspectives and understanding of the world; thank you to Sophia for your invaluable insights and readiness to debate ideas, to Anna for sharing your love of literature and new ideas, and to Heidi for your curiosity and thoughtful questions.
Andy Erickson has been a companion on numerous adventures through the mountains, valleys, deserts, and wild flowers of California and has shown me how to start campfires, find the most amazing campsites, navigate the stars, and construct the best road trip playlists.
And Hannah Schaupp has been a wonderful friend and support through the challenges and joys of both an undergraduate and graduate thesis and the many years in-between; thank you for all the lovely conversations and heartfelt encouragement.

I'd also like to thank all the communities that I have been a part of during my time at Caltech for teaching me new skills and supporting me outside my academic endeavors, including SEPAC, the Caltech Y, the CTLO, the Visiting Scientists program, Pasadena contra dancers, and the Caltech west coast swing group. Thanks to my B216 officemates and to the 121 L+R office for adopting me. Additional thanks also to Magnus Haw, Chris Kenseth, Anya Kent, Harrison Parker, and Jackie Lopez Parker for the great conversations and fun adventures as well.

Finally, my family has been incredibly supportive throughout all of my personal and academic journeys in my life. My parents, Jim Allen and JoAnn Williams, deserve abounding thanks for their patience with me, their unwavering support of my pursuits, their willingness to give me last-minute edits, their words of advice,

and their helpful feedback over the years. My sibling Sky Williams-Tao has been by my side for almost as long as I have been alive and has been a continual source of support, encouragement, thoughtful discussions, new perspectives, and camaraderie along the way.

ABSTRACT

Atmospheric hydroperoxides form as second generation products in the atmospheric oxidation of many volatile organic compounds (VOCs) during reactions of these VOCs with OH and HO_2 (i.e. HO_x), where HO_x are among the atmosphere's main oxidants and thus drivers of the majority of atmospheric chemistry. Once formed, the lifetime and ultimate fate of hydroperoxides are set by a variety of potential chemical and physical pathways that have different impacts on the atmosphere's oxidizing capacity, including either recycling HO_x or removing HO_x. This dissertation explores the role of hydroperoxides with several different structures through field and laboratory studies using CF_3O^- chemical ionization mass spectrometry (CIMS) to understand the role of these hydroperoxides in the oxidation chemistry of the remote atmosphere.

Hydrogen peroxide (H_2O_2) and methyl hydroperoxide (MHP, CH_3OOH) are two of the most abundant hydroperoxides found in oceanic environments. Both H_2O_2 and MHP were measured using time of flight and tandem quadrupole CIMS aboard the NASA DC-8 aircraft during the Atmospheric Tomography Mission, enabling a seasonal investigation into their global distribution with near pole-to-pole coverage across the Pacific and Atlantic Oceans and ranging in altitude from the marine boundary layer to the upper troposphere and lower stratosphere. Biomass burning is found to significantly enhance the formation of H_2O_2, leading to higher concentrations of this hydroperoxide in the equatorial Atlantic than in corresponding latitudes of the Pacific. These ATom observations are compared to two photochemical models, a diurnal steady-state box model and a global chemical transport model, to assess the relative contributions of photochemical loss, physical loss, and transport processes to the global hydroperoxide budget. These comparisons show that deposition of H_2O_2 plays a significant role in removing HO_x from the marine boundary layer while convection lofts MHP and impacts HO_x cycling in the upper troposphere.

Hydroxymethyl hydroperoxide (HMHP, $HOCH_2OOH$) and isoprene hydroxy hydroperoxides (ISOPOOH, HOC_5H_8OOH) are organic hydroperoxides derived from the oxidation of isoprene, one of the dominant biogenic VOCs in forested environments. The loss of HMHP from the atmosphere via reaction with OH is investigated in the laboratory using time of flight CIMS and laser induced fluorescence along with theoretical chemical modeling methods. Reaction with OH is found to be a

major sink of HMHP and an oxidation scheme is developed showing production of formic acid and formaldehyde from this reaction. To better distinguish the varying roles of structurally complex hydroperoxides, a novel field-deployable gas chromatograph integrated with a high resolution time of flight CIMS is developed that sensitively detects hydroperoxides along with a number of other oxidation products. This instrument is deployed at a rural forested site in northern Michigan during the PROPHET field campaign to probe the relative contribution of different ISOPOOH isomers to the oxidation pathways of isoprene.

PUBLISHED CONTENT AND CONTRIBUTIONS

Allen, H. M., et al. (2021). "H_2O_2 and CH_3OOH (MHP) in the remote atmosphere. II: Physical and chemical controls". In: *J. Geophys. Res. Atmos. [submitted]*.
H.M.A. conducted the measurements, analyzed the data, and wrote the manuscript.

Allen, H. M., et al. (2021). "H_2O_2 and CH_3OOH (MHP) in the remote atmosphere. I: Global distribution and regional influences". In: *J. Geophys. Res. Atmos. [submitted]*.
H.M.A. conducted the measurements, analyzed the data, and wrote the manuscript.

Vasquez, K. T., et al. (2020). "Rapid hydrolysis of tertiary isoprene nitrate efficiently removes NO_x from the atmosphere". In: *Proc. Nat. Acad. Sci.* 117.52, pp. 33011–33016. DOI: 10.1073/pnas.2017442117.
H.M.A. assisted in instrument development and data collection.

Travis, K. R., et al. (2020). "Constraining remote oxidation capacity with ATom observations". In: *Atmos. Chem. Phys.* 20, pp. 7753–7781. DOI: 10.5194/acp-20-7753-2020.
H.M.A. assisted in data collection

Thames, A. B., et al. (2020). "Missing OH reactivity in the global marine boundary layer". In: *Atmos. Chem. Phys.* 20, pp. 4013–4029. DOI: 10.5194/acp-20-4013-2020.
H.M.A. assisted in data collection.

Brune, W. H., et al. (2019). "Exploring oxidation in the remote free troposphere: Insights from Atmospheric Tomography (ATom)". In: *J. Geophys. Res. Atmos.* 125.1. DOI: 10.1029/2019JD031685.
H.M.A. assisted in data collection.

Wang, S., et al. (2019). "Atmospheric acetaldehyde: Importance of air-sea exchange and a missing source in the remote troposphere". In: *Geophys. Res. Lett.* 46.10, pp. 5601–5613. DOI: 10.1029/2019GL082034.
H.M.A. assisted in data collection.

Vasquez, K. T., et al. (2018). "Low-pressure gas chromatography with chemical ionization mass spectroscopy for quantification of multifunctional organic compounds in the atmosphere". In: *Atmos. Meas. Tech.* 11, pp. 6815–6832. DOI: 10.5194/amt-11-6815-2018.
H.M.A. assisted in instrument development and data collection.

Allen, H. M., et al. (2018). "Kinetics and product yields of the OH initiated oxidation of hydroxymethyl hydroperoxide". In: *J. Phys. Chem. A* 122.30, pp. 6292–6302. DOI: 10.1021/acs.jpca.8b04577.
H.M.A. conducted the experiments, analyzed the data, and wrote the manuscript.

TABLE OF CONTENTS

LIST OF ILLUSTRATIONS

LIST OF TABLES

Chapter 1

INTRODUCTION

1.1 Background and Motivation

The Earth's atmosphere is a rich chemical reactor in which hundreds of compounds are continuously introduced by natural (biogenic) and human-derived (anthropogenic) sources, whereupon they react in a myriad of chemical and physical pathways that act to transform these compounds. The bulk of the chemical mechanisms in the atmosphere are primarily driven by three atmospheric radicals: the hydroxyl radical (OH), the nitrate radical (NO_3), and ozone (O_3) (Seinfeld and Pandis, 2006). OH, in particular, is an extremely reactive molecule that drives a large portion of atmospheric chemistry through it's ability to oxidize several different types of compounds. As OH reacts in the atmosphere it forms the hydroxyl radical (HO_2) as a major byproduct; HO_2 in turn reacts to reform OH, leading to rapid interconversion between the two. As a result, OH and HO_2 are collectively known as the HO_x chemical family. This rapid cycling is often enhanced by the presence of the NO_x chemical family, comprising nitrogen oxide (NO) and nitrogen dioxide (NO_2), that results primarily from anthropogenic emissions. The NO_x family acts as catalysts that propagate radical chain reactions and results in the formation of ozone (O_3), a major pollutant and component of photochemical smog when present in high concentrations in the troposphere. Together, HO_x and NO_x set the oxidizing capacity of the atmosphere and thus dictate the type of chemistry a particular region will undergo.

Hydroperoxides are a class of chemical compounds that are connected to the atmospheric cycling of HO_x and NO_x. Hydroperoxides encompass a wide variety of compounds with different chemical structures, but all with the linking trait of containing an ROOH functional group. This structure arises when radicals from precursor compounds react with HO_x, and thus hydroperoxides form as a second generation product in atmospheric oxidation. The most common hydroperoxide is also the one with the simplest structure: hydrogen peroxide (H_2O_2). Hydroperoxides can also have an organic backbone, ranging from a single carbon such as in methyl hydroperoxide (MHP, CH_3OOH) and hydroxymethyl hydroperoxide (HMHP, $HOCH_3OOH$), to longer-chained compounds such as ethyl hydroperoxide

(CH_3CH_2OOH), to more complex structures such as the isoprene hydroperoxides (ISOPOOH, HOC_5H_3OOH). The structure and abundance of each hydroperoxide depends upon the region being sampled: H_2O_2 is the most prevalent hydroperoxide globally, MHP is the dominant organic hydroperoxide observed in remote regions above the ocean, while ISOPOOH is a common organic peroxide found in forested areas (Lee et al., 2000; Paulot et al., 2009b).

Hydroperoxides are of key significance in the atmosphere because they form through HO_x chemistry and thus act as reservoirs of HO_x and tracers for regions where HO_x chemistry is prevalent. Many compounds that undergo atmospheric oxidation form peroxy radicals (RO_2) after reaction with OH. These RO_2 radicals may then react with HO_2 to form hydroperoxides; however, RO_2 may instead react with NO, thereby following a chemical pathway that leads to the formation of different compounds. As a result of this competition for RO_2, the presence of hydroperoxides is generally indicative of a region dominated by high HO_x and low NO_x chemistry. In addition, physical processes such as advection (horizontal transport) and convection (vertical transport) can move peroxides far distances from their sources to remote regions of the atmosphere, such as the upper troposphere and lower stratosphere (UTLS) (Jaeglé et al., 1997, 2000). Hydroperoxides may then undergo chemical processing, such as photolysis or reaction with OH, releasing HO_x back into the atmosphere and thereby redistributing the oxidant pool. Finally, hydroperoxides may be permanently lost from the atmosphere due to deposition, and thereby decrease the atmosphere's oxidative potential.

Hydroperoxides may also act as oxidants in their own right, producing secondary organic aerosol (SOA) and harming plant tissue. In the aqueous phase, hydroperoxides such as H_2O_2 are efficient oxidizers of SO_2 (Penkett et al., 1979; Calvert et al., 1985; Lind et al., 1987; Meagher et al., 1990). The oxidized form of SO_2 is the sulfate ion, SO_4^{2-}, which is one of the main inorganic components of aerosol (Zhang et al., 2007). In the aqueous phase under acidic conditions, hydroperoxides may also participate in reactions with organic compounds, converting biogenic hydrocarbons to products that contribute to the formation of organic aerosol (Claeys et al., 2004). Hydroperoxides, due to their contribution to SOA production, thereby indirectly decrease atmospheric visibility, reduce air quality, and can alter Earth's climate. Hydroperoxides have also been implicated in the inhibition of certain peroxidase enzymes essential to plant function, leading to widespread plant death (Möller, 1989; Polle and Junkermann, 1994a,b). However, the magnitude of this

effect is under consideration as some studies note that under certain conditions, a continuous low exposure to ozone can increase a plant's resistance to the oxidative stress and ill-health caused by hydroperoxides (Sandermann et al., 1998; Mehlhorn, 1990).

1.2 Chemistry of Hydroperoxides in the Atmosphere

Formation of Hydroperoxdies

A majority of atmospheric chemistry, including the formation of hydroperoxides, is driven by reaction of the atmosphere's main oxidant, OH. This radical forms when sunlight with energy greater than 320 nm (i.e. UV light) passes through the atmosphere and causes the photooxidation of atmospheric O_3. When this reaction occurs in the presence of water vapor, most prominently in the troposphere, the resulting $O(^1D)$ radical will form OH (Eq 1.1).

$$\begin{aligned} O_3 + h\nu &\longrightarrow O(^1D) + O_2 \\ O(^1D) + H_2O &\longrightarrow 2\,OH \end{aligned} \tag{1.1}$$

OH is highly reactive and therefore has a very short lifetime on the atmosphere. It will quickly react with a wide variety of compounds including carbon monoxide (CO), methane (CH_4), and volatile organic compounds (VOCs) such as alkanes, alkenes, or other hydrocarbons. These reactions produce the hydroperoxide precursor HO_2. The reaction of CO with OH is the largest source of HO_2 globally, accounting for 30–40% of HO_2 production in the bulk of the atmosphere that occurs over the oceans (Whalley et al., 2010; Sommariva et al., 2004). OH oxidizes CO in the presence of oxygen to form HO_2 and CO_2 (Eq 1.2).

$$CO + OH \xrightarrow{O_2} CO_2 + HO_2 \tag{1.2}$$

However, HO_2 may also result from other atmospheric reactions such as photolysis (e.g. HCHO photolysis produces 20–45% of HO_2 in the remote atmosphere), OH oxidation of other VOCs (e.g. 22–28% in VOC-rich, low NO_x environments like forests), ozonolysis (~15% in forests and urban areas), and NO chemistry (significant in polluted urban areas, e.g. 65% HO_2 production in Mexico City) (Sommariva et al., 2004; Dusanter et al., 2009; Whalley et al., 2010; Griffith et al., 2013).

Similarly, the OH-initiated reaction of hydrocarbons produces the other hydroperoxide precursor, the peroxy radical (RO_2). The OH abstraction of hydrogen from these compounds in the presence of oxygen produces RO_2 as a product (Eq. 1.3).

$$RH + OH \xrightarrow{O_2} RO_2 + H_2O \tag{1.3}$$

For example, CH_4 is a major constituent of the atmosphere, the dominant atmospheric hydrocarbon, and a major greenhouse gas. There are many natural sources of CH_4, predominantly wetlands, which comprise 50–70% of CH_4 sources; yet global CH_4 levels have increased significantly since the industrial revolution and continue to increase at a rapid pace due to anthropogenic emissions from agriculture and waste (sewage and landfills), which now contribute approximately 50–70% of CH_4 (Kirschke et al., 2013; Turner et al., 2019). Once in the atmosphere, over 80% of CH_4 undergoes oxidation by OH to form the methyl peroxy radical (CH_3OO, Eq 1.4).

$$CH_4 + OH \xrightarrow{O_2} CH_3OO + H_2O \tag{1.4}$$

This reaction is fairly slow, yet because methane is so abundant and is primarily lost to OH, this reaction exerts a strong influence on the atmosphere (Kirschke et al., 2013). Hydrogen abstraction is the major reaction pathway for peroxy radical production from alkanes. However, peroxy radicals are also formed when OH adds to the double bond of atmospheric alkenes (Eq. 1.5),

$$(R_1R_2)C{=}C(R_3R_4) + OH \xrightarrow{O_2} (R_1R_2)(OH)C{-}C(OO)(R_3R_4) \tag{1.5}$$

where $R_{n=1,2,3,4}$ is any moiety attached to the alkene center. In this reaction, the OH adds to one side of the double bond while the peroxy radical moiety attaches to the other side and thus forms the precursor for hydroxy hydroperoxides.

Hydroperoxides form in the atmosphere from the reaction between HO_2 and RO_2 precursors, whereupon the RO_2 radical abstracts the hydrogen from HO_2 (Eq 1.6).

$$RO_2 + HO_2 \longrightarrow ROOH + O_2 \tag{1.6}$$

When the moiety in the peroxy radical is a hydrogen, i.e. R=H, then HO_2 undergoes the self-reaction to form H_2O_2 (Eq. 1.7).

$$HO_2 + HO_2 \longrightarrow H_2O_2 + O_2 \tag{1.7}$$

Note that the HO_2 self-reaction sequesters two HO_x radicals, making H_2O_2 a reservoir of HO_x. H_2O_2 production is thus highest in areas where there is strong production of its precursor, HO_2. These are typically areas conducive to photochemical activity, including areas with lots of solar radiation and higher temperatures, which favor HO_x production. H_2O_2 is also positively correlated with hydrocarbons, such as CO, which are precursors for HO_2 formation (Lee et al., 2000). If the moiety

in the peroxy radical is a carbon, e.g. CH_3OO, then the reaction proceeds very similarly to form methyl hydroperoxide (MHP) (Eq 1.8).

$$CH_3OO + HO_2 \longrightarrow CH_3OOH + O_2 \tag{1.8}$$

This reaction consumes one HO_x radical, but accounting for the HO_x consumed in CH_3OO formation, the production of MHP removes two HO_x from the atmosphere. Though RO_2 + HO_2 chemistry is the dominant hydroperoxide formation mechanism, hydroperoxides may also form in the ozonolysis of alkenes. This process forms a primary carbonyl and an energy-rich Criegee biradical, the latter of which may be stabilized by other atmospheric constituents such as H_2O vapor to form hydroperoxides (Seinfeld and Pandis, 2006).

Atmospheric Fate

Once hydroperoxides form, their lifetime in the atmosphere depends upon the amount of sunlight present, the mixing ratio of OH, and the amount of wind, rain, and other environmental factors. Hydroperoxides are typically lost from the atmosphere via either chemical reactions (e.g. photolysis or reaction with OH) or through physical removal mechanisms (e.g. deposition). The relative contribution of each of these loss methods is highly dependent upon the chemical properties and structure of each hydroperoxide. Larger and less polar peroxides (e.g. CH_3OOH or CH_3CH_2OOH) are more likely to undergo chemical loss (e.g. reaction with OH). They tend to have longer lifetimes and thus may be transported distances relatively far from where the compound originated. Smaller and more polar peroxides (e.g. H_2O_2 and $HOCH_2OOH$) are more susceptible to physical losses via wet and dry deposition. These more polar peroxides may also undergo uptake in aerosol and water droplets, in which they can act as oxidants of SO_2 and other compounds or may play a role in SOA formation (Lee et al., 2000).

The two primary chemical loss pathways for hydroperoxides are photolysis and reaction with OH. Photolysis is the decomposition of a chemical compound due to sunlight. This reaction occurs when sunlight in the UV region ($h\nu$) severs the O – O bond present in ROOH (Eq. 1.9).

$$ROOH + h\nu \longrightarrow RO + OH \tag{1.9}$$

Photolysis primarily occurs in the 300–400 nm band of UV light (peaking at 325 nm), as a result of the balance between ROOH absorption and the wavelengths of incoming solar radiation that reach the troposphere (Matthews et al., 2005; Roehl

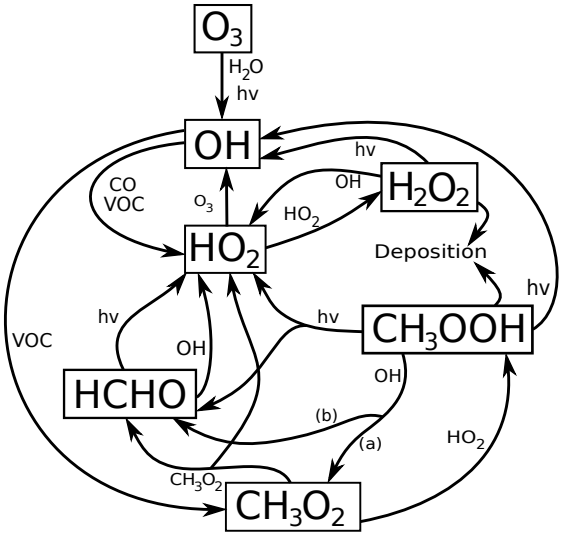

Figure 1.1: Hydroperoxide formation from HO_x chemistry and subsequent reaction pathways. The hydroperoxides H_2O_2 and MHP CH_3OOH form from HO_2 reactions and from VOC reactions in the atmosphere. They may be lost through by photolysis (hv), reaction with OH, and deposition. Adapted from Reeves and Penkett (2003).

et al., 2007). For H_2O_2, this reaction returns two OH to the atmosphere; for organic hydroperoxides, the resulting alkoxy radical (RO) rapidly decomposes in the presence of oxygen to an aldehyde and HO_2. For example, the CH_3O alkoxy radical formed in the photolysis of CH_3OOH results in the formation of HCHO and HO_2. Accounting for the reaction of RO, photolysis of organic hydroperoxides returns two HO_x and thus is a net neutral reaction in terms of global HO_x cycling, as photolysis releases the two HO_x that were consumed in the formation of the hydroperoxide. The cycling of HO_x due to photolysis of H_2O_2 and CH_3OOH is shown in Figure 1.1.

Similarly, the reaction of hydroperoxides with OH results in HO_x recycling in the atmosphere (Figure 1.1). The exact mechanism by which OH oxidizes the hydroperoxide depends upon the chemical structure of the hydroperoxide: OH may either abstract the hydrogen from the ROOH functional group, abstract a hydrogen from a different location in the hydroperoxide, or may add to a double bond if the hydroperoxide contains one. For example, the simplest organic hydroperoxide CH_3OOH has two pathways by which it reacts with OH, depending on the hydrogen abstracted (Eq. 1.10).

$$\begin{aligned} CH_3OOH + OH &\longrightarrow CH_3OO + H_2O \\ &\longrightarrow CH_2OOH + H_2O \end{aligned} \tag{1.10}$$

The branching ratio of this reaction varies between 0.65–0.83 in favor of CH_3O_2 formation, with a recommended average of 0.73 for CH_3OO formation and 0.27 for CH_2OOH formation (Niki et al., 1983; Vaghjiani and Ravishankara, 1989; Atkinson et al., 2006; Luo et al., 2010; Anglada et al., 2017). The two different channels of CH_3OOH + OH have different effects on the HO_x budget: the CH_3OO channel regenerates the MHP precursor, which may react with HO_2 to reform MHP and thereby catalyze loss of HO_x; the CH_2OOH produced in the second channel will spontaneously decompose to HCHO and OH, and further reactions of HCHO may form HO_2, leading to net neutral HO_x cycling. On the whole, hydroperoxide reactions with OH tends to result in a net loss of HO_x.

Hydroperoxide physical losses occur primarily via wet deposition and dry deposition. Wet deposition occurs when hydroperoxides shift from the gas phase to the aqueous phase due to absorption into atmospheric liquid water, such as might occur during cloud, rain, fog, sleet, or snow events. The extent to which a compound is lost to wet deposition depends upon its solubility, which is often described by its Henry's Law constant (also called the air-water partition coefficient). The Henry's Law constant is the ratio of a compound's partial pressure in air to the concentration of the compound in water at a given temperature; the higher the Henry's Law constant, the more soluble the compound and the more likely it is to undergo wet deposition. H_2O_2, for example, is highly soluble with a Henry's Law constant on order of $1{\times}10^5$ M atm^{-1}, meaning it is easily lost to the aqueous phase (Burkholder et al., 2015). Scavenging efficiency, the fraction of a compound that is taken up into atmospheric liquid water, is the other metric by which wet deposition is measured. The scavenging efficiencies for a highly soluble compound like H_2O_2 may be between 44–90% during rainout events, while a less soluble compound may be on order of 5–10% or less (Crutzen and Lawrence, 2000; Barth et al., 2001; Chang et al., 2004).

Dry deposition happens when hydroperoxides adhere to physical surfaces, such as via sedimentation under gravity or by turbulent transfer resulting in impaction and interception. For example, dry deposition occurs when wind blows hydroperoxides onto plant leaves in forests or onto the ocean surface in the remote atmosphere. The rate at which dry deposition happens depends upon several factors related to surface characteristics, such as surface roughness and total surface area, and on meteorological factors, such as atmospheric stability and wind speed. For a highly soluble compounds like H_2O_2, the rate is mainly driven by surface-layer turbulence

(Walcek, 1987). Both wet and dry deposition are considered a permanent sink of hydroperoxides and thus a permanent loss of HO_x from the atmosphere.

Influence of NO_x

Hydroperoxide chemistry in the atmosphere will change with the presence of the NO_x chemical family. NO_x comprises the chemical species NO and NO_2, which are anthropogenic pollutants arising from combustion process such as exists in the engines of gasoline and diesel vehicles. In the atmosphere, NO and NO_2 rapidly interconvert between each other, with sunlight photolyzing NO_2 to NO and NO reacting with O_3 to form NO_2 (Eq. 1.11).

$$\begin{aligned} NO_2 + h\nu &\xrightarrow{O_2} NO + O_3 \\ NO + O_3 &\longrightarrow NO_2 + O_2 \end{aligned} \tag{1.11}$$

The NO_x cycle generally leads to a stable concentrations of NO_x. However, NO also readily reacts with RO_2 to form NO_2 (Eq. 1.12).

$$RO_2 + NO \longrightarrow RO + NO_2 \tag{1.12}$$

Unlike in the typical NO_x cycling (Eq 1.11), the formation of NO_2 via RO_2 occurs without consumption of O_3. This reaction can therefore cause the rapid build-up of O_3 in the troposphere as NO_2 photolyzes to produce O_3 without significant O_3 loss. In addition, the RO formed may decompose and further react to form a more oxidized organic compound with co-production of HO_2 or NO_2, thus perpetuating the recycling of NO_x and the build-up of O_3.

Because NO reacts with both the hydroperoxide precursors HO_2 and RO_2, the abundance of hydroperoxides in the atmosphere is heavily dependent on the NO_x environment present. The reaction of NO with RO_2 is in direct competition with the reaction of HO_2 with RO_2 to form hydroperoxides, and thus the relative rates of these two RO_2 reactions (which in turn depend upon the relative concentrations of HO_2 and NO) is proportional to the amount of hydroperoxides that can form. At low enough NO_x, HO_2 is predominantly lost through the self-reaction to form H_2O_2 (Eq. 1.7) and through RO_2 chemistry to form organic hydroperoxides (Eq. 1.6). At high NO_x, NO will react directly with HO_2 to form NO_2 and OH (Eq. 1.13).

$$HO_2 + NO \longrightarrow NO_2 + OH \tag{1.13}$$

Or NO will react with RO_2 (Eq. 1.12), as occurs in the case of the simple organic peroxy radical CH_3OO (Eq. 1.14).

$$CH_3OO + NO \longrightarrow CH_3O + NO_2 \tag{1.14}$$

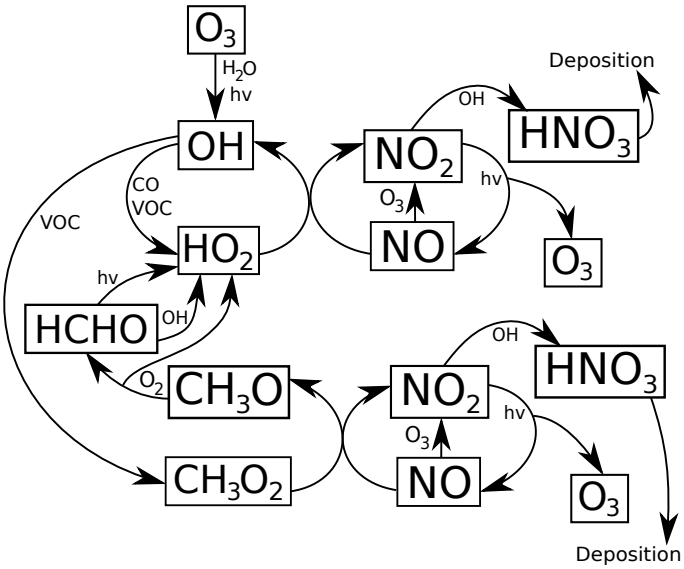

Figure 1.2: HO_x and RO_2 chemistry under high NO_x conditions. High NO_x suppresses peroxide formation because HO_2 and other RO_2 preferentially react with NO over HO_2 at high enough NO_x. The RO_2 + NO reaction can result in the build-up of tropospheric O_3, a main component of photochemical smog. Adapted from Reeves and Penkett (2003).

Due to these reactions, NO_x regulates the availability of HO_2 and as a result the NO_x cycle is tightly coupled with HO_x cycling and RO_2 chemistry as shown in Figure 1.2. The RO_2 + NO reaction occurs mainly in regions with strong anthropogenic influence, due to the source of NO_x, and is highly important in air quality considerations. The NO_2 produced in the RO_2 + NO reaction quickly photolyzes to NO and O_3. The resulting NO may then react with another RO_2, creating a catalytic chain that rapidly consumes RO_2 and builds NO_2 and thus O_3. Tropospheric O_3 is a pollutant that irritates the eyes and respiratory system, and is one of the main components of photochemical smog. The formation of hydroperoxides temporarily removes RO_2 from this ozone-production cycle.

1.3 Methodology for Studying Hydroperoxides

Much of the methodology for studying atmospheric chemistry, including hydroperoxides, falls into three main categories: laboratory studies, field studies, and modeling studies. Laboratory studies allow for investigations into specific chemical reaction pathways in a controlled environment and therefore enable a detailed mechanistic understanding of the atmosphere (e.g. see Nguyen et al. (2014)). Field studies broaden that scope into the full complexity of the chemistry and physics of the atmosphere in real-world conditions and enable the discovery of potential new areas for

investigation (e.g. Carlton et al. (2018)). Modeling provides a testing ground for the theories developed in the lab and field that gives a look into how well current mechanisms capture the relevant chemistry of the atmosphere (e.g. Prather et al. (2018)). Each method has its benefits and drawbacks, but together provide a comprehensive examination of the atmosphere.

The most common method for studying atmospheric chemistry in the laboratory is to use reaction chambers to simulate specific chemical reactions. These chambers consist of a large volume of air contained inside a Teflon bag that is filled with the relevant gas-phase compounds and allowed to react over a desired period of time. The chambers are surrounded by UV lights that simulate atmospheric sunlight and enable photochemistry to occur. An oxidant precursor, such as H_2O_2 or methyl nitrite (CH_3ONO), is added that will photolyze once the lights are turned on to generate HO_x and thereby initiate the chemical reactions. In a typical experiment, gases are added to the chamber sequentially, diluted to the appropriate concentration, the lights are turned on to begin the chemistry, and the concentration of different reactants and/or products are monitored over time using instruments sampling directly from the chamber. Several different types of instruments may be used depending on the compounds of interest. Chemical ionization mass spectrometry (CIMS) is a commonly utilized technique to measure hydroperoxides with high sensitivity (Crounse et al., 2006; St. Clair et al., 2010). Mass spectrometry (MS) is an analytical method that converts the desired compound into ions and distinguishes different ions based on their mass-to-charge ratio. Chemical ionization (CI) is a soft ionization technique used to form the ions for MS detection that reduces the extent to which measured compounds fragment upon entering the instrument.

Field studies complement laboratory investigations by assessing the atmospheric relevance of reactions measured in the lab under real meteorological conditions. Field studies are typically conducted by placing instruments in a location or configuration in which they can sample outside, ambient air. The scope of these studies can vary widely from a single instrument placed outdoors for a very short period of time (hours or days) to a complex, multi-instrument project ("campaign") conducted over months or years. These studies may occur across the globe in a variety of environments, including cities, farms, forests, mountains, polar tundra, and over the oceans, using one or more of a whole spectrum of platforms, including aircraft, satellites, balloons, ships and buoys, vehicles, and outdoor shelters. In general, most field studies fall into one of two categories: stationary, ground-based sites and

mobile, airborne measurements. The ground-based field studies investigate changes in atmospheric compounds due to temporal changes in meteorological conditions such as daylight, temperature, relative humidity, passing weather systems, etc at a single measurement site. Many ground-based sites also use towers to sample the atmosphere at various heights within the planetary boundary layer (e.g. below and above a forest canopy). By contrast, airborne studies sample a wide range of different latitudes, longitudes, and altitudes but observe each location at only one moment in time; thus airborne measurements have wider spacial coverage but without the temporal evolution observed at ground sites. Airborne studies are primarily conducted by placing instruments onto an aircraft with inlet attached to an external port that directs sample air from outside the aircraft into the instrument detector. A prominent aircraft used in atmospheric chemistry field campaigns is the NASA DC-8, a Douglas DC-8 jetliner aircraft that has been retrofitted by NASA into a flying laboratory able to carry 30,000 pounds of scientific instruments and equipment (Conner, 2017).

Laboratory and field measurements are often compared to atmospheric models to assess how well these computer simulations capture the chemistry of the atmosphere. Discrepancies that occur between models and either lab or field measurements provide a way to diagnose where gaps may exist in current understanding of atmospheric mechanisms. Models may be relatively simple, such as zero-dimensional photochemical box models that simulate the concentrations of a limited number of chemical reactions over time. These models are quick to run, easy to adjust, and are mostly used to represent specific processes occurring in laboratory reaction chambers. However, box models may also contain a much more complex mechanism with tens or hundreds of chemical reactions that simulate first, second, third, etc., generation oxidation products. More sophisticated models include global chemical transport models, which integrate atmospheric chemical mechanisms with meteorology across the latitudinal, longitudinal, and altitudinal domain of the globe. Global chemical transport models are often used to compare with field observations or to assess the global importance of a new mechanism developed in the laboratory.

1.4 Overview of Dissertation

This dissertation comprises several chapters related to the study of hydroperoxides in the atmosphere. These studies employ field measurements, laboratory experiments, and modeling to understand how hydroperoxides affect atmospheric chemistry in several different types of environments. In each instance, a CIMS instrument

was employed to measure hydroperoxides in ambient air or in a reaction chamber to understand the atmospheric relevance of these hydroperoxides, where they are most likely to form, and to understand the detailed mechanisms by which they are transformed or lost from the atmosphere.

Chapter 2 of this dissertation describes a field investigation into two of the globally dominant atmospheric hydroperoxides, hydrogen peroxide (H_2O_2) and methyl hydroperoxide (MHP, CH_3OOH), in the atmosphere above the Pacific and Atlantic Oceans. These compounds were measured using a time of flight CIMS and a triple quadrupole CIMS located onboard the NASA DC-8 aircraft as part of the Atmospheric Tomography (ATom) Mission. The ATom Mission comprised four deployments over three years — August 2016, February 2017, October 2017, and May 2018 — to gather data on how the chemistry in the remote atmosphere changes with latitude, longitude, and season. This chapter describes how the hydroperoxide measurements were made, presents a summary of the global distribution of these hydroperoxides across the four different seasons, and investigates the role that smoke from large-scale agricultural burning on the continents plays in altering the concentration of hydroperoxides above the Atlantic Ocean. This chapter thus seeks to answer the question: where do hydroperoxides form in the remote atmosphere?

Chapter 3 of this dissertation further expands upon the work done in Chapter 2 by delving into the specific chemical and physical mechanisms that result in the hydroperoxide concentrations measured during the ATom Mission. In this chapter, the CIMS measurements are compared with two atmospheric models: a simple photochemical box model and the global chemical transport model GEOS-Chem. These two models are used to investigate the loss of H_2O_2 and CH_3OOH to photochemistry and reaction with OH across latitude and altitude, to understand the role of deposition on H_2O_2 concentrations in the lowest region of the atmosphere, and to elucidate how convection (vertical transport during storms and other meteorological events) affects MHP in the upper troposphere and lower stratosphere. Hence this chapter seeks to answer the question: what are the chemical and physical processes that contribute to the fate of hydroperoxides in the remote atmosphere?

Chapter 4 describes a laboratory investigation into the reaction of hydroxymethyl hydroperoxide (HMHP, $HOCH_3OOH$) with the atmospheric oxidant OH. HMHP forms as a second generation product in forested regions due to the atmospheric reactions of a prominent biogenic compound, isoprene, with O_3. Reaction with OH is one of the most important atmospheric removal mechanisms for HMHP, and this

chapter presents measurements of the reaction rate and products formed in this reaction. The reactants and products were monitored over the time in an atmospheric reaction chamber using a time of flight CIMS instrument and a laser induced fluorescence (LIF) instrument. Based on these measurements, a detailed mechanism for how OH oxidizes HMHP into formic acid (FA, HCOOH) and formaldehyde (HCHO) is presented. This chapter therefore seeks to answer the question: how quickly does HMHP react with OH and what products form from this reaction?

Chapter 5 and the associated Appendix A outline the development of a gas chromatograph (GC) coupled with a high resolution time of flight CIMS that was deployed into the field to measure isoprene hydroxy hydroperoxides (ISOPOOH) in a forested site. ISOPOOH are the major second generation products from the reaction of isoprene with OH in low NO_x environments, such as exists in rural and forested areas. Understanding the subsequent chemistry of ISOPOOH often proves difficult because this compound forms many different isomers (compounds that have the same formula but a different arrangement of atoms and therefore different chemical properties) which cannot be distinguished by traditional CIMS. Thus a field-deployable GC component was developed that can be used to distinguish the different ISOPOOH isomers, thereby investigating the relative amount of these isomers in the atmosphere and their subsequent chemical pathways. As proof of concept, this instrument was deployed in the PROPHET field campaign that took place in northern Michigan during summer 2016. This chapter thereby seeks to answer the question: how can structurally complex hydroperoxides be measured in the atmosphere?

While each of the four main chapters in this dissertation stands alone as a solitary work — each seeking to investigate a specific scientific question — when collected together and bookended by the introduction in Chapter 1 and a brief summary and directions for future research in Chapter 6, these chapters provide new constraints on the formation and fate of atmospheric hydroperoxides.

Chapter 2

HYDROGEN PEROXIDE AND METHYL HYDROPEROXIDE IN THE REMOTE ATMOSPHERE: GLOBAL DISTRIBUTION AND REGIONAL INFLUENCES

2.1 Abstract

Atmospheric hydroperoxides are a significant component of the atmosphere's oxidizing capacity. Two of the most abundant hydroperoxides, hydrogen peroxide (H_2O_2) and methyl hydroperoxide (MHP, CH_3OOH), were measured in the remote atmosphere using chemical ionization mass spectrometry (CIMS) aboard the NASA DC-8 aircraft during the Atmospheric Tomography (ATom) Mission. These measurements present a seasonal investigation into the global distribution of these two hydroperoxides, with near pole-to-pole coverage across the Pacific and Atlantic Ocean basins and from the marine boundary layer to the upper troposphere and lower stratosphere. H_2O_2 mixing ratios are highest between 2–4 km altitude in the equatorial region of the Atlantic Ocean basin, where they reach global maximums of 3.6–6.5 ppbv depending on season. MHP mixing ratios reach global maximums of 4.3–8.6 ppbv and are highest between 1–3 km altitude, but peak in different regions depending on season. A major factor contributing to the global H_2O_2 distribution is the influence of biomass burning emissions in the Atlantic Ocean basin, encountered in all four seasons, where the highest H_2O_2 mixing ratios were found to correlate strongly with increased mixing ratios of the biomass burning tracers hydrogen cyanide (HCN) and carbon monoxide (CO). This biomass burning enhanced H_2O_2 by a factor of 1.3–2.2, on average, in the Atlantic compared with the Pacific Ocean basin.

Plain Language Summary

Hydroperoxides, a large class of compounds that contain the R – OOH chemical structure, exist in the gas phase in the atmosphere. These compounds are key to the chemistry of the atmosphere because of the role they play in the atmosphere's ability to process and ultimately remove chemical species. Two of the most abundant atmospheric hydroperoxides were measured as part of the Atmospheric Tomography (ATom) Mission, which collected samples of the atmosphere over the Pacific and Atlantic Ocean basins far from human influences. This paper presents a summary of

the global distribution of these hydroperoxides across the four different seasons (winter, spring, summer, and fall) and investigates the role that smoke from large-scale fires on the continents plays in altering the amount of atmospheric hydroperoxides above the Atlantic Ocean.

2.2 Introduction

Atmospheric hydroperoxides are a class of chemical compounds that are of key significance due to their role in altering the oxidizing power of the atmosphere via their connection to the atmosphere's main oxidant HO_x (OH and HO_2 radicals). Hydroperoxides consists of a wide variety of compounds with the linking trait of containing an ROOH functional group, of which hydrogen peroxide (H_2O_2) and methyl hydroperoxide (MHP, CH_3OOH) are generally the most abundant. H_2O_2 in the atmosphere is formed primarily through the self-reaction of HO_2:

$$HO_2 + HO_2 \longrightarrow H_2O_2 + O_2 \tag{2.1}$$

MHP primarily derives from the oxidation of methane (CH_4); CH_4 reacts with OH to form the methyl peroxy radical (CH_3OO) that subsequently reacts with HO_2 to form MHP:

$$CH_4 + OH \longrightarrow CH_3OO + H_2O \tag{2.2}$$

$$CH_3OO + HO_2 \longrightarrow CH_3OOH + O_2 \tag{2.3}$$

The photochemistry of other larger organic molecules, such as acetone, can also lead to methyl peroxy radical (CH_3OO) formation. Both the H_2O_2 and MHP formation reactions depend upon the local NO_x environment: high NO_x (NO and NO_2) limits the formation of H_2O_2 and MHP because NO competes with HO_2 for reaction with the intermediate peroxy radicals; low NO_x environments, such as occur in the remote atmosphere far from major NO_x sources, promote hydroperoxide formation. As a result of this competition, H_2O_2 and MHP are tracers for chemical regimes in which HO_2 + RO_2 chemistry is dominant.

Once formed, H_2O_2 and MHP have a lifetime of a day or two in the atmosphere. Physical processes such as deposition remove hydroperoxides in the boundary layer where turbulent winds are present (Walcek, 1987; Chang et al., 2004; Nguyen et al., 2015) whereas convection can move hydroperoxides to remote regions of the atmosphere, including the upper troposphere and lower stratosphere (Jaeglé et al., 1997, 2000). Hydroperoxides also undergo chemical loss through photolysis or reaction with OH, both of which release HO_x back into the atmosphere (Lee et al.,

2000). The relative importance of the different hydroperoxide loss mechanisms has a considerable impact on the distribution of H_2O_2 and MHP and results in highly variable hydroperoxide concentrations around the globe. Because H_2O_2 and MHP serve as both a reactive sink and a mobile reservoir of HO_x, understanding their distribution and the factors that contribute to this variability provides insight into the contribution of hydroperoxides to the global HO_x budget (Reeves and Penkett, 2003).

Several studies have investigated hydroperoxide distributions in the remote atmosphere, but due to the nature of sampling have typically been limited. Shipboard deployments have measured hydroperoxides in the remote marine boundary layer across several degrees of latitude (Jacob and Klockow, 1992; Weller and Schrens, 1993; Slemr and Tremmel, 1994; Martin et al., 1997; Kim et al., 2007; Fischer et al., 2015). Airborne measurements have typically sampled only one target area. Prior to this study, the most comprehensive aircraft campaign was the NASA Global Tropospheric Experiment (GTE) program in which hydroperoxides were measured during deployments sampling different paths in the western Pacific (September – October 1991 and January – February 1993), in the tropical Pacific (September – October 1996), and in the tropical Atlantic (September – October 1992) (Lee et al., 1998; O'Sullivan et al., 1999a). However, this campaign made only limited measurements in the polar and extra-polar regions or in the northern Atlantic, and was limited temporally. Other campaigns have filled in some of these gaps, such as aircraft flights in the Arctic and North Atlantic in fall 1997, winter-spring 2000, summer 2004, and spring-summer 2008 (Snow et al., 2003, 2007; Mao et al., 2010; Olson et al., 2012) or ground measurements made in Antarctica in the austral summers of 2000-2002 (Frey et al., 2005). However, with the exception of a satellite-based investigation of H_2O_2 above 5 km altitude (Allen et al., 2013), no studies have provided a comprehensive set of hydroperoxide measurements that capture remote atmospheric hydroperoxide distributions across latitude, longitude, altitude, and time of year.

Global measurements of H_2O_2 and MHP concentrations in the remote atmosphere with near pole-to-pole coverage were collected as part of the Atmospheric Tomography (ATom) Mission aircraft campaign that took place between summer 2016 and spring 2018. The goal of the campaign was to acquire a comprehensive suite of global-scale tomography data for reactive gases and aerosols in order to understand the chemical and physical processes controlling atmospheric composition (Prather

et al., 2017). These measurements were collected without consideration of cloud conditions, except when necessitated for aircraft safety or by air traffic control, thus reducing the clear-sky bias of many prior aircraft campaigns. The campaign sought to investigate the remote atmosphere over the Pacific and Atlantic Ocean basins, far from major land masses and anthropogenic influences. The remote atmosphere is where a significant portion of global atmospheric chemistry occurs, and comprises some of the cleanest, most sensitive areas of the atmosphere; it is therefore the region most susceptible to changing anthropogenic influences. However, the remote atmosphere is poorly sampled and therefore not well constrained in atmospheric models, hampering insight into how well current models capture the changing chemistry of the globe (Prather et al., 2018; Brune et al., 2020; Travis et al., 2020).

In this study, global climatological assessments of H_2O_2 and MHP across the four seasons based on observations from the ATom Mission, are presented for the first time. We discuss the chemical ionization mass spectrometry technique used to measure the hydroperoxide mixing ratios and how these techniques were implemented on the DC-8 during the ATom Mission. We then present the results of these measurements, including regional variations in H_2O_2 and MHP across the northern, mid, and southern Pacific and Atlantic Ocean basins. Finally, we highlight the significant impact of biomass burning in enhancing regional H_2O_2 production. Biomass burning has been posited as a source of atmospheric hydroperoxides, either through primary or secondary chemical production (Lee et al., 1997; Rinsland et al., 2007; Snow et al., 2007). Chapter 3 will further describe the chemical and physical controls on global hydroperoxide mixing ratios through comparisons between measurements and chemical models.

2.3 Methods

Atmospheric Tomography Mission

During the ATom Mission, over 20 unique instruments were installed aboard the NASA DC-8, which is a Douglas DC-8 jetliner aircraft that has been retrofitted to house the flying laboratory and has been in almost continual use by NASA for nearly 35 years. These instruments collected a variety of physical and chemical data, including meteorological parameters, actinic fluxes, reactive nitrogen species (NO_y), volatile organic compounds (VOCs), photochemical products and oxygenates, aerosols, greenhouse gases, O_3 depleting substances, and a variety of chemical tracers. For the majority of instruments, inlets located along the aircraft walls and windows brought ambient air into the aircraft cabin where the instrument

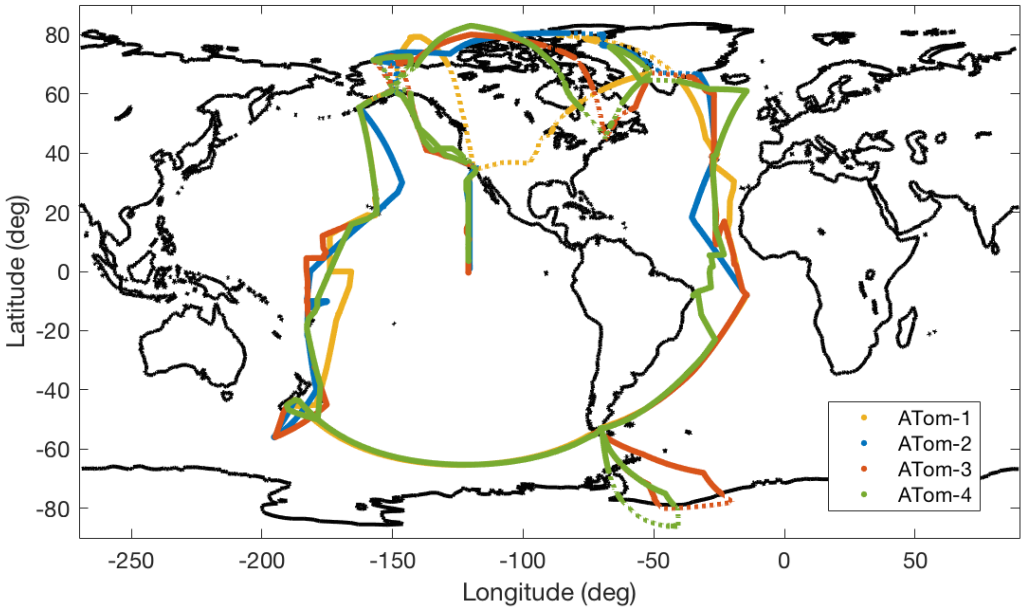

Figure 2.1: Map of the ATom campaign flight track. The four deployments encompass each of the four seasons (boreal listed): ATom-1 in August 2016 (summer), ATom-2 in February 2017 (winter), ATom-3 in October 2017 (fall), and ATom-4 in May 2018 (spring). Each deployment consisted of 11–13 flights with nearly continuous vertical profiling between 150 m and 13.5 km above ground level along the flight track. Excluded over land data is shown as dashed lines.

detectors and controls were located. The extensive payload aboard the DC-8 enables a wide range of chemical and physical phenomena to be investigated.

During ATom the DC-8 flew sequential vertical profiles over the remote Pacific and Atlantic Ocean basins in four separate month-long deployments. The deployments were scheduled to capture variation across each of the four seasons (boreal listed): ATom-1 in August 2016 (summer, 7/29/16–8/23/16), ATom-2 in February 2017 (winter, 1/26/17–2/21/18), ATom-3 in October 2017 (fall, 9/28/17–10/27/17), and ATom-4 in May 2018 (spring, 4/24/18–5/21/18). Each deployment consisted of 11–13 flights that followed a prescribed flight track to gather atmospheric cross-sectional data above the Pacific, Southern, Atlantic, and Arctic Oceans from latitudes spanning -85° to 85° (Figure 2.1). Two deployments, ATom-3 and -4, additionally included a flight to sample the atmosphere beneath the stratospheric O_3 hole above Antarctica. Along the flight track, the DC-8 underwent sequential slow ascents and descents to generate vertical profiles of the atmosphere, with profiles ranging from about 150 m to just under 13.5 km and therefore sampling from the marine boundary layer (MBL) to the upper troposphere and lower stratosphere (UTLS). Each profile (decent and

ascent) took approximately one hour of flight time. In total, approximately 320 profiles were collected over the four global circuits. These profiles were conducted to capture the large-scale variability that exists and to ensure unbiased sampling of the atmosphere. In addition, ATom was primarily flown over the remote ocean, but did pass over land masses due to requirements of the flight plan or travel logistics; all data present here have been filtered such that the data exclude measurements collected over land.

CIT-CIMS

Gas-phase hydroperoxides were measured using the California Institute of Technology Chemical Ionization Mass Spectrometers (CIT-CIMS), a dual instrument that combines a compact Time-of-Flight mass spectrometer (C-ToF, Tofwerk/Caltech) with a triple quadrupole mass spectrometer (Varian/Caltech). Both instruments employ a soft chemical ionization technique to detect oxygenated compounds with high sensitivity. The technique utilizes a CF_3O^- ion as a reagent that reacts with a variety of analytes to form anion products via two primary pathways: by transfer of a fluorine atom (Eq. 2.4) or by clustering with the analyte (Eq. 2.5).

$$X + CF_3O^- \longrightarrow X^-_{-H} \cdot HF + CF_2O \tag{2.4}$$

$$X + CF_3O^- \longleftrightarrow X \cdot CF_3O^- \tag{2.5}$$

The dominant pathway depends upon the acidity (or fluoride affinity) of the analyte, with less acidic compounds, such as hydroperoxides, more likely to undergo clustering with the reagent ion (Paulot et al., 2009a). Analytes that undergo fluoride transfer are detected at an m/z of analyte mass + 19 (Eq. 2.4) while analytes that undergo reagent ion clustering are detected at an m/z of analyte mass + 85 (Eq. 2.5). The CIMS technique and instrument details are further described in Crounse et al. (2006) and St. Clair et al. (2010) and summarized below, including updates to the instruments since previous publication.

The CIT-CIMS configuration onboard the NASA DC-8 consisted of the dual instrument bolted to the floor or wall of the interior of the aircraft with a shared inlet that extended to the outside of the aircraft. Ambient air flowed through a tapered aluminum inlet at a high flow rate traveling in the same direction as the aircraft; a fraction of the air was directed perpendicularly toward the instrument through a rear-cut inlet port. This inlet configuration enabled discrimination against large particles and other debris that had the potential to clog the inlet port. Upon redirection, the ambient air sample was brought to the interior of the aircraft through

a Pyrex glass tube, which was coated with a thin layer of fluoropolymer (Fluoropel PFC 801A, Cytonix Corp.) to reduce surface hydrophilicity and reduce loss to inlet surfaces. The air passed through the glass tube at a high rate (~40 m s^{-1}) and thereby further reduced wall effects. The glass tubing ended at the "Y-block", a junction that directed air into three separate streams: the C-ToF instrument, the triple quadrupole instrument, and the remainder exited the aircraft via an exhaust outlet (Figure 2.7).

For the C-ToF, the ambient air passed through a variable pinhole orifice and into a second Pyrex glass flow tube coated with hydrophobic fluoropolymer. The pinhole orifice automatically adjusted to control the flow tube pressure to a static set point (35 mbar) and resulted in a nominally constant mass flow of ambient air into the instrument (300–350 sccm) with relatively small variations caused by changing flow tube temperature. Upon entering the flow tube, the sample was diluted with with dry N_2 (1300 sccm) before interacting with the reagent ion. This dilution reduced the water mixing ratio as high water content interferes with analyte-ion clustering and increases background signals. The reagent ion was formed by passing 380 sccm of 1 ppm CF_3OOCF_3 in N_2 through a cylindrical ion source containing a layer of radioactive polonium-210 (Po-210, NRD LLC, ≤10 mCi). Ions are sampled into the mass filter through a pinhole orifice and then focused by a conical hexapole ion guide into the C-ToF mass spectrometer chamber. Compounds are separated in the mass spectrometer based on differences in their mass-to-charge ratio as an electric field accelerates them through the instrument. During ATom, the C-ToF data was used to report ambient mixing ratios for H_2O_2 (m/z = 119), hydrogen cyanide (HCN, m/z = 112), nitric acid (HNO_3, m/z = 82), peroxyacetic acid (PAA, m/z = 161), peroxynitric acid (PNA, m/z = 98), and sulfur dioxide (SO_2, m/z = 83 and 101), as well as MHP (m/z = 133) for ATom-4, at a 1 Hz frequency.

The ambient sample directed to the triple quadrupole mass spectrometer was diluted and ionized in a similar manner to that of the C-ToF. From the "Y-block", an approximately 1.5 m length of Teflon tubing carried the sample at a high flow to the "T-block", where a small flow (~350 sccm) passed through a pressure controlled pinhole orifice into the fluoropolymer-coated Pyrex flow tube (35 mbar). The sample was diluted with dry N_2 (1450 sccm) and mixed with a calibration gas (isotopically labeled MHP, CD_3OOH) then ionized with CF_3O^- before passing through a second pinhole orifice and a series of lenses into the mass spectrometer chamber. The mass spectrometer is a modified Varian 1200 GCMS that contains three quadrupoles. Upon entering the mass spectrometer, the first quadrupole per-

forms a mass filtration of the analyte stream; the selected primary ions pass to the collision-induced dissociation (CID) quadrupole region in which collision N_2 molecules causes fragmentation of the analyte ions; finally, a third quadrupole filters for specific secondary ions produced by the CID. This methodology enables the mass spectrometer to differentiate certain nominally isobaric compounds, which are indistinguishable on the C-ToF, by decomposing the parent ion into a unique pattern of secondary ions. As a result, analytes are detected by both the primary and secondary m/z signals. The triple quadrupole monitored MHP at $m/z = 133 \rightarrow m/z = 85$ and isotopically-labeled MHP calibration gas at $m/z = 136 \rightarrow m/z = 85$.

The flight pattern pursued during ATom resulted in a wide range of temperatures, pressures, and water vapor concentrations during sampling. Because the instrument measurements are sensitive to the temperature and water vapor mixing ratios in the ion-molecule reaction region (Figure 2.8), the CIT-CIMS was calibrated extensively in the laboratory, as well as during each ATom science flight. In the laboratory, the instruments were calibrated by introducing a known quantity of the desired compound — verified by FTIR, gravimetric analysis, or other analytical method — into the instruments and monitoring the signal as a function of water vapor. Pre-flight and in-flight calibrations were performed by introducing a small flow into the instrument from temperature-controlled diffusion vials containing either PAA or isotopically labeled MHP or a U-tube containing urea-H_2O_2. The reported MHP mixing ratios from the triple quadrupole instrument relied upon a continuous injection of labeled MHP (CD_3OOH) during the flights and used the ratio of ambient MHP to the labeled MHP to account for water vapor and temperature-dependent variations in the instrument sensitivity, a method that was introduced just prior to the ATom deployments. The ToF instrument sensitivity towards MHP declines rapidly at high water vapor and high temperature; therefore MHP mixing ratios are not reported above water mixing ratios of 7500 ppmv for ATom-4. In addition, the mass at which MHP is measured has a potential interference due to atmospheric methylene diol ($HOCH_2OH$, $m/z = 133$). Because this compound arises from formaldehyde and water, it is expected to be most prevalent in regions with high water vapor (e.g. the marine boundary layer), which corresponds to regions in which instrument sensitivity towards MHP is low (Figure 2.9). Further details about the calibrations as well as an estimate of the extent of the methylene diol interference are given in the Supporting Information.

In addition to calibrations, two forms of zeroing occurred periodically during science

flights to assess instrument background signals and interferences. A dry zero was performed by closing the inlet orifice, thereby preventing the ambient sample from entering the flow tube, and increasing the flow of dry N_2 to maintain 35 mbar in the flow tube. An ambient zero was performed by passing ambient air through a bicarbonate denuder and bicarbonate-coated nylon wool and palladium filter to remove compounds of interest but retain water vapor, thus monitoring background signals at the same relative humidity as was present in ambient samples. The data from each instrument were normalized to the sum of the ^{13}C reagent ion signal ($^{13}CF_3O^-$, m/z = 86) and reagent ion water cluster ($^{13}CF_3O^- \cdot H_2O$, m/z = 104) to correct for changes in the reagent ion current and then corrected for background interferences. A new synthetic approach to producing CF_3OOCF_3 was developed between ATom-2 and ATom-3, which greatly reduced known impurities in the synthetic mixture as the new CF_3OOCF_3 material reduced instrumental background signals for SO_2 and SF_6 by more than a factor of 50 (see the Supporting Information for further details). In addition, careful avoidance of using new PFA tubing in the plumbing reduced the background signals of m/z 133 in the ToF (likely arising from out-gassing of $CF_3C(O)OH$ from PFA) such that MHP could be measured from this instrument for ATom-4.

2.4 Results and Discussion

Global Cross Sections

The global hydroperoxide distribution shows characteristic latitude and altitude patterns, as can be seen in Figures 2.2 and 2.3. These figures show latitude-altitude cross-sections of global H_2O_2 and MHP, respectively, collected during each of the four ATom deployments; they do not make a distinction between the Pacific and Atlantic Ocean basins. Because hydroperoxide formation and major loss mechanisms are highly dependent on photochemistry, the subsolar point, the latitude at which the sun's rays are perpendicular to Earth's surface at noon, indicate where this photochemistry is most prominent. During the ATom deployments, the subsolar point varied from approximately $-19°$ to $-11°$ latitude in February, 13° to 20° in May, 10° to 18° in August, and $-14°$ to $-3°$ in October. In addition, the marine boundary layer height, which also affects hydroperoxide formation and loss, varied between approximately 50 m and 2500 m above sea level during the deployments.

For all four deployments, mixing ratios for both hydroperoxides peak in the equatorial region ($-20°$ to 20° degrees latitude); however, the range of latitudes over which

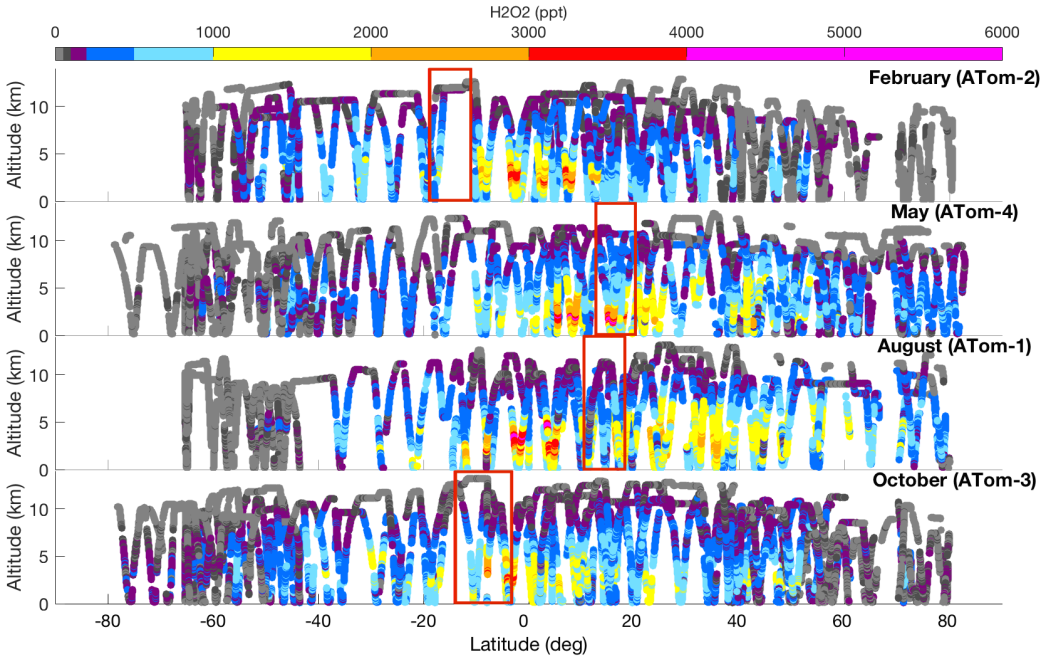

Figure 2.2: Mixing ratios of H_2O_2 across latitude and altitude. H_2O_2 mixing ratios dominate in the equatorial latitudes, but extend poleward with some progression due to time of year. Red boxes indicate the range of subsolar point latitudes during the deployment. Excludes data collected over land.

the hydroperoxide mixing ratios extend varies by season. Except for the northern hemisphere in August, H_2O_2 mixing ratios rarely reach appreciable levels in the polar regions (latitudes $>60°$ or $<-60°$). In February, high H_2O_2 mixing ratios (>1000 pptv; parts per trillion by volume) reach from latitudes of $-45°$ to $20°$, whereas in August high H_2O_2 mixing ratios reach a much wider and more northern latitudinal range of $-30°$ to near $70°$ (Figure 2.2). This shift follows the progression of sunlight and temperature as global photochemistry shifts northward in the boreal summer. Similarly, MHP mixing ratios show a seasonal shift hemispheric distributions, although the pattern is not as pronounced as is that of H_2O_2. In February, for example, high MHP mixing ratios (>1000 pptv) reach 30–40 degrees wider latitude range than those of H_2O_2 (Figure 2.3). This trend likely reflects the difference in hydroperoxide sources: H_2O_2 arises solely from HO_2 whereas MHP results from both HO_2 and CH_4 (Eq. 2.3). CH_4 has a long atmospheric lifetime ($\tau \sim 10$ years) and therefore is more well-mixed across latitudes, leading to a greater potential source distribution for MHP than for H_2O_2. In addition, MHP has a longer atmospheric lifetime than H_2O_2 because it is far less soluble ($\sim 10^3$ difference in Henry's Law constants; Lee et al. (2000)), leading to more efficient poleward transport.

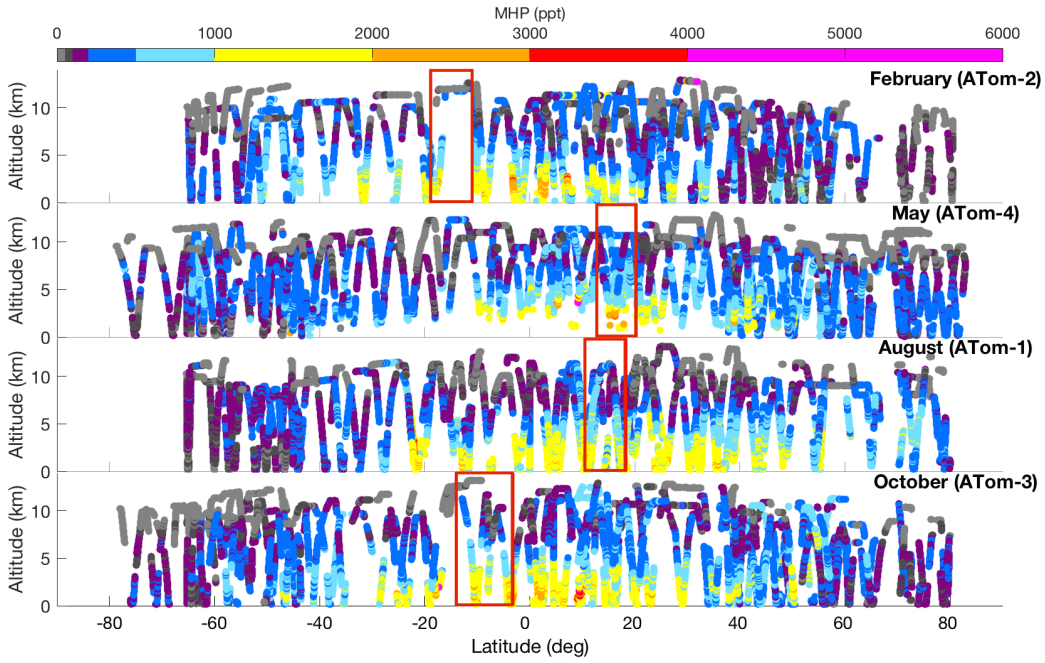

Figure 2.3: Mixing ratios of MHP across latitude and altitude. MHP mixing ratios show a wide distribution across latitudes as well as a shift between northern and southern hemispheric maximums due to time of year, though the pattern is not as pronounced as for H_2O_2. Red boxes indicate the range of subsolar point latitudes during the deployment. Excludes data collected over land.

The column variations in H_2O_2 and MHP mixing ratios show distinct patterns by season and latitude. For H_2O_2, the decrease with latitude is typically faster in the southern hemisphere than the northern hemisphere, though both are fastest in August. For the northern hemisphere, the column average of H_2O_2 mixing ratios declines by 4.3, 5.2, 5.2, and 4.7 pptv per degree latitude for February, May, August, and October, respectively; whereas in the southern hemisphere the column average decreases by 8.0, 4.5, 9.6, and 6.5 pptv per degree latitude for February, May, August, and October, respectively. By comparison Van Valin et al. (1987) measured a much faster decline of 40-50 pptv per degree of latitude increase, but measured over the continental United States rather than over the ocean in the remote atmosphere. The decline in column average MHP mixing ratios is very similar to that of H_2O_2, although note that the high water interference in the MHP measurements for ATom-4 (May) alters the averages for this deployment. In the northern hemisphere, the rate of column average MHP decrease is 4.9, 3.9, 5.0, 6.8 pptv/degree latitude while in the southern hemisphere, the decline is 7.1, 1.2, 7.1, and 9.0 pptv/degree latitude for February, May, August, and October, respectively.

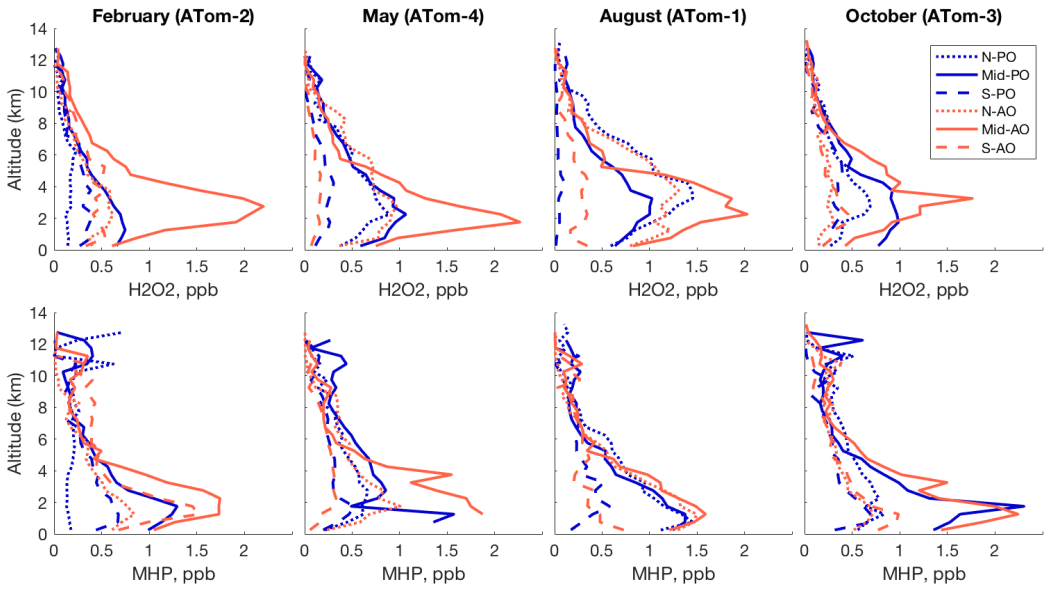

Figure 2.4: Average H_2O_2 and MHP mixing ratios with altitude for different ocean basin regions. The hydroperoxides are averaged over 0.5 km altitude bins and separated into north (20° to 60°) mid (−20° to 20°), and south (−60° to −20°) latitude bands of the Pacific (blue) and Atlantic (red) ocean basins.

Regional Profiles

The profiles of H_2O_2 and MHP mixing ratios averaged with altitude indicate clear structure that persists regardless of season. Figure 2.4 shows the ATom data averaged over 0.5 km altitude bins for the northern (20° to 60°), mid (−20° to 20°), and southern (−60° to −20°) latitude bands of the Pacific and Atlantic Ocean basins. In nearly all regions, the average H_2O_2 and MHP mixing ratios peak just above the boundary layer and decline with altitude in the free troposphere. For H_2O_2, this peak occurs between 2 and 4 km above the ocean surface while the peak MHP mixing ratio is typically at a slightly lower altitude (1 to 3 km). Both hydroperoxides exhibit a gradient in the marine boundary layers with lower mixing ratios close to the ocean surface, although this feature is more pronounced for H_2O_2. In the mid-Atlantic where the gradient is the strongest, maximum MHP mixing ratios are a factor of 1.3–1.7 times higher than within the boundary layer, compared with a factor of 2.5 – 4.1 times for H_2O_2. H_2O_2 has a higher Henry's Law coefficient than MHP (1×10^5 M atm^{-1} and 5×10^2 M atm^{-1} at 298K, respectively; Lee et al. (2000)) and therefore is more subject to deposition and wet scavenging that occurs in the turbulence of the mixed layer than MHP. Finally, the MHP profiles reveal a secondary peak in mixing ratios at altitudes above 8,000 m, not observed in the H_2O_2 profiles. Because MHP is less soluble than H_2O_2, it can be transported to the upper troposphere and lower

Table 2.1: Statistics[a] of H_2O_2 mixing ratios measured during ATom. Maximum[b] and mean[c] H_2O_2 mixing ratios are segmented into north (20° to 60°) mid (−20° to 20°), and south (−60° to 20°) latitude bands of the Pacific (PO) and Atlantic (AO) ocean basins, as well as the Arctic Ocean (latitudes >60°) and Southern Ocean (latitudes <−60°). All values are given in pptv.

		N-PO	Mid-PO	S-PO	N-AO	Mid-AO	S-AO	Arctic	S. Ocean
February	max	980	1300	1220	950	4030	1490	200	270
(ATom-2)	mean	110	270	170	270	540	180	30	50
May	max	2560	3720	1380	2580	6450	870	960	300
(ATom-4)	mean	330	410	130	420	550	90	170	30
August	max	2970	2950	510	2670	6190	1730	1920	140
(ATom-1)	mean	500	470	30	550	610	170	290	10
October	max	1760	2330	2960	1050	3630	1470	1080	540
(ATom-3)	mean	250	380	180	180	400	130	90	60

[a] Statistics based on 1 second time-averaged data

[b] Minimum values for each region are below detection limits

[c] Standard deviations on all mean values vary between a factor of 0.9–1.8 times the mean

Table 2.2: Statistics[a] of MHP mixing ratios measured during ATom. Maximum[b] and mean[c] MHP mixing ratios are segmented into north (20° to 60°) mid (−20° to 20°), and south (−60° to −20°) latitude bands of the Pacific (PO) and Atlantic (AO) ocean basins, as well as the Arctic Ocean (latitudes >60°) and Southern Ocean (latitudes <−60°). All values are given in pptv.

		N-PO	Mid-PO	S-PO	N-AO	Mid-AO	S-AO	Arctic	S. Ocean
February	max	7030	3320	1430	1470	3950	2290	460	480
(ATom-2)	mean	230	420	230	320	530	340	80	80
May	max	2120	2010	2970	2040	6690	1280	900	830
(ATom-4)	mean	300	410	220	320	320	170	160	160
August	max	2390	2490	4340	2460	2530	2420	1250	350
(ATom-1)	mean	460	540	240	480	480	280	280	80
October	max	2590	8640	1910	2200	4880	2360	800	540
(ATom-3)	mean	380	590	230	370	680	220	180	70

[a] Statistics based on 1 second time-averaged data

[b] Minimum values for each region are below detection limits

[c] Standard deviations on all mean values vary between a factor of 0.6–2.0 times the mean

stratosphere via convection (Jaeglé et al., 1997; Barth et al., 2016).

For the majority of the deployments, the average H_2O_2 mixing ratio was larger over the Atlantic Ocean than the Pacific Ocean (Figure 2.4). This trend is strongest in February, when the maximum H_2O_2 mixing ratio is 3 times higher in the mid-Atlantic than the mid-Pacific and the mean value is 2 times higher (Table 2.1). The trend weakens as the year progresses, but the mid-Atlantic to mid-Pacific ratio persists in other seasons (1.6–2.1 for the maximum and 1.1–1.3 for the mean H_2O_2). The mean H_2O_2 mixing ratios are similar to or slightly lower than those measured by other studies, which suggest H_2O_2 reaches mean mixing ratios of 1–3 ppbv (parts per billion by volume) in the remote marine lower troposphere in equatorial regions during the months of September–October (Lee et al., 1998; O'Sullivan et al., 1999a; Allen et al., 2013). In contrast to the mid-ocean regions, the northern and southern portion of the Atlantic and Pacific indicate a stronger seasonal role affecting H_2O_2. The northern and southern ocean basins vary by a factor of 2–3 between seasonal maximums or minimums in February and August (Table 2.1); however, this seasonality is not present in the southern Atlantic Ocean, suggesting that this region may be influenced by other factors.

The difference between the Atlantic and Pacific Ocean basins is smaller for MHP than for H_2O_2. Like H_2O_2, MHP is typically higher in the Atlantic than the Pacific; however the difference is much smaller than for H_2O_2 (Figure 2.4). For example, in August the mid-Atlantic and mid-Pacific maximum MHP mixing ratios are near parity. Similarly, the average MHP mixing ratio between the mid-Atlantic and mid-Pacific varies by a factor of 0.8–1.3, with mid-Atlantic dominating in May and August (Table 2.2). In May and October, both the northern and southern portions of the Atlantic and Pacific have very similar altitude profiles with weak altitude gradients and little difference between the two ocean basins (factor of 0.9–1.3 difference). In addition, the southern latitudes in February and the northern latitudes in August show profiles with shapes and peak average mixing ratios similar to those of the mid-ocean basins, indicating the wider latitudinal distribution of MHP than H_2O_2. Overall, the maximum MHP mixing ratios measured during ATom are similar but slightly higher than those measured previously which typically reached up to 1.25–5 ppbv in the equatorial regions and up to 2 ppbv in the northern Atlantic during the late boreal summer and early fall (Slemr and Tremmel, 1994; O'Sullivan et al., 1999a; Snow et al., 2007).

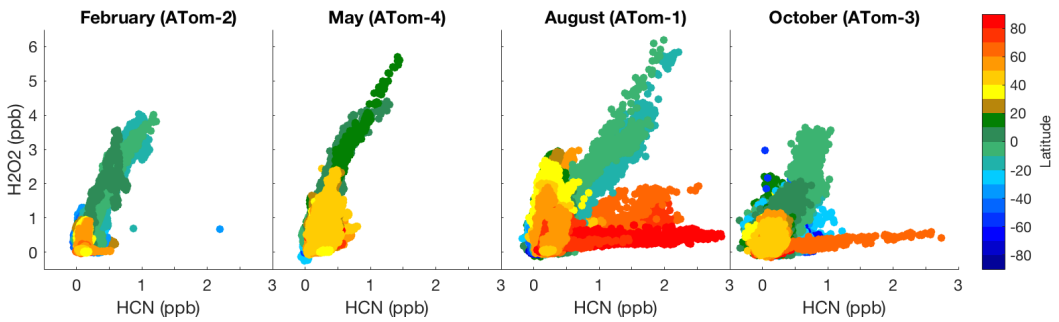

Figure 2.5: Correlation between H_2O_2 and HCN, colored by latitude. The periods of strong correlation between H_2O_2 and HCN, a major biomass burning tracer, indicates the production of H_2O_2 in regions influenced by biomass burning emissions. These biomass burning plumes occur primarily in the equatorial region (latitudes of $-20°$ to $20°$ throughout all times of the year sampled.

Influence of Biomass Burning

The large asymmetry between the tropical Atlantic and Pacific is correlated with the influence of biomass burning. Particle sampling during the ATom campaign revealed widespread biomass burning smoke throughout the remote troposphere, with both concentrated plumes in the Atlantic basin and extensive impact across the globe observed during all four deployments (Schill et al., 2020). As seen in Figure 2.5, enhanced H_2O_2 (including the highest measured mixing ratios during the campaign) correlate strongly with HCN. The primary source of HCN in the atmosphere is biomass burning combustion (Li et al., 2000; Singh et al., 2003); therefore the correlation of H_2O_2 with HCN and with another biomass burning tracer carbon monoxide (CO) indicates the significant evolution of H_2O_2 in the chemical aging of biomass burning plumes in the remote troposphere (Figure 2.10). These periods of H_2O_2 production occur primarily in the equatorial latitudes between $-20°$ and $20°$. Notably, high HCN mixing ratios are also observed during August and October in the Arctic (latitudes $>60°$), indicating biomass burning plumes in these regions as well. However, these plumes show only minor enhancements in H_2O_2. These northern plumes are likely less photochemically active due to the higher solar zenith angles and higher NO_x levels that compete for hydroperoxide precursor radicals.

In order to better assess the origin and aging of these biomass burning plumes, a 10-day back trajectory analysis was conducted along one minute intervals of the flight track (see the Supporting Information for further details). The aircraft encountered the regions of high H_2O_2 and HCN at altitudes between 1–4 km during either partial

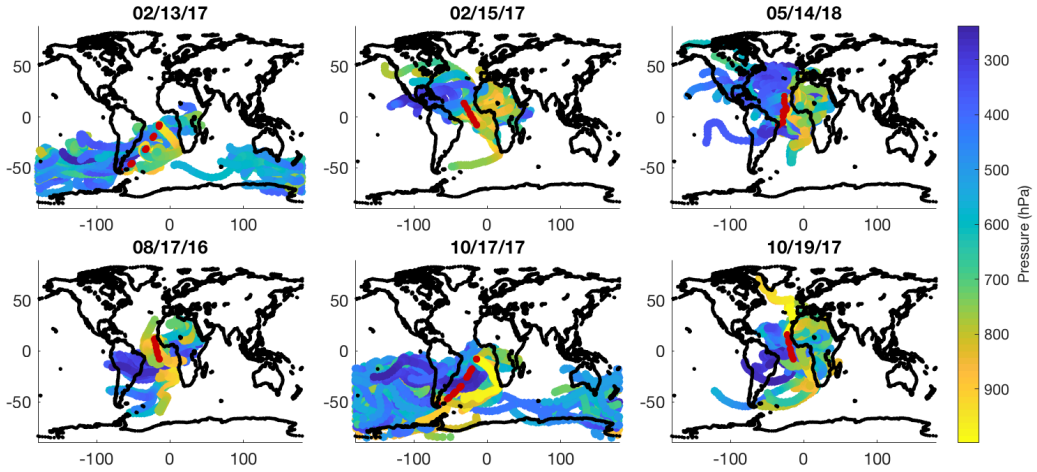

Figure 2.6: Average longitude, latitude, and pressure (altitude) for 10-day back trajectories of air masses encountered at each 1-minute interval along the flight track. Data and flight tracks (red) shown are portions of flights in which a strong photochemically processed biomass burning signature was detected based on a high H_2O_2 and HCN correlation (see Figure 2.5).

or full flights on 08/17/2016 (ATom-1), 02/13/2017 (ATom-2), 02/15/2017 (ATom-2), 10/17/2017 (ATom-3), 10/19/2017 (ATom-3), and 05/14/2018 (ATom-4). These flights all occurred between the southern tip of South America and the eastern coast of northern Africa, indicating that this influence extended to just the Atlantic Ocean basin. The results of the back trajectory analysis are shown in Figure 2.6 and indicate that the biomass burning plumes primarily originated from Africa, likely with some secondary influence from S. America, and produced H_2O_2 as the air mass migrated over the Atlantic Ocean during the course of several days as the bulk of the back trajectories passed at high altitudes over a portion of S. America and at low altitudes over a portion of the African continent or its coast.

The region of Africa that the air masses encountered influenced the latitudinal distribution of the H_2O_2 enhancement. In nearly all the deployments, the back trajectories passed over the northern portion of Africa before reaching the aircraft. Africa is the largest source of biomass burning emissions in the world and was responsible for 70% of the total burned area across the globe between 2001-2010 (Randerson et al., 2012). However, based on satellite imagery, African biomass burning occurs in the southern portion of the continent ($-50°$ to $-20°$ latitudes) during the boreal spring and summer months and shifts to the northern portion of the continent ($-20°$ to $0°$ latitudes) during the boreal fall and winter months (Roberts et al., 2009; Randerson

Table 2.3: Ratios and enhancement factors for H_2O_2 in the photochemically active biomass burning regions identified. Average and maximum H_2O_2 enhancement indicates H_2O_2 mixing ratios sampled during biomass burning influence areas compared with those sampled at the corresponding latitudes and altitudes in the Pacific Ocean basin. H_2O_2/CO indicates the ratio of these two species within the BB plumes.

		Avg En[a]	Max En[a]	H_2O_2/CO
February	ATom-2	2.0	3.1	0.010
May	ATom-4	1.6	1.8	0.020
August	ATom-1	2.2	3.6	0.021
October	ATom-3	1.3	1.2	0.021

[a] En = enhancement

et al., 2012). In the February and October deployments, the air masses passed either very close to or directly over the region of heaviest biomass burning (Figure 2.6). Correspondingly, these deployments show the greatest dispersion of biomass burning influence with high H_2O_2 across the full range of the S-AO and mid-AO. By contrast, the May and August deployments encountered air masses that likely had not passed directly over the regions of highest biomass burning intensity and the high H_2O_2 mixing ratios were limited to a section of the mid-AO. In addition, the wind speeds the aircraft encountered during the May and August deployments were low to moderate (speeds of 5–20 m/s) compared with those of the January and October deployments (typically 10–50 m/s), and therefore the air masses likely were more strongly diluted throughout the remote troposphere.

The magnitude of the H_2O_2 enhancement in biomass burning plumes varied by season. Typically, an enhancement ratio ($\Delta X = X_{plume} - X_{bckgnd}$ normalized to that of a long-lived tracer such as CO to account for dilution) would be used to compare in-plume mixing ratios with those of background air (Andreae, 2019). However, due to the nature of sampling during ATom, the enhancement ratio could not be measured directly. Instead, as a proxy the H_2O_2 enhancement ratios are calculated by finding the coordinates of the plume of strong H_2O_2-HCN correlation in the AO (generally between -50° or -10° to 20° latitudes and between 0.5 to 6.5 km altitude, see Figure 2.6 for exact portions of flight tracks) and comparing H_2O_2 mixing ratios in these plumes to H_2O_2 at the corresponding latitudes and altitudes of the PO (Table 2.3). The slope of the H_2O_2-CO linear regression within the AO plumes is also reported. The H_2O_2 mixing ratios encountered in the regions influenced by biomass burning were on average 150–760 pptv (factor of 1.3–2.2 times) higher than those in the

corresponding latitudes and altitudes of the PO (Table 2.3). Similarly, the maximum H_2O_2 mixing ratios were between 670–4470 pptv (factor of 1.2–3.6 times) higher. In each case, the strongest enhancement occurred in the boreal summer (August) followed by the austral summer (February).

This enhancement is likely the result of photochemical processing as the air mass was transported from the continent to the oceanic remote troposphere. The H_2O_2/CO ratios were 2×10^{-2} for most of the deployments, with the exception of February in which the ratio was 1×10^{-2} (Table 2.3; see the Supporting Information for details on the CO measurement). These values are higher than the 1.5×10^{-3} values measured by Yokelson et al. (2009) and the 4×10^{-3} value measured by Snow et al. (2007), but similar to the $(1–5)\times10^{-2}$ ratios of Lee et al. (1997). These variations are likely due to the photochemical age of the air mass sampled: Yokelson et al. (2009) sampled near the source of the fire (0.1–1.5 hours of plume aging) while Snow et al. (2007) and Lee et al. (1997) sampled 4–5 days downwind. The H_2O_2/CO ratio will increase with photochemical aging of the plume; for example, the H_2O_2/CO ratio can increase by a factor of 3–4 within the first 1.5 hours of aging (Yokelson et al., 2009). Thus, the H_2O_2 ratios indicate that the biomass burning influenced air masses sampled during ATom are likely on order of several days old (4–6), with ATom-2 perhaps sampling less photochemically aged air than the other deployments due to the much stronger winds encountered during this season.

MHP is also elevated in the biomass burning influenced regions, but unlike H_2O_2, it does not exhibit as strong enhancement or as clear correlation with biomass burning tracers. During February and May, the highest MHP mixing ratios were correlated with high HCN and CO and occurred in the same latitude and altitude as for H_2O_2 (Figures 2.11 and 2.12). However, there was significantly more scatter in the hydroperoxide to HCN correlations (R^2 of 0.79 for both seasons for H_2O_2 compared with 0.61 and 0.54, respectively, for MHP). The correlation between MHP and HCN was even weaker for the August and October deployments (R^2 of 0.86 and 0.58, respectively, for H_2O_2 compared with 0.14 and 0.34, respectively, for MHP). The lower correlation of MHP with these biomass burning tracers likely stems from the difference between H_2O_2 and MHP sources: H_2O_2 is solely formed from HO_x cycling while MHP forms from the interaction between both HO_x and CH_4 oxidation (Eq. 2.1 and 2.3). Unlike H_2O_2, MHP does exhibit an enhancement in mixing ratios that correlates with increased HCN and CO in the northern polar latitudes (above 60°) in August. This high latitude biomass burning influenced

air mass is likely highly influenced by continental pollution from N. America and contains higher mixing ratios of CH_4 (100 ppbv or 5% higher CH_4 in polar BB plume than equatorial BB plume), which may lead to higher CH_4 photochemical processing in the sunlit boreal summer month and result in the higher mixing ratios of MHP associated with this plume. Wet scavenging of H_2O_2 due to rain out may have also contributed to higher MHP than H_2O_2 in this plume.

2.5 Conclusions

The measurements collected using the CIT-CIMS during the four deployments of the ATom Mission show that atmospheric hydroperoxides exhibit highly variable mixing ratios that depend upon latitude, longitude, altitude, and season. H_2O_2 mixing ratios peak in the equatorial latitudes, reaching values as high as 3–6 ppbv in the mid Atlantic Ocean and 1–3.5 in the mid Pacific Ocean basin, depending on season. H_2O_2 mixing ratios in the mid latitudes varies with season, typically following the shift in sunlight, and declines at a yearly average rate of 5.8±2.0 pptv/degree latitude moving poleward. H_2O_2 peaks between 2–4 km above sea level, reflecting the balance between production that peaks at lower altitudes and faster loss due to wet and dry deposition at the surface. In addition, H_2O_2 mixing ratios are highly influenced by regional biomass burning events. Biomass burning plumes originating from Africa permeate the Atlantic Ocean basin and enhance H_2O_2 by a factor of 1.2–3.6 compared to the same latitudes in the Pacific Ocean basin.

MHP mixing ratios are similar to those of H_2O_2, but vary less with latitude. MHP mixing ratios are typically highest in the equatorial region, reaching maximum values within the atmospheric column of 3.0–8.6 ppbv in the Pacific Ocean and 2.5–6.7 ppbv in the Atlantic Ocean basin. These values are higher than those typically reported in the remote atmosphere (Slemr and Tremmel, 1994; O'Sullivan et al., 1999a; Lee et al., 2000; Snow et al., 2007). Higher MHP mixing ratios span from -60° to 60°, with some variation that follows the seasonal variations in sunlight. MHP mixing ratios decline at a yearly average rate of 8.1±2.5 pptv/degree latitude moving poleward. Like H_2O_2, MHP mixing ratios are highest in the lower troposphere just above the marine boundary layer, and exhibit a smaller gradient between the top of the marine boundary layer and the ocean surface than H_2O_2. MHP is not as strongly influenced as H_2O_2 by regional biomass burning emissions in the Atlantic Ocean basin, but this organic hydroperoxide does show some correlation with biomass burning tracers in February and May. In addition, MHP shows some correlation

with biomass burning influenced air in the northern polar latitudes in August which does not similarly exist for H_2O_2, likely due to either the differences in the sources or the differences in wet scavenging between these two hydroperoxides.

The distributions of H_2O_2 and MHP across geographical, altitudinal, and seasonal gradients reveal information about the atmospheric oxidizing capacity. Because these hydroperoxides arise primarily from HO_x chemistry and in direct competition with NO_x chemistry, regions where H_2O_2 and MHP are present in high mixing ratios are indicative of areas with strong photochemical HO_2 + RO_2 chemistry. This data set reveals the extensive nature of HO_2 + RO_2 chemistry in the remote troposphere, particularly in the equatorial Atlantic Ocean basin where influences such as emissions from biomass burning can increase HO_x generation. Finally, hydroperoxides alter the atmospheric oxidizing potential themselves through the physical and chemical processes that affect their atmospheric lifetimes. How these processes alter the global distribution of hydroperoxides and their effect on HO_x, including the role of H_2O_2 deposition and convective activity in vertical hydroperoxide transport, as well as comparisons to atmospheric models is explored in the next chapter.

Acknowledgments

Funding for this work was provided by NASA Grant No. NNX15AG61A. Additional support for H. M. A. was provided by the National Science Foundation Graduate Research Fellowship under Grant No. DGE-1144469 and additional support for M. J. K. was provided by the National Science Foundation Grant No. 1524860. The authors would like to thank the organizers of the ATom Mission, particularly S. C. Wofsy and T. B. Ryerson, for providing the opportunity to gather these data. We would also like to thank E. Czech, D. Jordan, the people at ESPO, as well as the pilots and crew of the DC-8 for the infrastructural support that made these measurements possible.

Data Availability

The data presented in this paper are available at https://doi.org/10.3334/ORNLDAAC/1581.

2.6 Supporting Information

Introduction

This supporting information provides further details on the analytical methods used to derive data and to support conclusions from this study. The instrument schematic (Figure 2.7), instrument calibration discussion (Figure 2.8), and CF_3OOCF_3 supple-

ment the CIT-CIMS description in the main paper by providing specific details on how the H_2O_2 and MHP data were collected and how mixing ratios were generated from raw signal. The discussion on the potential interference in the MHP measurement provides a potential bound on the extent to which a second atmospheric chemical species may appear at the mass used to measure MHP (Figure 2.9). The back trajectory analysis discussion provides further details on the methodology used to generate Figure 2.6 in the main text. The biomass burning correlations (Figures 2.10, 2.11, and 2.12) supplement Figure 2.5 and the discussion of the influence of biomass burning on hydroperoxides by showing the relationship between H_2O_2 or MHP and biomass burning tracers (HCN and CO) mentioned in the main text and by describing the instrumentation used to measure CO.

Instrument Schematic

A simplified schematic of the key components of the CIT-CIMS aboard the NASA DC-8 is given below. The CIT-CIMS directs air from outside the aircraft into the instrument via a partially-stopped tapered aluminum inlet from which a fraction of the air is directed perpendicularly at a high flow rate into the cabin using a rear-cut inlet port. The ambient air arrives at the "Y-block" which splits the sample into three separate streams to either the C-ToF instrument (300-350 sccm), the triple quadrupole instrument (~350 sccm), or an exhaust port (>1000 sccm) by which the majority of the air exits the aircraft. A small stream may also be diverted to the ambient zeroing system that consists of a bicarbonate denuder and bicarbonate-coated nylon wool filter to assess background signals at ambient water vapor concentrations. Before entering either the C-ToF or the triple quadrupole, the ambient air sample is diluted with N_2 (factor of ~5) in the flow tube and mixed with CF_3O^- in the ion-molecule mixing region. The CF_3O^- forms from gaseous CF_3OOCF_3 (1 ppm CF_3OOCF_3 in N_2) ionized by a cylindrical ion source. The sample then enters the mass spectrometer chamber.

Finally, two types of calibration gases may be used prior to or during flights: the "cold cal" and the "hot cal" systems. The cold cal system is used extensively by the triple quadrupole and periodically by the ToF instrument and consisted of peroxyacetic acid (PAA,CH_3CO_3H), urea-H_2O_2, and isotopically labeled MHP (CD_3OOH) at 0 °C to maintain a constant temperature and to slow hydroperoxide decomposition. The hot cal system is periodically occasionally used and consisted of acetic acid (AA, CH_3COOH) and ethylene glycol ($(CH_2OH)_2$) maintained at 50 °C. Both cal systems are controlled to a constant pressure (2000 mbar) and constant flows (ranging from

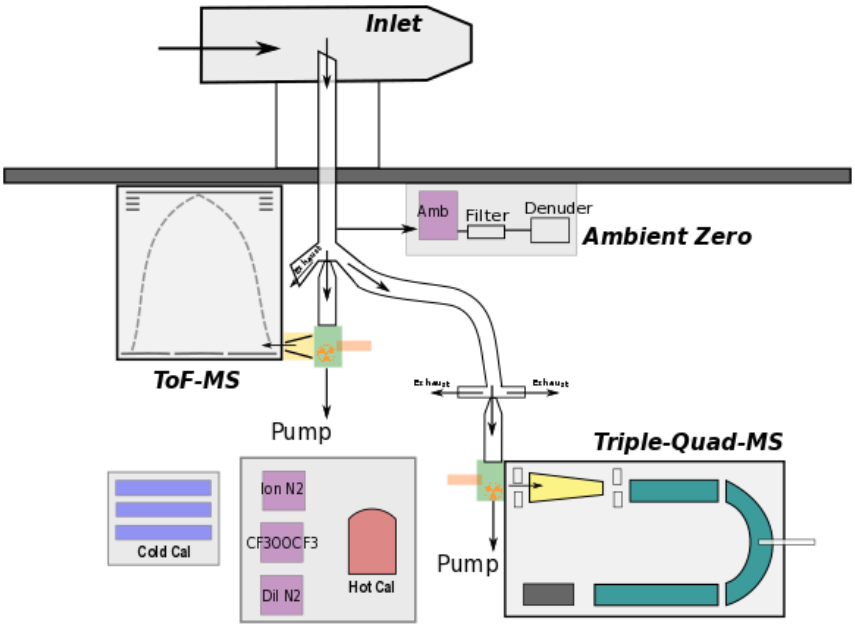

Figure 2.7: A simplified schematic of the key components of the CIT-CIMS aboard the NASA DC-8 aircraft. A more detailed version of a previous iteration of the ToF schematic can be found in Crounse et al. (2006) and of the triple quadrupole in St. Clair et al. (2010).

5–55 sccm) are maintained through the use of glass critical orifices. A more detailed description of a previous iteration of the ToF instrument can be found in Crounse et al. (2006) while a more detailed description of the triple quadrupole can be found in St. Clair et al. (2010).

Instrument Calibration

CIT-CIMS signals are sensitive to variations in temperature and water vapor in the instrument's ion-molecule reaction region and therefore must be accounted for using temperature and water-dependent calibrations. The ToF H_2O_2 signal (m/z 119) was calibrated in the laboratory for these dependencies by introducing a known quantity of H_2O_2 into the flow tube and either (1) measuring the signal under dry conditions at 298 K to assess the absolute calibration; (2) introducing water vapor using a variable flow from a Teflon pillow bag with a known mixing ratio of water vapor in N_2 while maintaining a constant flow tube pressure (35 mbar) and temperature, to determine the water sensitivity; or (3) varying temperature by using LN2 and heat gun to cool and heat the flow tube (in lab) under low water conditions or by in-flight calibrations across various temperatures (in field) to determine the temperature dependency. Figure 2.8 shows the results of these calibrations indicating how the ToF H_2O_2

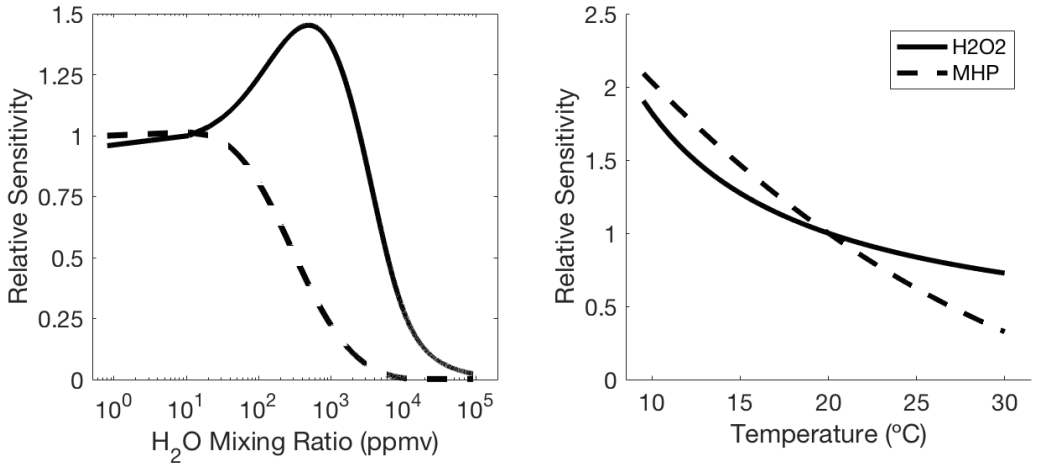

Figure 2.8: Relative sensitivity of ToF signals for H_2O_2 (m/z 119, solid) and MHP (m/z 133, dashed) as a function of the water mixing ratio in the instrument flow tube (left) or as a function of instrument flow tube temperature (right) for the range of water and temperature encountered during the ATom campaign.

signal changes with water and temperature. The H_2O_2 calibrations were verified during the ATom deployments prior to each flight by the addition of a small flow of calibration H_2O_2 through urea-H_2O_2/glass-wool mixture contained in a U-tube and temperature-controlled to 0 °C, along with a variable flow of water vapor from N_2 bubbled through distilled water. In addition, H_2O_2 calibrations were conducted approximately once every three hours during ATom flights.

MHP observations from the ATom Mission were derived from the triple quadrupole and the ToF instrument, which were calibrated using different methods. MHP mixing ratios from the triple quadrupole, reported for the majority of the ATom deployments, were calculated by comparing the ambient MHP signal (m/z 133 → m/z 85) to the signal from a standard addition of isotopically labeled MHP (CD_3OOH, m/z 136 → m/z 85). The absolute calibration of the labeled MHP source was found in the laboratory using an FTIR cross section of 3.20×10^{-19} molecule^{-1} at 2963.8 cm^{-1} (Niki et al., 1983). During the deployments, the calibration source was kept in a diffusion vial maintained at a constant temperature (0 °C) and pressure (2 bar) and a constant output was assumed. For ATom-4, changes in the synthetic approach to generate the reagent ion precursor, CF_3OOCF_3, combined with exclusion of new PFA tubing from the system, resulted in instrumental m/z 133 backgrounds that were low enough to enable the ToF to report MHP. We have found new PFA tubing has relatively high emissions of $CF_3C(O)OH$, which reacts with CF_3O^- to yield a product ion ($CF_3C(O)O^- \cdot HF$, m/z 133) and has the same nominal mass

as that of MHP. The ToF was calibrated for MHP by comparing changes in the m/z 136 isotopically-labeled MHP calibration source to changes in flow tube water and temperature collected during ATom preflight and in-flight calibration periods. Figure 2.8 shows the results of these comparisons indicating how the ToF MHP signal changes with water and temperature. Absolute MHP mixing ratios were found by comparing the relative ToF MHP signals to calibrated Triple signals.

Uncertainty in the CIT-CIMS measurements during ATom arose from a combination of uncertainty in instrument precision, background corrections, and in each of the applied calibrations: water-dependency, temperature-dependency, and absolute conversation factor. The uncertainty in instrument precision and in the absolute conversion factor, arising primarily from uncertainty in FTIR fits, persists across all measurement regimes and deployments. For the ToF H_2O_2 and MHP, this uncertainty is 50 pptv + 30% of the measurement value; for the triple quadrupole MHP, this uncertainty is 25 pptv + 30% of the measurement value. Other than the absolute calibration, the dominant source of uncertainty for the ToF is often the uncertainty in the background. For the triple, the dominant source of uncertainty is the uncertainty in the water-dependent sensitivity curves, which leads to an overall instrument uncertainty that is humidity dependent. In particular, the CIT-CIMS sensitivity toward hydroperoxides declines rapidly at high water vapor mixing ratios (above $\sim 10^3$ ppmv in the instrument flow tube, Figure 2.8), resulting in very high uncertainty in regions such as the marine boundary layer. Due to this decline in sensitivity, ToF MHP mixing ratios are not reported above 1.5×10^3 ppmv of H_2O in the flow tube, or ambient H_2O mixing ratios of 7500 ppmv.

Synthesis of CF_3OOCF_3

Beginning with ATom-3, the CIT-CIMS switched to using CF_3OOCF_3 reagent (precursor to CF_3O^- ion) obtained from a new source. Prior to this change, we gratefully acquired CF_3OOCF_3 from talented synthetic chemists at Clemson University (Darryl DesMarteau and more recently Joseph Thrasher). This material was generated through methods largely developed by DesMarteau (Marteau, 1970). While generally being quite pure, this material contained trace levels of several sulfur species, including SO_2 and SF_6, which proved difficult to remove from the main material and severely limited the CIMS ability to detect ambient SO_2. In an effort to overcome this limitation, we have developed a new synthetic route to CF_3OOCF_3. This synthesis will be described in detail in a separate manuscript. However, in short, CF_3OOCF_3 is formed from the photolysis of trifluoroacetic anhydride in the gas

phase, collected and purified, and finally thermally converted to CF_3OOCF_3 as has been described before (Marteau, 1970; Hohorst et al., 1973). This results in material containing more than 50 times less sulfur compounds (SO_2 and SF_6) than the material obtained from Clemson, and thus reduces the CIMS instrumental SO_2 background signals from ~3 ambient ppbv to <50 pptv for dry conditions.

Potential Interference in the MHP Measurement

Laboratory investigations indicate that a second compound, methylene diol (mediol, $HOCH_2OH$), is measured with high efficiency on the CIT-CIMS at the same mass as MHP. This compound is detected as $HOCH_2OH \cdot CF_3O^-$ at m/z 133 on the ToF and at both triple quadrupole masses of m/z 133 $\rightarrow$ m/z 85 and m/z 133 $\rightarrow$ m/z 133. Because MHP appears only at one of these fragment masses, mediol can be distinguished and has been observed in ambient measurements when both fragment masses are sampled. However, analytical challenges in obtaining a precise known and stable quantity of mediol preclude an accurate calibration of the instrument sensitivity towards the diol. In addition, the m/z 133 $\rightarrow$ m/z 133 mass has not been measured over the range of temperatures and water vapor mixing ratios needed to assess the variations in the relative ratio of the m/z 85 to m/z 133 fragments over the temperature and humidity regimes sampled during ATom. Instead, in this section we use estimated Henry's Law coefficients and HCHO measurements to assess the magnitude of mediol mixing ratios in the atmosphere and thus the potential for methylene diol to impact the CIT-CIMS MHP ambient observations.

Mediol exists in the atmosphere in both the gas and aqueous phase due to its formation from the hydration of formaldehyde. This conversion proceeds via:

$$HCHO_{(g)} \longleftrightarrow HCHO_{(aq)} \tag{2.6}$$

$$HCHO_{(aq)} + H_2O \longleftrightarrow CH_2(OH)_{2(aq)} \tag{2.7}$$

$$CH_2(OH)_{2(aq)} \longleftrightarrow CH_2(OH)_{2(g)} \tag{2.8}$$

The equilibration time for dissolved HCHO and methanediol is very fast (k = $2.04\times10^5 e^{-2936/T}$) s^{-1} for the forward reaction of Eq. 2.7) and in solution approximately 99% of formaledhyde has been hydrated to the diol ($K_{eq} = e^{3769/T-5.494}$) (Winkelman et al., 2002). However, the Henry's Law coefficient for mediol has not been previously reported and therefore the extent to which Eq. 2.8 occurs remains uncertain. The closest analogue with a measured Henry's Law coefficient is hydroxymethyl hydroperoxide (HMHP, $HOCH_2OOH$, 1.7×10^6 M atm^{-1} at 298 K), which has a reported temperature-dependent coefficient (Burkholder et al., 2015).

Another analogues are ethylene glycol (HOC_2H_4OH, 6.6×10^5 M atm^{-1} at 298 K) and several higher carbon diols that have Henry's Law coefficients in the range of 10^5 to 10^6 M atm^{-1} at 298 K.

Several laboratory studies were conducted to verify the expected order of magnitude for the Henry's Law coefficient of mediol. Formaldehyde was prepared by gently heating crystalline para-formaldehyde (Sigma-Aldrich) under vacuum and collecting the resulting vapor in two successive cryotraps: a −65 °C trap to collect impurities and a -196°C to collect monomeric HCHO, which was verified using FTIR. Experiments were conducted by filling a ~250 L Teflon bag with dry air and adding 300–400 ppmv HCHO. Liquid distilled water (0.5–1 L) was added to the bag by either 1) pouring the H_2O directly into the bag and allowing it to collect at the bottom or 2) placing a filled beaker directly inside the bag. For the later, a stir bar was added to the beaker and placed on a stir plate to ensure exchange between the air-liquid interface. The headspace in the Teflon bag was monitored using the triple quadrupole for up to 3 days. From these experiments, the Henry's Law coefficient is calculated using the ratio of HCHO added to the bag and mediol produced at the end of each experiment (assuming a standard instrument sensitivity) as well as the Henry's Law coefficient of HCHO reported in Burkholder et al. (2015). These laboratory experiments indicate that the mediol Henry's Law coefficient is on order of $10^{(7\pm1)}$ M atm^{-1} at room temperature, suggesting that the HMHP Henry's Law coefficient is a good proxy for that of mediol.

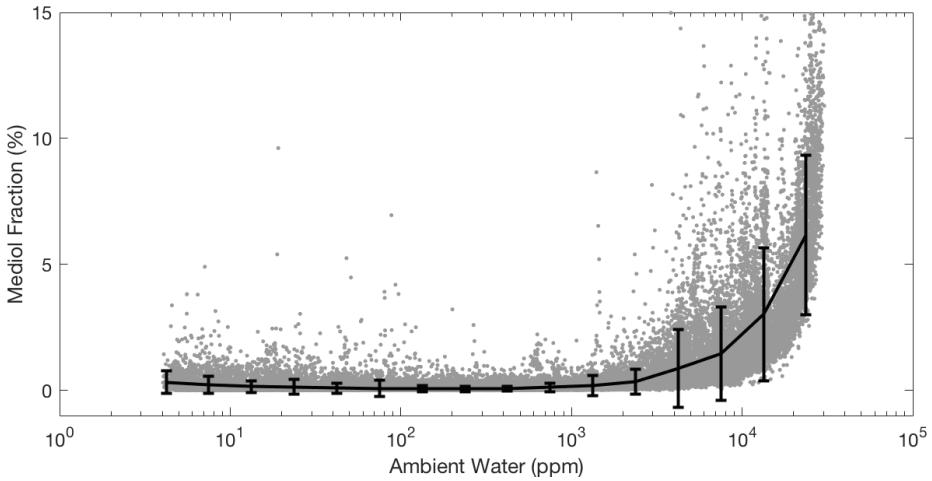

Figure 2.9: Estimated contribution of mediol to the m/z 133 signal on the CIT-CIMS, relative to the MHP contribution, over the range of ambient water encountered during the ATom campaign. Solid black line indicates the average and error bars indicate one standard deviation.

The extent of the potential mediol interference in the m/z 133 signal during the ATom campaign is estimated using measured HCHO mixing ratios and the reported temperature-dependent Henry's Law coefficient for HMHP, assumed to be similar to that of mediol. HCHO was measured onboard the NASA DC-8 during the ATom campaign using the in situ airborne formaldehyde (ISAF) instrument that employs laser induced fluorescence (LIF) to measure atmospheric HCHO with high sensitivity. The estimated mixing ratios of gas-phase mediol in the regions of the atmosphere sampled during ATom range from below detection limits (<1 pptv) to a maximum of 12 pptv. However, as indicated in Eq. 2.7, mediol is most prevalent in regions with high water vapor, which corresponds to regions with very low MHP sensitivity on the CIT-CIMS. As mentioned above, analytical challenges preclude obtaining a water-dependent calibration of mediol on the CIT-CIMS; instead, we assume a scenario in which mediol interactions with the reagent ion behave similarly to that of HMHP and instrument sensitivity increases with increasing water vapor. Using the water-dependent calibration of HMHP as an analogue for the diol, the CIT-CIMS may be up to ~150 times more sensitive to mediol than to MHP at the highest water vapor mixing ratios. The relative contribution of mediol to the m/z 133 signal during ATom thus likely varies from <1% in the free troposphere to 10% or higher (max of 30%) in the marine boundary layer (Figure 2.9). This interference may additionally help explain anomalously low convective transmission of MHP observed previously (see, for example, Barth et al. (2016)).

Back Trajectory Analysis

Back trajectories were calculated using the Traj3D model (Bowman, 1993; Bowman and Carrie, 2002) run with the National Centers for Environmental Predictions (NCEP) Global Forecast System (GFS) 0.5° by 0.5° resolution meteorology. A cluster of 245 trajectories was initialized in a cube with dimensions of 0.3° longitude by 0.3° latitude by 20 hPa pressure centered on one minute intervals on the aircraft position along the flight track and run backwards for 10 days. The latitude, longitude, and pressure altitude for each of the 245 trajectories were then averaged to a single latitude, longitude, and pressure for each one minute point along the flight track.

Biomass Burning Correlations

Atmospheric CO, CH_4, and CO_2 were measured using the NOAA Picarro (G2401m, Picarro, Santa Clara, CA), a commercial instrument that uses wavelength-scanned cavity ring down spectroscopy (WS-CRDS) as a detection method. CRDS is a time-

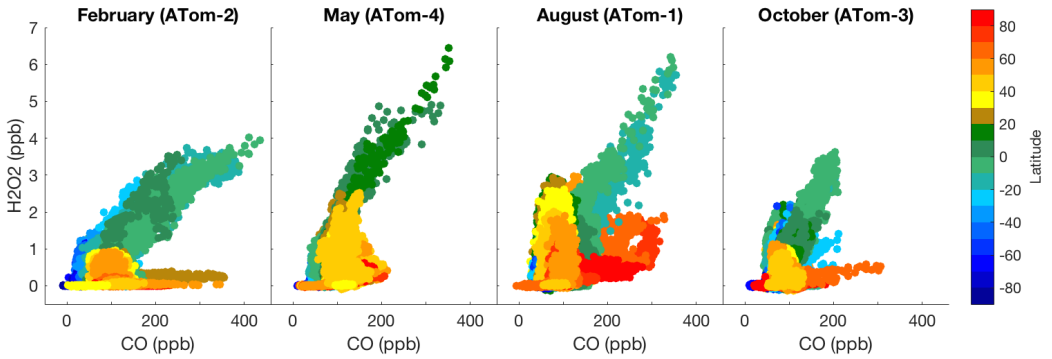

Figure 2.10: Correlation between CO and H_2O_2 for the ATom deployments, colored by latitude. The strong correlation between H_2O_2 and CO, a major biomass burning tracer, indicates the production of H_2O_2 in regions influenced by biomass burning emissions, primarily in the equatorial region (latitudes of $-20°$ to $20°$) throughout all times of the year sampled.

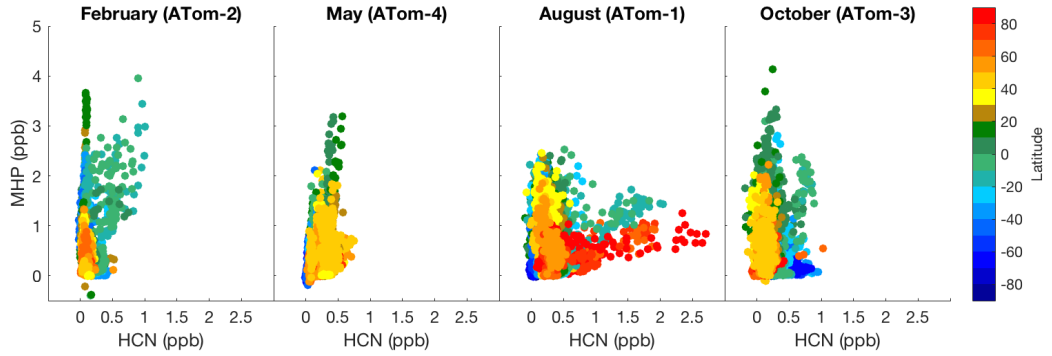

Figure 2.11: Correlation between HCN and MHP for the ATom deployments, colored by latitude. MHP has a moderate to very low correlation with the biomass burning tracer HCN in regions where the correlation of this tracer with H_2O_2 is very high (latitudes of $-20°$ to $20°$). However, MHP does show some enhancement with high HCN at polar latitudes ($>60°$) in August.

based measurement employing a near-infrared laser to measure spectral properties of compounds in an optical measurement cavity with an effective path length of up to 20 km. The NOAA Picarro instrument on ATom was modified to have a lower cell pressure set point (80 torr instead of 140 torr) as well as to have a shorter measurement interval (~1.2 seconds for ATom-1 and -2, ~ 2.0 seconds for ATom-3 and -4, compared with ~2.4 seconds originally) by reducing the number of CO spectroscopic peak scans. As a result, the CO measurement is slightly less precise than in the original configuration (1σ of the raw 1-2 second measurements was ~9 ppb for ATom-1 and -2 and ~4.5 for ATom-3 and -4). CO measurements are reported with 1 Hz frequency for ATom-1 and -2 and with 0.5 Hz frequency for

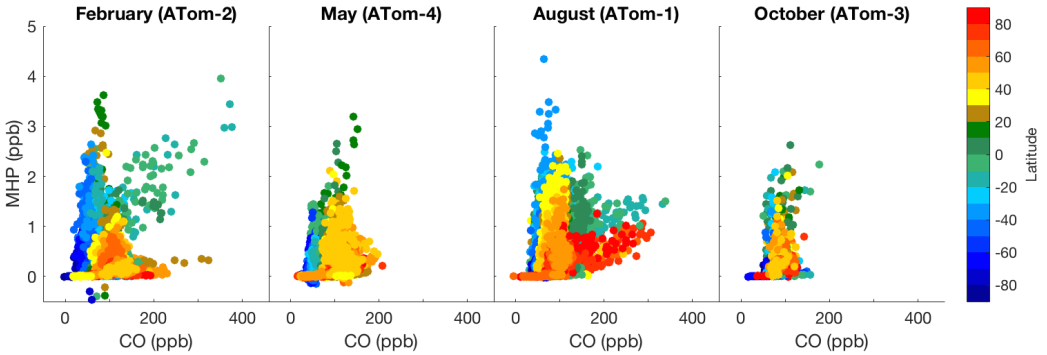

Figure 2.12: Correlation between CO and MHP for the ATom deployments, colored by latitude. MHP has moderate to low correlation with the biomass burning tracer CO in the regions where the correlation of this tracer with H_2O_2 is very high (latitudes of $-20°$ to $20°$).

ATom-3 and -4. See Crosson (2008) and Chen et al. (2013) for further details.

Chapter 3

HYDROGEN PEROXIDE AND METHYL HYDROPEROXIDE IN THE REMOTE ATMOSPHERE: CHEMICAL AND PHYSICAL CONTROLS

3.1 Abstract

Hydrogen peroxide (H_2O_2) and methyl hydroperoxide (MHP, CH_3OOH) serve as HO_x (OH and HO_2 radicals) reservoirs and therefore as useful tracers for regions with strong HO_x chemistry. Both hydroperoxides were measured during the 2016–2018 Atmospheric Tomography Mission (ATom) as part of a global survey of the remote troposphere over the Pacific and Atlantic Ocean basins conducted using the NASA DC-8 aircraft. These observations are compared to two photochemical models, a diurnal steady-state box model and the global chemical transport model GEOS-Chem, in order to assess the relative contributions of chemical and physical processes to the global hydroperoxide budget and their impact on atmospheric oxidation potential. We find that the models systematically under-predict H_2O_2 by 5–20% and over-predict MHP by 40–50% relative to measurements, with this discrepancy even higher in certain regions of the atmosphere. In the marine boundary layer, over-predictions of H_2O_2 are used to estimate H_2O_2 average deposition velocities of 1.0–1.32 cm s^{-1}, depending on season, which potentially contributes to up to 5–10% of HO_x loss in this region. The upper troposphere and lower stratosphere (UTLS) show the strongest under-predictions of MHP and over-predictions of H_2O_2, on average 2–3 times difference compared with the measurements, and the discrepancy is most prominent when the air mass has a high probability of recent convective influence.

Plain Language Summary

Hydrogen peroxide (H_2O_2) and methyl hydroperoxide (MHP, CH_3OOH) in the atmosphere can act as reservoirs for one of the main drivers of atmospheric chemistry, HO_x (HO_x = OH and HO_2). Both H_2O_2 and MHP were measured during the 2016–2018 Atmospheric Tomography Mission (ATom), which investigated the atmosphere over the oceans far from direct human influence. The measurements are compared to two types of models to assess our understanding of the chemical and physical process that affect the concentrations of H_2O_2 and MHP and their impact on the

chemistry of the surrounding area. We find that these models consistently predict H_2O_2 to be lower and MHP to be higher than was measured during ATom. We then use the discrepancy between the model and the measurements to investigate the role of deposition (removal of compounds from the Earth's atmosphere due to interactions with surfaces and with liquid water) on H_2O_2 in the lowest portion of atmosphere and the role of convection (vertical transport during storms and other meteorological events) on MHP in the upper portions of the atmosphere.

3.2 Introduction

Hydrogen peroxide (H_2O_2) and methyl hydroperoxide (MHP, CH_3OOH) are of key importance in the atmosphere because of their role in the cycling of the atmosphere's main oxidant HO_x (OH and HO_2 radicals). They are both reservoirs of HO_x due to their formation from HO_x chemistry. H_2O_2 arises primarily via the HO_2 self-reaction:

$$HO_2 + HO_2 \longrightarrow H_2O_2 + O_2 \tag{3.1}$$

Whereas MHP arises primarily via the reaction of HO_2 with the methyl peroxy radical (MPR, CH_3OO), which predominately comes from the reaction of methane (CH_4) with OH in the atmosphere. Although the photochemistry of other larger organic molecules, such as acetone, can also lead to MPR. MHP production from methane oxidation proceeds as:

$$CH_4 + OH \xrightarrow{O_2} CH_3OO + H_2O \tag{3.2}$$

$$CH_3OO + HO_2 \longrightarrow CH_3OOH + O_2 \tag{3.3}$$

The formation of H_2O_2 and MHP is highly dependent on the presence of NO_x (NO and NO_2) and mostly occurs in low NO_x environments. High NO_x limits their production because NO competes with HO_2 for reaction with the peroxy radical precursors (HO_2 and MPR) to instead form HNO_3 or NO_2 and CH_3O (decomposes to HCHO and HO_2). The abundance of H_2O_2 and MHP is thus indicative of a key branching in the oxidative chemistry of the troposphere: whether peroxy radicals react with HO_2 leading to radical termination or react with NO leading to radical propagation. This branching has particular consequences for atmospheric odd oxygen (O_x, comprising O_3 and the compounds with which it rapidly cycles) as the former leads to loss of O_x whereas the later leads to production of O_x.

Both H_2O_2 and MHP undergo photochemical loss via photolysis or reaction with

OH that return HO_x to the atmosphere. For H_2O_2, these losses are:

$$H_2O_2 + h\nu \longrightarrow 2OH \tag{3.4}$$

$$H_2O_2 + OH \longrightarrow HO_2 + H_2O \tag{3.5}$$

For MHP, these losses directly return HO_x as well as form formaldehyde (HCHO) which may further react to return HO_x to the atmosphere.

$$CH_3OOH + h\nu \longrightarrow CH_3O + OH \tag{3.6}$$

$$CH_3O \longrightarrow HCHO + HO_2 \tag{3.7}$$

$$CH_3OOH + OH \xrightarrow{\sim 0.7} CH_3OO + H_2O \tag{3.8}$$

$$\xrightarrow{\sim 0.3} HCHO + OH + H_2O \tag{3.9}$$

The branching ratio of the MHP + OH reaction varies between 0.65–0.83 in favor of CH_3OO formation, with a recommended average of 0.70 (Niki et al., 1983; Vaghjiani and Ravishankara, 1989; Atkinson et al., 2006; Anglada et al., 2017). For both hydroperoxides, photolysis recycles HO_x and results in a net of no change to total HO_x while reaction with OH is net oxidant consuming. However, hydroperoxide photochemical loss may not occur in the same region as their formation, resulting in transport of HO_x to areas that may have very different chemical regimes (e.g. Jaeglé et al. (2000)).

H_2O_2 and MHP are also subject to loss through wet and dry deposition that removes these HO_x reservoirs from the atmosphere, likely permanently. Deposition is separately parameterized as two distinct processes: dry deposition, which is the removal of gases or particles from the atmosphere due to impaction onto land and ocean surfaces following turbulent transfer; and wet deposition, which occurs when gases are incorporated into suspended liquid water either by in-cloud scavenging or by washout from falling precipitation. Depositional loss depends not only upon the chemical properties of the gas, such as solubility, but also upon a variety of factors including the planetary boundary layer height, surface properties (e.g. area, roughness, moisture content, etc.), cloud liquid water content, and meteorological parameters such as vertical wind speed (Walcek, 1987; Jobson et al., 1998; Hall and Claiborn, 1997; Chang et al., 2004; Nguyen et al., 2015). Due to its high solubility H_2O_2 is particularly susceptible to loss by both wet and dry deposition while the less soluble MHP is significantly less affected by both loss mechanisms (Lee et al., 2000). Hydroperoxide loss by deposition represents a net loss of oxidant as H_2O_2 and MHP are removed with no return of HO_x to the atmosphere.

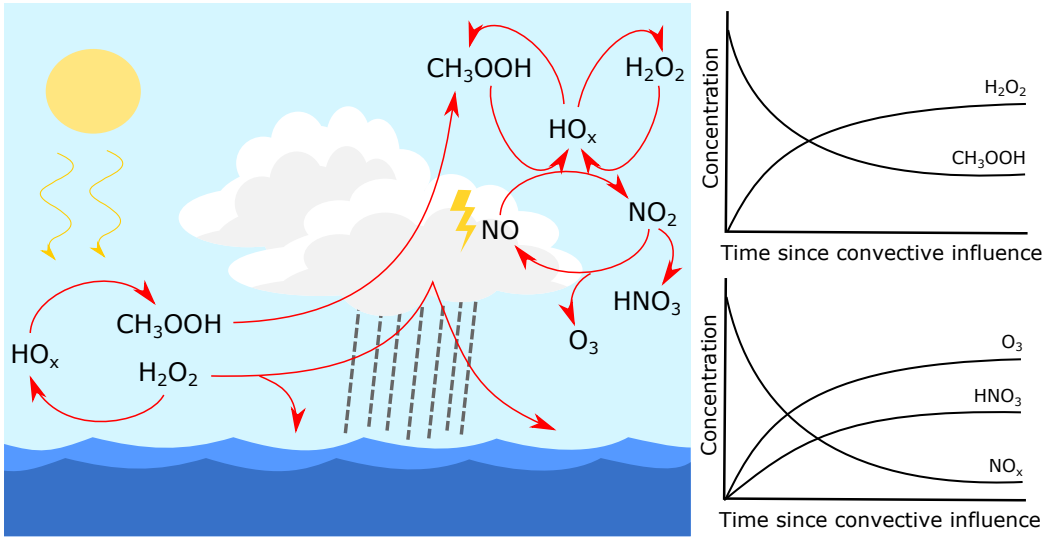

Figure 3.1: Schematic of hydroperoxide cycling in the remote atmosphere. (Right) In the lower troposphere, generation of HO_x forms H_2O_2 and MHP that cycle back to HO_x with photochemical reactions. H_2O_2 readily undergoes deposition, removing it from the atmosphere under both wet and dry conditions. MHP is less soluble and therefore may be lofted to the UTLS during convection events, where it participates in HO_x and NO_x (e.g. from lightning) chemistry. (Left) Plots representing the relative ratios of different atmospheric species following convection.

In addition to photochemical and depositional loss, hydroperoxides alter the atmosphere's oxidative potential via their transport in, for example, convective activity (Figure 3.1). Convection occurs when parcels of air become unstable with respect to vertical transport; with strong enough convection, large towering cumulus clouds form that can penetrate deep into the upper troposphere and lower stratosphere (UTLS, typically 8–12 km). Because MHP and H_2O_2 have different solubilities, the ratio of these two compounds can be used as a metric to identify areas with recent convective activity (see, e.g., Snow et al. (2007)). H_2O_2 and MHP have have similar mixing ratios in the boundary layer (H_2O_2/MHP ~1–3), but H_2O_2 is preferentially removed by cloud water and precipitation that forms during convection while MHP is lofted with minimal loss (Heikes et al., 1996; O'Sullivan et al., 1999b; Barth et al., 2016; Bela et al., 2018; Cuchiara et al., 2020). Following convection, MHP in the UTLS may be enhanced by 3–6 times background levels (Cohan et al., 1999; Jaeglé et al., 2000; Ravatta et al., 2001). Overall, the influence of these compounds on the UTLS due to convective transport lasts on order of 3–10 days based on the lifetime of MHP and H_2O_2 and the subsequent relaxation to local steady-state (Jaeglé et al., 1997; Bertram et al., 2007). However, in that time MHP may react to produce HO_x

and thereby redistribute HO_x to these remote regions. For example, MHP photolysis may contribute 20–40% of HO_x production in convective outflow, compared with just 3–10% in background UTLS air (Prather and Jacob, 1997; Cohan et al., 1999; Jaeglé et al., 2000; Ravatta et al., 2001). Through the transport and subsequent photochemistry of hydroperoxides, convection may result in the transport of HO_x from an oxidant consuming region in the marine boundary layer to an oxidant producing region in the UTLS.

In this study, the chemical and physical controls on global hydroperoxide mixing ratios are assessed through comparisons between global climatological measurements and photochemical models. The data collection methodology and global hydroperoxide distribution are outlined in a companion paper (Allen et al., 2021). Here, we discuss the relative role of photochemistry in setting hydroperoxide distributions across different latitudes and altitudes. We investigate the role of physical processes on the distribution of H_2O_2 and MHP, including estimating the rate of H_2O_2 deposition in the marine boundary layer needed to reconcile observations with box model predictions. Finally, we use GEOS-Chem, a global chemical transport model, to investigate the role of convection in lofting hydroperoxides and their impact on the UTLS.

3.3 Methods

Field Deployment: Atmospheric Tomography Mission

Measurements of global H_2O_2 and MHP were made during the Atmospheric Tomography (ATom) Mission, which used the NASA DC-8 to collect atmospheric vertical profiles of trace gases and aerosols in the remote atmosphere. The deployments were scheduled to sample each season: ATom-1 in August 2016 (7/29/16–8/23/16), ATom-2 in February 2017 (1/26/17–2/21/18), ATom-3 in October 2017 (9/28/17–10/27/17), and ATom-4 in May 2018 (4/24/18–5/21/18). Each deployment consisted of 11–13 flights that followed a prescribed flight track that spanning latitudes between -85° to 85° by first traveling southbound over the Pacific Ocean and then traveling northbound over the Atlantic Ocean. During each flight, the aircraft underwent continuous ascents and descents to gather vertical profiles ranging from about 180 m to just under 13,500 m altitudes above the ocean surface. Hydroperoxides were measured using the CIT-CIMS, which combines a time-of-flight and a triple quadrupole chemical ionization mass spectrometer using CF_3O^- ion chemistry to sensitively detect gas-phase atmospheric hydroperoxides. ATom primarily resulted in data collected over the remote ocean, but did include periods over land due to

flight requirements; the data presented here have been filtered to exclude the measurements collected over land masses. The ATom Mission and CIT-CIMS technique is discussed in much further detail in the companion paper (Allen et al., 2021).

GEOS-Chem

Observations of atmospheric hydroperoxide mixing ratios from ATom were compared to those predicted by the global transport model GEOS-Chem. GEOS-Chem is a three-dimensional atmospheric chemistry model driven by meteorological data from radio sondes and satellite observations of the Earth's land surface, atmosphere, ocean, and biogenic parameters (Bey et al., 2001). The core of GEOS-Chem is a chemical module designed to simulate atmospheric concentrations of various species taking into account emissions, chemistry, aerosol microphysics, and deposition. Further details on the chemical and physical mechanisms used in the GEOS-Chem simulations are given in the Supporting Information. The meteorological data is assimilated from the Goddard Earth Observing System (GEOS) of the NASA Global Modeling and Assimilation Office (GMAO). GEOS-Chem integrates the meteorological data using the GEOS Forward Processing (GEOS-FP) data archive with a resolution of 0.25° latitude by 0.325° longitude and 72 vertical atmospheric layers and a 3-hour temporal resolution (1-hour for surface data).

In this study, GEOS-Chem simulations were conducted for 2016–2018, with a one-year spin up, using GEOS-Chem v11-2d at 2° x 2.5° latitude-longitude grid resolution using the GEOS-FP meteorology archive. The model was updated with CH_3OO + OH chemistry (k = 1.6×10^{-10} cm^3 s^{-1}), as well as with improvements to certain emissions inventories, as described in Bates et al. (2021). Sensitivity studies were conducted on the rate of HO_2 loss on heterogenous surfaces by altering the uptake coefficient (γ) value, on MHP wet scavenging by altering the MHP Henry's Law Coefficient, and on the rate of the CH_3OO + OH reaction by altering the rate coefficient to assess the impact of this chemistry on H_2O_2 (see below and the Supporting Information). GEOS-Chem results are presented in two forms: one in which model times and locations are sampled to match the flight campaign data at 20 second temporal resolution and one with the outputs averaged over the month of each ATom deployment and centered on at -170° longitude (Pacific Ocean) and -25° longitude (Atlantic Ocean).

Photochemical Box Model

A zero-dimensional diurnal photochemical box model is used to evaluate the measurements of hydroperoxides against their concentrations as predicted at pseudo steady-state. The box model contains a detailed mechanism for remote tropospheric HO_x-NO_x-VOC chemistry that uses over 35 chemical species and 85 reactions. Compounds included in the model are either initiated with measured values when available or calculated from steady-state and parameters such as temperature, pressure, and H_2O mixing ratio are constrained to their observed values. The model does not include physical processes such as heterogeneous chemistry, transport, or wet or dry deposition. Data used in the model have been filtered such that the rate of NO_2 photolysis at each point is greater than $1{\times}10^{-3}$ s^{-1}, ensuring only measurements collected in daylight are used. Note the sparser model data for August (ATom-1), due to limited availability of peroxyacetic nitrate (PAN) measurements, creates high uncertainty at the most poleward extremes.

Using the observations as an initial point, the model calculates the diurnally varying production and loss of each chemical species over the course of 120 simulated hours. Photolysis rates for relevant species are calculated using actinic flux with cross sections and quantum yields from Burkholder et al. (2015). The actinic flux is produced from the Tropospheric Ultraviolet and Visible (TUV) radiation model (NCAR), which utilizes inputs of temperature, pressure, ozone column, and altitude to determine cloud-free actinic fluxes at the latitude, longitude, altitude, and time of year of the ATom measurements. Comparisons of model-generated photolysis rates with those available from actinic flux measurements using the Charged-coupled device Actinic Flux Spectroradiometers (CAFS) onboard indicate good agreement between the two and modeled photolysis rates have been adjusted to match CAFS observations where available. Chemical rates are calculated using temperature-dependent rate constants from Burkholder et al. (2015) and Jenkin et al. (2019). From the TUV-generated actinic flux of a 24-hour solar cycle, the box model calculates a 5-day diurnal pattern of compound mixing ratios at each point along the flight track. Five days was chosen because most compounds have achieved reached steady-state within this time frame.

3.4 Results and Discussion

Hydroperoxide Lifetime and Photochemistry

During ATom, H_2O_2 was primarily found in the lower troposphere within the tropical and subtropical latitudes, regions with high HO_2-formation potential. Based on box

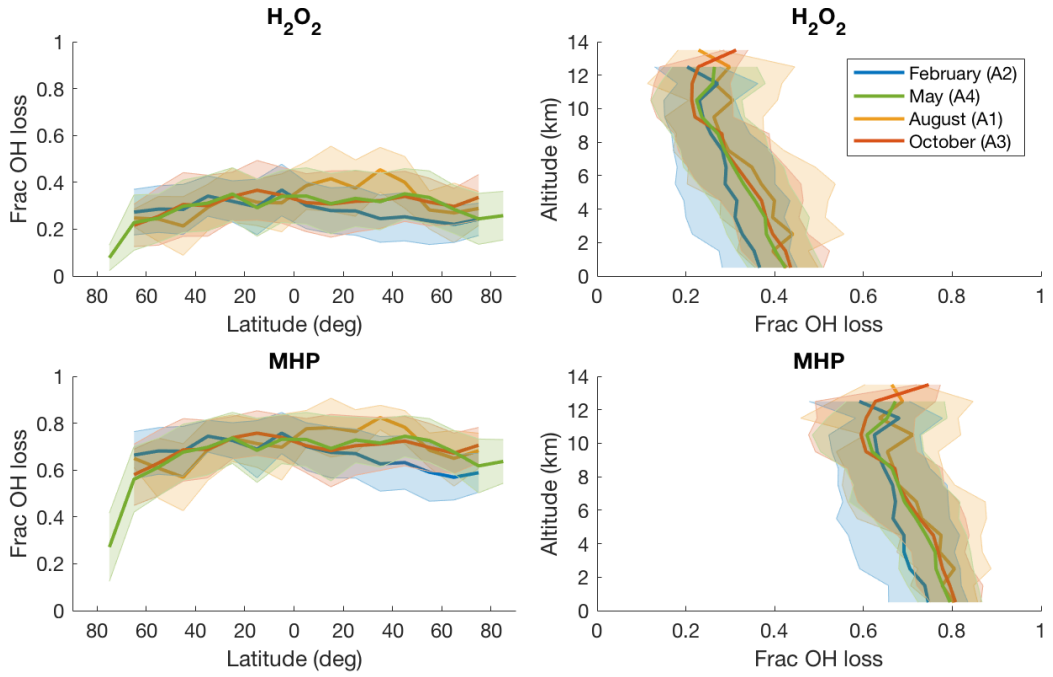

Figure 3.2: Modeled fraction of OH loss relative to photolysis loss for H_2O_2 and MHP across latitude and altitude bins for all four deployments of ATom. A1–A4 refers to the four different ATom deployments. Shading represents one sigma standard deviation of the mean.

model predictions, the highest production of H_2O_2 from HO_2 self-reaction occurs within latitudes of -10° to 20° degrees and quickly falls off poleward. Similarly, the highest production of H_2O_2 from the HO_2 self-reaction occurs within the boundary layer and lower troposphere (<2 km altitude) and quickly declines with increasing altitude. The highest estimated rate of H_2O_2 from this chemistry occurred in the October deployment (ATom-3) with an average rate of 7.1×10^{-4} s^{-1},or 1.3 ppb per day, while the lowest occurred during the February deployment (ATom-2) when the average production rate was just over half the October value at 4.3×10^{-4} s^{-1} or 0.6 ppb per day. However, H_2O_2 may also form in regions where other factors such as biomass burning drive high HO_x and VOC concentrations that lead to higher mixing ratios of this hydroperoxide (see Allen et al. (2021)).

Similarly, H_2O_2 photochemical loss occurs in regions with strong photochemical activity, primarily in the boundary layer of the tropical and subtropical latitudes. Of the photochemical loss (loss due to deposition is discussed in detail in the following section), H_2O_2 photolysis tends to comprise more than half the H_2O_2 loss relative to OH (Figure 3.2). On average, reaction with OH is 30–35% of H_2O_2 photochemical loss, with global minimums of 2–6% and maximums of 63–75%, depending on

season. The relative contribution of OH to H_2O_2 loss has a slight dependence on latitude, with the average OH loss peaking in the tropical and subtropical regions around 35–45% and photolysis slightly more prevalent closer to the poles. Similarly, Figure 3.2 shows some variation of photochemical loss depending on altitude. The average contribution of OH reaction to H_2O_2 loss is higher at lower altitudes (40-45% on average) and decreases at higher altitudes (20-25% on average), although some variation does exist at the highest altitudes above 12 km. The average OH loss rate is on order of 3.6×10^{-6} s^{-1} while the average photolysis loss rate is on order of 9.0×10^{-6} s^{-1}. Because H_2O_2 photolysis conserves HO_x while loss to OH represents a net loss of HO_x, areas with a high ratio of H_2O_2 loss to OH indicate regions that are net oxidant consuming.

The relative contribution of OH to the overall MHP photochemical loss exhibits latitudinal and altitudinal patterns very similar to that of H_2O_2. As shown in Figure 3.2, MHP loss to OH tends to comprise a slightly higher percentage of MHP photochemical loss than it does that of H_2O_2 photochemical loss. The average global value of MHP loss to OH varies from 66% (February, ATom-2) to 72% (August, ATom-1), with minimums of 12–25% and maximums of 90–95%, depending on season. The average percentage contribution of OH to photochemical loss shows a slight dependence on latitude and altitude. Loss to OH is typically highest in the tropical and subtropical region (contributing about 75%) and decreases moving poleward (to an average of 60%). Similarly, the OH loss is typically highest at low altitudes and decreases with increasing altitude. Note that prior to running the model, points along the flight track in which NO_2 photolysis was below 1×10^{-3} s^{-1} were excluded, leading to some potential biases in the poleward extremes. The average rate of photolysis is 7.3×10^{-6} s^{-1} while the average rate of OH loss is 15×10^{-6} s^{-1}. MHP may undergo deposition as well, but due to the relatively low Henry's Law constant of MHP this loss isn't nearly as prevalent as it is for H_2O_2.

The lifetime of H_2O_2 with respect to photochemical loss is 21 hours (daytime) on average and spans the range from just a few hours (4–8) to several hundred (>100) depending on sunlight availability. The H_2O_2 lifetime shows little dependence on altitude but a strong dependence on latitude. The H_2O_2 photochemical lifetime is shortest in the equatorial region and increases moving poleward. Similarly, the global average photochemical lifetime of MHP in the atmosphere is around 11 hours (daytime) and varies considerably between 1–3 hours to much longer (>50 hours) depending on atmospheric region. Like H_2O_2, MHP photochemical lifetime

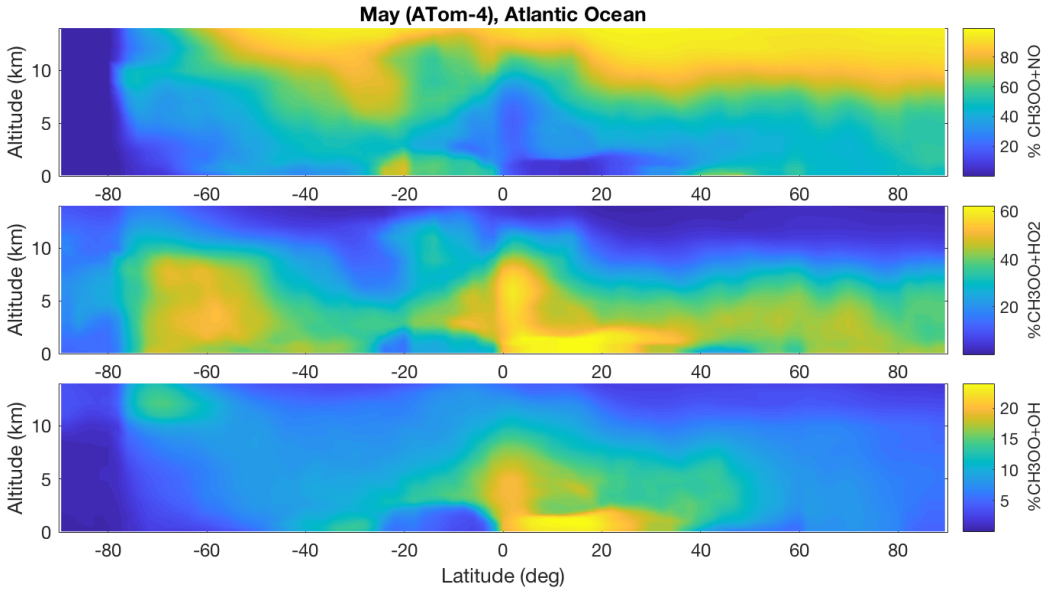

Figure 3.3: Modeled fraction of CH_3OO that reacts with NO (top), HO_2 (middle), or OH (bottom) across latitude and altitude for the Atlantic Ocean basin during the May deployment (ATom-4). Regions with high CH_3OO + HO_2 produce MHP and are net oxidant consuming. Note the different color bar scaling factors in each panel.

does not vary significantly with altitude but does show a latitudinal dependence. The MHP lifetime is shortest in the tropics and subtropics and increases moving poleward. While the H_2O_2 photochemical lifetime is longer than that of MHP, H_2O_2 is subject to much greater physical loss than MHP and thus the overall lifetime of these two species in the atmosphere is more similar when physical losses are taken into account.

In addition to H_2O_2 and MHP lifetime, the GEOS-Chem simulation reveals the distribution of atmospheric regions that tend to undergo either HO_x or NO_x dominated chemistry. Figure 3.3 compares the fraction of MPR that reacts with NO, HO_2, or OH in the Atlantic Ocean basin for the May (ATom-4) deployment. These reactions shows a slight latitudinal dependence, with MPR + HO_2 and MPR + OH dominant in the tropical and sub-tropical regions. However, these reactions have a stronger altitudinal dependence. In the lowest portion of the atmosphere, HO_2 contributes up to 60% of CH_3OO loss relative while reaction with OH contributes up to 25% of CH_3OO loss. The contribution of HO_2 to MPR reactions decreases with increasing altitude and declines to <10% in the upper troposphere (>8 km). This strong gradient with altitude correlates well with the expected distribution of both HO_x and NO sources. The role of CH_3OO + OH in MHP production will be

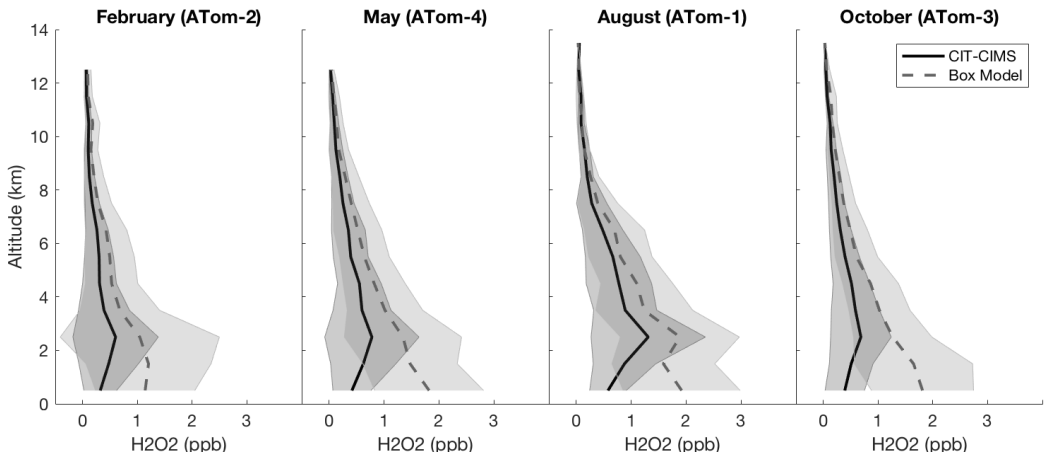

Figure 3.4: Comparison of H_2O_2 mixing ratios from measurements (CIT-CIMS) and those following chemical relaxation over 5 days after the measurements calculated using a photochemical box model. Throughout the lower troposphere, H_2O_2 mixing ratios are less than half of their steady state values, reflecting the importance of loss via wet and dry deposition. The results are averaged over 1 km altitude bins and shaded regions represent one standard deviation of the mean.

further explored in a following section.

H_2O_2 Deposition in the Marine Boundary Layer

Non-photochemical loss of H_2O_2 is estimated here by comparing measurements of H_2O_2 to predictions from a photochemical steady-state box model. The box model contains all expected chemistry affecting the hydroperoxide budget, but lacks any physical parameters such as transport, dry deposition, or wet scavenging. The box model severely over-predicts H_2O_2, particularly in the lower troposphere below 3–4 km altitude where the model on average predicts 2–4 times higher mixing ratios of H_2O_2 than are measured (Figure 3.4). This under-prediction is consistent across time of year. Given that deposition is expected to comprise a significant portion of H_2O_2 loss, the observed over-prediction by the model is likely a result of this missing non-photochemical loss term. In addition, MHP is less likely to undergo depositional loss and does not exhibit the same model disparity at low altitudes (Figure 3.12). Hence, the difference between the box model and the measurements is used to infer the extent of the missing loss rate and therefore the expected magnitude of H_2O_2 deposition. Assuming steady-state, the difference between the model and the measurements can be expressed as

$$NPL = \frac{L^2 \times ([H_2O_2]_{mod} - [H_2O_2]_{meas})}{P - L \times ([H_2O_2]_{mod} - [H_2O_2]_{meas})} \tag{3.10}$$

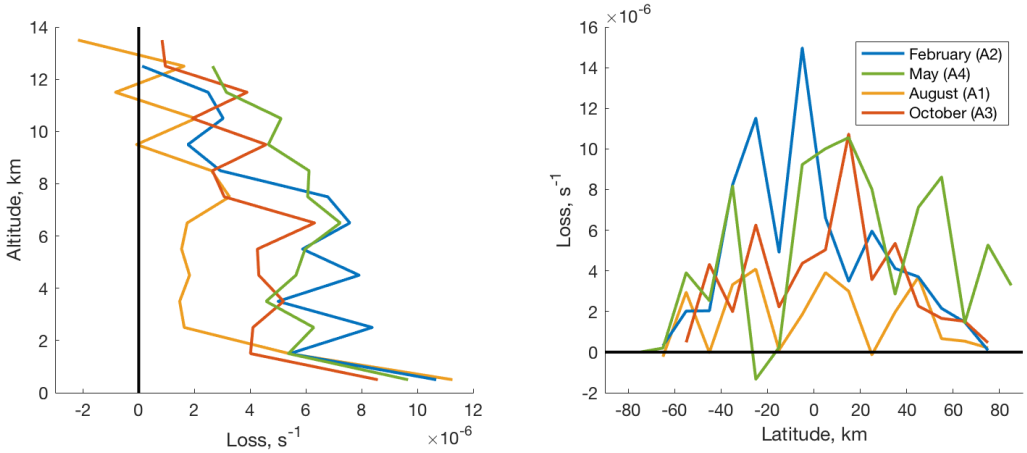

Figure 3.5: Calculation of the H_2O_2 non-photochemical loss (NPL) rate averaged over altitude (left) and latitude (right) for each deployment. The apparent loss was found by comparing the ATom measurements to the predictions by a photochemical box model and attributing the difference to a missing deposition loss term in the model. A1–A4 refer to the four different ATom deployments.

where NPL (Non-Photochemical Loss) is the missing loss rate (s^{-1}) needed to reconcile the model with the measurements, L is the H_2O_2 photochemical loss term, and P is the H_2O_2 production term (from HO_2 + HO_2 chemistry). Neglecting wet deposition, the dry deposition velocity averaged over the marine boundary layer can be estimated as

$$V_d = D \times \mathrm{BLH} \tag{3.11}$$

where BLH is the marine boundary layer height. Note that V_d at the surface will be twice this value.

Figure 3.5 indicates the estimated non-photochemical first-order loss for each deployment averaged over altitude and latitude calculated from Eq. 3.10. As expected from Figure 3.4, the loss rate is highest at low altitudes and decreases with increasing altitude. Within the boundary layer, the average rate varies considerably from (8–12)×10^{-6} s^{-1} depending on the month sampled (e.g. highest in August and lowest in October). From the model, the average total photochemical loss rate is on order of 13×10^{-6} s^{-1}, hence physical loss is highly competitive in the lower atmosphere and is estimated to result in the majority of H_2O_2 loss. Above 8 km the NPL rate declines to close to zero, indicating that the loss at these altitudes is primarily photochemical and that the UTLS is closer to photochemical steady-state. The NPL rate also shows some latitudinal dependence (Figure 3.5). The loss is highest in the tropics and subtropical latitudes and declines moving poleward. A

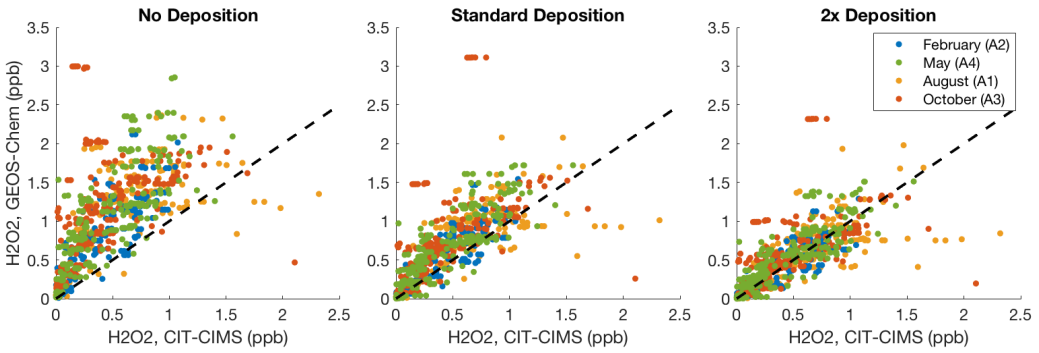

Figure 3.6: Correlation of CIT-CIMS measured vs GEOS-Chem simulated H_2O_2 mixing ratios for different deposition velocities in the non-polar remote marine boundary layer (altitudes <1km and latitudes between −60° and 60°). Doubling the H_2O_2 deposition rate (right) in the model provides a closer match to observed H_2O_2 mixing ratios below 1 km altitude compared with the standard deposition rate (center). The dashed line indicates a 1:1 (perfect) comparison.

low NPL rate in the subtropics (20–30°) suggests the influence of dry downwelling air in this region that is much closer to steady-state. Similarly, the poles show an average NPL rate that is close to zero, suggesting that on average physical losses are not as prevalent a loss mechanism as photochemistry in these regions.

The derived NPL term can be used to estimate the depositional velocity in the lower atmosphere, which depends upon the H_2O_2 loss rate and the height of the marine boundary layer. Because the regions in which D is negative, such as occurs at high latitudes (Figure 3.5), likely have other processes beyond dry deposition contributing to the apparent loss, the deposition velocity is only calculated using data from -30° to 30° latitudes. Eq. 3.11 gives median depositional velocities of 1.19, 1.32, 1.00, and 1.01 cm s−1 for the marine boundary layer average in February, May, August, and October, respectively. These velocities correspond to median wind speeds of 15, 8.3, 12, and 6.4 m s^{-1}, respectively, within the same latitude and altitude region. Previous estimates, conducted by comparing airborne or ship-based measurements with Lagrangian, chemical box, or global circulation models (EMAC), found a rate between 0.5–1.8 cm s^{-1} at wind speeds of 5–10 m s^{-1} (Stickler et al., 2007; Fischer et al., 2015). Hence the calculated deposition velocities in this study are within the range of previously estimated values. These studies note that the deposition rate primarily depends upon the transfer velocity of H_2O_2 to the ocean surface, which is determined by wind speed, rather than other parameters such as ocean uptake resistance. Other factors, such as entrainment, that may impact this analysis are evaluated in the Supporting Information.

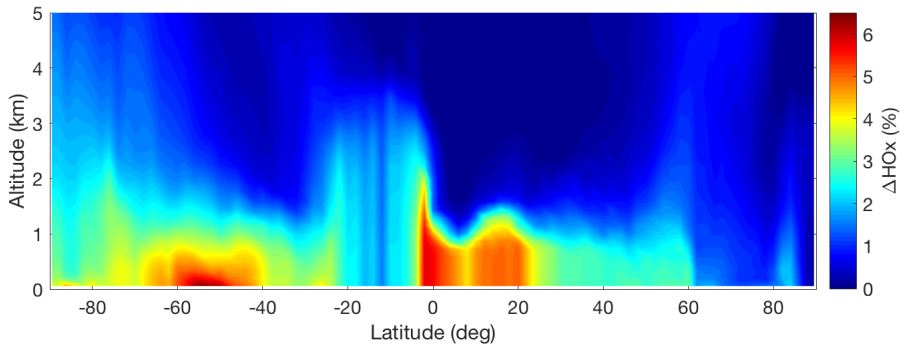

Figure 3.7: Effect of H_2O_2 deposition on HO_x in the Atlantic remote marine boundary layer during the October (ATom-3) deployment. Total HO_x in the boundary layer declines by 1–5% when H_2O_2 is removed compared with the high deposition simulation, particularly affecting the equatorial and mid-latitudes (40–60°), indicating where H_2O_2 deposition is most important.

Because H_2O_2 deposition represents a permanent loss from the atmosphere, this loss is net oxidant consuming. A H_2O_2 deposition rate of (8–12)$\times 10^{-6}$ s^{-1} results in an average net loss of 80 ppt H_2O_2 per day. Combined with H_2O_2 loss due to OH, this results in an average loss of 300 ppt HO_x per day in the remote marine boundary layer. To assess the total magnitude of this H_2O_2 deposition on HO_x, GEOS-Chem was run with zero H_2O_2 deposition and with the current ("standard") H_2O_2 deposition rate doubled. Doubling the standard H_2O_2 deposition rate decreases boundary layer H_2O_2 by 10–40% and provides a closer match to observed H_2O_2 mixing ratios at lower altitudes (<1 km altitude) for latitudes between −60° and 60° (Figure 3.6). Without deposition, H_2O_2 mixing ratios in the boundary layer are up to 2.5–4 times lower than their value in the high deposition run and result in a 5–10% increase (depending on season) in total HO_x, indicating the importance of H_2O_2 deposition as a HO_x sink in the marine boundary layer (Figure 3.7). These losses are especially prevalent at the equator and in the southern mid-latitudes (40–60°) in February and October and prevalent in the northern mid-latitudes (40–60°) and northern pole (>80°) in May and August.

MHP Transport via Convective Activity

The ability of GEOS-Chem in simulating H_2O_2 and MHP mixing ratios in the remote atmosphere depends on altitude. Correlations between the model and the measurements across the whole deployment (shown in the Supporting Information) for H_2O_2 indicate fairly good agreement between the model and the measurements, although the model does systematically over-predict H_2O_2. In particular, the months

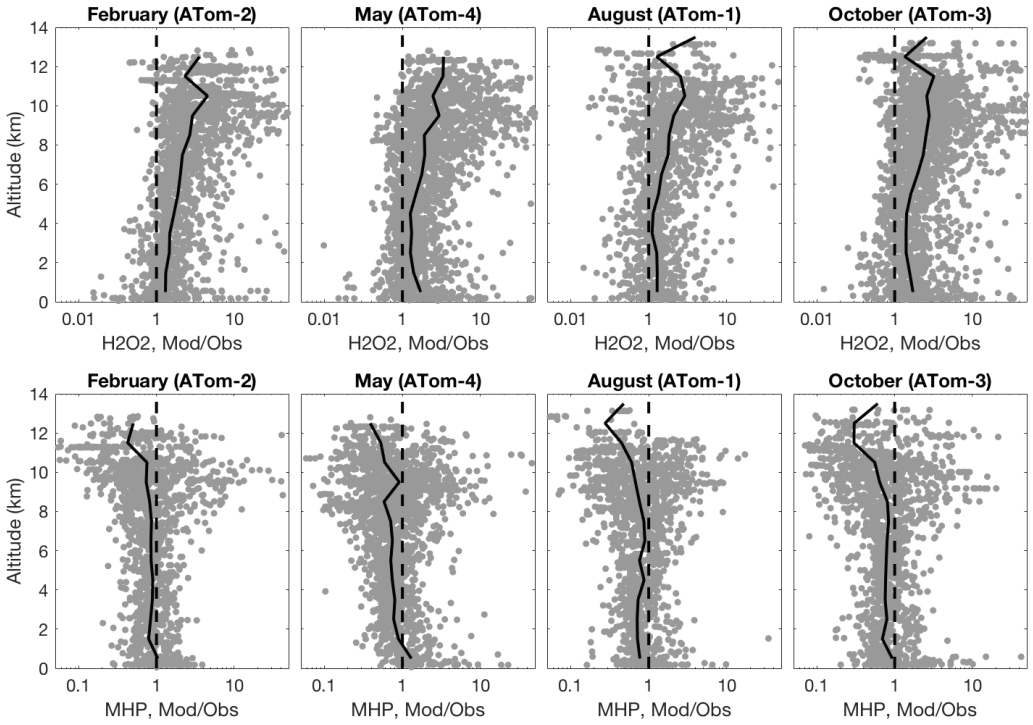

Figure 3.8: Ratio of measured (obs) H_2O_2 (top row) and MHP (bottom row) with that predicted by GEOS-Chem (model) as a function of altitude. The solid line indicates the median value for 1 km altitude bins and the dashed line represents 1:1 or prefect correlation between the model and the measurements. GEOS-Chem systematically over-predicts H_2O_2 and under-predicts MHP relative to the measurements at all altitudes, with the discrepancy most severe at altitudes above 8 km.

of August (ATom-1) and May (ATom-4) produce correlations between the model and the measurements with slopes of 1.03 and 1.05 with R^2 values of 0.69 and 0.72, respectively; the agreement is less good in February and October, with slopes of 1.13 and 1.18, respectively. However, this agreement worsens in the UTLS as indicated in Figure 3.8, which depicts the ratio of measured H_2O_2 and MHP to that predicted by GEOS-Chem. Above 8 km, the average ratio of the model to measurements ranges between 2–4, depending on season and altitude, and the model may be as much as 10 times higher than the measurements. The model and the measurements are less well correlated for MHP than for H_2O_2 across the deployment as a whole. Correlations between the model and the measurements for MHP are best in February (ATom-2) and October (ATom-3), which both give slopes of 0.58 with R^2 values of 0.65 and 0.75, respectively; in comparison, August and May give slopes of 0.57 and 0.49 (see the Supporting Information). This model under-prediction is most evident in the UTLS, where the ratio of model to measurements is on average 0.3–0.7 too

low (Figure 3.8).

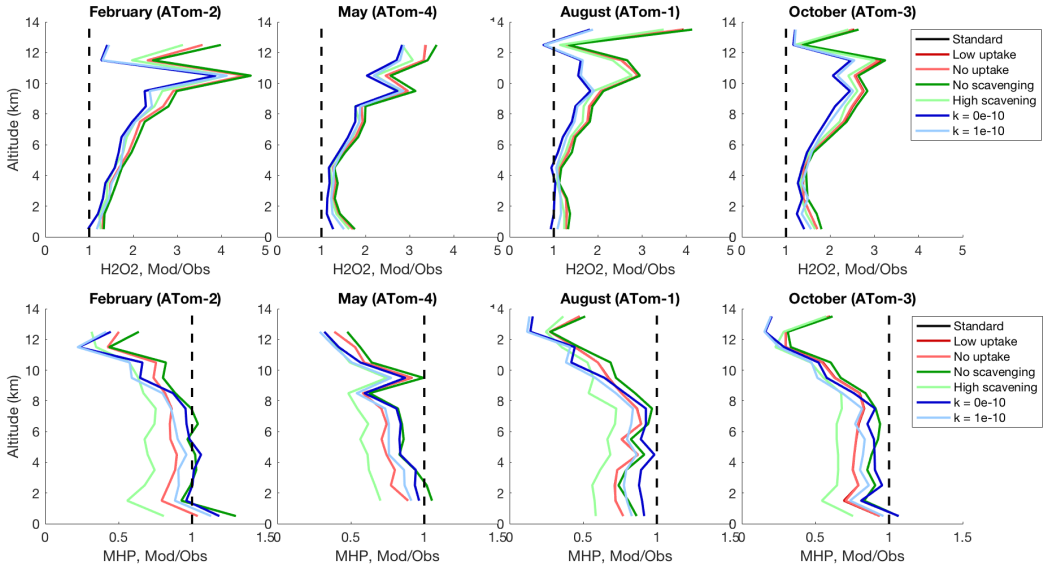

Figure 3.9: Ratio of measured (obs) and GEOS-Chem predicted (model) H_2O_2 (top row) and MHP (bottom row) averaged over altitude for several different model configurations. Standard refers to the current GEOS-Chem configuration; low and no uptake refers to alterations to the HO_2 uptake coefficient (γ); No and high scavenging refers to MHP wet deposition; and k refers to the CH_3OO + OH rate coefficient. Despite improvements in the lower troposphere, these alterations do not improve measurement and model correlation in the UTLS. The dashed line represents 1:1 or prefect correlation between the model and the measurements.

Several factors were investigated in GEOS-Chem to determine if they could account for the discrepancy between the model and the measurements including altering the rate of HO_2 loss on heterogeneous surfaces, the rate of CH_3OO + OH, and the wet scavenging of MHP (Figure 3.9). The standard GEOS-Chem configuration here uses a reactive uptake coefficient (γ) of 0.2 for HO_2 onto aerosol surfaces (Jacob et al., 2000; Mao et al., 2013). However, several studies have proposed γ values that span two orders of magnitude from 0.01–1 (Thornton et al., 2008; Mao et al., 2010; George et al., 2013). To test the effect of decreasing γ, thus potentially increasing HO_2 availability and hydroperoxide formation, GEOS-Chem was run with γ = 0.07 ("low uptake") and γ = 0 ("no uptake") (see the Supporting Information for further discussion of the HO_2 uptake coefficient). Considerable uncertainty exists in the estimates of the MHP scavenging efficiency (ranging from 5% to 84%) and a too high scavenging factor may lead to more efficient hydroperoxide removal than exists in the atmosphere (Mari et al., 2000; Barth et al., 2001, 2016; Hottmann et al., 2020). To test the effective bounds of MHP scavenging on the GEOS-Chem predictions

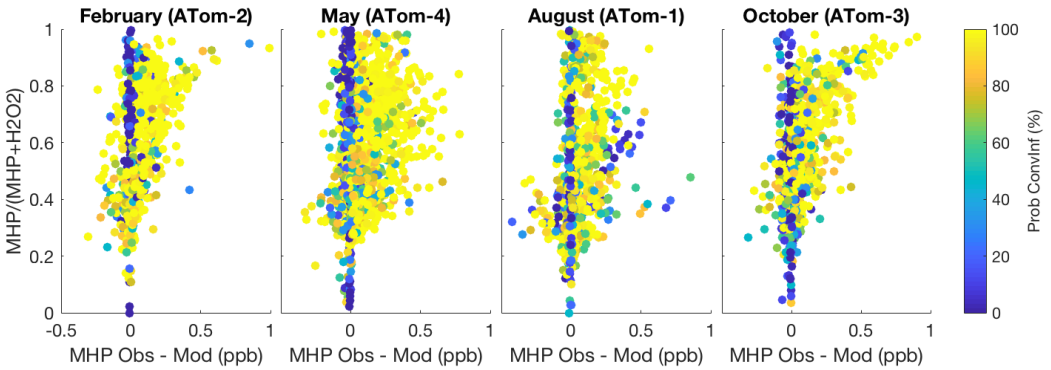

Figure 3.10: Difference between measured (CIT-CIMS) and modeled (GEOS-Chem) MHP compared with the measured MHP fraction of the hydroperoxide budget (measured MHP/(MHP+H_2O_2)) and colored by predicted the probability of convective influence (Prof ConvInf). Data shown is from above 5 km altitude. GEOS-Chem deviates most from the measurements at high MHP fraction and when there is a high probability of convection.

in the UTLS, a sensitivity study was conducted with no MHP wet deposition ("no scavenging") and with high MHP water uptake ("high scavenging"). Finally, several rate constants for the CH_3OO + OH reaction have been suggested (Fittschen, 2019). A lower rate constant would increase MHP precursor availability for reaction with HO_2 and to test this effect on MHP, GEOS-Chem was run with k = 1×10^{-10} cm^3 s^{-1} ("k = 0e-10") and with k = 0 cm^3 s^{-1} ("k = 1e-10"). Altering some of these parameters does produce better alignment between the model and the measurements in certain portions of the atmosphere. For example, MHP mixing ratios increase by a significant fraction, >50%) in the polar lower troposphere in the case of no MHP water uptake (see Supporting Information). However, these altering these parameters has only minor effects above 8 km altitudes and is not enough to fully account for the discrepancy between the model and the measurements in the UTLS.

The discrepancy between the measurements and GEOS-Chem in predicting the mixing ratios of H_2O_2 and MHP in the UTLS likely stems from the model's ability to capture the influence of convective activity on the distribution of hydroperoxides in this region. For altitudes above 5 km, the difference between measured MHP and GEOS-Chem predicted MHP correlates strongly with a high MHP/(MHP+H_2O_2) (Figure 3.10). The MHP/(MHP+H_2O_2) ratio is often used as a tracer for recent convective influence due to the difference in solubilities of these two compounds, where H_2O_2 is preferentially lost due to wet scavenging during convective events. Further confirming the influence of convective activity, the model deviations and MHP frac-

Table 3.1: Mean age (hours) of air mass encountered at 1 km altitude bins from 6–12 km, based on a comparison of the measured MHP/(MHP+H_2O_2) fraction to modeled changes in MHP/(MHP+H_2O_2) fraction since convective influence. Data is from −30° to 30° latitudes.

	6-7 km	7-8 km	8-9 km	9-10 km	10-11 km	11-12 km
February (ATom-2)	23±4	23±5	26±5	30±8	23±6	25±10
May (ATom-4)	16±4	19±4	23±6	28±7	26±8	21±8
August (ATom-2)	27±6	31±12	37±36	31±7	33±12	43±11
October (ATom-3)	19±2	20±3	23±4	23±6	26±7	24±10

[a] Range in values given is the standard deviation in calculated hours since CI for each altitude bin.

tion are compared to an estimation of the probability of convective influence based on a 10-day back trajectory analysis using the National Centers for Environmental Predictions (NCEP) Global Forecast System (GFS) meteorology (see the Supporting Information for further details). The convective influence probability is calculated based on the coincidence of the air parcel with clouds, high RH (above 50%), and cloud water. This metric also indicates that GEOS-Chem more accurately captures measured MHP at times when there is very little to no probability of convective influence and less accurately during times of high probability of convective influence (Figure 3.10). Studies have noted problems in the parameterization of tracer mass fluxes during convection in chemical transport models (Lawrence and Rasch, 2005; Zhang et al., 2021). Comparison to the ATom hydroperoxide data in the UTLS suggests that this treatment of convective mass fluxes in GEOS-Chem merits further investigation.

The importance of convection in influencing the chemistry of the UTLS is estimated using the chemistry of MHP/(MHP+H_2O_2) as a tracer for air mass age following convection. This estimation was done using the method outlined in Bertram et al. (2007) for the tropical and subtropical portion (latitudes between −30° and 30°) of ATom. Briefly, a diurnal photochemical steady-state model was initiated with a high MHP/H_2O_2 ratio and a high NO_x/HNO_3 ratio, simulating conditions found immediately following convection. Note that this model assumes that HNO_3 and H_2O_2 are scrubbed with near unit efficiency during convection and the model neglects dilution from surrounding background air. The model is initialized with MHP at 1 ppb and NO_x at 2 ppb, with H_2O_2 and HNO_3 at near to zero ppt levels ($\sim 10^{-10}$ ppt); all other species were initiated with their measured concentrations. The model progressed until steady-state was reached (~10 days) and an expression

was fit to the change in MHP/(MHP+H_2O_2) and NO_x/(NO_x+HNO_3) over the time between initiation to steady-state in 1 km altitude bins from 6 to 12 km (see Figures 3.16 and 3.17). This expression was then compared to the measured ratios in the same altitude bins to calculate the approximate age of air encountered at the high altitudes in the tropical and subtropical latitude band during the four seasons sampled as part of ATom.

The estimated chemical aging since convective activity for 1 km altitude bins between 6 and 12 km for each deployment is given in Table 3.1. The air mass age ranged from 16 to 43 hours, with the newest air in the lower atmosphere in May and the oldest air in the upper atmosphere in August. Across all four deployments, the average age in the lower region (6–7 km) is 21 hours and this age increases to 28 hours in the upper atmosphere (11–12 km). Note that the neglect of background air mixing likely biases the air mass to the lower end because dilution will lower the MHP mixing ratio and therefore decrease the MHP/H_2O_2 ratio. These ages are similar to those estimated by Bertram et al. (2007), using the same method over North America during summer 2004, who found nearly 50% of the air mass sampled had been convectively influenced within the previous day and 75% within the previous 5 days. This age is faster than suggested by comparison to air mass age calculated using back trajectory analysis, which gives an air mass age in the range of 67 to 115 hours with the most recently influenced air in the upper troposphere (10–11 km) and the air in the mid-troposphere (6–7 km) less recently influenced, likely due to the difference between physical and chemical aging (the latter primarily occurs only during sunlit hours). These results indicate the wide-spread influence of convection on the chemistry of UTLS with important implications for the chemistry occurring there. Because MHP transports HO_x to the typically low HO_x UTLS, wide-spread convection of hydroperoxides will highly affect HO_x and NO_x, and therefore O_x, cycling in this region of the atmosphere.

3.5 Conclusions

The observations of hydroperoxides collected during the ATom Mission indicate how these hydroperoxides impact the global oxidative budget of the atmosphere. H_2O_2 is primarily formed within at lower altitudes in the tropics due to the HO_2 self-reaction and primarily lost via photolysis in the same region. Globally, OH comprises an average of 30–35% of H_2O_2 photochemical loss, but this ratio is higher (40–45%) at lower altitudes and decreases in the UTLS (reaching 20–25% of loss). Similarly, the ATom data indicates that production of MHP from CH_3OO

+ HO_2 globally is about 30% of CH_3OO loss relative to NO, with a sharp gradient between the lower and upper atmosphere with the UTLS dominated by CH_3OO + NO chemistry. Loss to OH is a higher fraction of the MHP photochemical loss budget, with a global average of 68–74%, though with a similar latitudinal and altitudinal pattern as H_2O_2 photochemical loss. Photochemical loss is net oxidant conserving while reaction with OH is net oxidant consuming, and thus regions like the tropical marine boundary layer which have high hydroperoxide losses to OH have lower oxidative potential.

In addition to photochemical loss, these hydroperoxides affect HO_x due to their physical loss and transport mechanisms. For H_2O_2 within the marine boundary layer, a physical loss on order of $(8–12)\times10^{-6}$ s^{-1} is needed to reconcile predictions from a photochemical steady-state model with observations of H_2O_2 made during ATom. This loss rate corresponds to an expected deposition velocity of 1.00–1.32 cm s^{-1}, depending on season, and neglecting wet deposition as the aircraft generally avoided areas with precipitation. When combined with loss to OH reaction in the boundary layer, these values correspond to a removal of 300 ppt HO_x per day, estimated by GEOS-Chem to be up to 5–10% of total HO_x in the remote marine boundary layer. Though increasing the GEOS-Chem H_2O_2 deposition rate to twice it's current value, thus providing a better match H_2O_2 observations, results in an additional 1.5% decline in boundary layer HO_x.

Similarly, the UTLS is highly affected by the hydroperoxide budget. In this region, GEOS-Chem systematically over-predicts H_2O_2 and under-predicts MHP relative to ATom measurements in all seasons, with these deviations reaching a factor of up to 10–100 times difference. Sensitivity tests of HO_2 loss to heterogeneous surfaces, MHP wet deposition treatment, and reducing the rate of CH_3OO + OH in the model show that these parameters can better match the model and the measurements in the troposphere. However, altering these parameters is not enough to fully reconcile GEOS-Chem with the ATom measurements. Correlation with tracers of recent convective activity suggest that the discrepancy is likely caused by GEOS-Chem treatment of convective mass fluxes, which fail to accurately account for the transport of MHP from the lower troposphere to the UTLS during these events. Given the importance of MHP as a source of HO_x in the UTLS and the prevalence of convectively influenced air in this region (most sampled air masses in the equatorial UTLS, e.g., had been convectively influenced within the previous 5 days), more work is needed to address this issue.

Acknowledgements

Funding for this work was provided by NASA Grant No. NNX15AG61A. Additional support for H. M. A. was provided by the National Science Foundation Graduate Research Fellowship under Grant No. DGE-1144469 and additional support for M. J. K. was provided by the National Science Foundation Grant No. 1524860. The authors would like to thank the organizers of the ATom Mission, particularly S. C. Wofsy and T. B. Ryerson, for providing the opportunity to gather these data. We would also like to thank E. Czech, D. Jordan, and the people at ESPO, as well as the pilots and crew of the DC-8, for the infrastructural support that made these measurements possible.

Data Availability

The data presented in this paper are available at https://doi.org/10.3334/ORNLDAAC/1581.

3.6 Supporting Information

Introduction

This supporting information provides further details on the analytical methods used to derive data and to support conclusions from this study. The GEOS-Chem chemical and physical mechanism and discussion of heterogeneous HO_2 loss in GEOS-Chem supplement the GEOS-Chem section in the main paper by providing specific details on how the model works and considerations of a potential systematic discrepancy in the model (HO_2 loss on aerosol surfaces). The MHP comparison to the photochemical box model supports Figure 4 in the main text. The discussion on entrainment velocity supplements the analysis of H_2O_2 deposition by providing consideration of a potential interference in these results. The back trajectory analysis discussion provides further details on the methodology used to generate Figure 10 in the main text. The CIT-CIMS and GEOS-Chem correlation (Figures 3.13 and 3.14) and MHP scavenging analysis (Figure 3.15) provide further support for analysis described in Figure 9 and Section 3.3 in the main text. The photochemical box model convection simulation discussion (Figures 3.16 and 3.17) of convective influence during ATom by providing additional insight into the methods used to derive the results presented in Table 1.

GEOS-Chem Chemical and Physical Mechanism

The chemistry simulation in GEOS-Chem includes coupled HO_x-NO_x-VOC-O_3-halogen-aerosol tropospheric and stratospheric chemistry. The chemical mecha-

nisms and rate constants are consistent with recommendations from JPL and IUPAC (Atkinson et al., 2006; Burkholder et al., 2015). The model includes further mechanisms of PAN, isoprene, halogen and Criegee chemistry (Harvard, 2019). In addition to the gas-phase chemistry, GEOS-Chem includes gas-aerosol interactions through the effect of aerosol extinction on photolysis rates, heterogeneous chemistry, and gas-aerosol partitioning of semi-volatile compounds, including HO_2 uptake onto aerosol surfaces using parameters listed in Mao et al. (2010). Photolysis frequencies and rates are calculated using the Fast-JX scheme (Bian and Prather, 2002) and implemented according to Mao et al. (2010). Emissions in GEOS-Chem are from the Harvard-NASA Emission Component (HEMCO) module, which allows users to select from a variety of local and global emissions inventories (Keller et al., 2014).

GEOS-Chem includes various physical mechanisms to simulate transport, deposition, and convection of chemical species. The model implements chemical transport using the advection algorithm of Lin and Rood (1996), a multidimensional semi-Lagrangian transport scheme, along with the latitude-longitude grid of GEOS meteorological data. Dry deposition (loss due to gravitational settling and impaction) is based on a resistance-in-series model and includes aerosol loss to snow and ice surfaces. Wet deposition is treated in two cases: scavenging in wet convective updrafts and wash-out due to precipitating columns (Jacob et al., 2000). The wet scavenging due to convective updrafts depends upon several factors, including the conversion rate of cloud condensate to precipitate, the fraction of the compound in the liquid phase or cloud ice, and the retention efficiency of the compound in cloud condensation. Wet deposition primarily affects HNO_3, H_2O_2, CH_3OOH, and HCHO, among others, and the retention efficiencies of these compounds depends upon their Henry's law coefficient. Including wet scavenging in GEOS-Chem prevents soluble compounds from being transported and dispersed in the upper atmosphere due to convection.

Heterogeneous HO_2 Loss in GEOS-Chem

Studies have suggested that HO_2 may be lost via heterogeneous uptake onto aerosols, thereby decreasing the HO_x availability and reducing the formation of H_2O_2 and other peroxides. Comparison of HO_2 mixing ratios measured at a variety of sites with those predicted from models show consistently high HO_2 in models than was observed, particularly in the marine boundary layer, and potential indicates missing HO_2 loss processes in these models (Stone et al., 2012). Inclusion of HO_2 loss to aerosol surfaces was able to significantly improve agreement in model-measurement

correlations (Jacob et al., 2000; Mao et al., 2010). However, the extent to which heterogeneous loss occurs remains uncertain due to the complexity of this process and the uncertainty in potentially competing loss mechanisms. A comparison of modeled HO_2 and H_2O_2 mixing ratios over the Pacific and Atlantic with the latitude and altitude range afforded by the ATom data set may shed some light into the extent of HO_2 heterogenous uptake and the factors that affect this chemistry.

The efficacy of HO_2 heterogeneous loss is evaluated using γ, the reactive uptake coefficient, which is defined as the fraction of HO_2 collisions with aerosol surfaces that irreversibly react or are permanently trapped by the aerosol surface. There exist a range of purported γ values for HO_2 that span two orders of magnitude from 0.01–1, which have been derived from a variety of field measurements and laboratory studies (Jacob et al., 2000; Mao et al., 2010; George et al., 2013). In addition, the environment surrounding the aerosol can have a large impact on how conducive that particle is to chemical uptake. Thornton et al. (2008), for example, found that γ depends strongly on the particle phase, size, pH, and temperature. Using GEOS-Chem they report γ values of 0.1–0.3 in the tropical upper troposphere to <0.01 in the extra-polar lower troposphere; similarly, Mao et al. (2010) find γ values that range from 0.02 at 275 K to 0.5 at 220 K. The lowest γ are associated with solid surfaces, suggesting that only aqueous-aerosol plays a major role in the atmosphere (Mao et al., 2010; George et al., 2013); while the highest values of γ are associated with aqueous aerosols that contain transition metal ions, particularly copper and iron, which convert HO_2 to H_2O (Thornton and Abbatt, 2005; Mao et al., 2013). Despite these variations in γ, following Jacob et al. (2000) and Mao et al. (2013) current recommendations for GEOS-Chem and other chemical transport models utilize a static γ of 0.2 and full conversion of HO_2 on aerosol surfaces (Harvard, 2019).

Output from the GEOS-Chem model was compared to the ATom measurements to evaluate how different estimations of the reactive uptake coefficient affect HO_x and therefore the HO_2 budget. The model was run at γ values of 0.2 (standard), 0.07 (moderate), and 0 (no HO_2 heterogeneous loss). When the uptake coefficient is set to 0, more HO_2 is available leading to higher H_2O_2 mixing ratios. However, the simulations produce only a small effect on the H_2O_2 budget when the HO_2 heterogeneous update rate is varied. Compared to the standard simulation with γ=0.2, the production of H_2O_2 increases by very little, except in the polar regions during the summer months (Figure 3.11). In February and May, H_2O_2 increases by

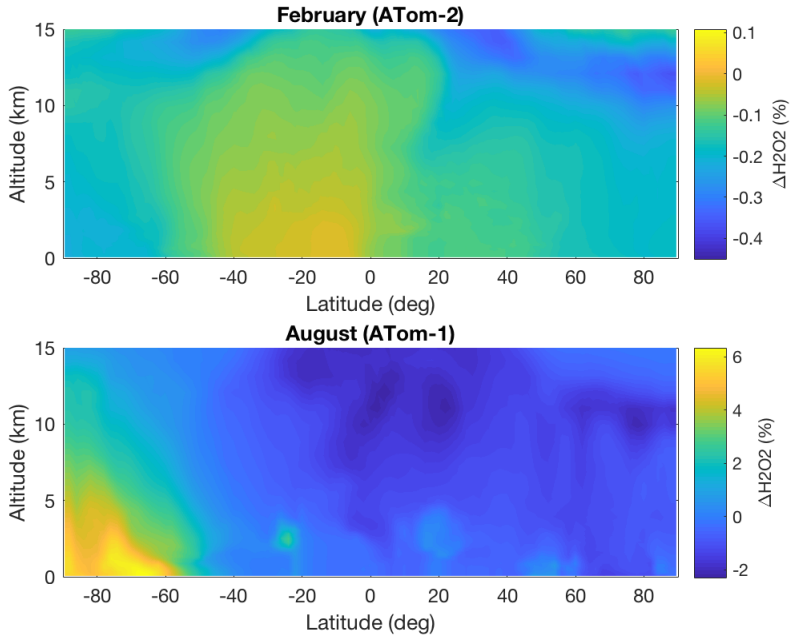

Figure 3.11: Effect of altering the HO_2 heterogeneous uptake coefficient (γ) on the H_2O_2 budget in GEOS-Chem. The GEOS-Chem model was run with $\gamma = 0.2$ (standard run) and with $\gamma = 0$ (no uptake), with the change in H_2O_2 mixing ratios shown as a function of latitude and altitude. An uptake coefficient of 0 leads to higher H_2O_2 mixing ratios in the polar marine boundary layer in summer but very little effect during the winter. Note the difference in coloring scaling factors between February and August.

only about 0.1% in the equatorial region and decreases by up to 0.3% in the polar regions. Most of the observed effect of altering γ occurs in the polar boundary layer of the south pole during August and in the polar boundary layer of the north pole during October. In both these cases, H_2O_2 increases by 5–10% when γ is 0 compared with the standard simulation. However, these are also areas in which the absolute H_2O_2 mixing ratio is fairly low; hence the bulk of the data, which samples in the tropics and subtropics, shows very little change.

MHP Comparison to Box Model

Figure 3.12 shows the MHP CIT-CIMS measurements compared with photochemical box model predicted MHP mixing ratios averaged over altitude. The model more accurately captures MHP at the lower altitudes compared with H_2O_2 as MHP is expected to undergo more photochemical and less depositional loss at these altitudes.

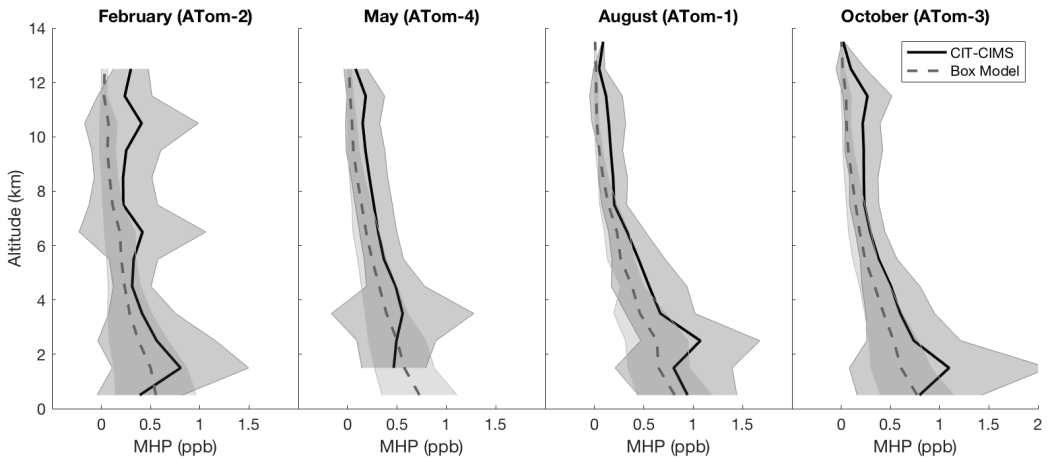

Figure 3.12: Comparison of MHP mixing ratios from measurements (CIT-CIMS) and those following chemical relaxation over 5 days after the measurements calculated using a photochemical box model. The model more accurately captures MHP in the lower troposphere because MHP is much less influenced by loss to wet and dry deposition. The results are averaged over 1 km altitude bins and shaded region represent one standard deviation of the mean.

Entrainment Velocity

To assess other factors that might convolute the analysis of H_2O_2 deposition velocity, the entrainment velocity of HCN was calculated and compared to the H_2O_2 deposition velocity. Entrainment is the mixing of an air mass into a second preexisting one, i.e. the movement of free tropospheric air into the marine boundary layer. This movement brings chemical compounds circulating aloft into the boundary layer and therefore may affect the deposition calculation by providing an unaccounted source of H_2O_2 that masks the true H_2O_2 loss due to deposition. In order to assess the potential extent of this influence on H_2O_2 mixing ratios, the entrainment rate of HCN was calculated. HCN is primarily lost from the atmosphere via deposition and does not have significant photochemical loss, giving HCN a long atmospheric lifetime of 6 months. Because of this long lifetime, HCN is considered well-mixed in the atmosphere, particularly above the marine boundary layer. An estimate of the entrainment velocity (V_e) can be made by comparing the flux of HCN to the ocean surface from deposition to the flux of free tropospheric HCN entrained into the boundary layer from above:

$$V_e = \frac{V_d \times [\mathrm{HCN}]_{\mathrm{BL}}}{[\mathrm{HCN}]_{\mathrm{FT}} - [\mathrm{HCN}]_{\mathrm{BL}}} \tag{3.12}$$

The deposition velocity (V_d) is assumed to be 0.12 cm s^{-1} (Singh et al., 2003; Li et al., 2003). This calculation gives an average entrainment velocity of 0.08, 0.03, 0.04,

and 0.08 cm s^{-1} for February, May, August, and October, respectively. Assuming that the entrainment rate for H_2O_2 is similar to that of HCN, these values are low enough that entrainment is likely not a major factor in the H_2O_2 budget. Instead, the transition between the upper troposphere and the boundary layer is likely a region in which H_2O_2 is lost from the atmosphere due to in-cloud scavenging rather than a source of H_2O_2 due to entrainment.

Back Trajectory Analysis

Back trajectories were calculated using the Traj3D model (Bowman, 1993; Bowman and Carrie, 2002) run with the National Centers for Environmental Protections (NCEP) Global Forecast System (GFS) 0.5° by 0.5° resolution meteorology. A cluster of 245 trajectories were initialized in a cube with dimensions of 0.3° longitude, 0.3° latitude, and 20 hPa pressure (altitude) centered on one minute intervals along the flight track and run backwards for 10 days. The latitude, longitude, and pressure altitude for each of the 245 trajectories were than averaged to a single latitude, longitude, and pressure for each one minute point along the flight track. The probability of convective influence for each parcel was calculated based on the coincidence of the parcel with clouds, high RH (above 50%), and cloud water. Cloud depth and height were obtained from the NASA Langley global gridded cloud products.

CIT-CIMS and GEOS-Chem Correlations

Figure 3.13 and 3.14 indicate correlations between the GEOS-Chem model and measurements made by the CIT-CIMS for H_2O_2 and MHP, respectively. The GEOS-Chem model overestimates H_2O_2 and underestimates MHP across all four seasons. These correlations exclude data collected over land.

MHP Scavenging in GEOS-Chem

The extent to which MHP scavenging in GEOS-Chem affects the predicted MHP mixing ratios in the upper troposphere and lower stratosphere is shown in Figure 3.15.

Photochemical Box Model Convection Simulation

In order to assess the effect of convection on the UTLS, the photochemical box model was initialized with measurements collected during ATom and a high ratio of MHP fraction [MHP/(MHP+H_2O_2] and of high NO_x fraction [NO_x/(NO_x+HNO_3)] to simulate conditions immediately following convection. The model progressed until steady-state was reached (~10 days). An expression was fit to the change in

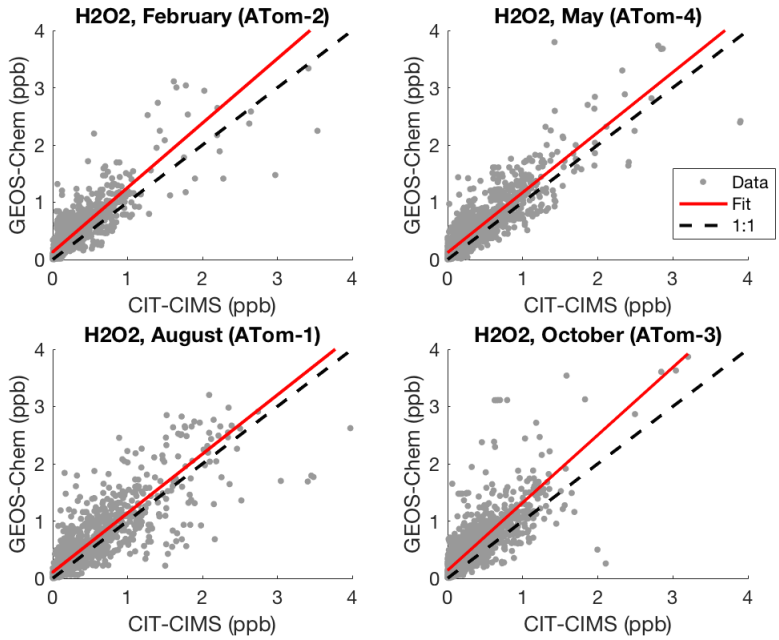

Figure 3.13: Correlation between CIT-CIMS measurements of H_2O_2 mixing ratios in the remote troposphere and those predicted by GEOS-Chem. Slopes of the correlations are 1.13, 1.05, 1.03, and 1.18 for February (ATom-2), May (Atom-4), August (ATom-1), and October (ATom-3), respectively, with R^2 values of 0.66, 0.72, 0.69, and 0.56, respectively.

MHP fraction and NO_x fraction between initiation and steady-state for 1 km altitude bins from 6 to 12 km as shown in Figures 3.16 and 3.17. This expression was then used to derive air mass ages for measurements collected between $-30°$ and $30°$ during ATom in the manner of Bertram et al. (2007).

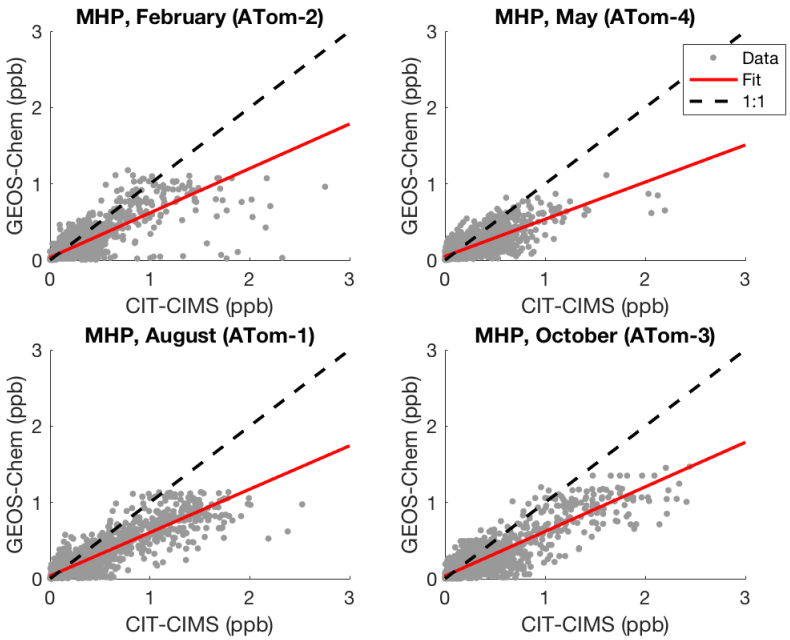

Figure 3.14: Correlation between CIT-CIMS measurements of MHP mixing ratios in the remote troposphere and those predicted by GEOS-Chem. Slopes of the correlations are 0.58, 0.49, 0.57, and 0.58 for February (ATom-2), May (Atom-4), August (ATom-1), and October (ATom-3), respectively, with R^2 values of 0.65, 0.58, 0.79, and 0.75, respectively.

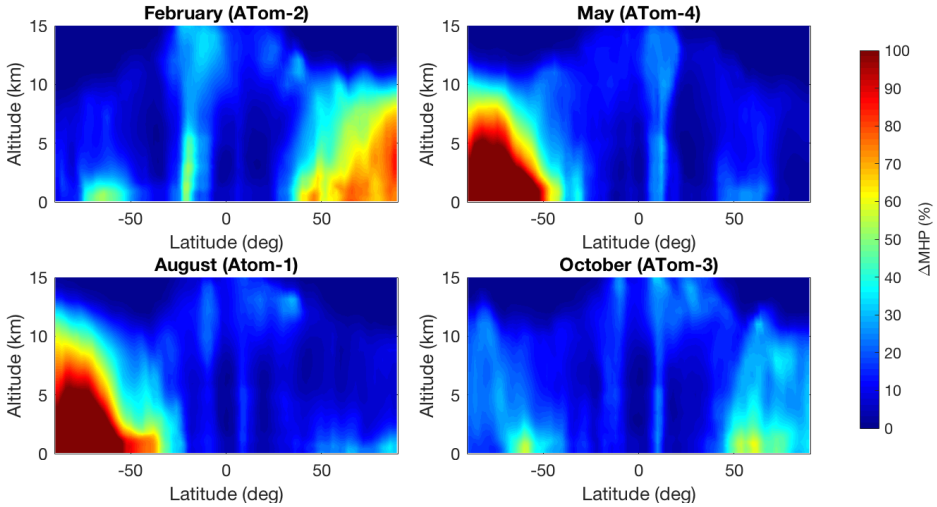

Figure 3.15: Difference in predicted MHP mixing ratios across latitude and altitudes when GEOS-Chem is run with no MHP wet deposition compared with the standard simulation. MHP mixing ratios increase significantly in the polar regions (>50% increase) but only by 20–30% in the equatorial UTLS. This increase in MHP mixing ratios brings the GEOS-Chem predicted mixing ratios closer to those measured, but is not enough to offset the difference between the model and the measurements.

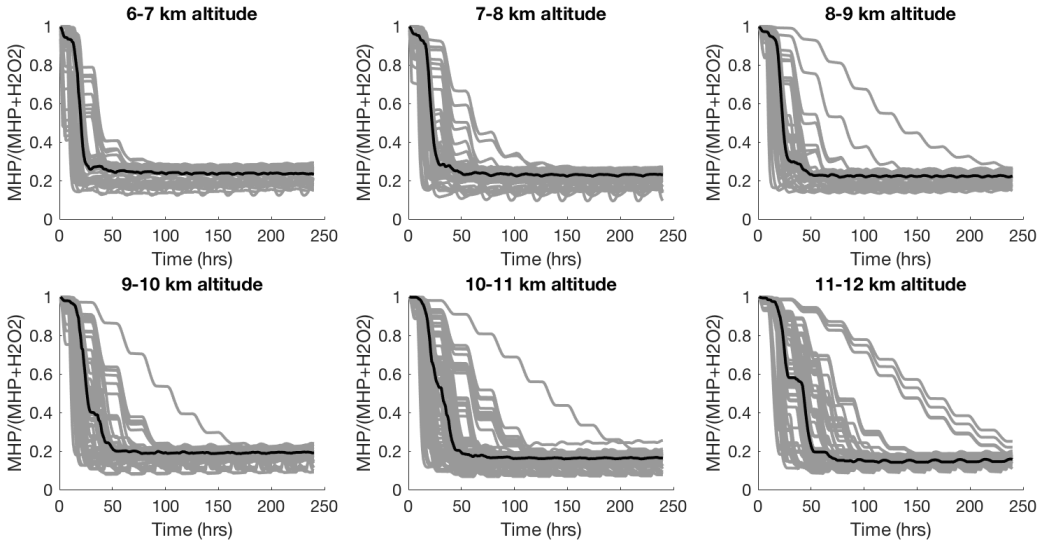

Figure 3.16: Modeled fraction of MHP/(MHP+H_2O_2) over time following convective activity for each altitude bin in the UTLS for ATom-1. An expression based on the mean change in MHP fraction (black) was fit based on model results for each data point in the altitude bin (gray).

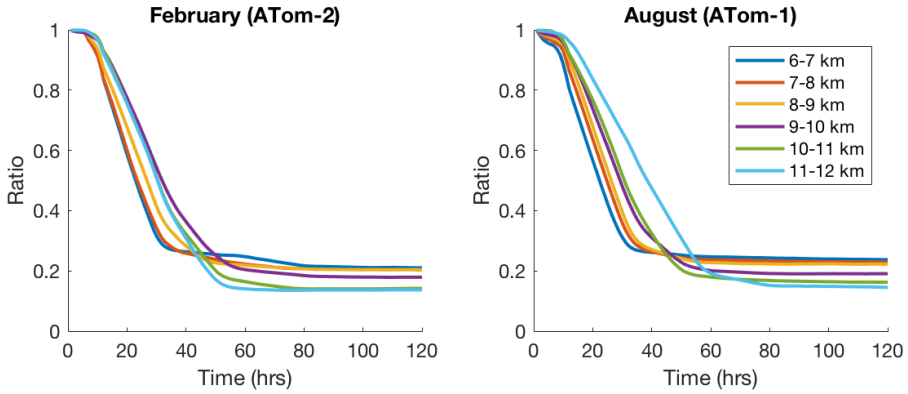

Figure 3.17: Modeled mean MHP/(MHP+H_2O_2) over time following convective activity for each altitude bin in February (ATom-2) and August (ATom-1). This mean change in MHP fraction for each 1 km altitude bin between 6 km and 12 m was fit to an expression and used to estimate the age of air masses sampled during ATom.

Chapter 4

KINETICS AND PRODUCT YIELDS OF THE OH INITIATED OXIDATION OF HYDROXYMETHYL HYDROPEROXIDE

4.1 Abstract

Hydroxymethyl hydroperoxide (HMHP), formed in the reaction of the C_1 Criegee intermediate with water, is among the most abundant organic peroxides in the atmosphere. Although reaction with OH is thought to represent one of the most important atmospheric removal processes for HMHP, this reaction has been largely unstudied in the laboratory. Here, we present measurements of the kinetics and products formed in the reaction of HMHP with OH. HMHP was oxidized by OH in an environmental chamber; the decay of the hydroperoxide and the formation of formic acid and formaldehyde were monitored over time using CF_3O^- chemical ionization mass spectrometry (CIMS) and laser induced fluorescence (LIF). The loss of HMHP by reaction with OH is measured relative to the loss of 1,2-butanediol [$k_{1,2-\text{butanediol+OH}}$ = $(27.0 \pm 5.6) \times 10^{-12}$ cm^3 molecule^{-1}s^{-1}]. We find that HMHP reacts with OH at 295 K with a rate coefficient of $(7.1 \pm 1.5) \times 10^{-12}$ cm^3 molecule^{-1}s^{-1}, with the formic acid to formaldehyde yield in a ratio of 0.88 ± 0.21 and independent of NO concentration (3×10^{10} – 1.5×10^{13} molecule cm^{-3}). We suggest that, exclusively, abstraction of the methyl hydrogen of HMHP results in formic acid while abstraction of the hydroperoxy hydrogen results in formaldehyde. We further evaluate the relative importance of HMHP sinks and use global simulations from GEOS-Chem to estimate that HMHP oxidation by OH contributes 1.7 Tg yr^{-1} (1-3%) of global annual formic acid production.

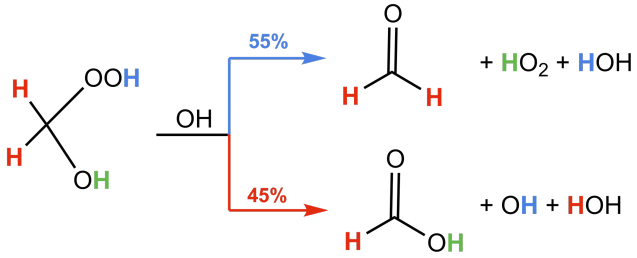

Figure 4.1: Schematic of HMHP oxidation by OH with product yields.

4.2 Introduction

Hydroperoxides significantly contribute to the chemistry of the atmosphere due to their high reactivity. These species alter the atmosphere's oxidative potential by acting as a reactive sink and transported reservoir of HO_x (Jaeglé et al., 1997, 2000; Lee et al., 2000). They act as oxidants of SO_2 in the aqueous phase to produce $SO_4{}^{2-}$, thereby reducing air quality and visibility (Lind et al., 1987; Zhou and Lee, 1992). In addition, hydroperoxides have been implicated in the inhibition of certain peroxidase enzymes essential to plant function (Marklund, 1971; Hewitt et al., 1990), although some studies note that under certain conditions exposure to ozone can increase plant resistance to oxidative stress from hydroperoxides (Sandermann et al., 1998; Mehlhorn, 1990).

Hydroxymethyl hydroperoxide ($HOCH_2OOH$, HMHP) is among the hydroperoxides observed in significant abundance in the atmosphere. Reported concentrations of HMHP vary considerably, but typically fall in the low ppbv range during the summer and have been reported up to 5 ppbv over forested regions (Lee et al., 1993; Fels and Junkermann, 1994; Weinstein-Lloyd et al., 1998; Nguyen et al., 2015). Recently, HMHP concentrations were measured during the SEAC4RS (Studies of Emissions, Atmospheric Composition, Clouds, and Climate Coupling by Regional Surveys) flight campaign traversing across the southeastern United States between August 6 and September 23, 2013. HMHP mixing ratios varied considerably depending on location and altitude, but within the boundary layer the average HMHP mixing ratio was 0.25 ppbv with a maximum of 4.0 ppbv (Figure 4.2).

HMHP forms when terminal alkenes react with ozone in the presence of water vapor (Qi et al., 2007; Crehuet et al., 2001; Gäb et al., 1985; Horie et al., 1994; Huang et al., 2013; Sauer et al., 1999; Nakajima and Endo, 2015). Upon attack by O_3, the alkene fragments into a carbonyl and an energy-rich intermediate, which may be collisionally stabilized to form the C_1 Criegee intermediate (CH_2OO). The C_1 Criegee intermediate then reacts with water vapor monomer or dimer (n=1,2) to form HMHP:

$$CH_2OO + (H_2O)_n \longrightarrow HOCH_2OOH + (H_2O)_{n-1} \tag{4.1}$$

Thus, ozonolysis of alkenes with terminal double bonds (such as isoprene and β-pinene as well as simpler alkenes such as ethene, propene, and 1-butene) contribute to HMHP formation (e.g. Figure 4.2).

Understanding the relative rates of production and removal mechanisms of HMHP

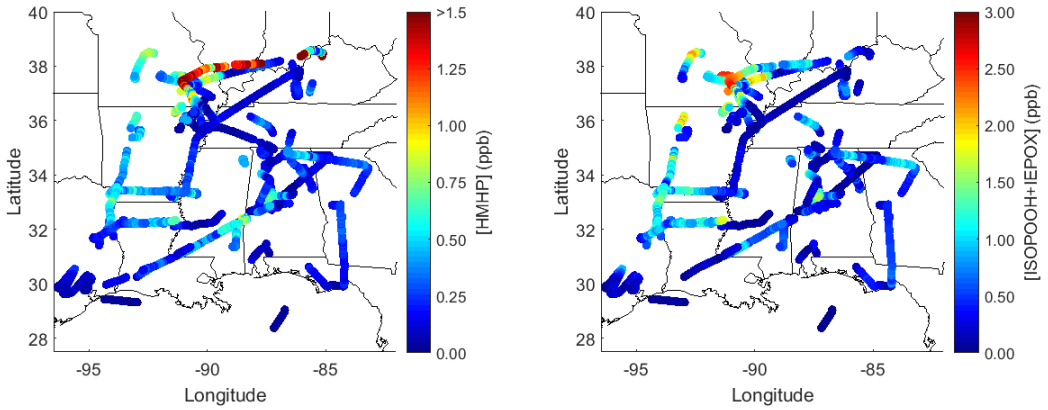

Figure 4.2: HMHP (left) and isoprene hydroxy hydroperoxide and epoxydiol (ISOPOOH + IEPOX, right) mixing ratios during the summer 2013 SEAC4RS flight campaign in the southeastern United States. ISOPOOH and IEPOX result from the OH oxidation of isoprene and are therefore indicative of regions with high isoprene mixing ratios. The average HMHP mixing ratio was 0.25 ppbv, but reached above 1 ppbv on several occasions during the campaign. HMHP mixing ratios were generally correlated with its precursor species, isoprene, as assessed by ISOPOOH + IEPOX.

is key to assessing its lifetime and importance in the atmosphere. HMHP undergoes three major atmospheric removal processes: photolysis, deposition, and reaction with the hydroxyl radical. Numerous studies investigating the spectroscopic properties of HMHP have concluded that photolysis is likely to be less significant than other atmospheric loss processes (photolysis rate of $J \sim 1 \times 10^{-6}$ s^{-1} under typical atmospheric conditions) (Su et al., 1979; Bauerle and Moortgat, 1999; Fry et al., 2006; Roehl et al., 2007; Eisfeld and Francisco, 2008). HMHP is highly water-soluble (Henry's Law constant of $H \sim 10^6$ M atm^{-1}; O'Sullivan et al. (1996)) and is therefore highly susceptible to rainout and dry deposition (Nguyen et al., 2015). Reaction with OH is expected to be an important sink of HMHP, with three possible H-abstraction pathways: abstraction of (a) the hydroperoxidic hydrogen, (b) the alkyl hydrogen, and (c) the alcoholic hydrogen (Francisco and Eisfeld, 2009). These pathways lead to the formation of formic acid (HCOOH) or formaldehyde (HCHO) with OH or HO_2 radicals as byproducts, respectively. However, the rate coefficient for this reaction has not been previously reported.

In this study, we investigate the reaction of HMHP with OH. HMHP was oxidized by OH in an environmental chamber, and the decay of the hydroperoxide was monitored over time using CF_3O^- chemical ionization mass spectrometry (CIMS). Product yields of formic acid and formaldehyde were characterized by CIMS and by

laser induced fluorescence (LIF), respectively. The yield of formic acid was further characterized under varying NO concentrations to assess the HMHP + OH oxidation pathways. HMHP sinks and the impact of HMHP oxidation on global formaldehyde and formic acid concentrations are interpreted in the context of simulations using GEOS-Chem to evaluate the global importance of HMHP oxidation.

4.3 Experimental Methods

Instrumentation

Chemical Ionization Mass Spectroscopy (CIMS) is a versatile and robust technique for detecting a variety of atmospheric compounds, including hydroperoxides. Reagents and oxidation products in this work were monitored using a compact time-of-flight CIMS (ToF-CIMS, Tofwerk/Caltech) that employs a CF_3O^- reagent ion for sensitive detection of gas-phase organic acids and multifunctional organic compounds. The CF_3O^- CIMS technique has been described in detail in Crounse et al. (2006); Paulot et al. (2009a), and St. Clair et al. (2010).

Briefly, the reagent ions form by passing 380 sccm of 1 ppm CF_3OOCF_3 in N_2 through a cylindrical ion source containing a layer of radioactive polonium-210 (NRD LLC, $\leq$10 mCi). The sample air is diluted with dry N_2 (1750 sccm) in a Pyrex glass flow tube with a hydrophobic coating (Fluoropel 801A, Cytonix) that is maintained at a pressure of 35 mbar. The diluted sample air then mixes with the reagent ions, which selectively ionize analytes by forming ion clusters (m/z = analyte mass + 85) or fluoride transfer ions (m/z = analyte mass + 19), the dominance of which depends on the acidity and fluoride affinity of the target analyte. Product ions are transferred through a pinhole orifice and a conical hexapole ion guide to the time-of-flight mass spectrometer chamber. Compounds are separated in the mass spectrometer based on differences in their mass-to-charge ratio as they accelerate through the instrument.

The ToF-CIMS provides 10 Hz resolution data for masses between m/z 19 and m/z 396. In this study, HMHP was monitored at *m/z* 149 (HMHP·CF_3O^-), the relative rate partner, 1,2-butanediol, was monitored at *m/z* 175 (1,2-butanediol·CF_3O^-), formic acid (FA) was monitored at *m/z* 65 (FA_{-H}·HF), and bis-HMP (bis-hydroxymethyl peroxide, $HOCH_2OOCH_2OH$) was monitored at both *m/z* 113 (bis-HMP_{-H}·HF) and *m/z* 179 (bis-HMP·CF_3O^-). All observed ion signals were normalized to the sum of the reagent anion signal ($^{13}CF_3O^-$ isotope at m/z 86) and the water signal (m/z 104, $H_2O{\cdot}^{13}CF_3O^-$ isotope) to account for fluctuations in the reagent ion concentration.

Detection limits for the ToF-CIMS are typically 10 pptv for a 1 second integration period.

In addition to the ToF-CIMS, other instruments were employed to assess concentrations of formaldehyde, NO, and O_3 over the course of the experiment. Formaldehyde product yields were characterized by the NASA In Situ Airborne Formaldehyde (ISAF) instrument (Cazorla et al., 2015). Briefly, the ISAF instrument employs a pulsed tunable fiber laser for LIF detection of HCHO. The laser operates at 353 nm, exciting a single rotational transition of the A–X band in HCHO. The instrument has a 10 Hz sampling frequency that is averaged to 1 second, at which the precision is typically better than 20% above 100 pptv. NO_x and O_3 concentrations throughout the experiment were monitored with a NO_x monitor (Teledyne 200EU) and an O_3 monitor (Teledyne 400E). All instruments sampled the chamber from an approximately 1 m loop of 0.635 cm OD PFA tubing.

Synthesis

A new method for synthesizing HMHP was performed in this study. The method is based on a technique described in Bauerle and Moortgat (1999), in which formaldehyde vapor is passed through hydrogen peroxide to generate HMHP. Here, HCHO was prepared by gently heating crystalline paraformaldehyde (Sigma-Aldrich) and passing the resulting vapor through two successive cryotraps at -65 °C and -196 °C to collect impurities and condense HCHO, respectively. A small (~10 sccm) flow of N_2 was then passed over the collected HCHO, held at -65 °C, and bubbled through urea hydrogen peroxide (Sigma-Aldrich, 97%, 1100 mg) in dichloromethane (DCM, 30 mL) held in a -30 °C cold bath. After approximately 5 minutes of flow, the -30 °C bath was removed and the reaction mixture allowed to warm to room temperature. HMHP formed from this method in a relative yield of approximately 4:1 HMHP to bis-HMP and with small amounts of HCHO and H_2O_2 also present (as determined by gas-phase analysis of an evaporated droplet of the synthetic mixture). Note that previous synthesis using a similar method found significant safety hazards upon concentration of the hydroperoxide product (e.g. Fry et al. (2006)).

Chamber Experiments

Experiments on HMHP + OH oxidation were conducted in a small environmental chamber. The chamber consisted of a 1 m^3 fluorinated ethylene propylene copolymer bag (Teflon-FEP, DuPont) within an enclosure equipped with UV lights (8 Sylvania 350 blacklights), and has been described previously (Bates et al., 2014; Praske et al.,

2015; Teng et al., 2015). The chamber was prepared by multiple flushes of dry air between successive experiments. Table 1 provides a description of experimental conditions.

Table 4.1: Summary of conditions used in HMHP oxidation experiments. Mixing ratios are given in ppbv. Experiments were performed at ambient laboratory temperature (295 K) and pressure (745 Torr).

Exp.	$[HMHP]_0$	$[OH\ source]_0$*	$[1,2\text{-}BD]_0$	$[NO]_0$	% HMHP Ox.	Objective
1	150	190	80	475	35%	Kinetics
2	90	200	15	460	40%	Kinetics
3	35	190	15	160	55%	Kinetics
4	165	100	—	445	30%	Yields
5	55	45	—	20	45%	NO_x dep.
6	70	30	—	500	30%	NO_x dep.
7	20	20	—	20	35%	NO_x dep.
8	10	60	—	25	50%	NO_x dep.
9	20	120	—	530	40%	NO_x dep.

*OH source was methyl nitrite for kinetics experiments and isopropyl nitrite for the yields experiment.

Reagents were added to the chamber sequentially after flushing the chamber bag with dry air and filling it to near 50% with zero air. NO (1993 ± 20 ppmv in N_2, Matheson) was prepared by filling an evacuated 500 cm^3 glass bulb to the desired pressure and backfilling with N_2 before adding to the chamber. Next, 1,2-butanediol (1,2-BD, ≥ 98%, Sigma-Aldrich) was added as a relative rate partner by flowing 20 L min^{-1} dry air over a small drop of the diol placed in a glass vial. 1,2-butanediol was chosen as a relative rate partner because it is detectable by the CF_3O^- CIMS technique and has a known OH reaction rate constant that is expected to be similar to that of HMHP + OH. A method similar to that outlined in Taylor et al. (1980) was used to synthesize the HO_x source used in this study, methyl nitrite (CH_3ONO). Approximately 200 ppbv of CH_3ONO was added to the chamber via serial dilution in a 500 cm^3 glass bulb. Finally, HMHP was added to the chamber by first cryo-collecting the sample to remove high volatility impurities generated from the synthesis. Zero air was passed for 10-30 seconds over a three way vial containing approximately 0.5–1.2 mL of synthesized HMHP in DCM and HMHP was subsequently trapped in a cold bath at -80 °C. Upon removal of the bath, the cryotrapped sample was flushed into the chamber with zero air for approximately 20 minutes until the remainder of the chamber volume was filled. H_2O_2 and HCHO

were present in the chamber in minor amounts (~5% and ~2% relative to HMHP, respectively) from the HMHP synthetic mixture described above.

Photooxidation was initiated after stabilization of the CIMS signals (15 to 50 min). The UV lights were turned on to generate OH radicals via

$$CH_3ONO + h\nu \xrightarrow{O_2} HO_2 + NO + HCHO \quad (4.2a)$$

$$HO_2 + NO \longrightarrow OH + NO_2 \quad (4.2b)$$

This process produced OH concentrations that were typically ~50 times greater than average atmospheric levels. Oxidation lasted until the OH precursor was depleted (~1 hour), utilizing 3 of the chamber's UV lights. Approximately 30–50% of HMHP was oxidized.

The chamber was prepared in a very similar manner for all experiments, with a few notable exceptions. For Exps. 4–9, 1,2-butanediol was not added to the chamber to minimize any interference in the product yield due to oxidation of this species. For Exp. 4, in which HCHO was measured, isopropyl nitrite was used as the OH source to preclude HCHO interference from CH_3ONO photolysis. In addition, a series of experiments were conducted to assess the NO_x dependence of the formic acid yield. In these experiments, a further step was taken to purify HMHP from the reaction mixture. The solvent and high volatility impurities were removed first by either flowing zero air over the reaction mixture at -80 °C or by placing the reaction mixture under vacuum. To isolate HMHP from the lower volatility bis-HMP synthetic byproduct, the remaining reaction mixture was collected in a cold trap and HMHP was eluted at a temperature of -15 °C.

Calibration

A gravimetric technique was used to calibrate the ToF-CIMS for formic acid. A commercially available formic acid standard (Sigma-Aldrich, 98%) was dissolved in water (1% w/w solution) and volatilized into the chamber by flowing a known amount of dry air over the sample until it had completely evaporated. The dry and water-dependent sensitivities were determined by addition of varying concentrations of water vapor to the sample before it entered the CIMS instrument. This water-vapor calibration was applied to the ToF-CIMS formic acid signal during analysis. Because there is no commercially available standard, the absolute sensitivity of HMHP could not be determined. Using the synthetic sample, a calibration for the change in HMHP sensitivity based on water vapor was performed in a manner

similar to that of formic acid. This relative calibration was used in analysis of the ToF-CIMS HMHP signals. The bis-HMP ToF-CIMS sensitivity relative to HMHP was estimated from ion-molecule collision rates, which were parameterized from the calculated dipole moment and polarizability of the neutral molecules (Su and Chesnavich, 1982; Garden et al., 2009; Paulot et al., 2009a). See the Supplemental Information for further details of the ToF-CIMS calibration procedures. HCHO instrument sensitivity for ISAF was determined via calibration against standard additions of a commercially available HCHO standard to zero air. See Cazorla et al. (2015) for further details of the ISAF calibration procedure.

Theoretical Methods

Reaction rate constants for the unimolecular reactions are calculated with the approach by Møller et al. (2016) using multi-conformer transition state theory with Eckart tunneling. The electronic energies are calculated using coupled cluster methods in Molpro2012, while zero-point vibrational energy corrections and partition functions are calculated using density functional theory in Gaussian 09 (Werner et al., 2012; Frisch et al., 2009). Rice-Ramsperger-Kassel-Marcus (RRKM) modeling of selected reactions is done using the Master Equation Solver for Multi-Energy well Reactions (MESMER) and the MultiWell program suite (Glowacki et al., 2012; Barker et al., 2017a). See Supplemental Information for details.

4.4 Results and Discussion

HMHP + OH Rate Coefficient

The HMHP + OH reaction rate coefficient (k_{HMHP}) relative to that of 1,2-butanediol + OH (k_{diol}) was determined at ambient temperature using data from experiments 1–3 (Table 4.1). The rate coefficient of 1,2-butanediol with OH is $(27.0 \pm 5.6) \times 10^{-12}$ cm^3 molecule^{-1}s^{-1} at T = 296 K (Bethel et al., 2001). To obtain the rate constant for HMHP + OH relative to that of 1,2-butanediol + OH, the natural logarithm of the HMHP mixing ratio (normalized to the initial concentration) was plotted as a function of the natural logarithm of the normalized 1,2-butanediol mixing ratios over the course of oxidation (Figure 4.3). The slope of a linear regression analysis incorporating error in both dimensions (York et al., 2004) gives the reaction rate of HMHP relative to 1,2-butanediol ($k_{\mathrm{HMHP}}[\mathrm{OH}]/k_{\mathrm{diol}}[\mathrm{OH}]$) for each experiment. Table 4.2 lists the relative rates $k_{\mathrm{HMHP}}/k_{\mathrm{diol}}$ and gives a recommended rate constant for the OH oxidation of HMHP (calculated by taking a mean of all experimental runs weighted by their respective uncertainties).

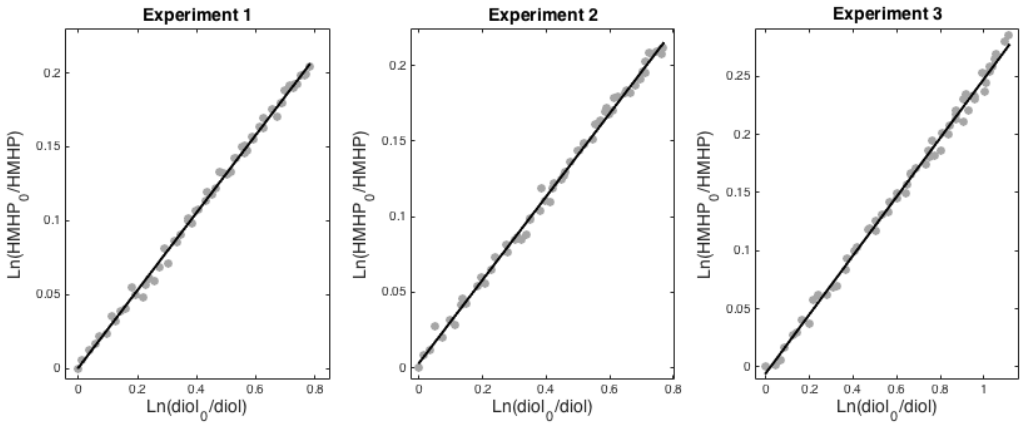

Figure 4.3: Fit (black) of the natural logarithmic decay of HMHP vs 1,2-butanediol (diol) during oxidation. HMHP and 1,2-butanediol data are measured at ToF-CIMS signals m/z 149 and m/z 175, respectively, and averaged over 30 s between 15 and 45 min into the oxidation. The relative decay is used to determine the HMHP + OH oxidation rate.

The uncertainty for all experiments is dominated by the 20% uncertainty in the 1,2-butanediol rate constant. Other appreciable sources of error arose from the loss of HMHP on the walls of the chamber, equilibration of the ToF-CIMS signals, and the error in the linear fit. To account for uptake of HMHP to the chamber walls, a first-order loss rate of $(0.8 \pm 0.2) \times 10^{-5}$ s^{-1} was used in the data analysis (5% correction to the HMHP data). This rate was determined by filling the chamber with 12 ppbv of HMHP and monitoring the decay of the signal in the dark. The signal from 1,2-butanediol was also corrected for minor wall loss (0.5% correction). In addition, HMHP mixing ratios were corrected for a minor loss due to photolysis ($J = 8.5 \times 10^{-7}$ s^{-1}, calculated from measured light flux in the chamber and from quantum yields and cross sections in Sander et al. (2011); total correction of <1%). Data from t<15 and t>45 minutes into the oxidation was not used in Figure 4.3 or to evaluate the kinetics of HMHP + OH (5% correction to the rate constant). The first few minutes of oxidation were disregarded to minimize error due to equilibration of sampling surfaces, such as chamber and tubing walls. At long oxidation times, most of the OH precursor had been depleted, causing photochemical reactions to slow and making relative loss to the chamber walls substantial.

HMHP Oxidation Products

Experiments to determine the yields of formic acid and HCHO from HMHP oxidation were conducted in a manner similar to that of the kinetics experiments. A

Table 4.2: Relative rate of HMHP + OH to 1,2-butanediol + OH (k_{HMHP}/k_{diol}) at 295 K for Experiments 1–3 and derived absolute HMHP + OH rate coefficient (10^{-12} cm^3 molecule^{-1}s^{-1}).

Experiment 1	Experiment 2	Experiment 3	**Rate Coefficient**
0.262 ± 0.008	0.275 ± 0.011	0.253 ± 0.015	7.1 ± 1.5

Uncertainties are 1σ standard deviations from measurement uncertainties; the rate coefficient also includes error in the 1,2-butanediol + OH rate coefficient.

constant correction factor of 0.10×[HMHP] was subtracted from all HCHO signals to account for an estimated HMHP decomposition in the ISAF HCHO instrument (see the Supplemental Information for more details). HMHP and formic acid were corrected for wall loss by applying the experimentally-derived wall loss rates to the data. Under the experimental conditions, formic acid wall loss is comparable to wall production, the sum of which is minor compared to total formic acid production from HMHP (~ 2.5%). The loss of formic acid and HCHO due to the reaction with OH was accounted for as described by Eq. VI of Atkinson et al. (1982) (1.5% for FA and up to 15% for HCHO; see the Supplemental Information). HCHO was also corrected for loss due to photolysis ($J = 1.7 \times 10^{-5}$ s^{-1}, calculated from measured light flux in the chamber and from quantum yields and cross sections in Sander et al. (2011); up to 5% correction). As previously discussed, bis-HMP was present in the chamber during the oxidation experiment. Observed formic acid mixing ratios were corrected for bis-HMP + OH production of formic acid, assuming that bis-HMP oxidation produces 2 equivalents of formic acid. This process is calculated to produce up to 40% of total formic acid, using a bis-HMP + OH rate coefficient that is 35% that of HMHP + OH as determined from the kinetics experiments (see the Supplemental Information).

The ratio of the formic acid to the HCHO yield was found in Exp. 4 by comparing the change in these species during the oxidation period and using a linear regression that accounts for error in both dimensions (York et al., 2004). These yields are assessed from data taken between t = 15 minutes and t = 45 minutes into the oxidation, to minimize error due to equilibration of sampling surfaces and to loss on chamber walls. The results of the linear regression analysis are presented in Figure 4.4. The reaction of HMHP with OH produces formic acid and HCHO in comparable amounts with a formic acid to HCHO product ratio of 0.88 ± 0.21. The reported

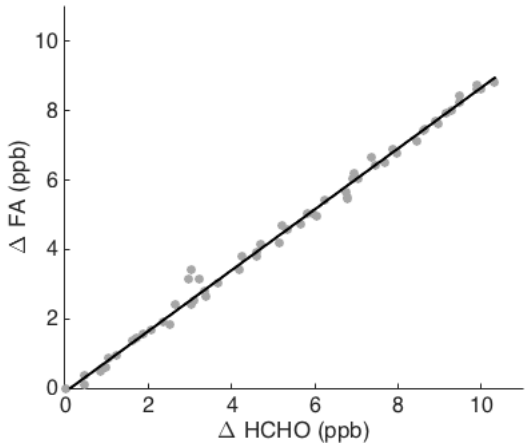

Figure 4.4: Production of formic acid (FA) compared with that of HCHO. Formic acid was measured on the ToF-CIMS at *m/z* 65 and HCHO data are from ISAF during Experiment 4. The signals are corrected for losses outlined in the text, and averaged over 30 s between 15 and 45 min into the oxidation. The black line indicates the best fit to the data.

uncertainty arises from the errors in the calibration of the ToF-CIMS data and from corrections due to HMHP interference in ISAF, product loss due to reaction with OH, and bis-HMP + OH production of formic acid as outlined above, as well as from uncertainty in the line of best fit.

To assess carbon closure from HMHP + OH, an upper limit to the HMHP sensitivity was estimated using the yield experiment. As discussed previously, the absolute sensitivity of the ToF-CIMS to HMHP is not well-known. Assuming that formic acid and HCHO are the only two products from HMHP + OH, the total change in HMHP mixing ratios over the experiment was assumed to be equal to the change in the sum of the two products. This mixing ratio was then used to derive an upper limit to the expected HMHP sensitivity on the ToF-CIMS. Using this sensitivity, we calculate HMHP yields from ethene ozonolysis experiments conducted in the 1 m^3 chamber (see the Supplemental Information). Within error, these yields are the same as those reported by Hasson et al. (2001b), consistent with formic acid and HCHO as the only major products from the reaction of HMHP with OH.

As shown in Figure 4.5, formic acid can form following abstraction of the methyl, alcoholic, or hydroperoxy hydrogens. Abstraction of the hydroperoxide H (pathway (a) in Figure 4.5) leads to the formation of the hydroxy peroxy radical ($HOCH_2OO$). This radical forms with excess energy from the abstraction and may react unimolecularly to lose HO_2 before undergoing collisional thermalization. Following

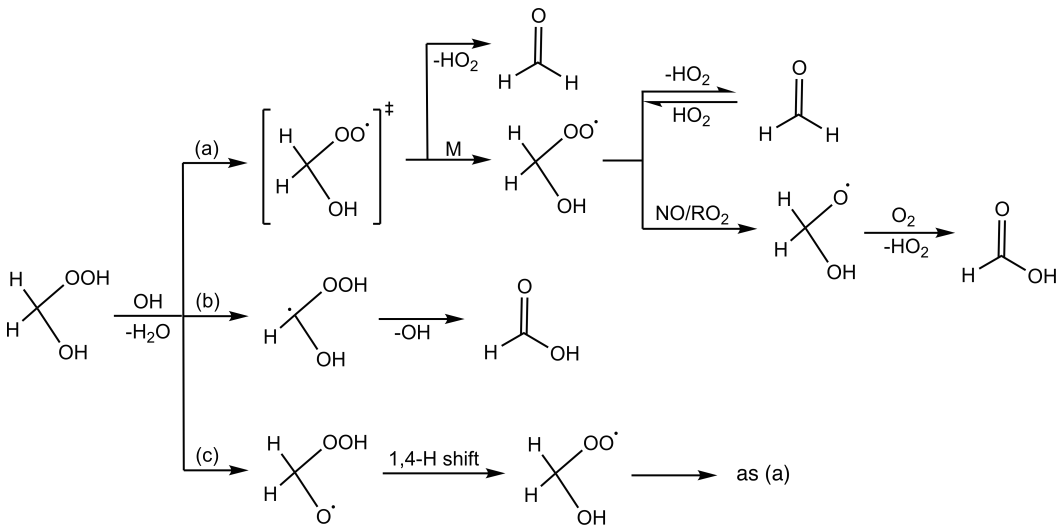

Figure 4.5: Mechanism of HMHP gas-phase oxidation by OH. HMHP oxidation may proceed via one of three pathways: (a) abstraction of the hydroperoxidic hydrogen, (b) abstraction of the methyl hydrogen, and (c) abstraction of the alcoholic hydrogen. In theory, pathway (a) may further bifuricate depending on the NO concentration.

stabilization, the radical has two possible subsequent reaction paths: unimolecular thermal decomposition to HO_2 and HCHO or bimolecular reaction with NO forming the hydroxy alkoxy radical ($HOCH_2O$), which then decomposes to H and formic acid (Su et al., 1979; Veyret et al., 1984; Henon et al., 2003; Francisco and Eisfeld, 2009). Pathway (b) leads directly to formation of formic acid. Francisco and Eisfeld (2009) performed a theoretical calculation of HMHP + OH and concluded that pathway (b) dominates the reactivity as they find that this pathway has the lowest reaction barrier. However, no previous experimental evidence has been reported to test these conclusions and the calculated barrier for ROOH abstraction is much higher than expected based on the reaction kinetics of other organic peroxides. Abstraction of the alcoholic H of HMHP (pathway (c) in Figure 4.5) leads to the formation of the $HOCH_2OO$ radical due to a favorable 1,4-H shift; however, this pathway is expected to be minor in comparison to pathways (a) and (b) due to the difference in known ROH vs. ROOH abstraction rates (Atkinson, 2007).

The formic acid yield was evaluated as a function of NO mixing ratio, which was varied between a few and more than 500 ppbv [$\sim(0.003–1.5) \times 10^{13}$ molecules cm^{-1}]. Results from these experiments indicate that there is no obvious dependence of the formic acid yield on the amount of NO present (Figure 4.6). The initial concentration of NO used in these experiments is listed in Table 4.1; note that NO concentrations in the chamber generally decrease from this value as the oxidation

proceeds. The imprecision in the measured yield is a result of the experimental challenges described above. These include the need to accurately describe the wall loss of the hydroperoxides and formic acid, as well as errors in accounting for formic acid production from the oxidation of bis-HMP.

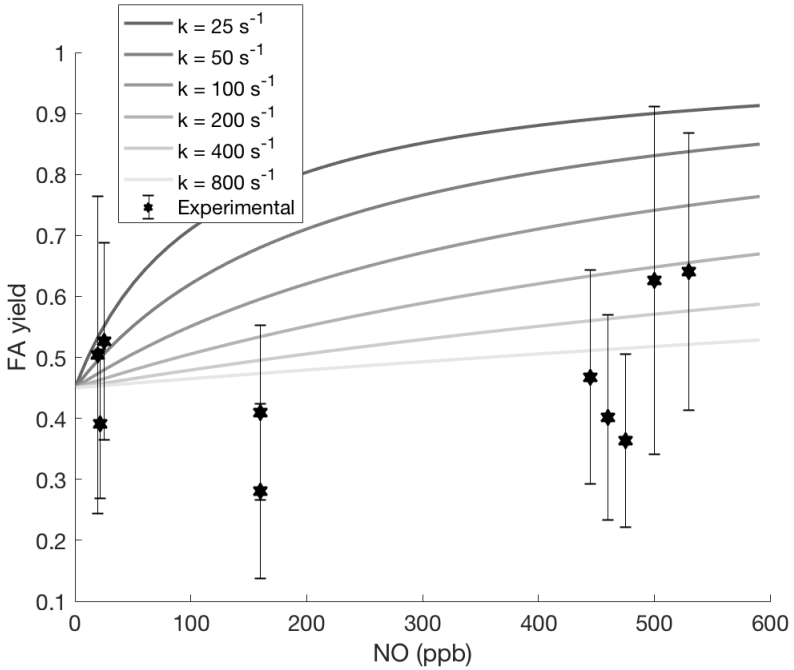

Figure 4.6: Correlation of experimental formic acid (FA) yields with derived uncertainty against initial NO mixing ratio. The formic acid yields do not appear to exhibit a dependence on NO, indicating that the unimolecular HO_2-loss rate is faster than expected from literature reports of thermalized $HOCH_2OO$. These yields are compared with those predicted by a box model using a range of unimolecular $HOCH_2OO$ decomposition rates.

The lack of dependence of the formic acid yield on [NO] shows some discrepancy with the predicted yield from reported unimolecular $HOCH_2OO$ decomposition rates. The decomposition rate of $HOCH_2OO$ has been measured to be quite slow, between 1.5 – 140 s^{-1} at T = 298 K (see Table 4.3). Even at the fastest experimentally-determined decomposition rate, reaction of the peroxy radical with NO would be expected to be competitive (pseudo first-order rate of 120 s^{-1} at highest NO concentrations) with the unimolecular decomposition. As a result, the formic acid yield would be expected to depend on NO, such that higher NO concentrations would predict greater formic acid yield. Shown in Figure 4.6 are kinetic box model calculations of the predicted formic acid yield when using unimolecular HO_2-loss rates of 25 s^{-1}, 50 s^{-1}, 100 s^{-1}, 200 s^{-1}, 400 s^{-1}, and 800 s^{-1} (see Supplemental

Information). The lack of clear dependence on [NO] suggests that the unimolecular decomposition in these experiments occurs at a rate of greater than a few hundred per second at T = 295 K.

Table 4.3: Reported rates of $HOCH_2OO$ decomposition

Study	Method	Rate (s^{-1})	Notes
Su et al. (1979)	FTIR	1.5	Kinetic simulations with experimental data
Veyret et al. (1982)	FTIR	30	Kinetic simulations with experimental data
Barnes et al. (1985)	FTIR	20	Measured loss of HO_2 by proxy (HO_2NO_2)
Veyret et al. (1989)	UV	125	Kinetic fits to loss of HO_2
Burrows et al. (1989)	UV/FTIR	140	Kinetic simulations of measured K_{eq}
Hermans et al. (2005)	MC-TST*	200	
Morajkar et al. (2013)	cw-CRDS	55	Measured loss of HO_2
This study	MC-TST*	440	See Supplemental Information

*Multifconformer transition state theory

The difference between the rate for unimolecular loss of HO_2 inferred in this study with those previously reported (Table 4.3) likely reflects some combination of experimental error and differences in the initial energy distribution of the $HOCH_2OO$ radicals. Most of the measured rates shown in Table 4.3 were determined by observing the loss of HCHO, HO_2, or the formation of the $HOCH_2OO$ radical in the presence of excess formaldehyde both with and without NO_x present. Morajkar et al. (2013), for example, invert the time dependence of HO_2 to diagnose two rate coefficients: the initial rapid loss of HO_2 is used to assess the rate of formation of $HOCH_2OO$ (the inverse of the unimolecular decomposition) and the second subsequent and much slower loss is used to infer the equilibrium coefficient; the proper assignment of the HO_2 dynamics is thus complicated. Theoretical calculations of $HOCH_2OO$ decomposition performed in this study suggest a significantly faster decomposition rate of 440 s^{-1} at 298 K (see Supplemental Information).

The rate of decomposition of $HOCH_2OO$ is also likely sensitive to how this species is formed. In the studies shown in Table 4.3, $HOCH_2OO$ is produced cold via the association reaction of HCHO + HO_2. In contrast, when $HOCH_2OO$ forms as a result of HMHP oxidation, some of the reaction exothermicity will be deposited in the peroxy radical, speeding the rate of decomposition. RRKM simulations of the experimental system (see Supplemental Information) suggest that, provided that less than 8 kcal mol^{-1} of the exothermicity deposits into H_2O, all of the $HOCH_2OO$ will decompose to formaldehyde and HO_2 before collisional stabilization. Hence,

we interpret the lack of NO-dependence of the formic acid yields as implying that the $HOCH_2OO$ formed from HMHP oxidation by OH decomposes at a rate sufficiently high such that formaldehyde is the only product following abstraction of the hydroperoxide hydrogen, both for conditions of this experiment and those relevant in the atmosphere.

From these results, we suggest that, exclusively, pathway (a) leads to formaldehyde formation while pathway (b) leads to formic acid formation, with branching ratios of 0.55 and 0.45, respectively. By comparison, Vaghjiani and Ravishankara (1989) studied the OH oxidation of HMHP's homologue, methyl hydroperoxide (MHP, CH_3OOH). At room temperature MHP reacts with OH at a rate about 0.75 times slower than that of HMHP with OH [$k_{\mathrm{MHP+OH}} = (5.4 \pm 0.4) \times 10^{-12}$ cm^3 molecule^{-1}s^{-1}] and with hydroperoxide and alkyl abstraction branching ratios of 0.70 and 0.30, respectively (Vaghjiani and Ravishankara, 1989). These branching ratios give very similar ROOH abstraction rates between HMHP and MHP, and suggest that the faster HMHP + OH kinetics results from an enhanced methyl abstraction reaction rate.

4.5 Atmospheric Implications

Atmospheric Fate of HMHP

Consideration of the three major atmospheric loss processes for HMHP (deposition, OH reaction, and photolysis) allows for the estimation of its total lifetime and the relative contribution of each loss mechanism. For example, HMHP fluxes and OH concentrations were measured in the southeastern United States during the Southern Oxidant and Aerosol Study (SOAS) in summer 2013. During the campaign, the diurnal-average OH concentration was typically around $1{\times}10^6$ molecules cm^{-3}, but on some days peaked at levels more than twice as large (Feiner et al., 2016). Our measured HMHP + OH rate coefficient produces a lifetime with respect to oxidation by OH, τ_{OH}, of between 15 and 40 hours. By comparison, the diurnal-average of the cloud-free atmospheric photodissociation rate at ground level is calculated by the Tropospheric Ultraviolet-Visible (TUV) radiation model (NCAR/ACD) to be 1.8×10^{-6} s^{-1}. This value gives an HMHP lifetime of about one week against photolysis in the boundary layer. Using the dry deposition velocity of HMHP measured by Nguyen et al. (2015) during SOAS (4 cm s^{-1}) and an assumed mixed layer depth of 1.5 km, the lifetime of HMHP with respect to dry deposition is 10 hours. For these conditions, oxidation by OH accounts for between approximately 20–40% of HMHP loss.

Global Modeling

To investigate the global importance of HMHP chemistry, we simulate the production and fate of HMHP using the chemical transport model GEOS-Chem. GEOS-Chem is a three-dimensional model of tropospheric chemistry driven by assimilated meteorological observations from the NASA Goddard Earth Observing System (GEOS) (Bey et al., 2001). The model includes isoprene oxidation chemistry (Mao et al., 2013), which has been extensively updated to reflect recent mechanistic studies (Praske et al., 2015; Bates et al., 2014; St. Clair et al., 2016a; Nguyen et al., 2016; Bates et al., 2016; Teng et al., 2017). We have updated the GEOS-Chem mechanism to include HMHP yields from alkene ozonolysis taken from Neeb et al. (1997), Hasson et al. (2001a), and Nguyen et al. (2016), as well as HMHP loss due to deposition from Nguyen et al. (2015), photolysis based on Roehl et al. (2007), and OH oxidation from the results presented in this study. We have assumed that the HMHP + OH rate coefficient exhibits the same temperature dependence as the reaction of MHP with OH. The simulations reported here were conducted for the year 2014 on a global $4^\circ \times 5^\circ$ latitude by longitude grid, following a 1-year model spin up, and use model version 10-01 with GEOS-FP meteorology.

HMHP forms in substantial quantities in regions with large biogenic VOC emissions. Globally, HMHP has a total annual production of 12.4 Tg yr^{-1}, with 8.6 Tg yr^{-1} of that from the approximately 7.5% of isoprene that reacts with ozone. The annually averaged boundary layer (z = 0–0.5 km) HMHP mixing ratios are typically around 0.1 ppbv, but reach up to 0.5 ppbv in the heavily forested regions of South America and Africa where isoprene emissions are largest (Figure 4.7A). In the southeastern United States, the GEOS-Chem predicted average HMHP mixing ratios for the summer of 2013 in the boundary layer are around 0.3 ppbv (see the Supplemental Information). By comparison, the average HMHP mixing ratio observed in the boundary layer in the southeastern United States during the SEAC4RS flight campaign in summer 2013 was 0.25 ppbv and reached as high as 4.0 ppbv (Figure 4.2).

As products of HMHP oxidation, global concentrations and distributions of formic acid and HCHO are altered when HMHP is included in the model. The model predicts that 40% of HMHP is lost to OH, thereby producing 1.7 Tg yr^{-1} of formic acid, with the remaining loss due to deposition (52%) and photolysis (7%). The magnitude of the OH oxidation pathway is substantial in the lower atmosphere; in certain locations up to 25% of local formic acid mixing ratios is simulated to arise from the oxidation of HMHP (Figure 4.7B). However, the global production of

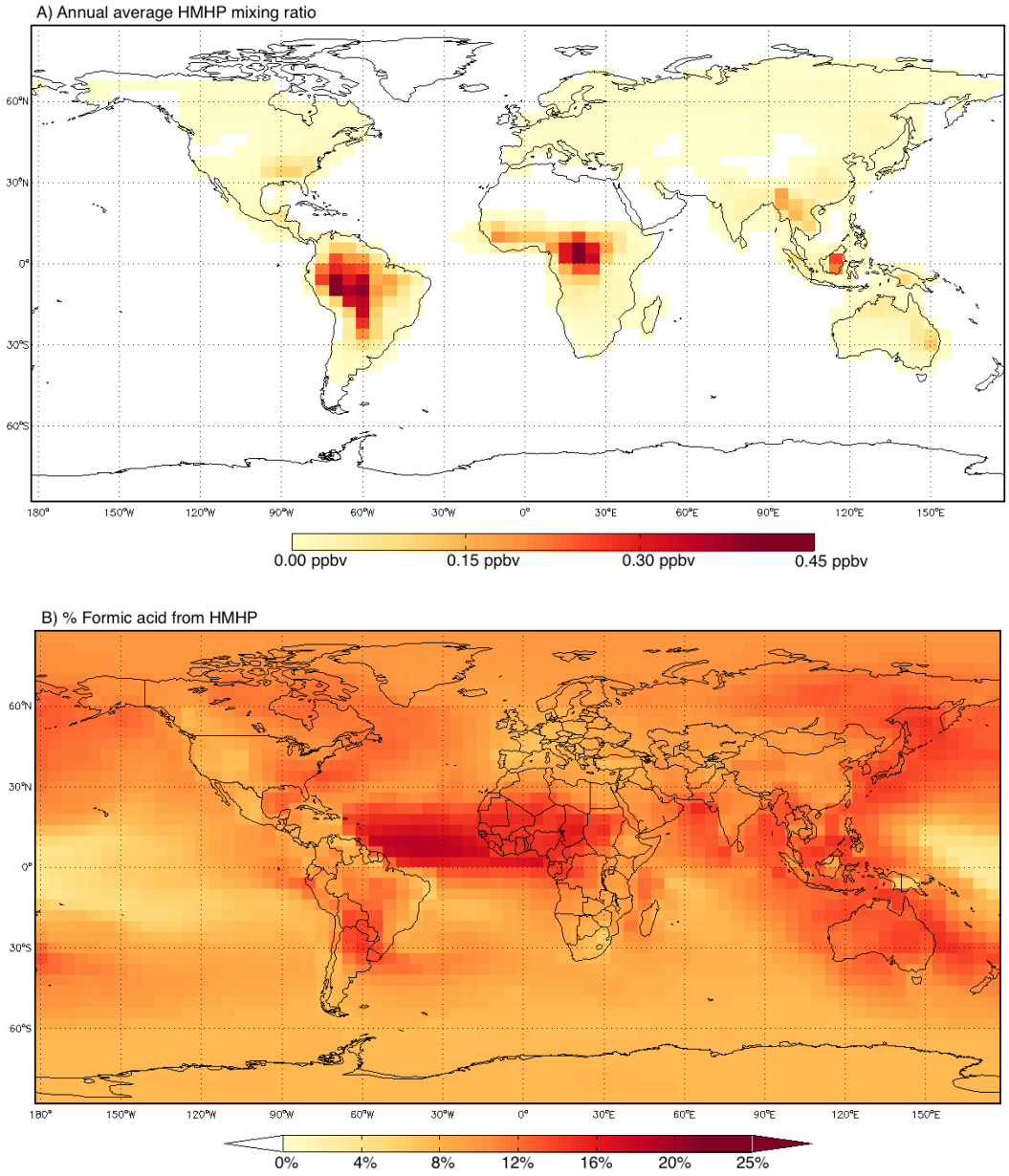

Figure 4.7: Annual average global distribution of HMHP and formic acid for 2014 from the updated HMHP and isoprene mechanism. A) HMHP mixing ratios between 0–0.5 km above the surface, and B) percent of modeled formic acid resulting from HMHP oxidation between 0–1 km.

formic acid from HMHP + OH is small compared with previous GEOS-Chem budget estimates of 51 Tg yr^{-1} of formic acid from photochemical oxidation and compared with estimates of 100-120 Tg y^{-1} from observations (Stavrakou et al., 2012; Millet et al., 2015). Instead, HMHP acts as an intermediate species, producing formic acid further from emissions sources and resulting in higher formic acid mixing

ratios in remote areas such as over the Atlantic Ocean. In contrast, the mixing ratios of HCHO are not significantly altered by inclusion of HMHP, as the model predicts only 0.1% of the total global annual HCHO production is due to HMHP oxidation, peaking at 1% of total local production in regions with high HMHP (see the Supplemental Information). Note that the mixing ratios of HMHP presented in Figure 4.7A are likely an underestimate as the ozonolysis of two important HMHP precursors, ethene and β-pinene, is not explicitly treated in the model. In addition, the contribution of HMHP oxidation to global formic acid concentrations is likely also a lower estimate. In these simulations, we assume that dry deposition represents a permanent loss of carbon from the atmosphere. If instead this process results in a flux of formic acid as suggested by Nguyen et al. (2015), this would further increase the atmospheric concentrations of this carboxylic acid from HMHP.

4.6 Conclusions

The reaction rate constant from the HMHP + OH reaction shows that OH oxidation is a major loss process for HMHP in the atmosphere. Both OH reaction and, likely, dry deposition of HMHP lead to the formation of formic acid, a notable point given that models currently underestimate the concentration of atmospheric formic acid compared with measurements. Studies such as Paulot et al. (2011) and Millet et al. (2015) indicate that measured summertime boundary layer concentrations of formic acid can be more than double the model predicted values. These authors suggest that the discrepancy necessitates a 2–3 times larger source of formic acid than models currently contain, most likely in the form of formic acid production from secondary chemistry of biogenic and other chemical precursors. The results of this study further constrain the formic acid budget from a hydroperoxide that forms in the oxidation of a variety of biogenic and anthropogenic precursors, and show that formic acid production from HMHP oxidation is not enough to account for the large discrepancy between models and observations. Additionally, given the importance of deposition to HMHP loss and potential for formic acid formation, this work highlights the need for improved understanding of surface chemistry.

Acknowledgements

This material is based upon work supported by the National Science Foundation Graduate Research Fellowship under Grant No. DGE-1144469; in addition, we acknowledge support from the NSF (Grant Nos. 1240604, 1628530, and 1628491) and NASA (Grants NNX12AC06G and NNX14AP46G). We acknowledge the Cen-

ter for Exploitation of Solar Energy, University of Copenhagen, and Danish Center for Scientific Computing for funding. We thank Daniel Jacob and the Atmospheric Chemistry Modeling Group at Harvard University for their work on the GEOS-Chem model. In addition, SEAC4RS data from the Lidar Applications Group at the NASA Langley Research Center and from the Meteorological Measurement System (MMS) instrument operated by Paul Bui's group from the NASA Ames Research Center aided in the analysis presented here.

4.7 Supplemental Information

ToF-CIMS Sensitivity

A series of experiments were performed to assess the sensitivity and water dependence of the ToF-CIMS to the compounds of interest in this study. To calibrate for formic acid, a gravimetric standard of commercially available formic acid (Sigma-Aldrich, 98%) was dissolved in water (1% w/w solution) and volatilized into the chamber by flowing a known amount of dry air over the sample. An experimentally determined dry calibration factor of 1.9×10^{-4} ± 20% normalized counts of m/z 65 per pptv formic acid (normalized to the sum of the signals of $^{13}CF_3O^-$ and $H_2O\cdot{}^{13}CF_3O^-$ at m/z 86 and 104, respectively) was then applied to the formic acid data. The HMHP and formic acid signals both exhibit a significant dependence on water vapor, resulting in up to 10% variation in the calibration factor over the water range present during the experiments. The relative water dependence of the instrument sensitivity toward formic acid and HMHP was characterized by filling the chamber with a static quantity of analyte and connecting a source of water vapor, which mixed with the analyte in the instrument's flow tube before reaching the instrument detector. The water vapor flow was controlled and systematically varied to give a calibration over an RH of 1–15%.

An upper limit to the HMHP sensitivity of the ToF-CIMS was calculated using the results of the yield experiment. Assuming that formic acid and HCHO are the only products of HMHP + OH (i.e. ΔHMHP = ΔFA + ΔHCHO), a sensitivity factor of 1.25×10^{-4} ± 23% normalized counts of m/z 149 per pptv of HMHP is estimated (Figure 4.8). This derived sensitivity was corroborated by measuring the HMHP yield from the reaction of ozone with ethene, which as been previously reported by Hasson et al. (2001b). In our experiment, the initial ethene concentration was determined by FTIR, with cross sections obtained from the PNNL database (Sharpe et al., 2004), and the decay of O_3 was monitored (Teledyne 400E) along with the formation of HMHP (ToF-CIMS). A kinetics model was used to derive the expected

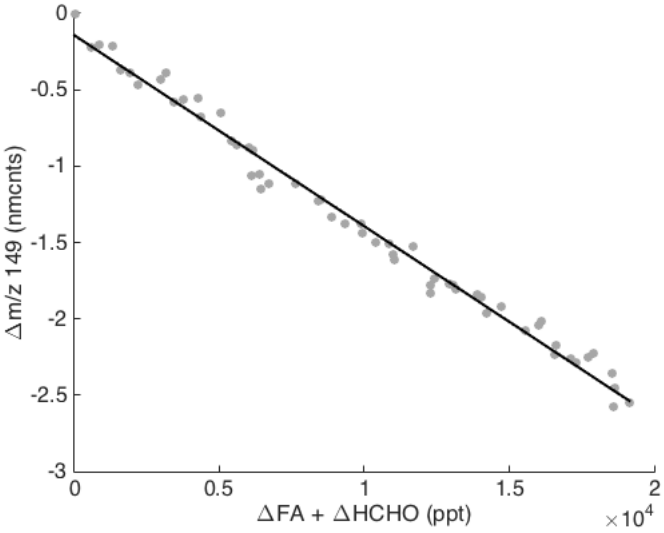

Figure 4.8: Calibration of ToF-CIMS signal for HMHP at m/z149. The calibration assumes that FA and HCHO are the only products from HMHP + OH to give ΔHMHP = ΔFA + ΔHCHO.

change in ethene over the course of the ozonolysis, while accounting for loss of ethene to OH chemistry. An OH yield of 0.22 from the ozone–alkene reaction was assumed based on Fenske et al. (2000). The results are compared with those reported by Hasson et al. (2001b) in Table 4.8.

Table 4.4: Comparison of calculated HMHP yields from ethene ozonolysis with those reported by Hasson et al. (2001b). The change in HMHP was determined using the calculated ToF-CIMS sensitivity of 1.25×10^{-4} normalized counts of m/z 149 per pptv HMHP.

$[ethene]_0$	$[O_3]_0$	RH	HMHP Yield[1]	Reported Yield[2]
660 ppbv	365 ppbv	5.6%	0.29±0.07	0.32±0.09
540 ppbv	360 ppbv	7.0%	0.27±0.06	0.34±0.09
260 ppbv	365 ppbv	4.7%	0.31±0.07	0.29±0.08

1. Yield derived from this study.
2. Reported yields from Hasson et al. (2001b).

Chemical theory was used to estimate the sensitivity of the ToF-CIMS measurement to bis-HMP. An upper limit to the ToF-CIMS sensitivity to a particular analyte can be calculated using the specific ion-molecule collision rate, which may be derived using the parameterization of Su and Chesnavich (1982). This parameterization relies upon the dipole moment and polarizability of the analyte, the mass of the ion and analyte, and the temperature to calculate the collision rate. We employ

Table 4.5: Average dipole (D) and polarizability (Å^3) at 298 K for HMHP and bis-HMP, calculated using the B3LYP/6-31+G(d) level of DFT.

Species	Dipole moment	Polarizability	Relative collision rate[1]
HMHP	1.85	4.33	1.59
bis-HMP	1.04	6.77	1
Formic acid	1.4	6.2	–

1. Calculated using the parameterization of Su and Chesnavich (1982).

DFT methods to calculate conformer averaged dipole moments and polarizabilities (Garden et al., 2009) for HMHP, bis-HMP, and formic acid, as listed in Table 4.5. These in turn are used to estimate the ratio of the CF_3O^-/molecule collision rates for HMHP to bis-HMP, which is found to be 1.59 (Table 4.5).

The CIMS reagent ion, CF_3O^-, ionizes analytes by either forming an ion cluster (m/z = analyte mass + 85) or a fluoride transfer ion (m/z = analyte mass + 19), depending upon the acidity and fluoride affinity of the target analyte. The signal for bis-HMP on the ToF-CIMS appears at both the clustering mass (m/z 179) and the transfer mass (m/z 113), with the transfer comprising 30% of the signal under dry conditions. Similarly, HMHP appears at both the clustering mass (m/z 149) and the transfer mass (m/z 83) with 25% at the transfer mass. The fraction of the signal at the transfer mass shows a small dependence on water, decreasing with increasing water levels. The calibration of bis-HMP using the relative collision rate above accounts for the appearance of both bis-HMP and HMHP at the two masses. However, the calibration of HMHP was performed only at mass m/z 149 and therefore the HMHP mixing ratios presented in this work include only the clustering mass.

Instrument Interferences

During the experiments, an HMHP (and/or bis-HMP) interference in the HCHO measurement from ISAF was found to occur, likely from conversion on instrument surfaces. A correction factor of 0.10×[HMHP] was subtracted from all HCHO signals to account for this interference. This factor was derived by adding HMHP to the chamber (with no photooxidation occurring) and overflowing the ISAF inlet with zero air directly at the instrument. The HCHO signal was found to have both a prompt decay (~5 ppbv or 2% relative to HMHP) and much longer timescale decay (~15 ppbv or 10% relative to HMHP) as shown between 21.4 and 21.5 UTC in Figure 4.9. The HCHO signal on ISAF has a typical decay time constant of 0.19

s (Cazorla et al., 2015), and therefore the observed prompt decay was inferred to be HCHO (an impurity in the HMHP synthetic mixture). The remaining HCHO seen in the long decay was therefore believed to result from HMHP (and/or bis-HMP) conversion to HCHO on instrument surfaces. Note that a more thorough investigation of the conversion of HMHP to HCHO on ISAF instrument surfaces, as was done for ISOPOOH conversion to HCHO (St. Clair et al., 2016b), would provide more confidence in the magnitude of the conversion rate.

Product Yields Timeseries

The decline of HMHP and production of formic acid and HCHO over the course of the experiment is shown in Figure 4.10.

OH+Product Correction

The loss of formic acid and HCHO due to their reaction with OH was accounted for in these experiments by using Eq. VI of Atkinson et al. (1982). This equation is given by

$$F = \left(\frac{k_{\mathrm{RH+OH}} - k_{\mathrm{X+OH}}}{k_{\mathrm{RH+OH}}}\right)\left\{\frac{1 - ([\mathrm{RH}]_t/[\mathrm{RH}]_0)}{([\mathrm{RH}]_t/[\mathrm{RH}]_0)^{k_{\mathrm{X+OH}}/k_{\mathrm{RH+OH}}} - ([\mathrm{RH}]_t/[\mathrm{RH}]_0)}\right\} \quad (4.3)$$

where F is the correction factor for loss due to product oxidation, RH is the initial reactant (in this case HMHP), and X is the product undergoing oxidation by OH (in this case either HCHO or formic acid). The rate constant $k_{\mathrm{RH+OH}}$ is the HMHP + OH rate constant derived in this study (7.1×10^{-12} cm^3 molecule^{-1}s^{-1}) and $k_{\mathrm{X+OH}}$ were taken from Atkinson et al. (2006).

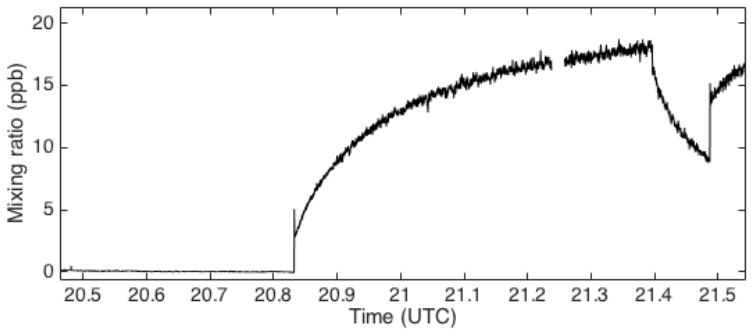

Figure 4.9: Timeseries of HCHO mixing ratios indicating potential HMHP interference in ISAF HCHO measurements. Soon after filling the chamber with HMHP (with no photooxidation), the chamber was sampled on ISAF at 20.85 UTC. A zeroing of ISAF occurred between 21.40 and 21.49 UTC, indicating a prompt and delayed time response of the HCHO signal.

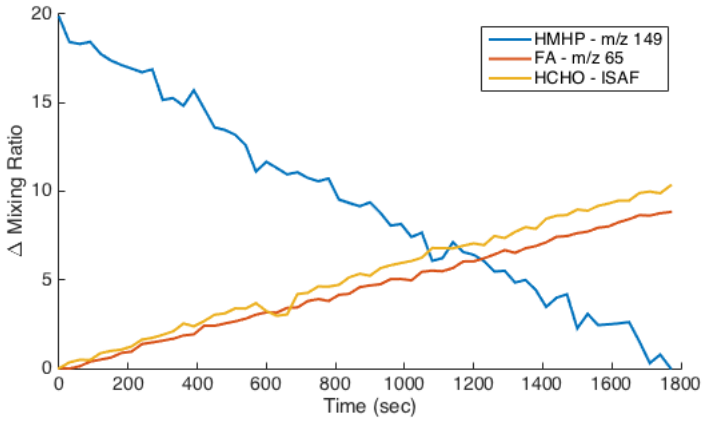

Figure 4.10: Timeseries of HMHP oxidation during yields experiment. Shown are the corrected 30 second averaged data.

Formic acid yields

The formic acid yields presented in Table 4.6 rely upon the derived upper limit of the HMHP and bis-HMP ToF-CIMS sensitivities as outlined above.

Table 4.6: Yield of formic acid from HMHP oxidation under varying NO_x conditions. The influence of bis-HMP on the formic acid yield is indicated by the fraction of formic acid production estimated to derive from bis-HMP oxidation. The formic acid yield from HMHP has been corrected for the bis-HMP interference. Initial mixing ratios are given in ppbv.

Exp. No.	$[HMHP]_0$	$[bis\text{-}HMP]_0$	Fraction from bis-HMP	Yield from HMHP
1	150	30	0.24	0.36 ± 0.14
2	90	20	0.29	0.40 ± 0.17
3	35	10	0.41	0.28 ± 0.14
4	165	30	0.22	0.47 ± 0.17
5	55	20	0.42	0.50 ± 0.26
6	70	20	0.34	0.62 ± 0.29
7	20	1	0.07	0.39 ± 0.12
8	10	0.1	0.01	0.53 ± 0.16
9	20	2.5	0.18	0.64 ± 0.22

The reported uncertainty in the formic acid yields for each experiment arises predominantly from uncertainty in the calibration of the ToF-CIMS data and in the correction due to oxidation of bis-HMP. The gravimetric technique was used to calibrate the ToF-CIMS for formic acid had an uncertainty of 20%. Because no commercial standard is available for HMHP, the upper limit to the ToF-CIMS sensi-

tivity to HMHP was calculated and a calibration factor with a 23% uncertainty was applied to the data.

As outlined above and indicated in Table 4.6, the bis-HMP correction was a substantial component of the uncertainty in the final formic acid yield. The estimation of formic acid from bis-HMP assumes that bis-HMP produces 2 equivalents of formic acid with each oxidation via

$$HOCH_2OOCH_2OH + OH \longrightarrow HCOOH + HOCH_2O \quad (4.4a)$$

$$HOCH_2O \longrightarrow HCOOH + H \quad (4.4b)$$

In this mechanism, the hydroxy alkoxy radical ($HOCH_2O$) decomposes to H and formic acid as given in Su et al. (1979); Veyret et al. (1984); Henon et al. (2003), and Francisco and Eisfeld (2009). The estimation of formic acid from bis-HMP also relies upon the rate coefficient of bis-HMP + OH relative to that of HMHP + OH. A relative rate coefficient of 35% was found using a method similar to that used to determine the HMHP + OH relative rate coefficient with 1,2-butanediol + OH as described in the main text. Briefly, the natural logarithm of the bis-HMP mixing ratio (normalized to the initial concentration and wall-loss corrected) was plotted as a function of the natural logarithm of the normalized (and wall-loss corrected) HMHP mixing ratios over the course of oxidation. The slope of a linear regression analysis gives the relative rate coefficient. An uncertainty of up to the total amount of the formic acid correction was assumed to be the error in the formic acid correction due to bis-HMP oxidation.

Kinetic Box Modeling

The kinetic model uses an ordinary differential equation solver with given photochemical reaction rates and mechanisms to determine reactant and product concentrations over time. The model is initiated with mixing ratios of HMHP, bis-HMP, CH_3ONO (photolytic OH source), NO, and formic acid, and contains the reactions shown in Figure 4 (main manuscript) along with the NO_x and HO_x cycling reactions. The reaction rates are drawn from either this study or Burkholder et al. (2015). With the kinetic box model constrained to the formic acid and formaldehyde data from Exp. 4, the fits of the model predict a branching ratio of 0.55 for pathway (a) and 0.45 for pathway (b) (Figure 4, main manuscript), in agreement with the experimentally-derived relative yield of HCHO to formic acid from HMHP + OH oxidation. The model was run using Matlab R2017b.

Theoretical Chemical Modeling

To further understand the pathways and dynamics of the system, we calculate the reaction rate constants for the unimolecular reactions and estimate the rate constants for the bimolecular reactions based on literature values. Based on these rate constants, an RRKM simulation is conducted for pathway (a) (see Figure 4.5) to assess the NO dependence of the formaldehyde (HCHO) and formic acid yield.

Rate Constants

For the unimolecular reactions, reaction rate constants from thermalized products (without excess energy, denoted canonical rate constants) are calculated using the approach described by Møller et al. (2016). Briefly, conformers are obtained using the MMFF force field in Spartan'14 (Wavefunction Inc., Irvine, CA), with a neutral charge enforced on the radical atom (Halgren, 1996). The resulting structures are optimized using B3LYP/6-31+G(d) in Gaussian09 (Becke, 1993; Lee et al., 1988; Hehre et al., 1972; Clark et al., 1983; Frisch et al., 1984, 2009). All conformers within 2 kcal/mol in electronic energy of the lowest-energy conformer are further optimized at the ωB97X-D/aug-cc-pVTZ level (Chai and Head-Gordon, 2008; Dunning, 1989; Kendall et al., 1992). For the lowest-energy conformer at this level, an RO-CCSD(T)-F12a/VDZ-F12//ωB97X-D/aug-cc-pVTZ (abbreviated F12) single-point calculation is conducted in Molpro2012 (Werner et al., 2012; Watts et al., 1993; Adler et al., 2007; Knizia et al., 2009; Werner et al., 2011; Peterson et al., 2008). Rate constants are then calculated using multi-conformer transition state theory (MC-TST) using the F12 electronic energy with ZPVE at the ωB97X-D/aug-cc-pVTZ level for the barrier height and ωB97X-D/aug-cc-pVTZ for the relative energy between conformers and partition functions (Eyring, 1935; Evans and Polanyi, 1935; Vereecken and Peeters, 2003; Møller et al., 2016). A tunneling coefficient is calculated using the Eckart approach based on the conformers obtained as the end-points of an IRC from the lowest-energy transition state (Eckart, 1930). For the Eckart calculation, the barrier heights are based on F12 electronic energy with ZPVE at the ωB97X-D/aug-cc-pVTZ level and the imaginary frequency of the transition state is calculated using ωB97X-D/aug-cc-pVTZ.

Figure 4.11 shows the three possible pathways ((a), (b), and (c)) for the oxidation of HMHP with OH including room temperature reaction rate constants. The calculated unimolecular rate constants (k_{calc}) are determined using the MC-TST approach described above. The bimolecular rate constants are determined from the literature and presented as pseudo-first order rate constants for comparability.

Abstraction of one of the hydrogens on carbon in pathway (b) leads to the formation of an unstable hydroxy hydroperoxy alkyl radical, which will spontaneously decompose to form formic acid and OH (Su et al., 1979; Veyret et al., 1984; Henon et al., 2003; Francisco and Eisfeld, 2009).

The abstraction of the -OH hydrogen (pathway (c)) leads to a hydroperoxy alkoxy radical (OCH_2OOH) with three different possible reactions. For the hydrogen abstraction by O_2, the generic value for the bimolecular rate constant of 8×10^{-15} cm^3 $molecule^{-1}$ s^{-1} is used (Devolder, 2003). Assuming 1 atm and 20% O_2, this corresponds to a pseudo-first order rate constant of 4.1×10^5 s^{-1}. The competing reactions have calculated rate constants of 3.7×10^6 s^{-1} (1,4 H-shift) and 4.4×10^{-2} s^{-1} (direct HO_2-loss). The dominant reaction for OCH_2OOH (and thereby pathway (c)) is therefore expected to be the 1,4 H-shift forming $HOCH_2OO$, the initial product in pathway (a), see below. Thus, performic acid is expected to be only a very minor product of the overall HMHP oxidation by OH.

Pathway (a) represents abstraction of the hydroperoxy hydrogen and leads directly to the hydroxy peroxy radical ($HOCH_2OO$). This radical has three possible reactions in the experiments described here: the unimolecular HO_2-loss leading to HCHO, the bimolecular reaction with NO forming the hydroxy alkoxy radical ($HOCH_2O$) and subsequently formic acid and finally, a 1,4 H-shift leading to OCH_2OOH which has a calculated rate constant of only 3×10^{-7} s^{-1} and is therefore disregarded.

Our MC-TST calculated reaction rate constant of 440 s^{-1} for the HO_2-loss reaction is higher than the experimental values ranging from 1.5 to 140 s^{-1} (Table 3 main manuscript). The most recent experimental value is 55 s^{-1} at 297 K (Morajkar et al., 2013). An earlier theoretical MC-TST value of 200 s^{-1} at 300 K (Hermans et al., 2005) also seems to be slightly higher than the experimental values. For the reaction of the peroxy radical with NO, a representative bimolecular rate constant of 9×10^{-12} cm^3 $molecule^{-1}$ s^{-1} at 298 K is used based on experimental rate constants for comparable systems showing only little difference across peroxy radicals (Orlando and Tyndall, 2012).

The competition between unimolecular HO_2-loss and bimolecular reaction with NO for the $HOCH_2OO$ peroxy radical formed in pathway (a) will depend on the concentration of NO and the excess energy of the peroxy radical. The experimental NO starting concentrations range from 20 ppbv to 530 ppbv. This corresponds to pseudo-unimolecular rate constants of 5 s^{-1} to 120 s^{-1} at 1 atm. With a rate constant for the unimolecular HO_2-loss in the range 1.5 - 440 s^{-1}, these canonical

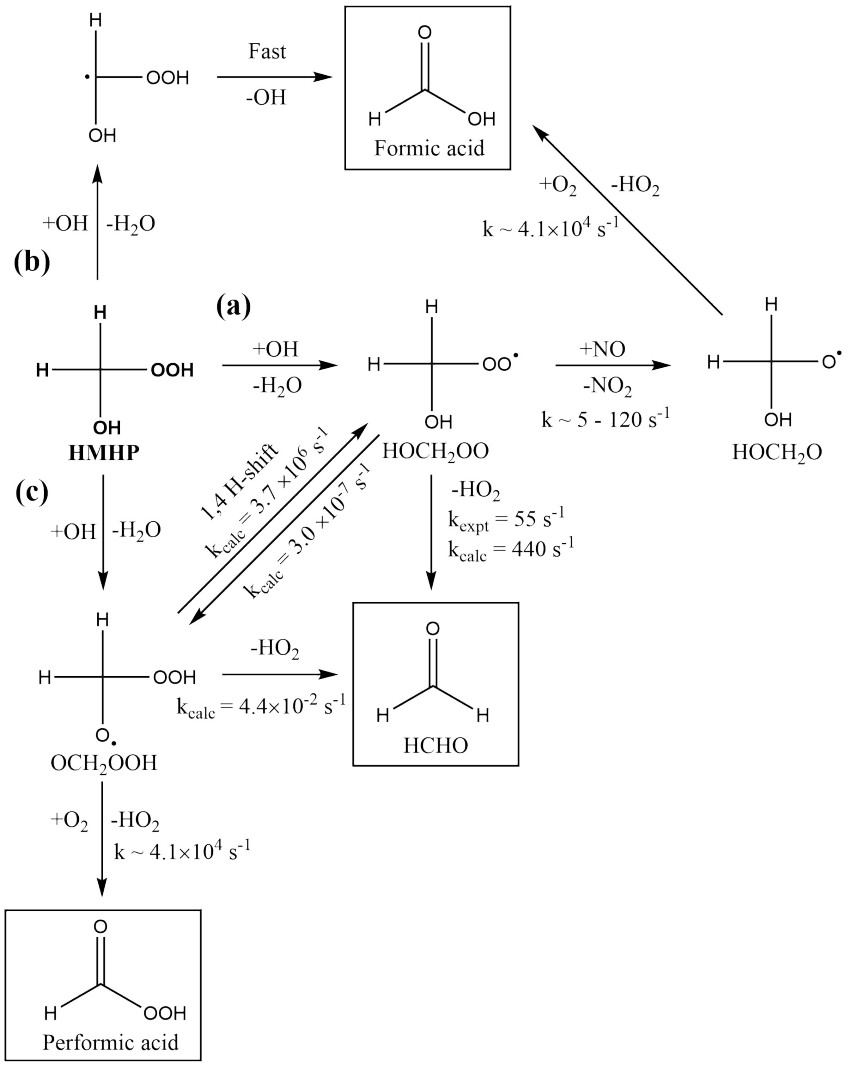

Figure 4.11: Mechanism of HMHP oxidation by OH showing the three different pathways of OH abstraction ((a),(b) and (c), see Figure 4, main manuscript) including canonical rate constants for the different reactions. Possible closed shell products are shown in black squares. For the bimolecular reactions, pseudo-first order rate constants are given for comparability. For reaction with NO, a bimolecular rate constant of 9×10^{-12} cm^3 molecule^{-1} s^{-1} has been used in combination with the experimental range of NO concentrations employed (20-530 ppbv). For the reactions with O_2, a bimolecular rate constant of 8×10^{-15} cm^3 molecule^{-1} s^{-1} has been used and assuming 1 atm of pressure and 20 % O_2, this yields a pseudo-first order rate constant of 4.1×10^4 s^{-1}. See text for further discussion of the rate constants.

rate constants suggest a comparable yield of formic acid and HCHO from pathway (a) and a significant effect of the NO concentration on the total product distribution, with higher NO concentrations yielding more formic acid. However, any excess energy of the peroxy radical will favor the unimolecular HO_2-loss to form HCHO,

as no collisions are required for this to occur.

RRKM Modeling of HMHP Oxidation Pathway (a)

To assess the fate of the peroxy radical formed in the HMHP oxidation pathway (a) and thus the dependence on NO concentration, an RRKM simulation was conducted using the Master Equation Solver for Multi-Energy well Reactions (MESMER) (Glowacki et al., 2012). The system modeled is shown schematically in Figure 4.12. The simulation is based on the lowest-energy conformers at the ωB97X-D/aug-cc-pVTZ level. Geometries and vibrational frequencies are calculated at this level, while the F12 single-point values are used for the electronic energy. Note that the energy of the alkoxy radical ($HOCH_2O$) has been lowered by 20 kcal/mol to prevent back-reaction and thus eliminate the need to include further reactions of this. This does not affect its rate of formation and thus the branching between the two competing reactions. As shown in Figure 4.11, this alkoxy radical would react with O_2 to form formic acid.

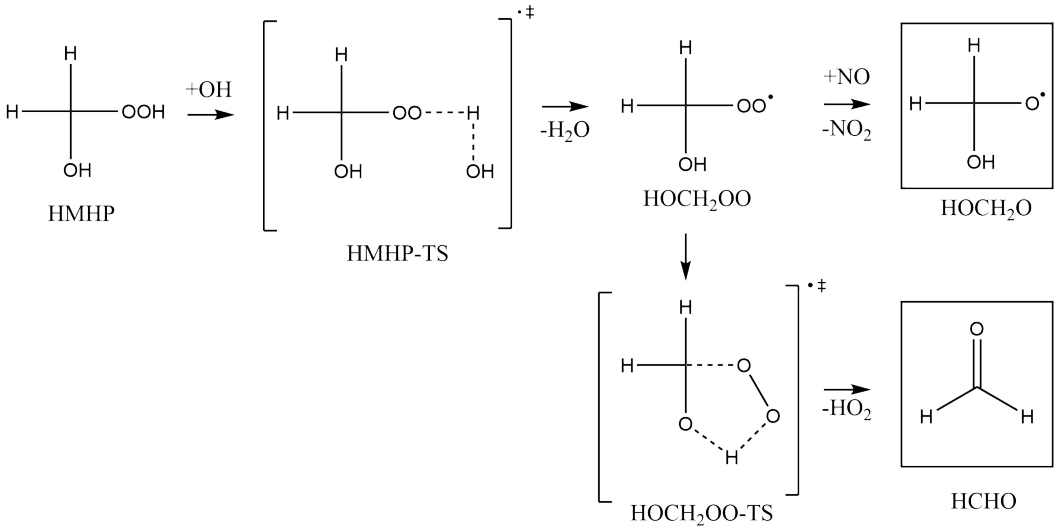

Figure 4.12: Scheme of HMHP oxidation pathway (a) which is modeled in MESMER with abbreviated names. The black squares represent sinks in which the simulation can end. Square brackets with double daggers denote transition states.

The Lennard-Jones parameters for all species (see Table 4.7) are taken from the user manual of MultiWell (Barker et al., 2017b). For the cases for which the exact compound was not available, a compound with the same number of non-hydrogen atoms was used. For the simulations, molecular N_2 was used as the bath gas. A grain size of 100 cm^{-1} was used with a span of energy grains up to $50k_bT$ above the highest stationary point. A test with a grain size of 50 cm^{-1} yields indistinguishable results

Table 4.7: Lennard-Jones parameters employed for all compounds. For each compound, its abbreviation, the model compound from which the Lennard-Jones parameters are obtained along with the σ (Å) and ε/k_B (K) are given. All values are taken from the user manual of MultiWell (Barker et al., 2017b).

Compound	Abbreviation	Model Compound	σ	ε/k_B
N_2 (bath gas)	N_2	N_2	3.74	82
Hydroxymethyl hydroperoxide	HMHP	1-C_4H_8	5.28	302
Hydroxyl radical	OH	H_2O	2.71	506
H-abstraction TS	HMHP-TS	$n-C_5H_{12}$	5.85	327
HMHP peroxy radical	$HOCH_2OO$	1-C_4H_8	5.28	302
HO_2-loss TS	$HOCH_2OO$-TS	1-C_4H_8	5.28	302
Formaldehyde	HCHO	C_2H_2	4.13	224
Alkoxy radical	$HOCH_2O$	C_3H_6	4.78	271
Water	H_2O	H_2O	2.71	506
Nitric oxide	NO	NO	3.49	117

suggesting that 100 cm^{-1} is a suitable choice for this system. The exponential-down collisional transfer model was used with ΔE_{down}= 225 cm^{-1}, as previously done with N_2 as the bath gas (Penner and Forst, 1977; Kurtén et al., 2015). All simulations are conducted at atmospheric conditions of 760 Torr and 298.15 K.

For the initial reaction of HMHP with OH, we use our experimentally determined rate constant of 7.1×10^{-12} cm^3 $molecule^{-1}$ s^{-1}. This represents an upper limit, as abstraction of the hydroperoxy hydrogen is only one of the three options, but this rate does not affect the product distribution. The aforementioned representative value of 9×10^{-12} cm^3 $molecule^{-1}$ s^{-1} for the bimolecular reaction of the peroxy radical with NO is used in the simulation (Orlando and Tyndall, 2012).

Figure 4.13 shows the energetics of the system being modeled, as well as the species distribution as a function of time under conditions corresponding to Experiment 4 ($[OH]_0$ = 100 ppbv and $[NO]_0$ = 445 ppbv). The simulation assumes that $[OH]_0$ = $[OH\ source]_0$. As all of the OH source does not photolyze at once experimentally, this value is higher than the experimental value. However, this affects only the rate by which HMHP is lost and not the product distribution.

The canonical RRKM rate constant for the HO_2-loss reaction obtained from the simulation is 620 s^{-1} at 300 K, in good agreement with the calculated MC-TST value of 440 s^{-1} at 298.15 K. The main source of the discrepancy is that the MESMER RRKM value is based on only a single conformer, while the MC-TST value is

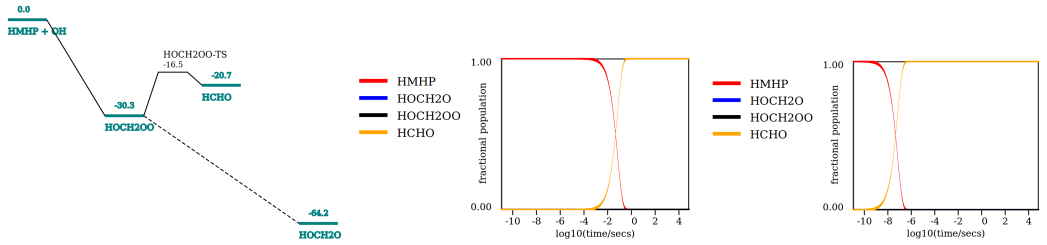

Figure 4.13: Left: Energetics of the system being modelled. All energies are zero-point corrected energies in kcal/mol relative to the separated reactants, HMHP and OH. Middle: Product yield as a function of time. The conditions for the simulation corresponds to Exp. 4 ($[OH]_0$ = 100 ppbv and $[NO]_0$ = 445 ppbv). Right: Product yield as a function of time. NO concentration as in Exp. 4 ($[NO]_0$ = 445 ppbv), but an OH concentration which is 10^6 times higher than in Exp. 4 to form the peroxy radical much earlier in the simulation and thus better illustrate the dynamics.

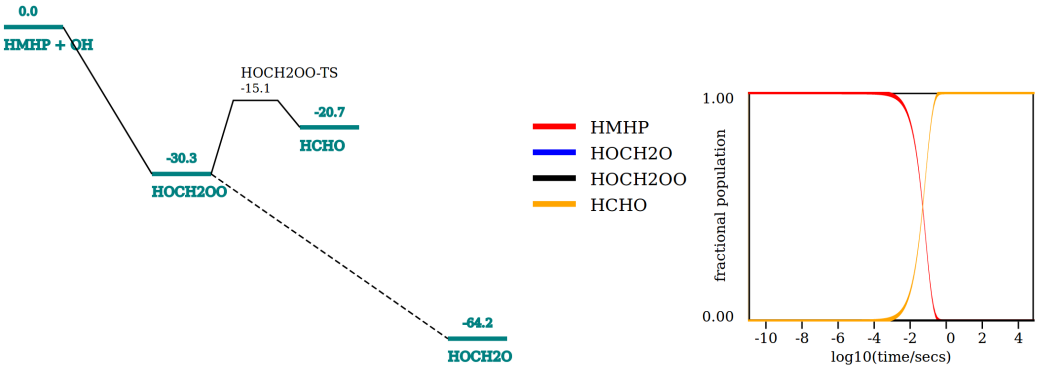

Figure 4.14: Left: Energetics of the system being modeled. All energies are zero-point corrected energies in kcal/mol relative to the separated reactants, HMHP and OH. The barrier for HO_2-loss has been increased to yield a canonical rate constant of 55 s^{-1} to match the experimental value (Morajkar et al., 2013). Right: Product yield as a function of time. The conditions for the simulation corresponds to experiment 4 ($[OH]_0$ = 100 ppbv and $[NO]_0$ = 445 ppbv).

calculated from all low-energy conformers. With a pseudo-unimolecular rate constant of 110 s^{-1} (corresponding to Exp. 4) for the reaction with NO, the canonical rate constants would suggest a significant yield of the alkoxy radical ($HOCH_2O$), and subsequently formic acid, under these conditions, depending on the exact rate constant for HO_2-loss. However, the simulation shows no formation of $HOCH_2O$ and 100 % yield of HCHO. The calculated energetics of the reaction shows that the reaction of HMHP + OH is exothermic by about 30 kcal mol^{-1}. This excess energy will be distributed between the formed products $HOCH_2OO$ and H_2O. Due

to the larger number of vibrational degrees of freedom, $HOCH_2OO$ is expected to possess most of this excess energy. For the MESMER simulations, $HOCH_2OO$ is modeled to possess all the excess energy, but the effect of this is tested in MultiWell (see below). The fact that all $HOCH_2OO$ yields HCHO despite the canonical rate constants for the two competing pathways being similar, suggests a significant effect from the excess energy of $HOCH_2OO$.

To further validate this, an RRKM simulation was conducted (Figure 4.13 right) in which the OH concentration was increased by a factor of 10^6 to form the peroxy radical ($HOCH_2OO$) much earlier in the simulation and thus allow a more detailed observation of the dynamics. The simulation shows complete conversion of HMHP to HCHO at time scales much faster than the canonical rate of 620 s^{-1} for the rate limiting HO_2-loss, which means that none of the peroxy radical ($HOCH_2OO$) is thermalized under these conditions. This shows that the excess energy from the abstraction does indeed drive the reaction to formaldehyde (HCHO).

A further test was conducted (Figure 4.14) in which the barrier for HO_2-loss was increased from 13.8 kcal/mol to 15.2 kcal/mol yielding a canonical rate constant of 55 s^{-1} in agreement with the experimental value (Morajkar et al., 2013). However, the RRKM simulation still shows complete conversion of $HOCH_2OO$ to HCHO.

As the HO_2-loss reaction occurs with essentially no peroxy radical being thermally stabilized, the yield of HCHO from pathway (a) is found to be 100 % and independent of NO concentration well beyond the range employed in the experiments.

Multiwell Modeling

To assess in greater detail the effect of the excess energy possessed by $HOCH_2OO$ and the time scale for the excess energy reaction, a simple simulation was conducted using the MultiWell program suite (Barker et al., 2017a; Barker, 2001, 2009). The simulation uses the same Lennard-Jones and energy transfer parameters as the MESMER simulation. The barrier for HO_2-loss has been set to 15.125 kcal/mol for the canonical rate to match the experimental value of 55 s^{-1} (Morajkar et al., 2013). The simulation includes only the irreversible HO_2-loss reaction converting $HOCH_2OO$ to HCHO. To account for the excess energy possessed by $HOCH_2OO$ from reaction of HMHP with OH, $HOCH_2OO$ is initiated with a specific amount of excess energy (the same results are obtained if it is simulated to have been formed from HMHP + OH).

The calculated (CCSD(T)-F12a/VDZ-F12//ωB97X-D/aug-cc-pVTZ) total excess

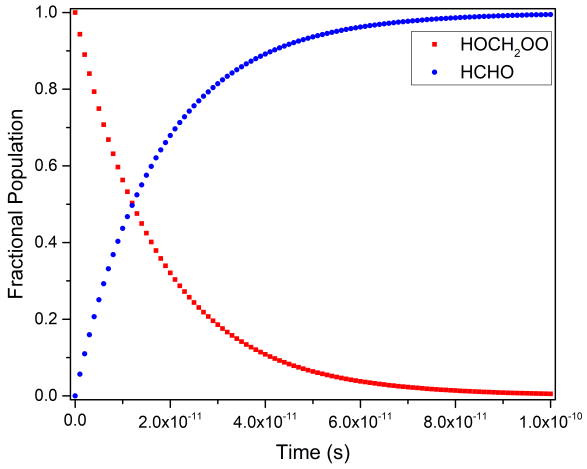

Figure 4.15: Fractional population of $HOCH_2OO$ and HCHO as a function of time for the simulation for which $HOCH_2OO$ possesses the full 30.3 kcal/mol of excess energy.

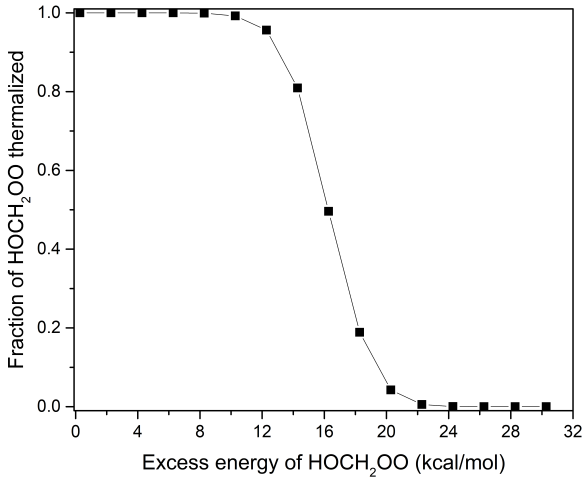

Figure 4.16: Fractional population of $HOCH_2OO$ thermalized before reacting to form HCHO as a function of the amount of excess energy given. The maximum of 30.3 kcal/mol corresponds to the calculated value relative to the free HMHP and OH, i.e. no excess energy is assigned to the H_2O leaving fragment. The fractional populations are read after 10^{-8} s^{-1}, after complete thermalization but before reaction from the thermalized $HOCH_2OO$.

energy is 30.28 kcal/mol (energy difference between the free HMHP and OH and the free $HOCH_2OO$ and H_2O including ZPVE). If all of this excess energy is given to $HOCH_2OO$, the MultiWell simulation (see Figure 4.15) clearly shows that none of the $HOCH_2OO$ is thermalized and all has reacted to form HCHO within 1×10^{-10} s. From the data, a rate constant for the reaction with excess energy of 5×10^{10} s^{-1} is obtained.

In Figure 4.16, we show the fraction of $HOCH_2OO$ that is thermalized as a function of the amount of excess energy possessed by $HOCH_2OO$. As the excess energy decreases below 22 kcal/mol, the amount of $HOCH_2OO$ that is thermalized (and thus does not react directly to form HCHO) starts to increase. Around 16 kcal/mol, half of the $HOCH_2OO$ reacts to form HCHO directly and half is thermalized.

GEOS-Chem Modeling

To investigate the global importance of HMHP chemistry, we updated and ran the chemical transport model GEOS-Chem. GEOS-Chem is a three-dimensional model of tropospheric chemistry driven by assimilated meteorological observations from the NASA Goddard Earth Observing System (GEOS) (Bey et al., 2001). The model includes isoprene oxidation chemistry (Mao et al., 2013), which has been extensively updated to reflect recent mechanistic studies (Praske et al., 2015; Bates et al., 2014; St. Clair et al., 2016a; Nguyen et al., 2016; Bates et al., 2016; Teng et al., 2017). We have updated the GEOS-Chem mechanism to include HMHP yields from alkene ozonolysis taken from Neeb et al. (1997), Hasson et al. (2001b,a), and Nguyen et al. (2016) as well as HMHP loss due to deposition from Nguyen et al. (2015), photolysis based on Roehl et al. (2007), and oxidation from the results presented in this study. We have assumed that the HMHP + OH rate coefficient exhibits the same temperature dependence as the reaction of its homologue, methyl hydroperoxide (MHP, CH_3OOH) with OH (-Ea/R = 200 K) . The simulations reported here were conducted for the year 2014 on a global $4^\circ \times 5^\circ$ latitude by longitude grid, following a 1-year model spin up, and use model version 10-01 with GEOS-FP meteorology.

Results from GEOS-Chem modeling are shown in Figures 4.17, 4.18, and 4.19. The impact of including HMHP in the model on HCHO mixing ratios in the lowest 1 km of the atmosphere is shown in Figure 4.17. The model predicts a total annual production of 1.22 Tg yr^{-1} of HCHO from HMHP oxidation, or 0.1% of total global HCHO production. By comparison, the model predicts a larger effect of HMHP on formic acid mixing ratios, with maximum of 0.12 ppbv increase in certain regions. The average predicted HMHP mixing ratios from August 2013 are shown in Figure 4.19. The GEOS-Chem model shows mixing ratios in the summertime boundary layer are lower than those observed during the SEAC4RS flight campaign during August 2013.

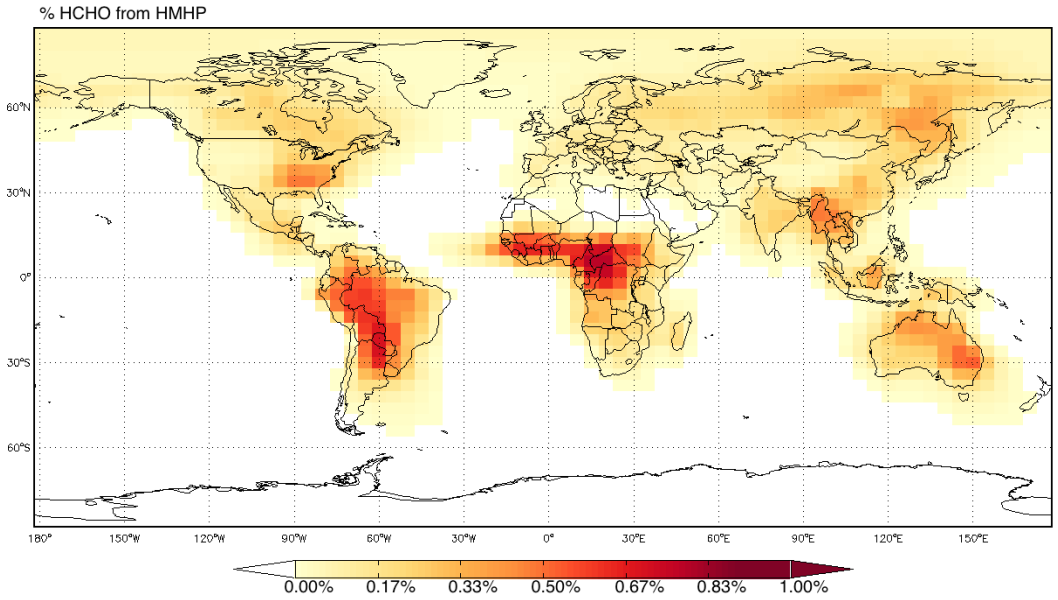

Figure 4.17: Annual average global distribution for 2014 of the percent of HCHO resulting from HMHP oxidation between 0–1 km above the surface.

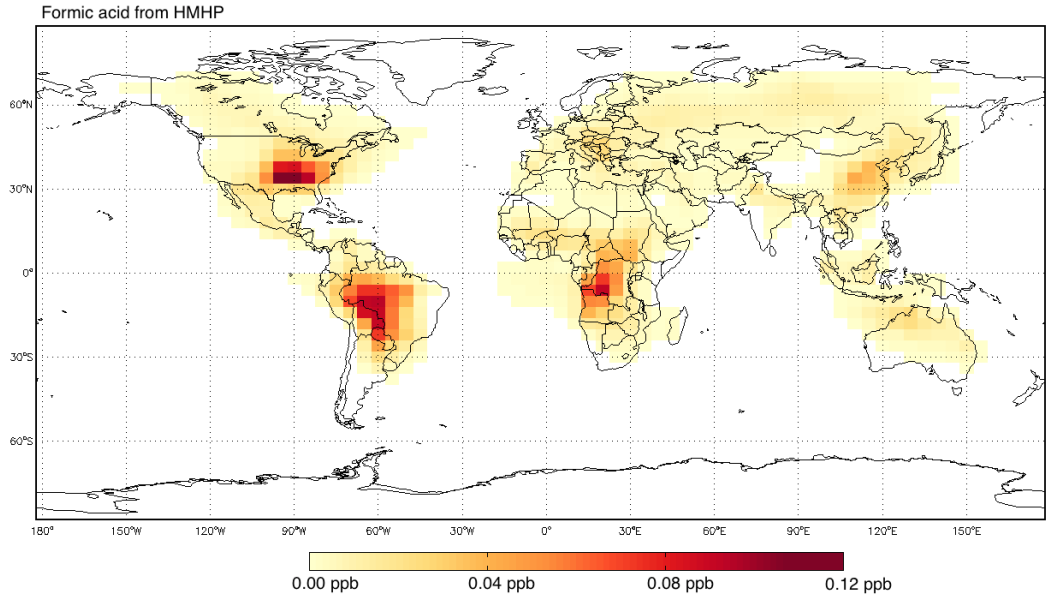

Figure 4.18: Annual average global distribution for 2014 of formic acid mixing ratios resulting from HMHP oxidation between 0–1 km above the surface.

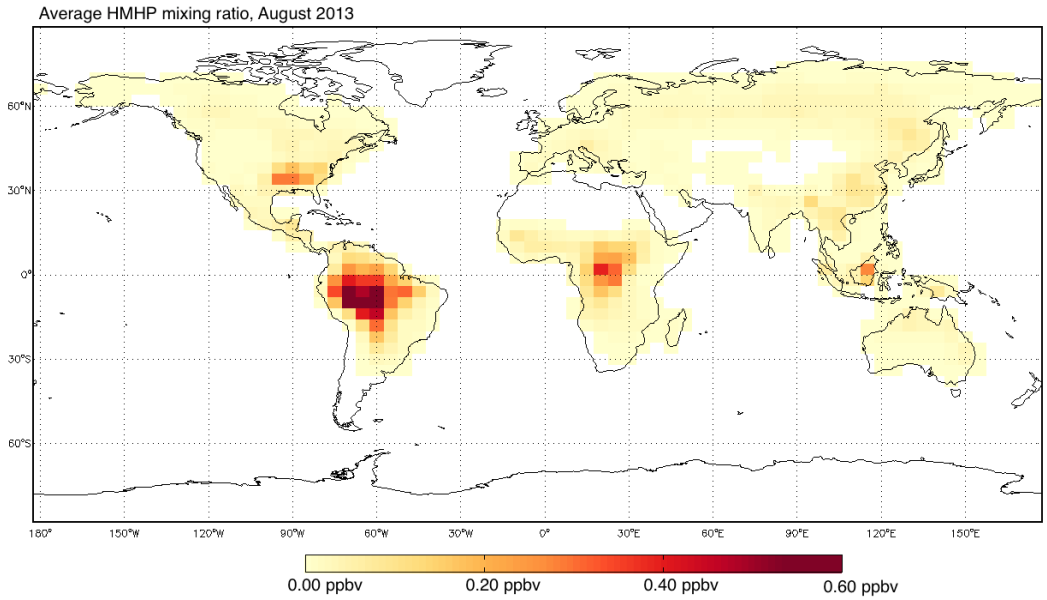

Figure 4.19: Average global distribution of HMHP during August 2013 for mixing ratios between 0–0.5 km above the surface.

Chapter 5

INVESTIGATING ISOPRENE-DERIVED HYDROPEROXIDES IN A FORESTED ENVIRONMENT

5.1 Abstract

Isoprene, a biogenic volatile organic compound, is the dominant non-methane hydrocarbon emitted to the atmosphere. Isoprene undergoes rapid oxidation to form a large variety of products, including hydroperoxides. Hydroperoxides play a significant role in altering the atmosphere's oxidative potential by acting as a reactive sink and mobile reservoir of OH radicals. This study describes the use of chemical ionization mass spectrometry (CIMS), a fast and versatile technique for quantifying a large range of compounds, to investigate the formation and oxidation of hydroperoxides derived from isoprene. In particular, this study and associated Appendix A outlines the development of a novel high resolution time of flight CIMS with an integrated gas chromatograph component (GC-HR-ToF-CIMS). As proof of concept, this instrument was deployed this instrument at a field site during the PROPHET field campaign in summer 2016. Data gathered during this campaign show that isoprene undergoes HO_x dominated chemistry to form substantial quantities of isoprene hydroxy hydroperoxides and its oxidation products in rural northern Michigan.

5.2 Introduction

Isoprene is a volatile organic compound (VOC) emitted as a byproduct of photosynthesis or photorespiration in deciduous vegetation, and is the dominant non-methane hydrocarbon emitted to the atmosphere. Annual emissions of this VOC total to approximately 500 Tg, which accounts for approximately half of global annual biogenic VOC emissions (Guenther et al., 2006). In the atmosphere, isoprene rapidly undergoes oxidation by either OH radical, O_3, or NO_3 radical to form a large variety of products, including a number of compounds in the hydroperoxide structural class. For example, ozonolysis of isoprene leads to the formation of hydroxymethyl hydroperoxide (HMHP), while OH oxidation leads to the formation of isoprene hydroxy hydroperoxides (ISOPOOH). Hydroperoxides play a significant role in dictating the chemistry that occurs in the atmosphere. These species can alter the atmosphere's oxidative potential by acting as a reactive sink and mobile reservoir of OH (Lee et al., 2000). They also directly act as oxidants of SO_2 in the aqueous

phase to produce SO_4^{2-}, thereby reducing air quality from increased concentrations of this visibility-reducing aerosol and from the formation of acid rain (Lind et al., 1987; Zhou and Lee, 1992). In addition, hydroperoxides have been implicated in the inhibition of peroxidase enzymes essential to plant function; the uptake of these species by plant leaves may cause leaf necrosis and therefore contribute to forest decline (Marklund, 1971; Gäb et al., 1985; Becker et al., 1990; Hewitt et al., 1990).

The most prevalent oxidation isoprene pathway in the atmosphere is via reaction with OH radicals. This occurs very rapidly during the daytime, and the lifetime of isopene against oxidation by OH is on order of 1-2 hours (Seinfeld and Pandis, 2006). Upon oxidation by OH following isoprene emission, the resulting radical undergoes O_2 addition to form an organic peroxy radical (RO_2). Two pathways then dominate the fate of this RO_2, depending upon the amount of NO_x present in the atmosphere. Under high NO_x conditions, RO_2 reacts to form either hydroxynitrates or formaldehyde and methyl vinyl ketone (MVK), methacrolein (MACR) and HO_2 (Paulot et al., 2009b). In environments with low NO_x, such as exist in remote forested regions, the dominant products from HO_x (=OH+HO_2) mediated chemistry are isoprene hydroxy hydroperoxides (ISOPOOH), formed in greater than 70% yield and with an estimated production of 181 TgC y^{-1} (Paulot et al., 2009b; St. Clair et al., 2016a). ISOPOOH forms with multiple isomers, including (1,2)-ISOPOOH, (4-3)-ISOPOOH and δ-ISOPOOH (Figure 5.1), and with an estimated ambient isomer distribution of 67%, 29%, and 4%, respectively (St. Clair et al., 2016a).

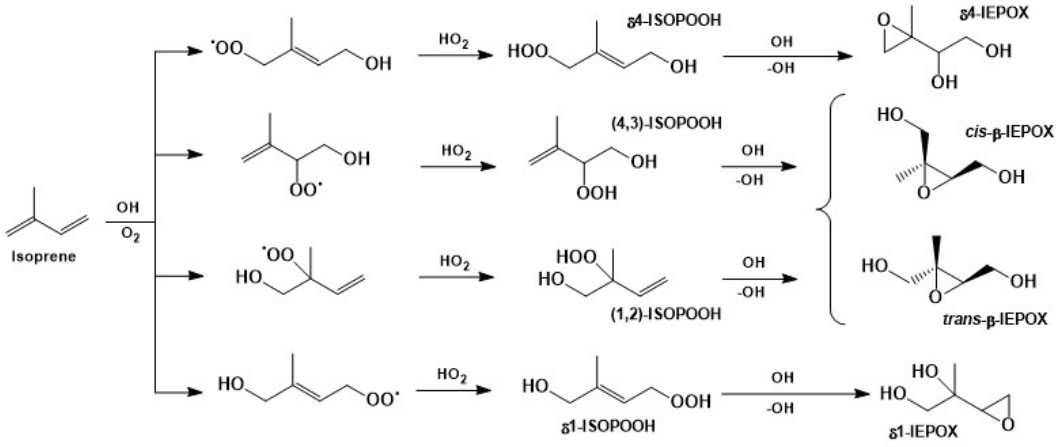

Figure 5.1: Mechanism of isoprene gas-phase oxidation by OH in a low NO_x environment. Initial products are dominated by isomers of isoprene hydroxyhdroxides (ISOPOOH), which undergo subsequent oxidation to form the isoprene epoxydiols (IEPOX). Figure adapted from Bates et al. (2014).

The functional groups and low vapor pressure of ISOPOOH provide reactive sites for numerous reactions that can lead to highly functionalized, low-volatility compounds. The lifetime of ISOPOOH with respect to oxidation by OH is fairly short, approximately 3 to 5 hours with around [OH] = 10^6 radicals cm^{-3} (Paulot et al., 2009b), indicating that a significant fraction of newly generated ISOPOOH quickly undergoes further oxidation. Under low NO_x conditions, a number of low volatility products form following the addition of OH to ISOPOOH, including dihydroperoxydiols, aldehydes, and ketones; together these channels account for approximately 15% of ISOPOOH+OH reactivity. The dominant products of ISOPOOH oxidation, however, are the isoprene epoxydiols (IEPOX) (Figure 5.1), formed in yields exceeding 75% and with an estimated global production of 115 TgC y^{-1} (St. Clair et al., 2016a). The production of IEPOX has significant ramifications for the troposphere. The oxidation of ISOPOOH via this pathway recycles OH, contributing to sustained HO_x concentrations in remote forested regions (Lelieveld et al., 2008; Paulot et al., 2009b). In addition, isoprene oxidation products act as precursors to secondary organic aerosol (SOA) formation (Wang et al., 2005; Kroll and Seinfeld, 2008), thereby impacting human health and global climate. Experimental IEPOX isomer distributions and oxidation rates are consistent with the relative concentrations of their hydrolysis products in ambient aerosol, indicating the direct role of IEPOX as an SOA precursor (Bates et al., 2014).

5.3 Experimental Methods

Chemical Ionization Mass Spectroscopy (CIMS) is a versatile and robust technique for investigating a variety of atmospheric compounds, including hydroperoxides. The Wennberg group in particular has developed a compact time-of-flight CIMS (C-ToF-CIMS) that utilizes a soft chemical ionization technique to detect multifunctional volatile organic compounds with high sensitivity. This technique employs ion clustering chemistry of CF_3O^- via

$$[Z] + CF_3O^- \longrightarrow Z \cdot CF_3O^- \tag{5.1}$$

to measure analyte hydroperoxides and other species, such as hydroxynitrates, hydroxyketones, and acids (depicted as [Z] above), with detection limits near 10 parts per trillion (ppt) (Crounse et al., 2006).

However, the C-ToF-CIMS does not provide information about isomer distribution, leaving significant ambiguity in situations where multiple isomers are present such as in the oxidation of isoprene to ISOPOOH. As a result, mass spectroscopy is

often combined with gas chromatography (GC), which separates compounds and their isomers before analytes enter the mass spectrometer. While a GC component has been combined with the C-ToF-CIMS in a laboratory setting, prior to this field study the combination of isomer separation from GC and sensitive compound detection from CF_3O^- CIMS had not been deployed in the field to study ambient isomer distributions. This section thus describes the development of a novel gas chromatograph high resolution time of flight CIMS (GC-HR-ToF-CIMS). The integrated GC-HR-ToF-CIMS builds upon the existent C-ToF-CIMS, but develops several of the instrument subsystems in order to produce an instrument that can operate continuously in the field, with high efficiency transmission through both the GC and CIMS components.

Furthermore, this study outlines the first deployment of the GC-HR-ToF-CIMS in a comprehensive field campaign. The instrument was deployed as part of the Program for Research on Oxidants, Photochemistry, Emissions, and Transport – Atmospheric Measurements of Oxidants in Summer (PROPHET–AMOS) field campaign at a forested site in Northern Michigan during the summer of 2016 (http://sites.google.com/a/umich.edu/prophet-amos/). The forest at this site consists of a mixture of broad leaf and coniferous trees, resulting in VOC emissions dominated by isoprene. In addition, the rural location means the atmosphere above the site is characterized by low NO_x chemistry. The GC-HR-ToF-CIMS was deployed above the tree canopy to monitor the concentrations of isoprene oxidation products, and from these data the concentrations and ambient isomer distributions of hydroperoxides formed from low NO_x isoprene oxidation are characterized.

GC-HR-ToF-CIMS

The GC-HR-ToF-CIMS is described in detail in Appendix A with a brief overview given here.

The GC-HR-ToF-CIMS employs CF_3O^- cluster chemistry to selectively detect multifunctional organic compounds such as hydroperoxides with high sensitivity. The ToF-MS component differs from the C-ToF-CIMS in that the mass spectrometer used in this instrument can operate in two ion optical modes: a single-reflection configuration ("V mode"), which has higher sensitivity but lower resolving power, and a two-reflectron configuration ("W mode"), which yields higher resolving power but lower sensitivity (DeCarlo et al., 2006). The single-reflection configuration (**T** as depicted in Figure 5.2) closely matches the sensitivity and resolving power of

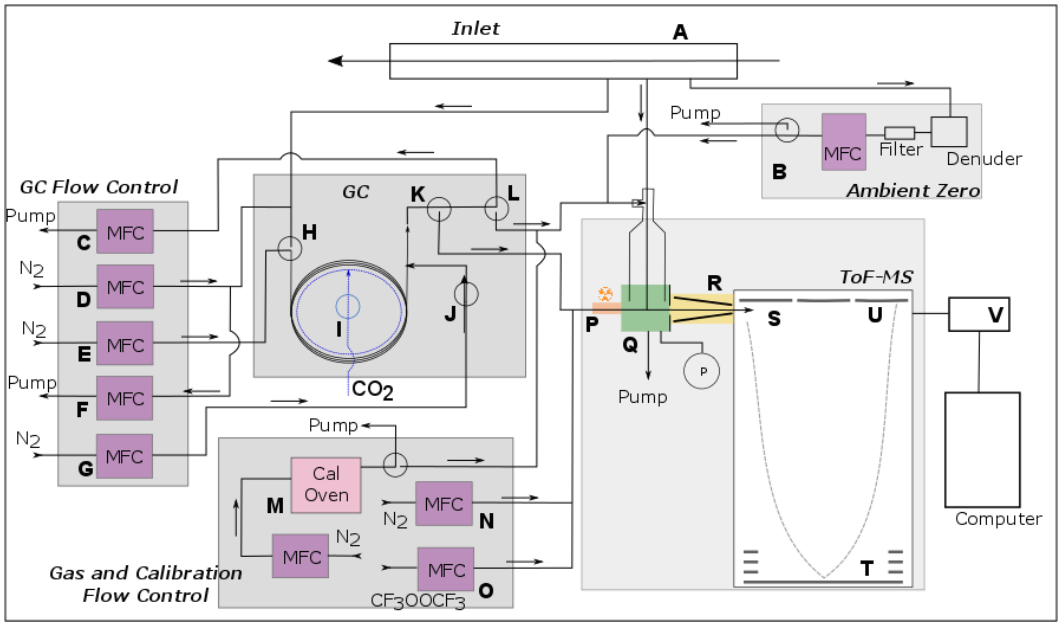

Figure 5.2: Schematic of the GC-HR-ToF-CIMS, with A) glass inlet; B) denuder, filter, mass flow controller (MFC), and three-way valve for performing an ambient zero; C) bypass MFC and pump, 200 sccm; D) GC dilution flow, 1000 sccm N_2; E) GC column flow, 8 sccm N_2; F) intake MFC and pump, 500 sccm; G) pickup flow, 200 sccm; H) three-way valve to control GC sampling; I) CO_2 flow for cryogenic trapping of sample; J) two-way valve to control pickup flow; K) three-way valve to control GC high sensitivity mode; L) three-way valve to control GC normal sensivity mode; M) heater block containing calibration compounds; N) CIMS dilution flow, 1500 sccm N_2; O) reagent gas flow, 400 sccm of 1 ppm CF_3OOCF_3 in N_2; P) radioactive ionization source, Po^{210}; Q) ion-molecule reaction region; R) hexapole ion guide; S) ion pulser; T) ion reflectron; U) microchannel plate detector; V) analog-to-digital converter.

the C-ToF-CIMS; the double-reflectron mode was not utilized in this study. The rest of the front-end hardware, including the ionization source, ion-molecule mixing region, and hexapole (**P**, *Q*, and *R* in Figure 5.2) mimics that of the C-ToF-CIMS with slight geometry updates.

The development of a field-deployable automated GC-CIMS required the largest innovation in the GC subsystem. Due to the low ambient concentrations and high volatility of many of the compounds of interest, analytes are cryofocused before flowing through the length of the GC column (1 m RTX-1701 megabore column, Restek). Cryotrapping is accomplished by flowing liquid CO_2 through a small length of restrictor tubing (inner diameter less than 1/16 in.) before the CO_2 rapidly expands to enter a much larger tubing (inner diameter of near 1/8 in.) running the length of

the column (**I** in Figure 5.2). The rapid expansion of CO_2 from liquid to gas causes swift cooling at the point of contact on the head of the GC column. Temperature control occurs during cooling by simultaneously employing resistive heaters at the desired setpoint, which are placed in thermal contact with the column by physical contact with a copper band that spans the length of the column. The temperature of the cryotrap is maintained at -15 to -25 °C, as many of the compounds of interest undergo decomposition in the presence of liquid or ice water in the column. The given temperature range, in addition to dilution of ambient samples (**D** in Figure 5.2), ensures that the specific humidity in the GC samples remains lower than the condensation vapor pressure while maximizing the number of analytes that can be trapped.

After cryofocusing for 5–15 minutes, the analytes elute through the GC column. A temperature ramping profile was employed as follows during elution: temperature ramps from approximately -15 °C to 30 °C over 5 minutes, then increases from 30 °C to 60 °C at 3 °C min^{-3}, and from 60 °C to 130 °C at 10 °C min^{-1}. Once the temperature profile finishes, the column maintains 130 °C for 2 minutes to ensure column cleanliness for the next GC. A flow of 8 sccm N_2 (**E** in Figure 5.2) carries analytes through the GC column as they elute. After analytes pass through the GC column, they may be introduced into the mass spectrometer either through the sample flow tube (**L** in Figure 5.2) or via the ionization source flow (**K** in Figure 5.2). Flowing the GC output through the flow tube allows for direct comparison of signal integration with direct CIMS measurements (i.e. signals observed when the GC is not utilized); this method is labeled "normal sensitivity" mode. Introduction of analytes through the ionization source provides significantly higher sensitivity in detection (denoted as "high sensitivity" mode), as this method passes analytes directly into the reagent ion flow. During this study, the GC was exclusively used in the high sensitivity mode.

When the GC-HR-ToF-CIMS is employed to sample ambient air, such as during field campaigns, the instrument cycles between four different modes. For the first half hour of every hour, the instrument samples ambient air directly into the flow tube of the mass spectrometer, neglecting the GC component. This mode allows direct quantification of the concentrations of various species. During this time the GC performs the cryotrapping of analytes. The second half of the hour is then given to GC elution and analysis. In addition, twice each hour the instrument performs a test of two types of zeroing. The first is a dry zero in which the flow

tube is overfilled with dry N_2 to give a measure of instrument background signals. The second is a wet zero or "ambient zero", which is designed to remove reactive volatile compounds from ambient air samples, providing a measure of the instrument background signals observed at the same relative humidity as is present in ambient samples. The ambient zero system consists of a bicarbonate denuder and a filter composed of bicarbonate-coated nylon wool. The dry zero lasts for two minutes and the ambient zero lasts for 4 minutes.

The CG-HR-ToF-CIMS provides 10 Hz resolution data for masses between m/z 19 and m/z 378. In this study, isoprene nitrates were monitored at *m/z* 232 (ISOPN·CF_3O^-), ISOPOOH and IEPOX were monitored at *m/z* 203 (ISOPOOH·CF_3O^- + IEPOX·CF_3O^-), HPALD was monitored at *m/z* 201 (HPALD·CF_3O^-), and IEPOX oxidation products were monitored at *m/z* 187 and 189. All observed ion signals were normalized to the reagent anion signal (*m/z* 86) and the water signal (*m/z* 104) for the same reasons as listed for the C-ToF-CIMS. In addition, in this study, the 10 Hz data collection was averaged down to one minute for direct CIMS signals and five seconds for GC signals.

PROPHET Field Study

Measurement of isoprene oxidation products with the GC-HR-ToF-CIMS took place in northern Michigan as part of the PROPHET-AMOS field campaign between July 1 and July 31, 2016. The site is located at the northern edge of the lower Michigan peninsula (45°33' N, 84°43' W). The field site is situated in a rural location surrounded by densely forested area with few urban areas. The nearest town is Pellston, MI (~5.5 km west, population ~800), followed by Cheboygen, MI (25 km northeast, population ~4,800), Petosky, MI (~30 km southwest, population ~5,800), and Traverse City, MI (~110 km southwest, population ~15,000). Depending upon wind direction, the field site may be influenced by anthropogenic emissions from the closest urban centers, including Detroit, MI (~380 km southeast, metropolitan population ~4,000,000), Milwaukee, WI (~375 km southwest, metropolitan population ~1,500,000), Chicago, IL (>450 km southeast, metropolitan population ~9,700,000), and Toronto, ON, Canada (>450 km southwest, metropolitan population ~6,000,000). To the north of the site lies the Canadian boreal forest.

The forested location means that biogenic emissions, particularly isoprene, comprise the majority of the VOC concentrations in this area. Historically, winds predominantly arrive from the west; hence the site is largely upwind of major pollution

sources. The forest in this location is characterized as "mixed" or "transition" and consists of mixed aspen that represents recent growth and pine that represents older growth, in addition to red oak and northern hardwood (maple, beech, birch, etc.) trees (Carroll et al., 2001). Of the biogenic VOCs emitted from these trees, isoprene by far dominates at >95% of the total terpenoid flux with an average cumulative flux of 2.49 gC m^{-2} between June and September due to the large presence of aspen trees (90% of isoprene emissions). Monoterpene and sesquiterpene emissions account for 4% and 0.3% or 0.105 gC m^{-2} and 0.007 gC m^{-3} average cumulative fluxes of biogenic VOC emissions, respectively (Ortega et al., 2006; Westberg et al., 2001).

The GC-HR-ToF-CIMS was situated on the top platform of a 31 m research tower, facing west. This placed the instrument well above the forest canopy height, which averaged between 20–25 m above ground level. Ambient air was sampled through a glass inlet (**A** in Figure 5.2) that extended approximately 30 cm from the edge of the tower, and which was equipped with a pump that pulled air through the inlet at a very high rate. Three instrument intake lines were located along the glass inlet for the ambient zero, the GC, and directly to the CIMS. These lines sub-sampled at about 200 sccm perpendicular to the high inlet flow, minimizing the potential intake of particles and other objects that might constrict flow into the instrument. The instrument was housed in a temperature controlled and insulated enclosure to protect it from the elements.

In addition to the GC-HR-ToF-CIMS, three supporting instruments were co-located with the CIMS. Two three-dimensional ultrasonic anemometers ("sonics", Campbell Scientific, model CSAT3) measured wind speeds in three orthogonal directions. The two sonics extended approximately 2 m from the edge of the tower in opposite directions: one was located on top of the instrument enclosure, facing west and vertically positioned approximately 1 m above the instrument inlet; the second sonic was positioned at approximately the same vertical height as the instrument inlet, but was approximately 4 m east and 0.25 m to the south. Finally, a weather station was placed on the roof of the enclosure that included sensors to measure relative humidity, temperature, barometric pressure, solar radiation, wind speed, and wind direction.

5.4 Results and Discussion

The atmosphere at the field site in Michigan exhibited high VOC and low NO_x chemistry, promoting the formation of isoprene hydroxy hydroperoxides. In partic-

ular, a several day period between July 22 and July 26 exhibited warm temperatures (maximums around 30 °C) and sunny conditions that led to very high biogenic VOC emissions. On July 23rd, in particular, isoprene concentrations increased to over 40 ppb at canopy level (~ 20 m) during the daytime, as measured by a proton-transfer-reaction with quadrupole ion guide time-of-flight mass spectrometer (PTR-QiTOF, operated by the Millet group from the University of Minnesota). Hence, the results of this section will focus on this five-day period.

A preliminary estimation of the relative concentrations of isoprene oxidation products during the selected five-day period are shown in Figure 5.4. Note that further corrections are needed to ascertain exact concentrations and the ones presented here are approximate only. The concentrations of isoprene nitrates (ISOPN) were fairly low throughout the campaign, with mixing ratios in the 0–50 ppt range. By contrast, the concentration of ISOPOOH+IEPOX was significantly higher and peaked between 100–400 ppt, depending on day, and varying between 5 to 10 times higher than ISOPN. ISOPN and ISOPOOH+IEPOX dominate under low NO_x and high HO_x conditions, respectively, when RO_2 lifetimes are short (often < 0.1 s). However, a third pathway exists for isoprene oxidation when RO_2 lifetimes are long enough (10's of seconds range). Under these conditions, the RO_2 lifetime is long enough that the isoprene peroxy radical in the 1,4 or 4,1 configuration may undergo 1,6-H shift isomerization to form the C_5-hydroperoxyaldehydes (HPALD) (Crounse et al., 2011).

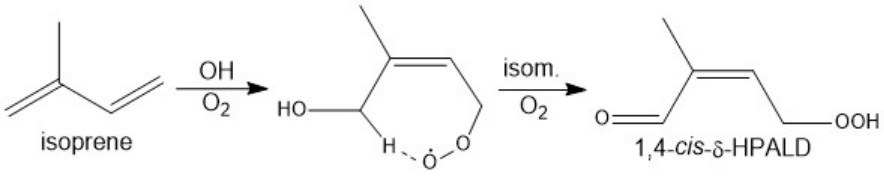

Figure 5.3: Formation of HPALD from isomerization of isoprene.

In Michigan, the mixing ratio of m/z 201, the mass associated with HPALD, exhibited peaks between approximately 50–150 ppt. These concentrations are comparable to those of ISOPOOH+IEPOX, with mixing ratios of the latter falling with 80%-100% of those of HPALD. However, note should be made that while m/z 201 is mostly attributed to HPALD, this mass may include other species as well (see Appendix A). The comparison of these oxidation products indicate that this region of northern Michigan shows HO_x and isomerization dominated chemistry, with isoprene mainly following these routes.

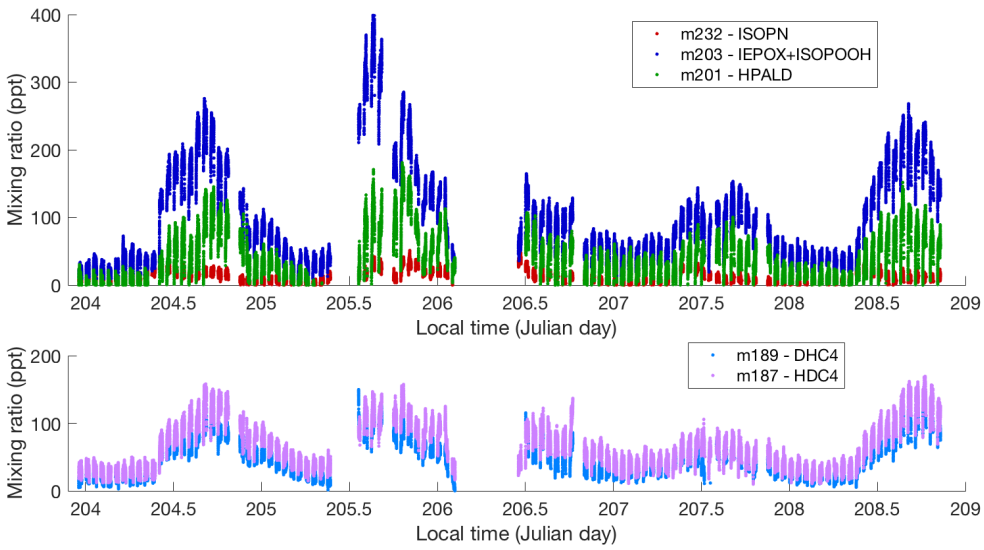

Figure 5.4: Isoprene oxidation products during July 22 (Julian Day 204) to July 26 (Julian day 208) at PROPHET as measured by direct sampling on the GC-HR-ToF-CIMS. (Top) Estimated mixing ratios of isoprene nitrates (ISOPN), ISOPOOH+IEPOX, and HPALD (+ other compounds). ISOPOOH+IEPOX and HPALD exhibited much higher concentrations than ISOPN, indicating low NO_x conditions. (Bottom) Estimated mixing ratios of IEPOX oxidation products.

In addition to the early generation products, the GC-HR-ToF-CIMS provides information on the subsequent reaction pathways as ISOPOOH and IEPOX undergo further oxidation in the atmosphere. IEPOX oxidation under low NO_x conditions leads to a range of products, including acetic and formic acids, glycolaldehyde, hydroxyacetone, and C_4 and C_5 organic compounds. Figure 5.4 (bottom) indicates the preliminary mixing ratios of two of the most prevalent C_4 and C_5 masses typically formed in IEPOX oxidation by OH, m/z 187 and 189, identified as C_4 hydroxy dicarbonyls and C_4 dihydroxy carbonyls, respectively. The relative yields of these two masses differs greatly depending upon the structure of the parent IEPOX isomer. Under low NO_x conditions, cis-β-IEPOX will produce approximately 37% of m/z 189 and 10% of m/z 187, while $trans$-β-IEPOX will produce approximately 22% of m/z 198 and only 4% of m/z 187 (Bates et al., 2014). Hence the ratio of these species can provide information about the relative pathways of IEPOX+OH oxidation. In addition, IEPOX+OH yields a small amount of a compound at m/z 201 (~11% from both isomers), which appears at the same m/z as HPALD. The mixing ratio of these masses is also complicated by the minor formation of non-IEPOX products at m/z 201 and 189 from ISOPOOH+OH oxidation.

The GC component of the GC-HR-ToF-CIMS provides a key resource for distin-

guishing compounds that appear at the same m/z in the CIMS. The two double bonds of isoprene mean that oxidation by OH can lead to multiple reaction routes and often produces multiple isomers of ISOPOOH, IEPOX, ISOPN, and other species. Figure 5.5 (top) indicates the different compounds observed during the afternoon of July 23 at m/z 203, 201, and 232. Tentative assignments of these species are based on experiments performed with the C-ToF-CIMS (e.g. Bates et al. (2014) and Teng et al. (2015)). Fitting these peaks to a Gaussian shape gives the distribution of these isomers relative to each other. The isomer distribution obtained by a ratio of peak areas was approximately 2.2:1 for 1,2- vs. 4,3-ISOPOOH; 1.5:1 for the cis- vs. $trans$-β-IEPOX isomers; 5.3:1 for the 1,2- vs 4,3-ISOPN; and 2.1:1 for the 4,1- and 1,4-cis-δ-HPALD isomers. Overall, these peak areas indicate that ISOPOOH is the most abundant species of the four, followed by IEPOX, ISOPN, then HPALD, with a ratio of 23.7 to 19.3 to 5.5 to 1, respectively. The relative abundance of these isomers is close to that expected from laboratory experiments. In particular, the ratio of cis- to $trans$-β-IEPOX is matches more closely with yields expected from the 1,2-ISOPOOH isomer than from 4,3-ISOPOOH, consistent with the greater observed abundance of 1,2-ISOPOOH.

In addition to isomer distribution, understanding the formation and loss pathways of these species is key to understanding how isoprene transforms throughout the atmosphere. Figure 5.5 (bottom) shows the gas chromatograms of m/z 203 over a twelve hour period during July 23, 2016. These chromatograms indicate that ISOPOOH and IEPOX begin with a relatively even isomer distribution in the early morning before the sun rises. As the morning progresses and concentrations peak in the mid-afternoon, the 1,2-ISOPOOH isomer begins to dominate, followed by the IEPOX isomers, and then by the 4,3-ISOPOOH isomer. Abstraction of the H that places the radical on the C_2 rather than the C_3 carbon is more favorable due to the higher substitution of the C_2 carbon. As a result, the 1,2-ISOPOOH pathway would be more favored and more likely to form in the atmosphere. The 4,3-ISOPOOH isomer also reacts more quickly, leading to the lower observed concentrations of this isomer compared to the 1,2-ISOPOOH. However, as the oxidation continues, the expected distributions become more complicated as rates and yields vary for each species. A photochemical box model can be used to describe the product and loss pathways of these species, and thereby assess the expected distribution of each isomer. This comparison will help to assess if current understanding of isoprene chemistry can accurately capture observations of the atmosphere.

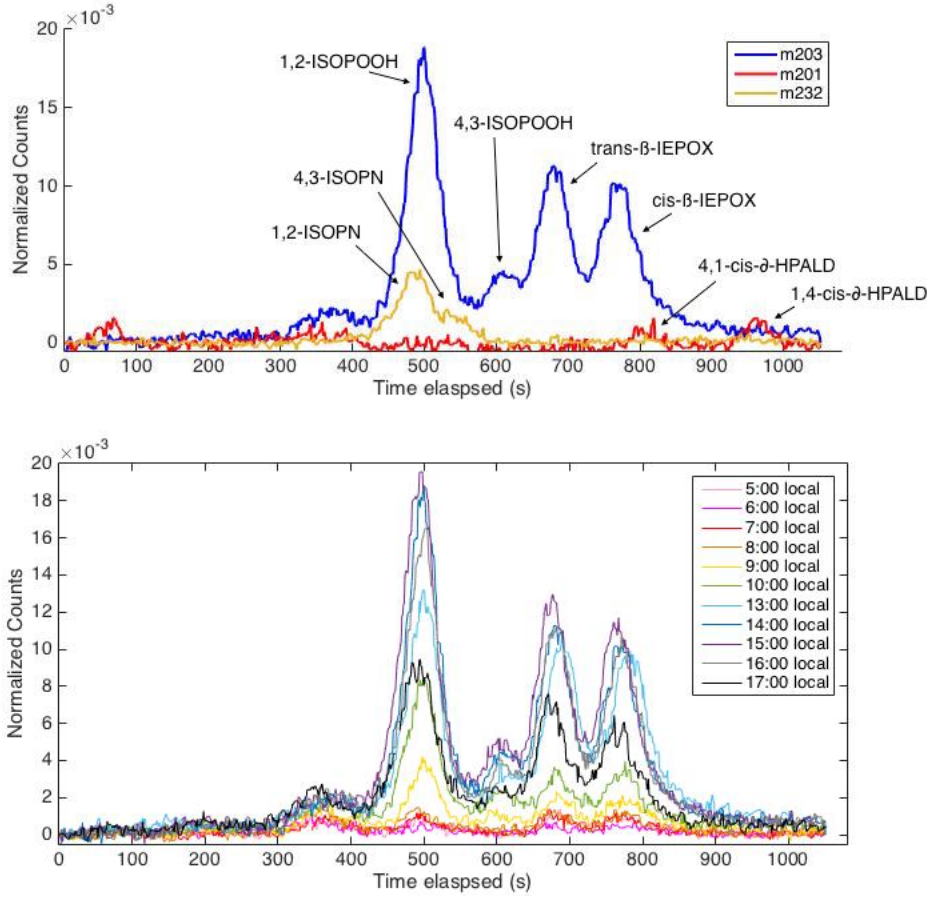

Figure 5.5: Gas chromatographs collected during the PROPHET campaign. (Top) GC traces of m/z 203 (IEPOX+ISOPOOH), m/z 201 (HPALD), and m/z 232 (ISOPN) indicating tentative assignment of general isomer distribution during PROPHET. Data from 14:00 on July 23, 2016. (Bottom) GC traces of m/z 203 showing chromatographic separation of isomers of ISOPOOH and IEPOX and the increase in concentrations over the course of the day. Data from July 23, 2016.

5.5 Conclusions

To better understand atmospheric hydroperoxides, a novel field-ready GC-HR-ToF-CIMS was deployed and this instrument was deployed at a field site during the PROPHET 2016 campaign. Many laboratory studies have investigated the formation and oxidation reactions of ISOPOOH, IEPOX, and ISOPN, but evaluation of their importance in the atmosphere has been hampered by limitations on measurement techniques. The GC-HR-ToF-CIMS provides key new measurements of these species by combining a chromatographic separation technique with CIMS to sensitively detect concentrations and isomer distributions of ISOPOOH, IEPOX, ISOPN, and other species. Furthermore, this instrument can be deployed in multiple locations to gather data on the atmospheric distribution of these species in regions with

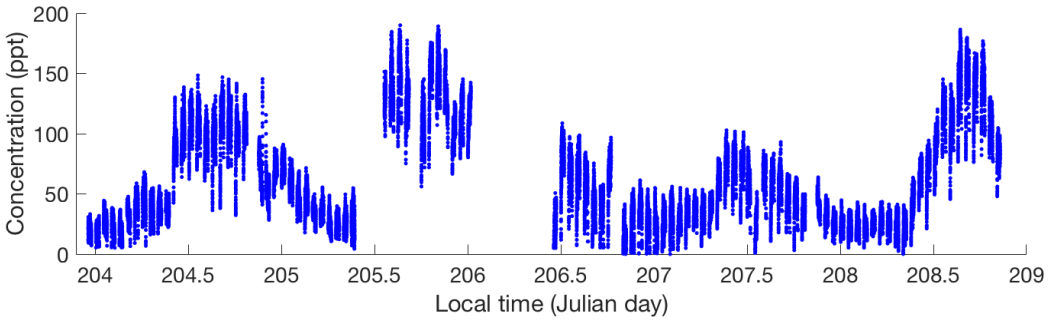

Figure 5.6: Estimated concentration of m/z 149, assigned to HMHP, during July 22–July 26, 2016 at the PROPHET site.

varying conditions, such as high and low NO_x concentrations.

While at PROPHET, the HR-GC-ToF-CIMS collected data on a vast range of oxidized species and the HR-GC-ToF-CIMS may be used to investigate other reaction channels present in the atmosphere at Michigan. For example, the ozonolysis of isoprene produces hydroxymethyl hydroperoxide (HMHP, $HOCH_2OOH$), which was measured at the site in significant concentrations (Figure 5.6). Using the rates and yields presented above, a box model can be constructed to determine the expected concentrations of HMHP, formic acid, and formaldehyde and compare them to those observed at Michigan. In addition, isoprene may undergo oxidation by NO_3 radicals during the night to form a range of compounds including nitrooxy hydroperoxides among others (Perring et al., 2009). Other biogenic VOCs such as monoterpenes α- and β-pinene were also present at the site. These VOCs react with OH, O_3, and NO_3 in competing pathways. Although the concentration of the monoterpenes is smaller than that of isoprene, some monoterpene hydroxynitrates were observed, and the monoterpene species likely contribute to the oxidative budget of this forested region. In addition, more analysis remains to be done on the ISOPOOH, IEPOX, and ISOPN oxidation pathways. For example, using isomer yields and rate constants from Bates et al. (2014) and St. Clair et al. (2016a), the PROPHET GC and CIMS data can be used to determine the contribution of ISOPOOH and IEPOX to SOA formation. The GC-HR-ToF-CIMS provides a vast range of masses, and we have only begun to tease apart this complex data set.

Finally, two sonics were located near the GC-HR-ToF-CIMS inlet, providing data that can be used to estimate fluxes and dry deposition velocities. Understanding ambient flux and dry deposition rates are key for model representations of atmosphere-biosphere interactions, and thereby understanding OH reactivity above and below the

forest canopy. Biosphere exchange within the atmospheric boundary layer is driven by wind turbulence, therefore fluxes can be estimated using micrometeorological methods such as eddy covariance (EC). The EC flux (F_x) of the desired species x is determined by

$$F_x = \overline{w'x'} \tag{5.2}$$

where w is the vertical wind component, and primes denote the deviations from the mean value (overbars) of a typical flux period. The deposition velocity (V_d, with units cm s^{-1}) can then be found via the EC flux and the mixing ratio of the species.

$$V_d = -\frac{F_x}{\overline{x}} \tag{5.3}$$

Underlying these calculations are the assumptions that the measurement is stationary, the surface is homogenous so that the horizontal wind components are unimportant, and the scale of chemical exchange is slow in relation to flux variation (Nguyen et al., 2015). Because these turbulent eddies occur on a high-frequency timescale, sampling of compound mixing ratios must occur at a 1 Hz or faster sampling frequency. The high sampling frequency of direct sampling on the GC-HR-ToF-CIMS and the sonics allow the eddy covariance methods to be employed on oxidized VOC sampled at the site. The flux and dry deposition velocities of compounds such as ISOPOOH and IEPOX measured at PROPHET have yet to be determined, but may play an important role in the atmosphere present there.

Acknowledgements

There are many people who helped to co-author the work presented in this chapter. Professor Paul Wennberg provided substantial guidance and motivating force on these projects. Dr. John Crounse was instrumental in providing mentorship and assistance in each project, particularly in building and deploying the GC-HR-ToF-CIMS. Lab-mates Dr. Anke Nölscher, Krystal Vasquez, and Eric Praske contributed to building the GC-HR-ToF-CIMS and deploying it during the PROPHET campaign. Steven Bertman from Western Michigan University organized the PROPHET campaign and made the measurements in Michigan possible. Finally, NSF provided funding for the GC-HR-ToF-CIMS project and deployment.

Chapter 6

CONCLUSIONS AND OUTLOOK

The work in this dissertation has sought to elucidate different mechanisms by which gas-phase hydroperoxides form and the pathways by which they either transform or are removed from the atmosphere. The connection between hydroperoxides and cycling of the atmosphere's main oxidants, HO_x, as well as the changes in hydroperoxide chemistry due to atmospherically prevalent NO_x, mean that understanding these hydroperoxides is necessary for understanding the oxidizing capacity of the atmosphere. Towards this end, each chapter in this dissertation targeted a specific set of hydroperoxides to understand the regions in which they form, their chemical processes, and how they impact atmospheric HO_x and NO_x. While this dissertation has significantly advanced constraints on these processes, this work has opened potential new lines of inquiry and more work may be done to address remaining questions.

Chapter 2 investigated two of the simplest and yet most abundant hydroperoxides — H_2O_2 and CH_3OOH (MHP) — in the remote atmosphere above the Pacific and Atlantic Oceans. This chapter showed that these two peroxides have highly variable mixing ratios that greatly depend on the latitude, longitude, altitude, and time of year being sampled; though these two hydroperoxides tend to be highest closer to the equatorial regions and peak in altitude just above the marine boundary layer. In addition, this chapter revealed a major distinction between the atmospheres of the remote Pacific and remote Atlantic due to the influence of biomass burning from the African continent in driving high H_2O_2 in the Atlantic across all four seasons. While these measurements made during the Atmospheric Tomography Mission are meant to provide a representative picture of atmosphere, they were nonetheless collected in a particular moment in time. Continued sampling of hydroperoxides in the remote atmosphere would reveal how these compounds change not just with season, but with longer-scale atmospheric changes that result from changes in the Earth system due to increased human population (thus increased pollution and other human influences on the remote atmosphere) as well as due to the changing climate.

Continuing the study into H_2O_2 and CH_3OOH in the remote oceanic atmosphere, Chapter 3 gave a particular focus to the chemistry and physical losses affecting these

hydroperoxides. In particular, this chapter showed that globally H_2O_2 is primarily lost to photolysis while MHP is primarily lost to reaction with OH. This chapter also showed that deposition plays a large role in H_2O_2 in the marine boundary layer and its impact on HO_x as well as the prevalent role that convection plays in lofting MHP and affecting the hydroperoxide budget in the upper troposphere and lower stratosphere. Comparisons to the global chemical transport model GEOS-Chem revealed that while there are regions in which the models accurately predict hydroperoxide mixing ratios, more refinements are need in the model to full capture this chemistry. Implementation of the derived H_2O_2 deposition rate, for example, will help align the model with H_2O_2 measurements made in the boundary layer. In the upper troposphere and lower stratosphere, convection likely influences the disagreement between measured and modeled H_2O_2 and MHP, but more investigation is needed to diagnose the exact causes of the discrepancy.

The next chapter, Chapter 4, focused on the reaction of the single carbon hydroxy hydroperoxide $HOCH_2OOH$ (HMHP) with the atmospheric oxidant OH. This chapter found the reaction rate of HMHP with OH is fast enough that nearly half of HMHP in the atmosphere is likely lost via this pathway. In this reaction mechanism, OH abstracts either from the methyl hydrogen to produce formic acid or from the peroxy hydrogen to produce formaldehyde. Models tend to under-predict formic acid relative to measurements and inclusion of formic acid as a product of HMHP oxidation produces a small but notable increase in global estimates of formic acid from models. While this study investigated the impact of formic acid from HMHP on a global scale, HMHP and its impact on formic acid is likely to be much more substantial in forested regions where HMHP is produced. The results of this study have informed subsequent investigations that show that chemical pathways formed in isoprene oxidation, of which HMHP is a product, accounts for a significant fraction of formic acid production in forested environments (Alwe et al., 2019; Link et al., 2020).

Finally, Chapter 5 and the associated Appendix A describe a new analytical method for better measuring hydroperoxides, such as the larger organic hydroperoxides formed in the oxidation of isoprene in forested environments. A field-deployable gas chromatograph was developed and combined with high resolution CIMS to sensitively detect atmospheric hydroperoxides and to separate isobaric hydroperoxide isomers that would otherwise appear at the same mass using only CIMS. ISOPOOH, for example, was measured in substantial quantities in a forested site in rural northern

Michigan and the GC-CIMS technique revealed the ambient distribution of two different isomers of this hydroxy hydroperoxide. The GC-HR-ToF-CIMS instrument developed in this chapter has been further used to show the role of hydroperoxides in investigations of the atmospheric oxidation pathways of other compounds such as pentane (C_5H_{12}, anthropogenic), crotonaldehyde ($CH_3CHCHCHO$, anthropogenic), α-pinene ($C_{10}H_{16}$, terpene, biogenic), and β-pinene ($C_{10}H_{16}$, terpene, biogenic) (Praske et al., 2019; Møller et al., 2019; Xu et al., 2019). Future studies using this instrument in laboratory and field settings will further elucidate the important role of hydroperoxides in the atmosphere.

BIBLIOGRAPHY

Adler, T. B., Knizia, G., and Werner, H.-J. "A simple and efficient CCSD(T)-F12 approximation." *J. Chem. Phys.* 127: 221106, (2007).

Allen, H. M., Crounse, J. D., Kim, M. J., Tang, A. P., Ray, E. A., McKain, K., Sweeney, C., and Wennberg, P. O. "H_2O_2 and CH_3OOH (MHP) in the remote atmosphere. I: Global distribution and regional influences." *J. Geophys. Res. Atmos.* submitted, (2021).

Allen, N. D. C., Abad, G. G., Bernath, P. F., and Boone, C. D. "Satellite observations of the global distribution of hydrogen peroxide (H_2O_2) from ACE." *J. Quant. Spec. Rad. Trans.* 115: 66–77, (2013).

Alwe, H. D., Millet, D. B., Chen, X., Raff, J. D., Payne, Z. C., and Fledderman, K. "Oxidation of volatile organic compounds as the major source of formic acid in a mixed forest canopy." *Geopys. Res. Lett.* 46: 2940–2948, (2019).

Andreae, M. O. "Emission of trace gases and aerosols from biomass burning – an updated assessment." *Atmos. Chem. Phys.* 19: 8523–8546, (2019).

Anglada, J. M., Crehuet, R., Martins-Costa, M., Francisco, J. S., and Ruiz-López, M. "The atmospheric oxidation of CH_3OOH by the OH radical: the effect of water vapor." *Phys. Chem. Chem. Phys.* 19: 12331–12342, (2017).

Atkinson, R. "Gas-phase tropospheric chemistry of organic compounds: A review." *Atmos. Environ.* 41: S200–S240, (2007).

Atkinson, R., Aschmann, S. M., Carter, W. P. L., Winer, A. M., and Pitts, J. N. "Alkyl nitrate formation from the NO_x-air photooxidations of C_2–C_8 n-alkanes." *J. Phys. Chem.* 86: 4563–4569, (1982).

Atkinson, R., Baulch, D. L., Cox, R. A., Crowley, J. N., Hampson, R. F., Hynes, R. G., Jenkin, M. E., Rossi, M. J., and Troe, J. "Evaluated kinetic and photochemical data for atmospheric chemistry: Volume II — gas phase reactions of organic species." *Atmos. Chem. Phys.* 6: 3625–4055, (2006).

Barker, J. R. "Multiple-Well, multiple-path unimolecular reaction systems. I. MultiWell computer program suite." *Internat. J. Chem. Kinet.* 33: 232–245, (2001).

———. "Energy transfer in master equation simulations: A new approach." *Internat. J. Chem. Kinet.* 41: 748–763, (2009).

Barker, J. R., Nguyen, T. L., Stanton, J. F., Aieta, C., Ceotto, M., Gabas, F., Kumar, T. J. D., Li, C. G. L., Lohr, L. L., Maranzana, A., Ortiz, N. F., Preses, J. M., Simmie, J. M., Sonk, J. A., and Stimac, P. J. "MultiWell-2017 Program Suite." 2017a. University of Michigan, Ann Arbor.

———. "MultiWell Program Suite User Manual (MultiWell-2017)." 2017b. University of Michigan, Ann Arbor.

Barnes, I., Becker, K. H., Fink, E. H., Reimer, A., and Zabel, F. "FTIR spectroscopic study of the gas-phase reaction of HO_2 with H_2CO." *Chem. Phys. Lett.* 115: 1–8, (1985).

Barth, M. C, Bela, M. M., Fried, A., Wennberg, P. O., Crounse, J. D., St. Clair, J. M., Blake, N. J., Blake, D. R., Homeyer, C. R., Brune, W. H., Zhang, L., Mao, J., Ren, X., B., Ryerson. T., Pollack, I. B., Peischl, J., Cohen, R. C., Nault, B. A., Huey, L. G., Liu, X., and Cantrell, C. A. "Convective transport and scavenging of peroxides by thunderstorms observed over the central U.S. during DC3." *J. Geophys. Res. Atmos.* 121: 4272–4295, (2016).

Barth, M. C., Stuart, A. L., and Skamarock, W. C. "Numerical simulations of the July 10, 1996 Stratospheric-Tropospheric Experiment: Radiation, Aerosols, and Ozone (STERAO) – Deep Convection experiment storm: redistribution of soluble tracers." *J. Geophys. Res.* 106: 12381–12400, (2001).

Bates, K. H., Crounse, J. D., St. Clair, J. M., Bennett, N. B., Nguyen, T. B., Seinfeld, J. H., Stoltz, B. M., and O., Wennberg. P. "Gas phase production and loss of isoprene epoxydiols." *J. Phys. Chem. A* 118: 1237–1246, (2016).

Bates, K. H., Jacob, D. J., Wang, S., Hornbrook, R. S., Apel, E. C., Kim, M. J., Millet, D. B., Wells, K. C., Chen, X., Brewer, J. F., Ray, E. A., Commane, R., Diskin, G. S., and Wofsy, S. C. "The global budget of atmospheric methanol: new constraints on secondary, oceanic, and terrestrial sources." *J. Geophys. Res. Atmos.* 126: e2020JD033439, (2021).

Bates, K. H., Nguyen, T. B., Teng, A. P., Crounse, J. D., Kjaergaard, H. G., Stoltz, B. M., Seinfeld, J. H., and O., Wennberg. P. "Production and fate of C_4 dihydroxycarbonyl compounds from isoprene oxidation." *J. Phys. Chem. A* 120: 106–117, (2014).

Bauerle, S. and Moortgat, G. K. "Absorption cross-sections of $HOCH_2OOH$ vapor between 205 and 360 nm at 298 K." *Chem. Phys. Lett.* 309: 43–48, (1999).

Becke, A. D. "Density-functional thermochemistry. III. The role of exact exchange." *J. Chem. Phys.* 98: 5648–5652, (1993).

Becker, K. H., Brockmann, K. J., and Bechara, J. "Production of hydrogen peroxide in forest air by reaction of ozone with terpenes." *Nature* 346: 256–258, (1990).

Bela, M. M., Barth, M. C., Toon, O. B., Fried, A., Ziegler, C., Cummings, K. A., Li, Y., Pickering, K. E., Homeyer, C. R., Morrison, H., Yang, Q., Mecikalski, R. M., Carey, L., Biggerstaff, M. I., Betten, D. P., and Alford, A. A. "Effects of scavenging, entrainment, and aqueous chemistry on peroxides and formaldehyde in deep convective outflow over the Central and Southeastern United States." *J. Geophys. Res. Atmos.* 123: 7594–7614, (2018).

Bertram, T. H., Perring, A. E., Wooldridge, P. J., Crounse, J. D., Kwan, A. J., Wennberg, P. O., Scheuer, E., Dibb, J., Avery, M., Sachse, G., Vay, S. A., Crawford, J. H., McNaughton, C. S., Clarke, A., Pickering, K. E., Fuelberg, H., Huey, G., Blake, D. R., Singh, H. B., Hall, S. R., Shetter, R. E., Fried, A., Heikes, B. G., and Cohen, R. C. "Direct measurements of the convective recycling of the upper troposphere." *Science* 315: 816–820, (2007).

Bethel, H. L., Atkinson, R., and Arey, J. "Kinetics and products of the reactions of selected diols with the OH radical." *Int. J. Chem. Kinet.* 33: 310–316, (2001).

Bey, I., Jacob, D. J., Yantosca, R. M., Logan, J. A., Field, B. D., Fiore, A. M., Li, Q., Liu, H. Y., Mickley, L. J., and Schultz, M. G. "Global modeling of tropospheric chemistry with assimilated meteorology: Model description and evaluation." *J. Geophys. Res.* 106: 23073–23095, (2001).

Bian, H. and Prather, M. J. "Fast-J2: Accurate simulation of stratospheric photolysis in global chemical models." *J. Atmos. Chem.* 41: 281–296, (2002).

Bowman, K. P. "Large-scale isentropic mixing properties of the Antarctic polar vortex from analyzed winds." *J. Geophys. Res. Atmos.* 98: 23013–23027, (1993).

Bowman, K. P. and Carrie, G. D. "The mean-meridional transport circulation of the troposphere in an idealized GCM." *J. Atmos. Sci.* 59: 1502–1514, (2002).

Brune, W. H., Miller, D. O., Thames, A. B., Allen, H. M., Apel, E. C., Blake, D. R., Bui, T. P., Commane, R., Crounse, J. D., Daube, B. C., Diskin, G> S., DiGangi, J. P., Elkins, J. W., Hall, S. R., Hanisco, T. F., Hannun, R. A., Hintsa, E. J., Hornbrook, R. S., Kim, M. J., McKain, K., Moore, F. L., Neuman, J. A., Nicely, J. M., Peischl, J., Ryerson, T. B., St. Clair, J. M., Sweeney, C., Teng, A. P., Thompson, C., Ullmann, K., Veres, P. R., Wennberg, P. O., and Wolfe, G. M. "Exploring oxidation in the remote free troposphere: insights from atmospheric tomography (ATom)." *J. Geophys. Res. Atmos.* 125: e2019JD031685, (2020).

Burkholder, J. B., Sander, S. P., Abbatt, J., Barker, J. R., Huie, R. E., Kolb, C. E., Kurylo, M. J., Orkin, V. L., Wilmouth, D. M., and Wine, P. H. "Chemical kinetics and photochemical data for use in atmospheric studies, evaluation No. 18." 2015. JPL publication 15-10, Jet Propulsion Laboratory, Pasadena.

Burrows, J. P., Moortgat, G. K., Tyndall, G. S., Cox, R. A., Jenkin, M. E., Hayman, G. D., and Veyret, B. "Kinetics and mechanism of the photooxidation of formaldehyde: 2. Molecular modulation studies." *J. Phys. Chem.* 93: 2375–2382, (1989).

Calvert, J. G., Lazrus, A., Kok, G. L., Heikes, B. G., Walega, J. G., Lind, J., and Cantrell, C. A. "Chemical mechanisms of acid generation in the troposphere." *Nature* 317: 27–35, (1985).

Carlton, A. G., de Gouw, J., Jimenez, J. L., Ambrose, J. L., Attwood, A. R., Brown, S., Baker, K. R., Brock, C., Cohen, R. C., Edgerton, S., Farkas, C. M., Farmer, D., Goldstein, A. H., Gratz, L., Guenther, A., Hunt, S., Jaglé, L., Jaffe, D. A., Mak, J., McClure, C., Nenes, A., Nguyen, T. K., Pierce, J. R., de Sa, S., Selin, N. E., Shah, V., Shaw, S., Shepson, P. B., Song, S., Stutz, J., Surratt, J. D., Turpin, B. J., Warneke, C., Washenfelder, R. A., Wennberg, P. O., and Zhou, X. "Synthesis of the Southeast Atmosphere Studies: Investigating fundamental atmospheric chemistry questions." *Full. Amer. Meteor. Soc.* 99: 547–567, (2018).

Carroll, M. A., Bertman, S. B., and Shepson, P. B. "Overview of the program for research on oxidants: PHotochemistry, Emissions, and Transport (PROPHET) summer 1998 measurements intensive." *J. Geophys. Res.* 106: 24275–24288, (2001).

Cazorla, M., Wolfe, G. M., Bailey, S. A., Swanson, A. K., Arkinson, H. L., and Hanisco, T. F. "A new airborne laser-induced fluorescence instrument for in situ detection of formaldehyde throughout the troposphere and lower stratosphere." *Atoms. Meas. Tech.* 8: 541–552, (2015).

Chai, J.-D. and Head-Gordon, M. "Long-range corrected hybrid density functionals with damped atom-atom dispersion corrections." *Phys. Chem. Chem. Phys.* 10: 6615–6620, (2008).

Chang, W., Lee, M., and Heikes, B. G. "One-dimensional photochemical study of H_2O_2, CH_3OOH, and HCHO in the marine boundary layer during Pacific Exploratory Mission in the Tropics (PEM-Tropics) B." *J. Geophys. Res.* 109: D06307, (2004).

Chen, H., Karion, A., Rella, C. W., Winderlich, J., Gerbig, C., Filges, A., Newberger, T., Sweeny, C., and Tans, P. P. "Accurate measurements of carbon monoxide in humid air using the cavity ring-down spectroscopy (CRDS) technique." *Atmos. Meas. Tech.* 6: 1031–1040, (2013).

Claeys, M., Wang, W., Ion, A. C., Kourtchev, I., Gelencsér, A., and Maenhaut, W. "Formation of secondary organic aerosols from isoprene and its gas-phase oxidation products through reaction with hydrogen peroxide." *Atmos. Environ.* 38: 4093–4098, (2004).

Clark, T., Chandrasekhar, J., Spitznagel, G. W., and Schleyer, P. "Efficient diffuse function-augmented basis sets for anion calculations. III. The 3-21+G basis set for first-row elements, Li–F." *J. Comput. Chem.* 4: 294–301, (1983).

Cohan, D. S., Schultz, M. G., Jacob, D. J., Heikes, B. G., and Blake, D. R. "Convective injection and photochemical decay of peroxides in the tropical upper troposphere: methyl iodide as a tracer of marine convection." *J. Geophys. Res.* 104: 5717–5724, (1999).

Conner, Monroe. "DC-8 Program Overview." 2017. Accessed 29 April 2021. https://www.nasa.gov/centers/armstrong/aircraft/DC-8/overview.html

Crehuet, R., Anglada, J. M., and Bofill, J. M. "Tropospheric formation of hydroxymethyl hydroperoxide, formic acid, H_2O_2, and OH from carbonyl oxide in the presence of water vapor: a theoretical study of the reaction mechanism." *Chem. Eur. J.* 7: 2227–2235, (2001).

Crosson, E. R. "A cavity ring-down analyzer for measuring atmospheric levels of methane, carbon dioxide, and water vapor." *Applied Phys. B* 92: 403–408, (2008).

Crounse, J. D., McKinney, K. A., Kwan, A. J., and Wennberg, P. O. "Measurement of gas-phase hydroperoxides by chemical ionization mass spectrometry." *Anal. Chem.* 78: 6726–6732, (2006).

Crounse, J. D., Paulot, F., Kjaergaard, H. G., and Wennberg, P. O. "Peroxy radical isomerization in the oxidation of isoprene." *Phys. Chem. Chem. Phys.* 13: 13607–13613, (2011).

Crutzen, P. J. and Lawrence, M. G. "The impact of precipitation scavenging on the transport of trace gases: a 3-dimensional model sensitivity study." *J. Atmos. Chem.* 37: 81–112, (2000).

Cuchiara, G. C., Fried, A., Barth, M. C., Bela, M., Homeyer, C. R., Gaubert, B., Walega, J., Weibring, P., Richter, D., Wennberg, P., Crounse, J., Kim, M., Diskin, G., Hanisco, T. F., Wolfe, G. M., Beyersdorf, A., Peischl, J., Pollack, J. B., St. Clair, J. M., Woods, S., Tanelli, S., Bui, T. V., Dean-Day, J., Huey, L. G., and Heath, N. "Vertical transport, entrainment, and scavenging processes affecting trace gases in a modeled and observed SEAC^{4}RS case study." *J. Geophys. Res. Atmos.* 125: e2019JD031957, (2020).

DeCarlo, P. F., Kimmel, J. R., Trimborn, A., Northway, M. J., Jayne, J. T., Aiken, A. C., Gonin, M., Fuhrer, K., Horvath, T., Docherty, K. S., Worsnop, D. R., and Jimenez, J. L. "Field-deployable, high-resolution, time-of-flight aerosol mass spectrometer." *Anal. Chem.* 78: 8281–8289, (2006).

Devolder, P. "Atmospheric fate of small alkoxy radicals: recent experimental and theoretical advances." *J. Photochem. and Photobio. A: Chemistry* 157: 137–147, (2003).

Dunning, T. H. "Gaussian basis sets for use in correlated molecular calculations. I. The atoms boron through neon and hydrogen." *J. Chem. Phys.* 90: 1007–1023, (1989).

Dusanter, S., Vimal, D., Stevens, P. S., Volkamer, R., Molina, L. T., Baker, A., Meinardi, S., Blake, D., Sheehy, P., Merten, A., Zhang, R., Zheng, J., Fortner, E. C., Junkermann, W., Dubey, M., Rahn, T., Eichinger, B., Lewandowski, P.,

Prueger, J., and Holder, H. "Measurements of OH and HO_2 concentrations during the MCMA-2006 field campaign – Part 2: Model comparison and radical budget." *Atmos. Chem. Phys.* 9: 6655–6675, (2009).

Eckart, C. "The Penetration of a Potential Barrier by Electrons." *Phys. Rev.* 35: 1303–1309, (1930).

Eisfeld, W. and Francisco, J. S. "Excited states and photodissociation of hydroxymethyl hydroperoxide." *J. Chem. Phys.* 128: 174304, (2008).

Evans, M. G. and Polanyi, M. "Some applications of the transition state method to the calculation of reaction velocities, especially in solution." *Trans. Faraday Soc.* 31: 875–894, (1935).

Eyring, H. "The Activated Complex in Chemical Reactions." *J. Chem. Phys.* 3: 107–115, (1935).

Feiner, P. A., Brune, W. H., Miller, D. O., Zhang, L., Cohen, R. C., Romer, P. S., Goldstein, A. H., Keutsch, F. N., Skog, K. M., Wennberg, P. O., Nguyen, T. B., Teng, A. P., DeGouw, J., Koss, A., Wild, R. J., Brown, S. S., Guenther, A., Edgerton, E., Baumann, K., and Fry, J. L. "Testing atmospheric oxidation in an Alabama forest." *J. Atmos. Sci.* 73: 4699–4710, (2016).

Fels, M. and Junkermann, W. "The occurrence of organic peroxides in air at a mountain site." *Geophys. Res. Lett.* 21: 341–344, (1994).

Fenske, J. D., Hasson, A. S., Paulson, S. E., Kuwata, K. T., Ho, A., and Houk, K. N. "Pressure dependence of the OH radical yield from ozone–alkene reactions." *J. Phys. Chem.* 104: 7821–7833, (2000).

Fischer, H., Pozzer, A., Schmitt, T., Jöckel, P., Klippel, T., Taraborrelli, D., and Lelieveld, J. "Hydrogen peroxide in the marine boundary layer over the South Atlantic during the OOMPH cruise in March 2007." *Atmos. Chem. Phys.* 15: 6971–6980, (2015).

Fittschen, C. "The reaction of peroxy radicals with OH radicals." *Chem. Phys. Lett.* 725: 102–108, (2019).

Francisco, J. S. and Eisfeld, W. "Atmospheric oxidation mechanism of hydroxymethyl hydroperoxide." *J. Phys. Chem. A* 113: 7593–7600, (2009).

Frey, M. M., Stewart, R. W., McConnell, J. R., and Bales, R. C. "Atmospheric hydroperoxides in West Antarctica: Links to stratospheric ozone and atmospheric oxidation capacity." *J. Geophys. Res.* 110: D23301, (2005).

Frisch, M. J., Pople, J. A., and Binkley, J. S. "Self-consistent molecular orbital methods 25. Supplementary functions for Gaussian basis sets." *J. Chem. Phys.* 80: 3265–3269, (1984).

Frisch, M. J., Trucks, G. W., Schlegel, H. B., Scuseria, G. E., Robb, M. A., Cheeseman, J. R., Scalmani, G., Barone, V., Mennucci, B., Petersson, G. A., Nakatsuji, H., Caricato, M., Li, X., Hratchian, H. P., Izmaylov, A. F., Bloino, J., Zheng, G., Sonnenberg, J. L., Hada, M., Ehara, M., Toyota, K., Fukuda, R., Hasegawa, J., Ishida, M., Nakajima, T., Honda, Y., Kitao, O., Nakai, H., Vreven, T., Montgomery, J. A., Jr., Peralta, J. E., Ogliaro, F., Bearpark, M., Heyd, J. J., Brothers, E., Kudin, K. N., Staroverov, V. N., Kobayashi, R., Normand, J., Raghavachari, K., Rendell, A., Burant, J. C., Iyengar, S. S., Tomasi, J., Cossi, M., Rega, N., Millam, J. M., Klene, M., Knox, J. E., Cross, J. B., Bakken, V., Adamo, C., Jaramillo, J., Gomperts, R., Stratmann, R. E., Yazyev, O., Austin, A. J., Cammi, R., Pomelli, C., Ochterski, J. W., Martin, R. L., Morokuma, K., Zakrzewski, V. G., Voth, G. A., Salvador, P., Dannenberg, J. J., Dapprich, S., Daniels, A. D., Farkas, Ö., Foresman, J. B., Ortiz, J. V., Cioslowski, J., and Fox, D. J. "Gaussian 09 Revision D.01." 2009. Gaussian Inc. Wallingford CT 2009.

Fry, J. L., Matthews, J., Lane, J. R., Roehl, C. M., Sinha, A., Kjaergaard, H. G., and Wennberg, P. O. "OH-stretch vibrational spectroscopy of hydroxymethyl hydroperoxide." *J. Phys. Chem. A* 110: 7072–7079, (2006).

Gäb, S., Hellpointner, E., Turner, W. V., and Korte, F. "Hydroxymethyl hydroperoxide and bis(hydroxymethyl) peroxide from gas-phase ozonolysis of naturally occuring alkenes." *Nature* 316: 535–536, (1985).

Garden, A. L., Paulot, F., Crounse, J. D., Maxwell-Cameron, I. J., Wennberg, P. O., and Kjaergaard, H. G. "Calculation of conformationally weighted dipole moments useful in ion-molecule collision rate estimates." *Chemical Physics Letters* 474: 45–50, (2009).

George, I. J., Matthews, P. S. J., Whalley, L. K., Brooks, B., Goddard, A., Baeza-Romero, M. T., and Heard, D. E. "Measurements of uptake coefficients for heterogeneous loss of HO_2 onto submicron inorganic salt aerosols." *Phys. Chem. Chem. Phys.* 15: 12829–12845, (2013).

Glowacki, D. R., Liang, C.-H., Morley, C., Pilling, M. J., and Robertson, S. H. "MESMER: an open-source master equation solver for multi-energy well reactions." *J. Phys. Chem. A* 116: 9545–9560, (2012).

Griffith, S. M., Hansen, R. F., Dusanter, S., Stevens, P. S., Alaghmand, M., Bertman, S. B., Carroll, M. A., Erickson, M., Galloway, M., Grossberg, N., Hottle, J., Hou, J., Jobson, B. T., Kammrath, A., Keutsch, F. N., Lefer, B. L., Mielke, L. H., O'Brien, A., Shepson, P. B., Thurlow, M., Wallace, W., Zhang, N., and Zhou, X. L. "OH and HO_2 radical chemistry during PROPHET 2008 and CABINEX 2009 – Part 1: Measurements and model comparison." *Atmos. Chem. Phys.* 13: 5403–5423, (2013).

Guenther, A., Karl, T., Harley, P., Wiedinmyer, C., Palmer, P. I., and Geron, C. "Estimates of global terrestrial isoprene emissions using MEGAN (Model of

Emissions of Gases and Aerosols from Nature)." *Atmos. Chem. Phys.* 6: 3181–3210, (2006).

Halgren, T. A. "Merck molecular force field. I. Basis, form, scope, parameterization, and performance of MMFF94." *J. Comput. Chem.* 17: 490–519, (1996).

Hall, B. D. and Claiborn, C. S. "Measurements of the dry deposition of peroxides to a Canadian boreal forest." *J. Geophys. Res.* 102: 29343–29353, (1997).

Harvard, Atmospheric Chemistry Modeling Group. "GEOS-Chem." 2019. Online. `http://www.geos-chem.org`

Hasson, A. S., Ho, A. W., Kuwata, K. T., and Paulson, S. E. "Production of stabilized Criegee intermeidates and peroxides in the gas phase ozonolysis of alkenes: 2. asymmetric and biogenic alkenes." *J. Geophys. Res.* 106: 34143–34153, (2001a).

Hasson, A. S., Orzechowska, G., and Paulson, S. E. "Production of stabilized Criegee intermediates and peroxides in the gas phase ozonolysis of alkenes: 1. ethene, trans-2-butene, and 2,3-dimethyl-2-butene." *J. Geophys. Res.* 106: 34131–34142, (2001b).

Hehre, W. J., Ditchfield, R., and Pople, J. A. "Self-consistent molecular orbital methods. XII. Further extensions of Gaussian-Type basis sets for use in molecular orbital studies of organic molecules." *J. Chem. Phys.* 56: 2257–2261, (1972).

Heikes, B. G., Lee, M., Bradshaw, J., Sandholm, S., Davis, D. D., Crawford, J., Rodriguez, J., Liu, S., McKeen, S., Thornton, D., Bandy, A., Gregory, G., Talbot, R., Talbot, R., and Blake, D. "Hydrogen peroxide and methylhydroperoxide distributions related to ozone and odd hydrogen over the North Pacific in the fall of 1991." *J. Geophys. Res.* 101: 1891–1905, (1996).

Henon, E., Bohr, F., Sokolowski-Gomex, N., and Caralp, F. "Degradation of three oxygenated alkoxy radicals of atmospheric interest: $HOCH_2O^\bullet$, $CH_3OCH_2O^\bullet$, $CH_3OCH_2OCH_2O^\bullet$, RRKM theoretical study of the β-C-H bond scission and the 1,6-isomerisation kinetics." *Proc. Nat. Acad. Sci.* 5: 5431–5437, (2003).

Hermans, I., Müller, J.-F., Nguygen, T. L., Jacobs, P. A., and Peeters, J. "Kinetics of α-hydroxy-alkylperoxyl radicals in oxidation processes. $HO_2^\bullet$-initiated oxidation of ketones/aldehydes near the tropopause." *J. Phys. Chem. A* 109: 4303–4311, (2005).

Hewitt, C. N., Kok, G. L., and Fall, R. "Hydroperoxides in plants exposed to ozone mediate air pollution damage to alkene emitters." *Nature* 344: 56–58, (1990).

Hohorst, F. A., D., DesMarteau D., Anderson, L. R., Gould, D. E., and Fox, W. B. "Reactions of bis(trifluoromethyl) trixoide." *J. Am. Chem. Soc.* 95: 3866–3869, (1973).

Horie, O., Neeb, P., Limbach, S., and Moortgat, G. K. "Formation of formic acid and organic peroxides in the ozonolysis of ethene with added water vapour." *Geophys. Res. Lett.* 21: 1523–1526, (1994).

Hottmann, B., Hafermann, S., Tomsche, L., Marno, D., Martinez, M., Harder, H., Pozzer, A., Neumaier, M., Zahn, A., Bohn, B., Stratmann, G., Ziereis, H., Lelieveld, J., and Fischer, H. "Impact of the South Asian monsoon outflow on atmospheric hydroperoxides in the upper troposphere." *Atmos. Chem. Phys.* 20: 12655–12673, (2020).

Huang, D., Chen, Z. M., Zhao, Y., and Liang, H. "Newly observed peroxides and the water effect on the formation and removal of hydroxyalkyl hydroperoxides in the ozonolysis of isoprene." *Atos. Chem. Phys.* 13: 5671–5683, (2013).

Jacob, D. J., Liu, H., Mari, C., and Yantosca, R. M. "Harvard wet deposition scheme for GMI." *Harvard University Atmospheric Chemistry Modeling Group* online: 1–6, (2000).

Jacob, P and Klockow, D. "Hydrogen peroxide measurements in the marine atmosphere." *J. Atmos. Chem.* 15: 353–360, (1992).

Jaeglé, L., Jacob, D. J., Brune, W. H., Faloona, I., Tan, D., Heikes, B. G., Kondo, Y., Sachse, G. W., Anderson, B., Gregory, G. L., Singh, H. B., Pueschel, R., Ferry, G., Blake, D. R., and Shetter, R. E. "Photochemistry of HO_x in the upper troposphere at northern midlatitudes." *J. Geophys. Res.* 105: 3877–3892, (2000).

Jaeglé, L., Jacob, D. J., Wennberg, P. O., Spivakovsky, C. M., Hanisco, T. F., Lanzendorf, E. J., Hintsa, E. J., Fahey, D. W., Keim, E. R., Proffitt, M. H., Atlas, E. L., Flocke, F., Schauffler, S., McElroy, C. T., Midwinter, C., Pfister, L., and Wilson, J. C. "Observed OH and HO_2 in the upper troposphere suggest a major source from convective injection of peroxides." *Geophys. Res. Lett.* 24: 3181–3184, (1997).

Jenkin, M. E., Valorso, R., Aumont, B., and Rickard, A. R. "Estimation of rate coefficients and branching ratios for reactions of organic peroxy radicals for use in automated mechanism construction." *Atmos. Chem. Phys.* 19: 7691–7717, (2019).

Jobson, B. T, Frost, G. J., McKeen, S. A., Ryerson, T. B., Buhr, M. P., Parrish, D. D., Trainer, M., and Fehsenfeld, F. C. "Hydrogen peroxide dry deposition lifetime determined from observed loss rates in a power plant plume." *J. Geophys. Res.* 103: 22617–22628, (1998).

Keller, C. A., Long, M. S., Yantosca, R. M., Da Silva, A. M., Pawson, S., and Jacob, D. J. "HEMCO v1.0: a versatile, ESMF-compliant component for calculating emissions in atmospheric models." *Geosci. Model Dev.* 7: 1409–1417, (2014).

Kendall, R. A., Dunning, T. H., and Harrison, R. J. "Electron affinities of the first-row atoms revisited. Systematic basis sets and wave functions." *J. Chem. Phys.* 96: 6796–6806, (1992).

Kim, Y.-M., Lee, M., Chang, W., Lee, G., Kim, K.-R., and Kato, S. "Atmospheric peroxides over the North Pacific during IOC 2002 shipboard experiment." *Chemosphere* 69: 1638–1646, (2007).

Kirschke, S., Bousquet, P., Ciais, P., Saunois, M., Canadell, J. G., Dlugokencky, E. J., Bergamaschi, P., Bergmann, D., Blake, D. R., Bruhwiler, L., Cameron-Smith, P., Castaldi, S., Chevallier, F., Feng, L., Fraser, A., Heimann, M., Hodson, E. L., Houweling, S., Josse, B., Fraser, P. J., Krummel, P. B., Lamarque, J.-F., Langenfelds, R. L., Le Quéré, C., Naik, V., O'Doherty, S., Palmer, P. I., Pison, I., Plummer, D., Poulter, B., Prinn, R. G., Rigby, M., Ringeval, B., Santini, M., Schmidt, M., Shindell, D. T., Simpson, I. J., Spahni, R., Spahni, R., Steele, L. P., Strode, S. A., Sudo, K., Szopa, S., van der Werf, G. R., Voulgarakis, A., van Weele, M., Weiss, R. F., Williams, J. E., and Zeng, G. "Three decades of global methane sources and sinks." *Nat. Geo.* 6: 813–823, (2013).

Knizia, G., Adler, T. B., and Werner, H.-J. "Simplified CCSD(T)-F12 methods: Theory and benchmarks." *J. Chem. Phys.* 130: 54104, (2009).

Kroll, J. H. and Seinfeld, J. H. "Chemistry of secondary organic aerosol: Formation and evolution of low-volatility organics in the atmosphere." *Atmos. Environ.* 42: 3593–3624, (2008).

Kurtén, T., Rissanen, M. P., Mackeprang, K., Thornton, J. A., Hyttinen, N., Jørgensen, S., Ehn, M., and Kjaergaard, H. G. "Computational Study of Hydrogen Shifts and Ring-Opening Mechanisms in α-Pinene Ozonolysis Products." *J. Phys. Chem. A* 119: 11366–11375, (2015).

Lawrence, M. G. and Rasch, P. J. "Tracer transport in deep convective updrafts: plume ensemble versus bulk formulations." *J. Atmos. Sci.* 62: 2880–2894, (2005).

Lee, C., Yang, W., and Parr, R. G. "Development of the Colle-Salvetti correlation-energy formula into a functional of the electron density." *Phys. Rev. B* 37: 785–789, (1988).

Lee, J. H., Leahy, D. F., Tang, I. N., and Newman, L. "Measurement and speciation of gas phase peroxides in the atmosphere." *J. Geophys. Res.* 98: 2911–2915, (1993).

Lee, M., Heikes, B. G., and Jacob, D. J. "Enhancements of hydroperoxides and formaldehyde in biomass burning impacted air and their effect on atmospheric oxidant cycles." *J. Geophys. Res.* 103: 13201–13212, (1998).

Lee, M., Heikes, B. G., Jacob, D. J., Sachse, G., and Anderson, B. "Hydrogen peroxide, organic hydroperoxide, and formaldehyde as primary pollutants from biomass burning." *J. Geophys. Res.* 102: 1301–1309, (1997).

Lee, M., Heikes, B. G., and O'Sullivan, D. W. "Hydrogen peroxide and organic hydroperoxide in the troposphere: A review." *Atmos. Environ.* 34: 3475–3494, (2000).

Lelieveld, J., Butler, T. M., Crowley, J. N., Dillon, T. J., Fischer, H., Ganzeveld, L., Harder, H., Lawrence, M. G., Martinez, M., and Taraborrelli, D. "Atmospheric oxidation capacity sustained by a tropical forest." *Nature* 452: 737–740, (2008).

Li, Q., Jacob, D. J., Bey, I., Yantosca, R. M., Zhao, Y., Kondo, Y., and Notholt, J. "Atmospheric hydrogen cyanide (HCN): biomass burning source, ocean sink?" *Geophys. Res. Lett.* 27: 357–360, (2000).

Li, Q., Jacob, D. J., Yantosca, R. M., Heald, C. L., Singh, H. B., Koike, M., Zhao, Y., Sachse, G. W., and Streets, D. G. "A global three-dimensional model analysis of the atmospheric budgets of HCN and CH_3CN: Constraints from aircraft and ground measurements." *J. Geophys. Res.* 108: 8827, (2003).

Lin, S.-J. and Rood, R. B. "Multidimensional flux-form semi-lagrangian transport schemes." *Mon. Wea. Rev.* 124: 2046–2070, (1996).

Lind, J. A., Lazrus, A. L., and Kok, G. L. "Aqueous phase oxidation of sulfur(IV) by hydrogen peroxide, methylhydroperoxide, and peroxyacetic acid." *J. Geophys. Res.* 92: 4171–4177, (1987).

Link, M. F., Nguyen, T. B., Bates, K., Müller, J.-F., and Farmer, D. K. "Can isoprene oxidation explain high concentrations of atmospheric formic acid and acetic acid over forests?" *ACS Earth Space Chem.* 4: 730–740, (2020).

Luo, J., Jia, X., Gao, Y., Song, G., Yu, Y., Wang, R., and Pan, X. "Theoretical study on the kinetics of OH radical reactions with CH_3OOH and CH_3CH_2OOH." *J. Comp. Chem.* 32: 987–997, (2010).

Mao, J., Jacob, D. J., Evans, J. R., Olson, J. R., Ren, X., Brune, W. H., St. Clair, J. M., Crounse, J. D., Spencer, K. M., Beaver, M. R., Wennberg, P. O., Cubison, J. L., Jimenez, J. L., Fried, A., Weibring, P., Walega, J. G., Hall, S. R., Weinheimer, A. J., Cohen, R. C., Chen, G., Crawford, J. H., McNaughton, C., Clarke, A. D., Jaeglé, L., Fisher, J. A., Yantosca, R. M., Le Sager, P., and Carouge, C. "Chemistry of hydrogen oxide radicals (HO_x) in the Arctic troposphere in spring." *Atmos. Chem. Phys.* 10: 5823–5838, (2010).

Mao, J., Paulot, F., Jacob, D. J., Cohen, R. C., Crounse, J. D., Wennberg, P. O., Keller, C. A., Hudman, R. C., Barkley, M. P., and Horowitz, L. W. "Ozone and organic nitrates over the eastern United States: Sensitivity to isoprene chemistry." *J. Geophys. Res. Atmos.* 118: 11256–11268, (2013).

Mari, C., Jacob, D. J., and Bechtold, P. "Transport and scavenging of soluble gases in a deep convective cloud." *J. Geophys. Res.* 105: 22255–22267, (2000).

Marklund, S. "The simultaneous determination of bis(hydroxymethyl)peroxide (BHMP), hydroxymethylhydroproxide (HMP), and H_2O_2 with titanium(IV). Equilibria between the peroxides and the stabilities of HMP and BHMP at physiological conditions." *Acta Chem. Scand.* 25: 3517–3531, (1971).

Marteau, D. D. "Reaction of bis(fluoroxy)difluoromethane with cesium trifluoromethoxide." *Inorg. Chem.* 9: 2179–2181, (1970).

Martin, D., Tsivou, M., Bonsang, B., Abonnel, C., Carsey, T., Springer-Young, M., Pszenny, A., and Suhre, K. "Hydrogen peroxide int he marine atmospheric boundary layer during the Atlantic Stratocumulus Transition Experiment / Marine Aerosol and Gas Exchange experiment in the eastern subtropical North Atlantic." *J. Geosphys. Res.* 102: 6003–6015, (1997).

Matthews, J., Sinha, A., and Francisco, J. S. "The importance of weak absorption features in promoting tropospheric radical production." *Proc. Nat. Acad. Sci.* 102: 7449–7452, (2005).

Meagher, J. F., Olszyna, K. J., and Weatherford, F. P. "The availability of H_2O_2 and O_3 for aqueous phase oxidation of SO_2: The question of linearity." *Atmos. Environ.* 24A: 1825–1829, (1990).

Mehlhorn, H. "Ethylene-promoted ascorbate peroxidase activity protects plants against hydrogen peroxide, ozone and paraquat." *Plants and Environ.* 13: 971–976, (1990).

Millet, D. B., Baasandorj, M., Farmer, D. K., Thornton, J. A., Baumann, K., Brophy, P., Chaliyakunnel, S., de Gouw, J. A., Graus, M., Hu, L., Koss, A., Lee, B. H., Lopez-Hilfiker, F. D., Neuman, J. A., Paulot, F., Peischl, J., Pollack, I. B., Ryerson, T. B., Warneke, C., Williams, B. J., and Xu, J. "A large and ubiquitous source of atmospheric formic acid." *Atmos. Chem. Phys.* 15: 6283–6304, (2015).

Möller, D. "The possible role of H_2O_2 in new-type forest decline." *Atmos. Environ.* 23: 1625–1627, (1989).

Møller, K. H., Otkjær, R. V., Hyttinen, N., Kurtén, T., and Kjaergaard, H. G. "Cost-effective implementation of multiconformer transition state theory for peroxy radical hydrogen shift reactions." *J. Phys. Chem. A* 120: 10072–10087, (2016).

Møller, K. H., Praske, E., Xu, L., Crounse, J. D., Wennberg, P. O., and Kjaergaard, H. G. "Stereoselectivity in atmospheric autoxidation." *J. Phys. Chem. Lett.* 10: 6260–6266, (2019).

Morajkar, P., Schoemaecker, C., Okumura, M., and Fittschen, C. "Direct measurement of the equilibrium constants of the reaction of formaldehyde and acetaldehyde with HO_2 radicals." *Int. J. Chem. Kinet.* 46: 245–259, (2013).

Nakajima, M. and Endo, Y. "Observation of hydroxymethyl hydroperoxide in a reaction system containing CH_2OO and water vapor through pure rotational spectroscopy." *J. Chem. Phys.* 143: 164307, (2015).

Neeb, P., Sauer, F., Horie, O., and Moortgat, G. K. "Formation of hydroxymethyl hydroperoxide and formic acid in alkene ozonolysis in the presence of water vapour." *Atmos. Environ.* 31: 1417–1423, (1997).

Nguyen, T. B., Crounse, J. D., Schwantes, R. H., Teng, A. P., Bates, K. H., Zhang, X., St. Clair, J. M., Brune, W. H., Tyndall, G. S., Keutsch, F. N., Seinfeld, J. H., and Wennberg, P. O. "Overview of the Focused Isoprene eXperiment at the California Institute of Technology (FIXCIT): mechanistic chamber studies on the oxidation of biogenic compounds." *Atmos. Chem. Phys.* 14: 13531–13549, (2014).

Nguyen, T. B., Crounse, J. D., Teng, A. P., St. Clair, J. M., Paulot, F., Wolfe, G. M., and Wennberg, P. O. "Rapid deposition of oxidized biogenic compounds to a temperate forest." *Proc. Nat. Acad. Sci.* 112: E392–E401, (2015).

Nguyen, T. B., Tyndall, G. S., Crounse, J. D., Teng, A. P., Bates, K. H., Schwantes, R. H., Coggon, M. M., Zhang, L., Feiner, P., Miller, D. O., Skog, K. M., Rivera-Rios, J. C., Dorris, M., Olson, K. F., Koss, A., Wild, R. J., Brown, A. H., S. S. Goldstein, de Gouw, J. A., Brune, W. H., Keutsch, F. N., Seinfeld, J. H., and Wennberg, P. O. "Atmospheric fates of Criegee intermediates in the ozonolysis of isoprene." *Phys. Chem. Chem. Phys.* 18: 10241, (2016).

Niki, H., Maker, P. D., Savage, C. M., and Breitenback, L. P. "A Fourier transform infrared study of the kinetics and mechanism for the reaction HO + CH_3OOH." *J. Phys. Chem.* 87: 2190–2193, (1983).

Olson, J. R., Crawford, J. H., Brune, W., Mao, J., Ren, X., Fried, A., Anderson, B., Apel, E., Beaver, M., Blake, D., Chen, G., Crounse, J., Dibb, J., Diskin, G., Hall, S. R., Huey, L. G., Knapp, D., Richter, D., Riemer, D., St. Clair, J., Ullmann, K., Walega, J., Weibring, P., Weinheimer, A., Wennberg, P., and Wisthaler, A. "An analysis of fast photochemistry over high northern latitudes during spring and summer using in-situ observations from ARCTAS and TOPSE." *Atmos. Chem. Phys.* 12: 6799–6825, (2012).

Orlando, J. J. and Tyndall, G. S. "Laboratory studies of organic peroxy radical chemistry: an overview with emphasis on recent issues of atmospheric significance." *Chem. Soc. Rev.* 41: 6294–6317, (2012).

Ortega, J., Helmig, D., Guenther, A., Harley, P., Pressley, S., and Vogel, C. "Flux estimates and OH reaction potential of reactive biogenic volatile organic compounds (BVOCs) from a mixed northern hardwood forest." *Atmos. Environ.* 41: 5479–5495, (2006).

O'Sullivan, D. W., Heikes, B. G., Lee, M., Chang, W., Gregory, G. L., Blake, D. R., and Sachse, G. W. "Distribution of hydrogen peroxide and methyl hydroperoxide

over the Pacific and South Atlantic Oceans." *J. Geophys. Res.* 104: 5635–5646, (1999a).

———. "Distribution of hydrogen peroxide and methylhydroperixde over the Pacific and South Atlantic Oceans." *J. Geophys. Res.* 104: 5635–5646, (1999b).

O'Sullivan, D. W., Lee, M., Noone, B. C., and Heikes, B. G. "Henry's law constant determinations for hydrogen peroxide, methyl hydroperoxide, hydroxymethyl hydroperoxide, ethyl hydroperoxide, and peroxyacetic acid." *J. Phys. Chem* 100: 3241–3247, (1996).

Paulot, F., Crounse, J. D., Kjaergaard, H. G., Kroll, J. H., Seinfeld, J. H., and Wennberg, P. O. "Isoprene photooxidation: new insights into the production of acids and organic nitrates." *Atmos. Chem. Phys.* 9: 1479–1501, (2009a).

Paulot, F., Crounse, J. D., Kjaergaard, H. G., Kürten, A., St. Clair, J. M., Seinfeld, J. H., and Wennberg, P. O. "Unexpected expoxide formation in the gas-phase photooxidation of isoprene." *Science* 325: 730–733, (2009b).

Paulot, F., Wunch, D., Crounse, J. D., Toon, G. C., Millet, D. B., DeCarlo, P. F., Vigouroux, C., Deutscher, N. M., González Abad, G., Notholt, J., Warneke, T., Hannigan, J. W., Warneke, C., de Gouw, J. A., Dunlea, E. J., De Mazière, M., Griffith, D. W. T., Bernath, P., Jimenez, J. L., and Wennberg, P. O. "Importance of secondary sources in the atmospheric budgets of formic and acetic acids." *Atmos. Chem. Phys.* 11: 1989–2013, (2011).

Penkett, S. A., Jones, B. M. R., Brice, K. A., and Eggleton, A. E. J. "The importance of atmospheric ozone and hydrogen peroxide in oxidizing sulphur dioxide in cloud and rainwater." *Atmos. Environ.* 13: 123–137, (1979).

Penner, A. P. and Forst, W. "Analytic solution of relaxation in a system with exponential transition probabilities." *J. Chem. Phys.* 67: 5296–5307, (1977).

Perring, A. E., Wisthaler, A., Graus, M., Wooldridge, P. J., Lockwood, A. L., Mielke, L. H., Shepson, P. B., Hansel, A., and Cohen, R. C. "A product study of the isoprene+NO_3 reacton." *Atmos. Chem. Phys.* 9: 4945–4956, (2009).

Peterson, Kirk A., Adler, Thomas B., and Werner, Hans-Joachim. "Systematically convergent basis sets for explicitly correlated wavefunctions: The atoms H, He, B-Ne, and Al-Ar." *J. Chem. Phys.* 128: 84102, (2008).

Polle, A. and Junkermann, W. "Does atmospheric hydrogen peroxide contribute to damage to forest trees?" *Environ. Sci. Technol.* 28: 812–815, (1994a).

———. "Inhibition of apoplastic and symplastic peroxidase activity from Norway Spruce by the photooxidant hydroxymethyl hydroperoxide." *Plant Physiol.* 104: 617–621, (1994b).

Praske, E., Crounse, J. D., Bates, K. H., Kurtén, T., Kjaergaard, H. G., and Wennberg, P. O. "Atmospheric fate of methyl vinyl ketone: Peroxy radical reactions with NO and HO_2." *J. Phys. Chem. A* 119: 4562–4572, (2015).

Praske, E., Otkjaer, R. V., Crounse, J. D., Hethcox, J. C., Stoltz, B. M., Kjaergaard, H. G., and Wennberg, P. O. "Intramolecular hydrogen shift chemistry of hydroperoxy substituted peroxy radicals." *J. Phys. Chem. A* 123: 590–600, (2019).

Prather, M. J., Flynn, C. M., Zhu, X., Steenrod, S. D., Strode, S. A., Fiore, A. M., Correa, G., Murray, L. T., and Lamarque, J.-F. "How well can global chemistry models calculate the reactivity of short-lived greenhouse gases in the remote troposphere, knowing the chemical composition." *Atmos. Meas. Tech.* 11: 2653–2668, (2018).

Prather, M. J. and Jacob, D. J. "A persistent imbalance in HO_x and NO_x photochemistry of the upper troposphere driven by deep tropical convection." *Geophys. Res. Lett.* 24: 3189–3192, (1997).

Prather, M. J., Zhu, X., Flynn, C. M., Strode, S. A., Rodriquez, J. M., Steenrod, S. D., Liu, J., Lamarque, J.-F., Fiore, A. M., Horowitz, L. W., Mao, J., Murray, L. T., Shindell, D. T., and Wofsy, S. C. "Global atmospheric chemistry – which air matters." *Atmos. Chem. Phys.* 17: 9081–9102, (2017).

Qi, B., Chao, Y. T., and Chen, Z. M. "Mechanism and kinetics of the production of hydroxymethyl hydroperoxide in ethene/ozone/water gas-phase system." *Sci. China Ser. B-Chem* 50: 425–431, (2007).

Randerson, J. T., Chen, Y., van der Werf, G. R, Rogers, B. M., and Morton, D. C. "Global burned area and biomass burning emissions from small fires." *J. Geophys. Res.* 117: G04012, (2012).

Ravatta, F., Jacob, D. J., Brune, W. H., Heikes, B. G., Anderson, B. E., Blake, D. R., Gregory, G. L., Sachse, G. W., Sandholm, S. T., Shetter, R. E., Singh, H. B., and Talbot, R. W. "Experimental evidence for the importance of convected methylhydroperoxide as a source of hydrogen oxide (HO_x) radicals in the tropical upper troposphere." *J. Geophys. Res.* 106: 32709–32716, (2001).

Reeves, C. E. and Penkett, S. A. "Measurements of peroxides and what they tell us." *Chem. Rev.* 103: 5199–5218, (2003).

Rinsland, C. P., Coheur, P. F., Herbin, H., Clerbaux, C., Boone, C., Bernath, P., and Chiou, L. S. "Detection of elevated tropospheric hydrogen peroxide (H_2O_2) mixing ratios in atmospheric chemistry experiment (ACE) subtropical infrared solar occultation spectra." *J. Quant. Spectrosc. Radiat. Transfer* 107: 340–348, (2007).

Roberts, G., Wooster, M. J., and Lagoudakis, E. "Annual and diurnal african biomass burning temporal dynamics." *Biogeosciences* 6: 849–866, (2009).

Roehl, C. M., Marka, Z., Fry, J. L., and Wennberg, P. O. "Near-UV photolysis cross sections of CH_3OOH and $HOCH_2OOH$ determined via action spectroscopy." *Atmos. Chem. Phys.* 7: 713–720, (2007).

Sander, S. P., Abbatt, J., Barker, J. R., Burkholder, J. B., Friedl, R. R., Golden, D. M., Huie, R. E., Kolb, C. E., Kurylo, M. J., Moortgat, G. K., Orkin, V. L., and Wine, P. H. "Chemical kinetics and photochemical data for use in atmospheric studies, evaluation no. 17." JPL Publication 10-6, Jet Propulsion Laboratory, Pasadena, 2011.

Sandermann, H. Jr., Ernst, D., Heller, W., and Langebartels, C. "Ozone: an abiotic elicitor of plant defense reactions." *Trends Plant Sci.* 3: 47–50, (1998).

Sauer, F., Schäfer, C., Neeb, P., Horie, O., and Moortgat, G. K. "Formation of hydrogen peroxide in the ozonolysis of isoprene and simple alkenes under humid conditions." *Atmos. Environ.* 33: 229–241, (1999).

Schill, G. P., Froyd, K. D., Bian, H., Kupc, A., Williamson, C., Brock, C. A., Ray, E., Hornbrook, R. S., Hills, A. J., Apel, E. C., Chin, M., Colarco, P. R., and Murphy, D. M. "Widespread biomass burning smoke throughout the remote troposphere." *Nat. Geosci.* 13: 422–427, (2020).

Seinfeld, J. H. and Pandis, S. N. *Atmospheric chemistry and physics: from air pollution to climate change*. Hoboken, N.J.: Wiley, 2006, 2nd ed.

Sharpe, S. W., Johnson, T. J., Sams, R. L., Che, P. M., Rhoderick, G. C., and Johnson, P. A. "Gas-phase databases for quantitative infrared spectroscopy." *Appl. Spectrosc.* 58: 1452–1461, (2004).

Singh, H. B., Salas, L., Herlth, D., Koyler, R., Czech, E., Viezee, W., Li, Q., Jacob, D. J., Blake, D., Sachse, G., Harward, C. N., Fuelberg, H., Kiley, C. M., Zhao, Y., and Kondo, Y. "In situ measurements of HCN and CH_3CN over the Pacific Ocean: sources, sinks, and budgets." *J. Geophys. Res.* 108: 8795, (2003).

Slemr, F. and Tremmel, H. G. "Hydroperoxides in the marine troposphere over the Atlantic Ocean." *J. Atmos. Chem.* 19: 371–404, (1994).

Snow, J. A., Heikes, B. G., Merrill, J. T., Wimmers, A. J., Moody, J. L., and Cantrell, C. A. "Winter-spring evolution and variability of HO_x reservoir species, hydrogen peroxide, and methyl hydroperoxide, in the northern middle to high latitudes." *J. Geophys. Res.* 108: 8362, (2003).

Snow, J. A., Heikes, B. G., Shen, H., O'Sullivan, D. W., Fried, A., and Walega, J. "Hydrogen peroxide, methyl hydroperoxide, and formaldehyde over North America and the North Atlantic." *J. Geophys. Res.* 112: D12S07, (2007).

Sommariva, R., Haggerstone, A.-L., Carpenter, L. J., Carslaw, N., Creasey, D. J., Heard, D. E., Lee, J. D., Lewis, A. C., Pilling, M. J., and Zádor, J. "OH and

HO_2 chemistry in clean marine air during SOAPEX-2." *Atmos. Chem. Phys.* 4: 839–856, (2004).

St. Clair, J. M., McCabe, D. C., Crounse, J. D., Steiner, U., and Wennberg, P. O. "Chemical ionization tandem mass spectrometer for the in situ measurement of methyl hydrogen peroxide." *Rev. Sci. Instru.* 81: 094102, (2010).

St. Clair, J. M., Rivera-Rios, J. C., Crounse, J. D., Knap, H. C., Bates, K. H., Teng, A. P., Jørgensen, S., Kjaergaard, H. G., Keutsch, F. N., and Wennberg, P. O. "Kinetics and products of the reaction of the first-generation isoprene hydroxy hydroperoxide (ISOPOOH) with OH." *J. Phys. Chem. A* 120: 1441–1451, (2016a).

St. Clair, J. M., Rivera-Rios, J. C., Crounse, J. D., Praske, E., Kim, M. J., Wolfe, G. M., Keutsch, F. N., Wennberg, P. O., and Hanisco, T. F. "Investigation of a potential HCHO measurement artifact from ISOPOOH." *Atmos. Meas. Tech.* 9: 4561–4568, (2016b).

Stavrakou, T., Müller, J.-F., Peeters, J., Razavi, A., Clarisse, L., Clerbaux, C., Coheur, P.-F., Hurtmans, D., De Maziére, M., Vigouroux, C., Deutscher, N. M., Griffith, D. W. T., Jones, N., and Paton-Walsh, C. "Satellite evidence for a large source of formic acid from boreal and tropical forests." *Nat. Geosci.* 5: 26–30, (2012).

Stickler, A., Fischer, H., Bozem, H., Gurk, C., Schiller, C., Martinex-Harder, M., Kubistin, D., Harder, H., Williams, J., Eerdekens, G., Yassaa, N., Ganzeveld, L., Sander, R., and Lelieveld, J. "Chemistry, transport and dry deposition of trace gases in the boundary layer over the tropical Atlantic Ocean and the Guyanas during the GABRIEL field campaign." *Atmos. Chem. Phys.* 7: 3933–3956, (2007).

Stone, D., Whalley, L. K., and Heard, D. E. "Tropospheric OH and HO_2 radicals: field measurements and model comparisons." *Chem. Soc. Rev.* 41: 6348–6404, (2012).

Su, F., Calvert, J. G., and Shaw, J. H. "Mechanism of the photooxidation of gaseous formaldehyde." *J. Phys. Chem.* 83: 3185–3191, (1979).

Su, T. and Chesnavich, W. J. "Parameterization of the ion-polar molecule collision rate constant by trajectory calculations." *J. Chem. Phys.* 76: 5183–5183, (1982).

Taylor, W. D., Allston, T. D., Moscato, M. J., Fazekas, G. B., Kozlowski, R., and Takacs, G. A. "Atmospheric photo-dissociation lifetimes for nitromethane, methyl nitrite, and methyl nitrate." *Int. J. Chem. Kinet.* 12: 231–240, (1980).

Teng, A. P., Counse, J. D., Lee, L., St. Clair, J. M., Cohen, R. C., and Wennberg, P. O. "Hydroxy nitrate production in the OH-initiated oxidation of alkenes." *Atmos. Chem. Phys.* 15: 4297–4316, (2015).

Teng, A. P., Crounse, J. D., and Wennberg, P. O. "Isoprene peroxy radical dynamics." *J. Am. Chem. Soc.* 139: 5367–5377, (2017).

Thornton, J. and Abbatt, P. D. "Measurements of HO_2 uptake to aqueous aerosol: Mass accommodation coefficients and net reactive loss." *J. Geophys. Res.* 110: D08309, (2005).

Thornton, J. A., Jaeglé, L., and McNeill, V. F. "Assessing known pathways for HO_2 loss in aqueous atmospheric aerosols: Regional and global impacts on tropospheric oxidants." *J. Geophys. Res.* 113: D05303, (2008).

Travis, K. R., Heald, C. L., Allen, H. M., Apel, E. C., R., Arnold. S., Blake, D. R., Brune, W. H., Chen, X., Commane, R., Crounse, J. D., Daube, B. C., Diskin, G> S., Elkins, J. W., Evans, M. J., Hall, S. R., Hintsa, E. J., Hornbrook, R. S., Kasibhatla, P. S., Kim, M. J., Luo, G., McKain, K., Millet, D. B., Moore, F. L., Peischl, J., Ryerson, T. B., Sherwen, T., Thames, A. B., Ullmann, K., Wang, X., Wennberg, P. O., Wolfe, G. M., and Yu, F. "Constraining remote oxidation capacity with ATom observations." *Atmos. Chem. Phys.* 20: 7753–7781, (2020).

Turner, A. J., Frankenberg, C., and Kort, E. A. "Interpreting contemporary trends in atmospheric methane." *Proc. Nat. Acad. Sci.* 116: 2805–2813, (2019).

Vaghjiani, G. L. and Ravishankara, A. R. "Kinetics and mechanism of OH reaction with CH_3OOH." *J. Phys. Chem.* 93: 1948–1959, (1989).

Van Valin, C. C., Ray, J. D., Boatman, J. F., and Gunter, R. L. "Hydrogen peroxide in air during winter over the south-central United States." *Geophys. Res. Lett.* 14: 1146–1149, (1987).

Vereecken, L. and Peeters, J. "The 1,5-H-shift in 1-butoxy: A case study in the rigorous implementation of transition state theory for a multirotamer system." *J. Chem. Phys.* 119: 5159–5170, (2003).

Veyret, B., Lesclaux, R., Rayez, M.-T., Cox, R. A., and Moortgat, G. K. "Kinetics and mechanism of the photooxidation of formaldehyde. 1. Flash photolysis study." *J. Phys. Chem.* 93: 2368–2374, (1989).

Veyret, B., Rayez, J.-C., and Lesclaux, R. "Mechanism of the photooxidation of formaldehyde studied by flash photolysis of CH_2O-O_2-NO mixtures." *J. Phys. Chem.* 86: 3424–3430, (1982).

Veyret, B., Roussel, P., and Lesclaux, R. "Mechanism of the chain process forming H_2 in the photooxidation of formaldehyde." *Int. J. Chem. Kinet.* 16: 1599–1608, (1984).

Walcek, C. J. "A theoretical estimate of O_3 and H_2O_2 dry deposition over the northeast United States." *Atmos. Environ.* 21: 2649–2659, (1987).

Wang, W., Kourtchev, I., Graham, B., Cafmeyer, J., Maenhaut, W., and Claeys, M. "Characterization of oxygenated derivatives of isoprene related to 2-methyltetrols in Amazonian aerosols using trimethylsilylation and gas chromatography/ion trap mass spectrometry." *Rapid Commun. Mass Spectrom.* 19: 1343–1351, (2005).

Watts, J. D., Gauss, J., and Bartlett, R. J. "Coupled-cluster methods with noniterative triple excitations for restricted open-shell Hartree-Fock and other general single determinant reference functions. Energies and analytical gradients." *J. Chem. Phys.* 98: 8718–8733, (1993).

Weinstein-Lloyd, J. B., Lee, J. H., Daum, P. H., Kleinman, L. I., Nunnermacker, L. J., Springston, S. R., and Newman, L. "Measurements of peroxides and related species during the 1995 summer intensive of the Southern Oxidants Study in Nashville, Tennessee." *J. Geophys. Res.* 103: 22361–22373, (1998).

Weller, R. and Schrens, O. "H_2O_2 in the marine troposphere and seawater of the Atlantic Ocean (48° – 63°)." *Geophys. Res. Lett.* 20: 125–128, (1993).

Werner, H.-J., Knizia, G., and Manby, F. R. "Explicitly correlated coupled cluster methods with pair-specific geminals." *Mol. Phys.* 109: 407–417, (2011).

Werner, H.-J., Knowles, P. J., Knizia, G., Manby, F. R., Schütz, M., Celani, P., Györffy, W., Kats, D., Korona, T., Lindh, R., Mitrushenkov, A., Rauhut, G., Shamasundar, K. R., Adler, T. B., Amos, R. D., Bernhardsson, A., Berning, A., Cooper, D. L., Deegan, M. J. O., Dobbyn, A. J., Eckert, F., Goll, E., Hampel, C., Hesselmann, A., Hetzer, G., Hrenar, T., Jansen, G., Köppl, C., Liu, Y., Lloyd, A. W., Mata, R. A., May, A. J., McNicholas, S. J., Meyer, W., Mura, M. E., Nicklass, A., O'Neill, D. P., Palmieri, P., Peng, D., Pflüger, K., Pitzer, R., Reiher, M., Shiozaki, T., Stoll, H., Stone, A. J., Tarroni, R., Thorsteinsson, T., and Wang, M. "MOLPRO, version 2012.1, a package of ab initio programs." 2012. See http://www.molpro.net.

Westberg, H., Lamb, B., Hafer, R., Hills, A., Shepson, P., and Vogel, C. "Measurement of isoprene fluxes at the PROPHET site." *J. Geophys. Res.* 106: 24347–24358, (2001).

Whalley, L. K., Furneaux, K. L., Goddard, A., Lee, J. D., Mahajan, A., Oetjen, H., Read, K. A., Kaaden, N., Carpenter, L. J., Lewis, A. C., Plane, J. M. C., Saltzman, E. S., Wiedensohler, A., and Heard, D. E. "The chemistry of OH and HO_2 radicals in the boundary layer over the tropical Atlantic Ocean." *Atmos. Chem. Phys.* 10: 1555–1576, (2010).

Winkelman, J. G. M., Voorwinde, O. K., Ottens, M., Beenackers, A. A. C. M., and Janssen, L. P. B. M. "Kinetics and chemical equilibrium of the hydration of formaldehyde." *Chem. Eng. Sci.* 57: 4067–4076, (2002).

Xu, L., Møller, K. H., Crounse, J. D., Otkjaer, R. V., Kjaergaard, H. G., and Wennberg, P. O. "Unimolecular reactions of peroxy radicals formed in the oxidation of α-pinene and β-pinene by hydroxyl radicals." *J. Phys. Chem. A* 123: 1661–1674, (2019).

Yokelson, R. J., Crounse, J. D., DeCarlo, P. F., Karl, T., Urbanski, S., Atlas, E., Campos, T., Shinozuka, Y., Kapustin, V., Clarke, A. D., Weinheimer, A., Knapp, D. J., Montzka, D. D., Holloway, J., Weibring, P., Flocke, F., Zheng, W., Toohey, D., Wennberg, P. O., Wiedinmyer, C., Mauldin, L., Fried, A., Richter, D., Walega, J., Jimenez, J. L., Adachi, K., Buseck, P. R., Hall, S. R., and Shetter, R. "Emissions from biomass burning in the Yucatan." *Atmos. Chem. Phys.* 9: 5785–5812, (2009).

York, D., Evensen, N. M., Martínez, M. L., and Delgado, J. D. B. "Unified equations for the slope, intercept, and standard errors of the best straight line." *Am. J. Phys.* 72: 367–375, (2004).

Zhang, B., Liu, H., Crawford, J. H., Chen, G., Fairlie, D., Chambers, S., Kang, C.-H., Williams, A. G., Zhang, K., Considine, D. B., Sulprizio, M. P., and Yantosca, R. M. "Simulation of radon-222 with the GEOS-Chem model: Emissions, seasonality, and convective transport." *Atmos. Chem. Phys.* 21: 1861–1887, (2021).

Zhang, Q., Jimenez, J. L., Canagaratna, M. R., Allan, J. D., Coe, H., Ulbrich, I., Alfarra, M. R., Takami, A., Middlebrook, A. M., Sun, Y. L., Dzepina, K., Dunlea, E., Docherty, K., DeCarlo, P. F., Salcedo, D., Onasch, T., Jayne, J. T., Miyoshi, T., Shimono, A., Katakeyama, S., Takegawa, N., Kondo, Y., Schneider, J., Drewnick, F., Borrmann, S., Weimer, S., Demerjian, K., Williams, P., Bower, K., Bahreini, R., Cottrell, L., Griffin, R. J., Rautiainen, J., Y., Sun. J., Zhang, Y. M., and Worsnop, D. R. "Ubiquity and dominance of oxygenated species in organic aerosols in anthropogenically-influenced Northern Hemisphere midlatitudes." *Geophys. Res. Lett.* 34: L13801, (2007).

Zhou, X. and Lee, Y.-N. "Aqueous solubility and reaction kinetics of hydroxymethyl hydroperoxide." *J. Phys. Chem.* 96: 265–272, (1992).

Appendix A

LOW-PRESSURE GAS CHROMATOGRAPHY WITH CHEMICAL IONIZATION MASS SPECTROMETRY FOR QUANTIFICATION OF MULTIFUNCTIONAL ORGANIC COMPOUNDS IN THE ATMOSPHERE

Published as:
Vasquez, K. T., H. M. Allen, J. D. Crounse, E. Praske, L. Xu, A. C. Noelscher, and P. O. Wennberg (2018). "Low-pressure gas chromatography with chemical ionization mass spectrometry for quantification of multifunctional organic compounds in the atmosphere". In: *Atmos. Meas. Tech.*, 11, pp. 6815–6832. DOI: 10.5194/amt-11-6815-2018.

A.1 Abstract

Oxygenated volatile organic compounds (OVOCs) are formed during the oxidation of gas-phase hydrocarbons in the atmosphere. However, analytical challenges have hampered ambient measurements for many of these species, leaving unanswered questions regarding their atmospheric fate. We present the development of an in situ gas chromatography (GC) technique that, when combined with the sensitive and specific detection of chemical ionization mass spectrometry (CIMS), is capable of the isomer-resolved detection of a wide range of OVOCs. The instrument addresses many of the issues typically associated with chromatographic separation of such compounds (e.g., analyte degradation). The performance of the instrumentation is assessed through data obtained in the laboratory and during two field studies. We show that this instrument is able to successfully measure otherwise difficult-to-quantify compounds (e.g., organic hydroperoxides and organic nitrates) and observe the diurnal variations in a number of their isomers.

A.2 Introduction

The composition of the atmosphere is determined through a dynamic array of chemical emission, transport, deposition, and photochemical processing. Our ability to accurately predict future trends in both air quality and climate change depends on understanding these processes. Of particular interest is the photooxidation of non-methane hydrocarbons (NMHCs), which influence the distributions of key at-

mospheric constituents such as ozone (O3) and secondary organic aerosol (SOA). While decades of research have provided much insight into the link between atmospheric composition and chemistry, significant knowledge gaps still persist and the atmospheric degradation pathways of many NMHCs remain poorly understood.

The gas-phase oxidation of NMHCs is typically initiated by one of several atmospheric oxidants (i.e., OH, NO_3, or O_3) converting these hydrocarbons into oxygen-containing, often multifunctional, intermediates. These first-generation oxygenated volatile organic compounds, or OVOCs, can undergo further transformations through a number of competing physical and photochemical sinks (Atkinson and Arey, 2003; Mellouki et al., 2015), each of which can have a unique effect on the atmosphere. Some OVOCs can undergo photochemical fragmentation to smaller species, often through conversion of NO to NO_2 leading to local ozone formation, while others (such as those with longer atmospheric lifetimes) can be transported downwind prior to oxidation, extending their effects to regional and global scales. Chemical oxidation can also cause OVOCs to increase their functionality, creating large low-volatility, multifunctional products that partition into the particle phase and contribute to the formation and growth of aerosol. In addition, it has been shown that significant portions of OVOCs can be removed from the atmosphere through fast deposition processes (Nguyen et al., 2015), which can greatly affect the chemical cycling of many important compounds.

It is the relative importance of each possible sink that establishes the dominant tropospheric fate of these compounds and thereby the impact of their hydrocarbon precursors (Koppmann and Wildt, 2008). This seemingly straightforward relationship can quickly become complicated, however, especially for larger compounds (>C3). A prime example of this can be seen during the OH oxidation of isoprene, a highly abundant and reactive biogenic VOC, which produces six isomeric peroxy radicals (RO_2). Changes in the relative abundance of these radicals can result in vastly different ratios of its OVOC products (Orlando and Tyndall, 2012; Teng et al., 2017; Wennberg et al., 2018), allowing isoprene to have a profound effect on ozone or SOA through its bimolecular reaction products — isoprene hydroxy nitrates (IHNs) and isoprene hydroxy hydroperoxides (ISOPOOHs), respectively — or the OH radical that is recycled during the subsequent chemistry of products formed from the unimolecular RO_2 reaction channel (e.g., hydroperoxy aldehydes or HPALDs; Peeters et al., 2014). These structural effects are also apparent throughout the later-generation chemistry of isoprene and other NMHCs and the outputs

of global chemistry transport models can be quite sensitive to this isomer-specific chemistry. For example, ozone production, in particular, has been shown to be highly dependent on the assumed yields and reaction rates of specific organic nitrate isomers (Squire et al., 2015), which together determine the net NO_x recycling capabilities of each compound.

Despite its importance, our understanding of this intricate chemistry has been hindered by the lack of instrumentation capable of providing isomer-resolved measurements of important OVOCs. Recent progress has been made in this respect for laboratory studies (e.g., Bates et al., 2014, 2016; Lee et al., 2014; Teng et al., 2015, 2017; Schwantes et al., 2015; Praske et al., 2015, 2018). Analytical techniques for ambient measurements, however, suffer from either high detection limits and/or large instrumental losses of these reactive analytes (Vairavamurthy et al., 1992; Apel et al., 2003, 2008; Clemitshaw, 2004), and so the focus has typically been on smaller, more abundant compounds (Mellouki et al., 2003; Goldan et al., 2004; Koppmann and Wildt, 2008; Hellén et al., 2017).

Gas chromatography (GC) can reach the detection limits needed to measure a variety of larger OVOCs by preconcentrating analytes prior to separation and utilizing detection methods such as flame ionization detection (FID) or electron impact mass spectrometry (EI-MS) (Ras et al., 2009). As a result, this technique is increasingly popular and has been or is currently being developed for the in situ detection of carbonyls (Apel et al., 2003; Zhao et al., 2013), organic acids (Hellén et al., 2017), organic nitrates (Mills et al., 2016), and other oxygenated organic compounds (e.g., Clemitshaw, 2004; Millet et al., 2005; Goldan et al., 2004; Koppmann and Wildt, 2008; Roukos et al., 2009; Lerner et al., 2017). Nevertheless, these field-deployable GC techniques come with their own analytical challenges as the non-specificity of common detectors such as GC-FID and overall difficulty in differentiating fragmentation patterns of isobaric and isomeric species with GC-MS can create data sets that hide the intricacies of crucial structure-activity relationships of individual compounds. In addition, the multifunctional nature of these compounds makes them highly reactive, increasing the likelihood that they will be lost or converted into different species through surface-enhanced reactions that can occur at various stages of GC analysis. Converted species can be subsequently detected (e.g., Rivera-Rios et al., 2014); thus identifying such artifacts necessitates authentic calibrations even for species not being targeted. Due to the lack of commercially available standards for many species of interest, this can quickly become labor intensive or simply not

feasible, leading to large uncertainties in these types of measurements and much confusion regarding chemical mechanism elucidation.

Table A.1: Examples of OVOCs measured in this study.

Compound	Abbreviation	Example structure
Isoprene hydroxy nitrate	IHN	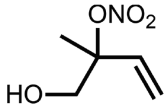
Isoprene hydroxy hydroperoxide	ISOPOOH	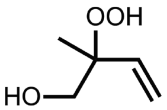
Isoprene epoxydiol	IEPOX	
Isoprene hydroxyperoxy aldehyde	HPALD	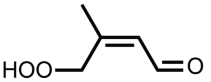
Isoprene carbonyl nitrate	ICN	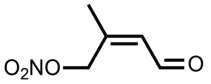
Propene hydroxy nitrate	Propene HN	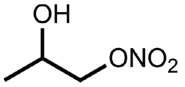
Butene hydroxy nitrate	Butene HN	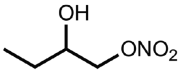
Propanone nitrate	PROPNN	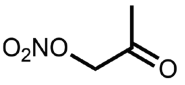
Hydroxymethyl hydroperoxide	HMHP	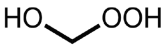

Here, we present the development and deployment of a new GC method that uses the highly sensitive detection of chemical ionization mass spectrometry (CIMS) for the near-real-time detection of a number of OVOCs. With this instrumentation, we address many of the historical issues associated with the use of GC for atmospheric field sampling, allowing for the preservation of difficult-to-measure compounds and enabling isomer-resolved measurements of a wide array of compounds. Compounds discussed in this study are shown in Table A.1. To distinguish among isomers of hydroxynitrates, ISOPOOH, HPALD, and isoprene carbonyl nitrates (ICNs), we employ an abbreviated naming scheme in which the first number denotes the carbon position where the oxidant originally adds to the parent alkene and the second denotes the position of the additional functional group (e.g., for 1,2-IHN the hydroxy group is located on the first carbon of the isoprene backbone (C1), followed by a nitrooxy

group at C2).

A.3 Instrument Description

The GC high-resolution time-of-flight (HRToF) CIMS integrates the use of a metal-free, low-pressure gas chromatography (LP-GC) instrument positioned upstream of a HRToFCIMS (Tofwerk and Caltech). This combination allows for two main sampling modes: (1) direct atmospheric sampling for the real-time quantification of gas-phase species (hereafter, direct CIMS sampling) and (2) GC-CIMS analysis for the collection, separation, and quantification of ambient isomer distributions of select OVOCs. The overall design of this instrumentation is based upon an existing test bed that has been used in previous laboratory studies (e.g., Bates et al., 2014; Lee et al., 2014; Teng et al., 2015, 2017; Schwantes et al., 2015). However, in those studies, the GC prototype required a short length of the column to be manually submerged into a chilled isopropanol bath, a setup that is cumbersome, if not impossible, to use outside of a laboratory setting. These studies were also performed under very low humidities. Here, we have field-hardened this design such that GC operation is automated and chromatography is reproducible under a variety of field conditions. A simplified schematic of the GC-HRToF-CIMS is shown in Fig. A.1, highlighting the main flow paths of direct CIMS sampling (orange) as well as GC trapping (blue and purple) and eluting (red and purple). Details of the GC automation are discussed in Sect. A3.

HRToF-CIMS

The HRToF-CIMS builds upon methods developed with a previous custom-built quadrupole CIMS (Crounse et al., 2006, later upgraded to a cToF-CIMS). Ambient air is drawn at high flow rate (~2000 slpm, P ~1 atm) through a custom Teflon-coated glass inlet (3.81 cm I.D. × 76.2 cm long; Fig. A.1B). A small fraction of this flow is subsampled perpendicular to the main flow in order to discriminate against large particles and debris and directed to the CIMS, the GC, or a zeroing system through short lengths of 6.35mm O.D. PFA tubing. When measured directly by the CIMS, ambient air, diluted with dry N2, flows through a fluoropolymercoated (Cytonix PFC801A) glass flow tube (Fig. A.1F) to ensure a well-mixed gas stream prior to chemical ionization by CF_3O^- reagent ions (m/z 85). The flow tube pressure is held at 35 mbar and samples ambient air at a constant flow rate of 180 sccm as regulated by a critical orifice (Fig. A.1G). This ambient air is then diluted by a factor of 10 with dry N2 (Fig. A.1I). Two valves located upstream of this orifice

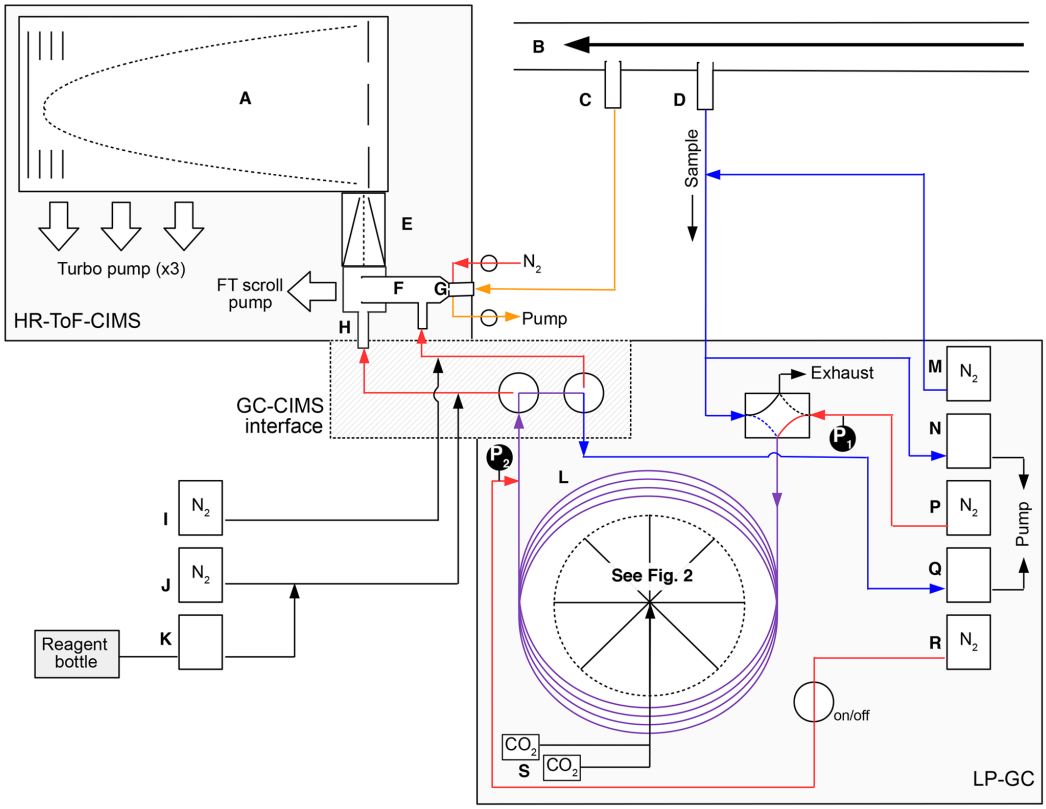

Figure A.1: A simplified instrument schematic of GC-HRToF-CIMS showing the HRToF-CIMS, the LP-GC, and the interface between the two systems. The main components are (A) time-of-flight mass spectrometer, (B) Teflon-coated glass inlet, (C) CIMS sampling port, (D) GC-CIMS sampling port, (E) hexapole ion guide, (F) Teflon-coated glass flow tube, (G) critical orifice, (H) 210-Po ionization source, (I) CIMS dilution flow, (J) CIMS ion source dilution flow, (K) CF_3OOCF_3 reagent flow, (L) GC column and cryotrap, (M) GC dilution flow, (N) GC sample intake pump, (P) GC column flow, (Q) GC bypass pump, (R) GC N2 pickup flow, and (S) CO2 solenoid valves. Pressure gauges at the head and tail of the column are denoted by P1 and P2, respectively. Select instrument flow states are differentiated by the various line colors, for which orange represents the flow path during direct CIMS sampling, blue represents the path GC trapping, and red represents the path during GC elution. Analytical lines that are used during both GC trapping and eluting are purple. Diagram is not to scale.

ensure a constant mass flow through the flow tube by pumping on the inlet (×0.5 slpm). When the instrument switches to a different analysis mode (e.g., performs a GC or zeroes), these valves are toggled to overfill the flow tube with dry nitrogen and prevent ambient air from being sampled through this flow path.

The CF_3O^- ion chemistry has been described in detail elsewhere (Huey et al., 1996; Amelynck et al., 2000a, b; Crounse et al., 2006; Paulot et al., 2009a, b; St. Clair et al., 2010; Hyttinen et al., 2018). Briefly, CF_3O^- is formed by passing 380 sccm of 1 ppmv CF_3OOCF_3 in N_2 through a cylindrical tube (Fig. A.1H) containing a layer of polonium-210 (NRD LLC P-2021, initial activity: 370 MBq). Alpha particles produced from the radioactive decay of the polonium react with the N_2 gas to produce electrons that react rapidly with CF_3OOCF_3 to produce CF_3O^- ions, which, in turn, react with analytes by forming clusters (m/z = analyte mass + 85) or fluoride-transfer (m/z = analyte mass + 19) product ions. This method allows for the detection of small organic acids and other oxygenated multifunctional compounds with high sensitivity (LOD ~ 10 pptv during direct sampling for 1 s integration period) and minimal fragmentation.

Following ionization, the ions are directed via a conical hexapole ion guide into the high-resolution mass spectrometer (Tofwerk), which collects data for masses between m/z 19 and m/z 396 at 10 Hz time resolution. The HRToF-CIMS has a mass resolving power of 3000 m/1m, allowing for the separation of some ions with different elemental composition but the same nominal mass.

GC: Design and Automation

Chromatographic separation of analytes is achieved on a short (1 m) megabore column encased between two aluminum plates. These plates measure 130mm × 130mm × 5mm (total mass = 466 g), creating the compact design shown in Fig. A.2. The column is housed within a rectangular groove (0.8mm wide × 2.4mm deep) machined into the bottom plate, which serves to hold the column in place and provides for good thermal contact with the metal as it loops 2.5 times around the plate. The temperature of the metal assembly can be controlled over a large range (−60 to 200 °C; maximum heating rate of 42 °C min^{-1}) using a combination of CO_2 coolant and an electrical heating system that consists of a temperature ramping controller (Watlow F4 series), heaters (~400W; KH series, Omega; Fig. A.2a), and three resistance temperature detectors (RTDs, F3102, Omega; Fig. A.2b, numbered). Sample collection and elution are controlled using automated solenoid

valves (NResearch, Inc.) to direct gas to one of a number of vacuum outlets (Fig. A.1F, H, and Q). These processes occur in parallel with direct CIMS sampling to minimize interruptions in data collection.

The GC is cooled through the evaporation and expansion of liquid CO_2, which enters from the center of each plate and flows along eight radial grooves. An O-ring seal forces the CO_2 to exit through ports located near the radius of the column. The movement of the CO_2 from the center to the outside of the plate establishes a temperature gradient in the same direction. Symmetry enables the entire column to remain at a similar temperature, in spite of this gradient. In contrast, a previous version of this GC assembly used during this instrument's first deployment allowed CO_2 to enter from a single point along the column diameter (see Supplement Fig. A.14), resulting in large temperature gradients across the column and degradation of the chromatography (e.g., irregular peak shapes).

The CO_2 flow is controlled by two solenoid valves (Series 9, Parker; Fig. A.1S) connected to ~29 cm × 0.25 mm I.D. and ~35 cm × 0.15 mm I.D. PEEK restrictors. With both valves open, a total CO_2 flow rate of 25 slpm (as gas) is admitted to cool the GC assembly to −20 °C within the allotted 10 min period. During trapping, only the solenoid valve connected to the 0.15 mm I.D. restrictor remains open to minimize CO_2 usage. Fine control over the GC temperature was accomplished by utilizing a proportional-integral-derivative (PID) control loop with the heaters and the RTD located on the column ring (Fig. A.2, red no. 2 on the diagram). Additional efficiency was gained by insulating the GC assembly with Nomex™ felt and wrapping the felt with Kapton tape to prevent water vapor from diffusing to and condensing on the cold plates, as well as placing the entire instrument in a temperature-controlled, weatherproofed enclosure. Altogether, this resulted in reproducible temperature profiles with minimal temperature gradients across the column (less than 2 °C) during field operation (see Fig. A.15).

GC: Operating Parameters

To initiate sample collection, ambient air is subsampled from the main instrument inlet (1 slpm; Fig. A.1N) and diluted by a factor of 15 to 30 (Fig. A.1M), depending on the relative humidity (RH) of the sample. The diluted air is pulled through the pre-cooled 0.53 mm I.D. RTX-1701 megabore column (Restek) by a flow-controlled pump (220 sccm; Fig. A.1Q) and targeted compounds are cryofocused on the head of the column over a 10 min period at −20 °C (as discussed in later sections, the choice

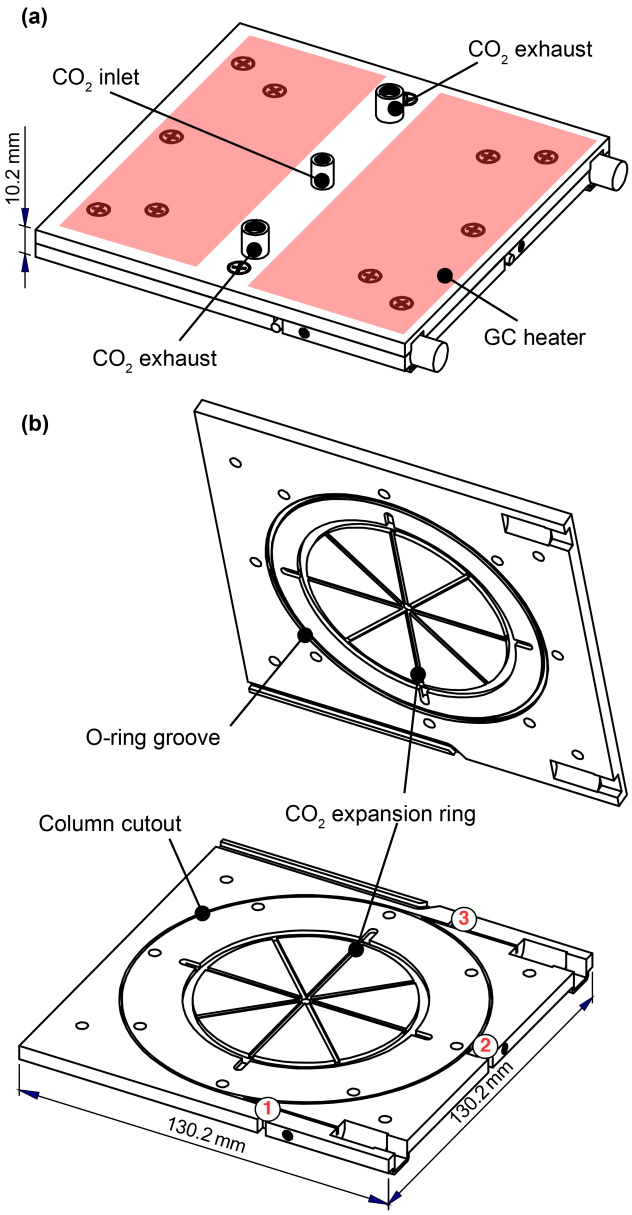

Figure A.2: Schematic of the GC cryotrap and heating unit. Column sits in a groove machined into one plate, providing good thermal contact. CO_2 enters from the center of both plates and expands in the eight radial spokes before exiting through four exhaust ports. Heaters are adhered to the outside of the GC assembly; two of these heaters are shown above in red. The temperature is measured at three locations near the column: (1) near the inlet of the column, (2) on the column ring, and (3) near the outlet of the column.

of the dilution and trapping temperature is a compromise between adequately cryofocusing the maximum amount of analyte while avoiding the collection of water). Following collection, a four-port Teflon solenoid valve (SH360T042, NResearch) is switched, allowing N_2 carrier gas to enter the column at a constant flow rate of 5 sccm (Horiba Z512, Fig. A.1P), and two three-way valves (225T032, NResearch) are toggled to direct the column effluent to either the flow tube (Fig. A.1F) or the ion source (Fig. A.1H) of the mass spectrometer — in both configurations, the entire length of column is held under low-pressure conditions (<260 mbar at P1 (Fig. A.1)). Compounds are then separated on the column using the following automated temperature program: a 3 min temperature ramp to 20 °C (~13 °C min^{-1}), followed by a 3 °C min^{-1} ramp to 50 °C, followed by a 10 °C min^{-1} increase to 120 °C for a total temperature ramping time of 20 min. Following completion of the temperature program, the column is baked at 120 °C for an additional 2 min to remove remaining analytes.

Table A.2: Comparison of elution temperature (°C) and retention time (minutes, in parentheses) for isoprene nitrates.

Study	Column	1-OH 2-N	4-OH 3-N	*Z* 4-OH 1-N
Mills et al. (2016)	Rtx-1701[a]	N/A	110 (26.1)	119.2 (36.5))
Mills et al. (2016)	Rtx-200[a]	N/A	101.1 (16.7)	110 (22.4)
This study	Rtx-1701[b]	42.4 (10.5)	45.1 (11.4)	63.2 (14.5)
Study	Column	*E* 4-OH 1-N	*Z* 1-OH 4-N	*E* 1-OH 4-N
Mills et al. (2016)	Rtx-1701[a]	133.7 (39.3)	133.2 (39.4)	142.7 (41.2)
Mills et al. (2016)	Rtx-200[a]	110 (25.1)	110 (23.3)	110 (26.5)
This study	Rtx-1701[b]	71.3 (15.3)	71.3 (15.3)	76.4 (15.8)

[a] Column is 30m, 0.32mm I.D., 1 μm phase thickness.

[b] Column is 1m, 0.53mm I.D., 3 μm phase thickness.

As mentioned above, connecting the GC outlet directly to the mass spectrometer allows the entire column to remain at sub-ambient pressures during elution (180 mbar (into ion source) or 260 mbar (into flow tube) at P_1). This allows for low-pressure chromatography, which provides several advantages over conventional GC methods (Sapozhnikova and Lehotay, 2015). For instance, low pressures support the use of short, large bore columns without significant loss in peak separation. This becomes especially advantageous during cryotrapping as this larger I.D. column allows for a greater volume of analytes to be sampled, beneficially impacting the instrument signal-to-noise ratio. In addition, low-pressure conditions also allow for faster analysis times at lower elution temperatures (Table A.2). The decrease in analysis time provides this instrument with sufficient time resolution to capture

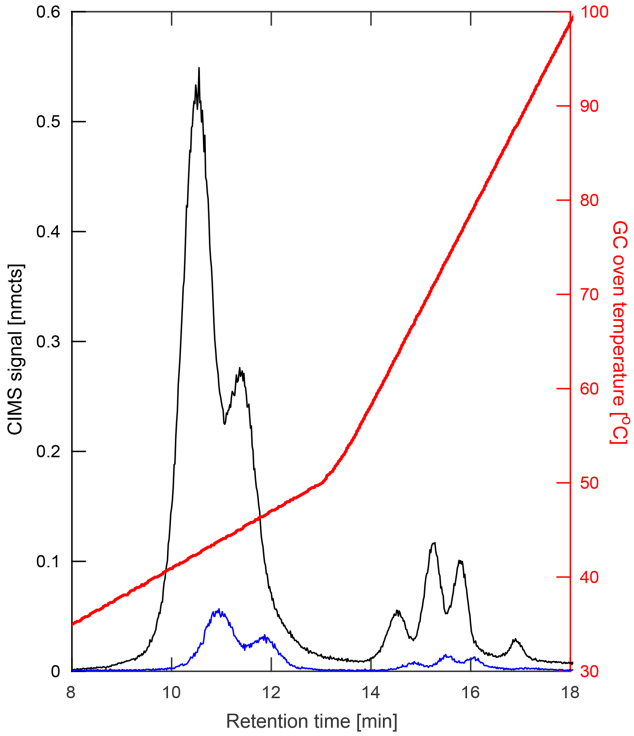

Figure A.3: Comparison of chromatograms of the IHN isomers obtained from the two different GC analysis modes in which the same amount of analyte is collected on the column but is directed into either the ion source (black) or flow tube (blue). GCs that are directed into the ion source result in approximately a 10-fold signal increase compared to flow tube GC analysis. In addition, compounds analyzed via the ion source typically elute at lower temperatures compared to flow tube analysis, an advantage for sampling fragile multifunctional compounds.

diurnal variations in measured species (one GC cycle per hour), while lower elution temperatures allow this method to be applied for analysis of thermally labile species, as discussed in later sections.

GC-CIMS Interface

Following the column, a 100-200 sccm N_2 pickup flow (Fig. A.1R) is added to the 5 sccm column flow to decrease the residence time in the PFA tubing connecting the GC to the mass spectrometer. As mentioned above, solenoid valves direct the analytes into the CIMS instrument, either through the flow tube (similar to direct CIMS sampling) or directly into the ion source. Unlike direct ambient sampling, it is possible to pass the GC flow through the ion source as oxygen is not retained on the column during trapping. In other cases, oxygen that enters the ion source is ionized (O_2^-) and causes interferences at many m/z values.

Figure A.3 shows a comparison of two chromatograms obtained by these different analysis modes. Introduction via the flow tube (hereafter FT mode; Fig. A.3, blue) allows for interaction of analytes with only CF_3O^- (and CF_3O^- derived) reagent ions, providing a straightforward comparison to the direct CIMS samples as well as quantification of the GC transmission of analytes. However, due to tubing and gas flow configurations, the pressure within the column is greater under FT mode than when directed to the ion source region. Therefore, compounds tend to elute later and at higher temperatures, making introduction into the ion source (hereafter IS mode; Fig. A.3, black) the preferred analysis mode when separating more thermally labile compounds in the current instrument configuration.

IS mode also creates an enhancement in instrument sensitivity due to the increase in analyte-reagent ion interaction time (as the analytes can interact with CF_3O^- as soon as it forms, rather than mixing with the ions downstream) and overall drier conditions. The enhancement in sensitivity is quantified through comparison to the direct CIMS measurements, which show a multiplicative enhancement factor that is nonlinearly dependent on the gas flow entering the ion source. For the instrument flows used in this work, the ion source enhancement was determined to be 9.8 ± 0.8, which was determined by comparing peak areas produced when operating in FT vs. IS mode (see Supplement). Additional discrepancies between IS mode and direct CIMS measurements may result from analyte interactions with the metal walls of the ionizer. In addition, direct electron attachment to analytes (often followed by fragmentation) can occur in the ion source, though differences between the two GC modes are typically explained within error by the enhancement factor. These fragment ions, however, provide additional structural information. For example, different fragment ions may arise from the fragmentation of a primary nitrate versus a tertiary nitrate (see Fig. A.19).

Instrument Housing and Supporting Equipment

The GC-HRToF-CIMS was placed in a weatherproofed, temperature-controlled enclosure during field sampling to protect the instrument electronics and allow for efficient GC cooling. In total, the instrument enclosure measured 1.1m × 1.7m × 0.9m (W × H × D), taking up a footprint of approximately 1m2 (Fig. A.4).Weatherproofing was created by using Thermolite^{TM} insulated paneling (Laminators, Inc.) that covered the aluminum instrument rack (80/20, Inc.) and was aided by weather stripping placed between the panels and the rack. For temperature control, two Ice Qube HVAC units (IQ1700B and IQ2700B, Blade series, cooling

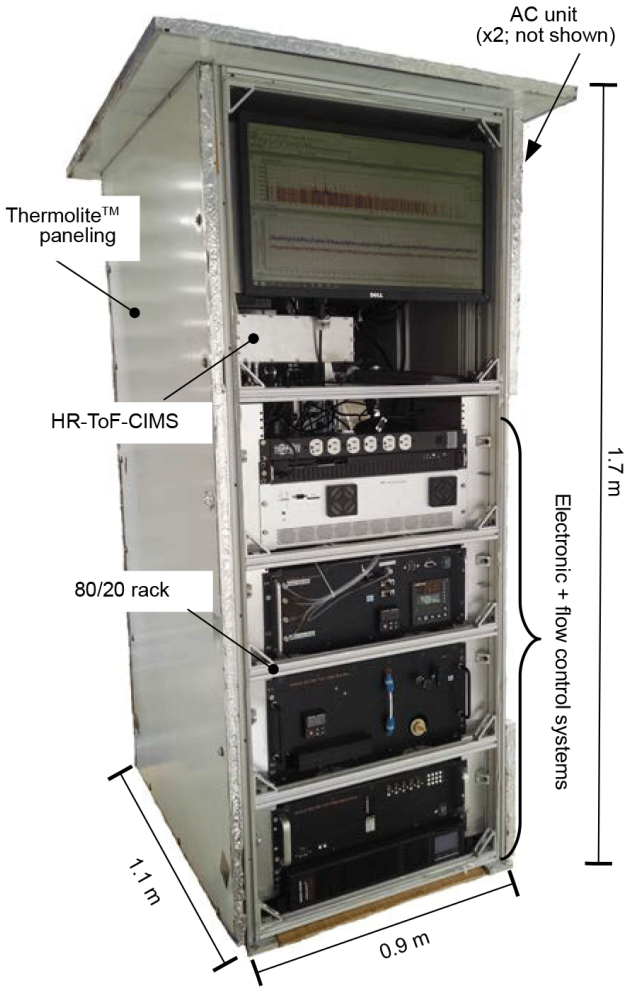

Figure A.4: The weatherproofed and temperature-controlled enclosure in which the instrument resides during field sampling. The front panel of the enclosure is removed in this photo.

power = 498 and 791 W, respectively) were attached to one side of the enclosure to remove the heat produced by the instrument. During the range of ambient temperatures experienced during these studies (8.7–37.8 °C), the internal temperature of the enclosure remained at or below 30 °C under normal operating conditions.

Along with the instrument enclosure, two scroll pumps (nXDS 20i, Edwards) were located separately from the instrument in their own weather-resistant container and were used to back the three turbomolecular pumps (TwisTorr 304 FS, Agilent) and the flow tube attached to the mass spectrometer. A weather station was also co-located with the instrument during the two field studies. It included sensors for air temperature, RH, solar irradiance, wind direction, wind speed, and atmospheric pressure.

Instrument Calibration

Instrument sensitivity was assessed in the laboratory using a select number of commercially available compounds. These experiments were performed using authentic standards for hydrogen cyanide (HCN), sulfur dioxide (SO_2), hydroxyacetone (HAc), and glycolaldehyde (GLYC). The absolute concentrations of these compounds were quantitatively determined by Fourier transform infrared (FTIR) spectroscopy before undergoing dilution and CIMS sampling (see Supplement for additional details regarding calibration procedures). However, because many compounds of interest are not commercially available and difficult to synthesize and purify, these four standard gases were simultaneously sampled on the cToF-CIMS (which uses the same chemical ionization technique) to directly compare the compound sensitivities between these two instruments. On average, the cToFCIMS was observed to be 1.4 times more sensitive than the HRToF-CIMS for the four gases tested. We used this factor to proxy sensitivities for other compounds that had been previously determined for the cToF-CIMS through calibrations or estimated using ion-molecule collision rates as described in Paulot et al. (2009a), Garden et al. (2009), Crounse et al. (2011), Schwantes et al. (2015), and Teng et al. (2017).

For the chromatography, preliminary peak assignment was based on previous laboratory studies that were performed on the test bed this field deployable system was based upon (Bates et al., 2014; Nguyen et al., 2014; Lee et al., 2014; Praske et al., 2015; Teng et al., 2015), as detailed in the Supplement of Teng et al. (2017). Many of these studies used synthesized standards that had been developed for compounds such as ISOPOOH (Rivera-Rios et al., 2014; St Clair et al., 2016), IEPOX (Bates et al., 2014), and IHN (Teng et al., 2017), while others oxidized parent hydrocarbons in a chamber and determined elution orders based on assumptions regarding physical chemistry of reaction intermediates, as in Teng et al. (2015). However, due to differences in the analytical setups, verification of these assignments and their retention times have also been made for a number of targeted compounds through laboratory experiments described in more detail in the Supplement. The results from one of these studies is shown in Fig. A.5, which compares the retention times for alkyl hydroxy nitrates derived from propene (propene HN) and three structural isomers of butene (butene HN) created in the chamber bag with chromatograms gathered in the field.

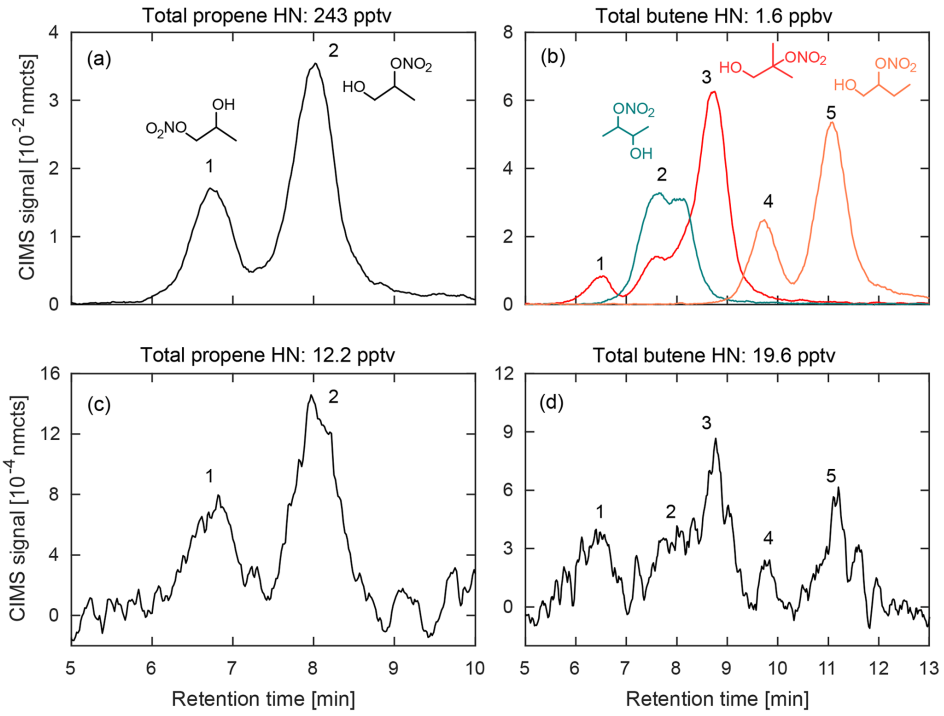

Figure A.5: Comparison of hydroxy nitrates formed during chamber experiments (a–b) from propene (left) and three structural isomers of butene (right; 1-butene (orange), 2-butene (teal), and 2-methyl-propene (red); dominant hydroxynitrate structures shown) with the corresponding m/z signal observed during a 2017 field study in Pasadena, CA (c–d). Data shown are a 10 s average.

Instrumental Backgrounds

In the field, we use two methods to quantify the instrumental background signals caused by interfering ions present at targeted analyte masses. In the first method, the instrument undergoes a "dry zero" at which the CIMS flow tube is overfilled with dry nitrogen so that no ambient air is sampled during this time. In this method, the humidity within the instrument changes substantially compared with ambient measurements. The second method, an "ambient zero", passes air from the main inlet through a zeroing assembly, which includes a sodium bicarbonate denuder and a scrubber filled with Pd-coated alumina pellets. The scrubbed air then enters the flow tube after instrument flows are adjusted to mimic near-ambient humidity levels. During field sampling, both zeroing methods occur twice each hour during a 6 min period that separates the CIMS and GC-CIMS measurements. The dry zero is most similar to the GC measurements and can assess the health of the instrument over the course of a campaign as these backgrounds should not change over time, while the ambient zero captures background signals that are adjusted for the water-dependent

sensitivity of the compounds measured during direct CIMS sampling.

Data Processing

Data from the mass spectrometer are collected using data acquisition software provided by Tofwerk (TofDaq). These data are later combined with the instrument component readbacks collected using single-board computers (Diamond Systems) and converted into a MATLAB file using in-house developed scripts. To account for fluctuations in the reagent ion, observed mass signals are normalized to the signal associated with the isotope of the reagent ion ($^{13}CF_3O^-$, m/z 86) and its cluster with water ($[H_2O \cdot {}^{13}CF_3O]^-$, m/z 104). The analyte signal is defined as this normalized absolute number of counts (nmcts) recorded at m/z.

For the chromatography, we modified an open-source MATLAB peak-fit function (O'Haver, 2017). Peak areas are determined for desired masses by subtracting a baseline and fitting the chromatograms with the appropriate peak shapes as shown in Fig. A.6 for ISOPOOH and its isobaric oxidation product, isoprene epoxydiol (IEPOX, m/z 203; St Clair et al., 2016). These areas are then scaled by the relative CIMS sensitives of each isomer (see Supplement), ion source enhancement (if applicable), and a transmission factor. The resulting values are then normalized by volume of air collected on the column in order to obtain the corresponding ambient mixing ratios.

A.4 Discussion

Sample Collection

Due to their lower volatility and highly reactive nature, the accuracy and precision of ambient OVOC measurements can be greatly limited by the sample collection method. GC sampling techniques often used in atmospheric chemistry collect gas-phase compounds on solid adsorbents (e.g., TENAX) that have been developed to combat some of the aforementioned issues (such as preventing the co-collection of water by trapping analytes at higher temperatures; Demeestere et al., 2007; Ras et al., 2009). However, the use of OVOC-specific adsorbents has shown problems with the formation of artifacts caused by the reaction of ozone, NO_2, and other compounds trapped on the sorbent surfaces (Klenø et al., 2002; Nozière et al., 2015; Mills et al., 2016) and can lead to significant analyte loss, especially for polar and/or labile compounds such as tertiary organic nitrates (as suggested in Mills et al., 2016), organic hydroperoxides, and other highly functionalized compounds. In addition, high humidity can result in increased water uptake into the sorbent materials during

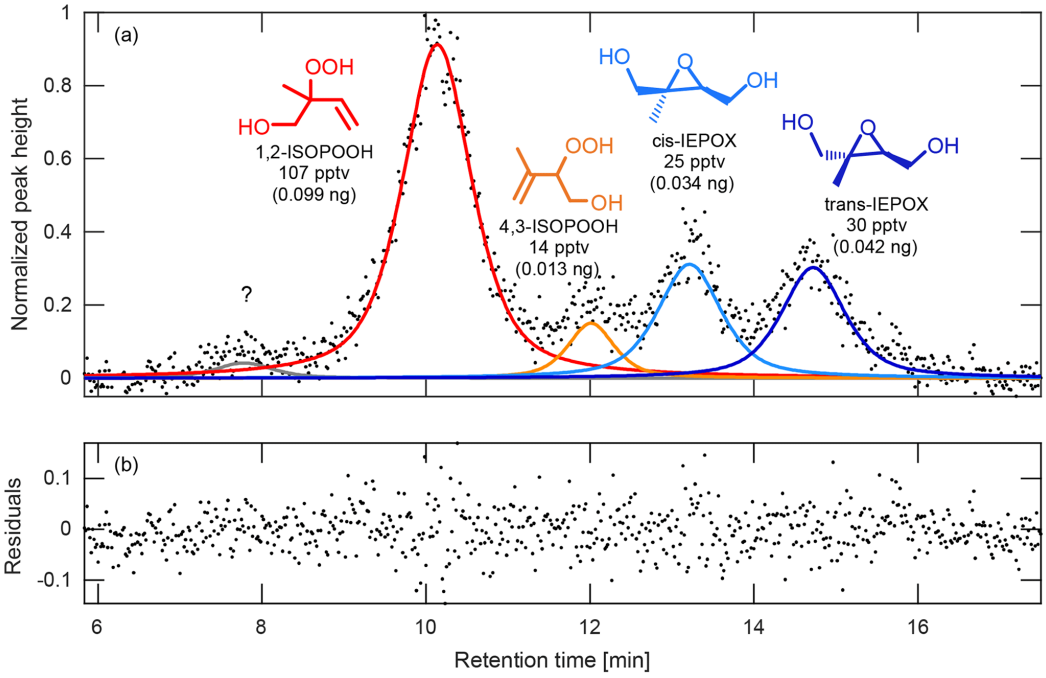

Figure A.6: (a) Chromatogram, peak fits, and (b) resulting fit residuals obtained from the peak-fit MATLAB function for the deconvolution and integration of ambient ISOPOOH and IEPOX isomers observed during the PROPHET 2016 field study. The isomers observed during this study were 1,2-ISOPOOH (red), 4,3-ISOPOOH (orange), cis-IEPOX (light blue), and trans-IEPOX (dark blue). In addition, an unknown peak (gray) can be seen eluting at 7.8 min prior to the ISOPOOH and IEPOX isomer species. To obtain the ambient mixing ratios, peaks are deconvoluted and integrated using an appropriate peak shape (in this case, a Gaussian-Lorentzian blend), scaled by the relative CIMS sensitivities of each isomer (see Supplement), ion source enhancement (if applicable), and estimated transmission factor, and then normalized by volume of air collected on the column. The GC signal shown here has been normalized to the largest peak height. Amounts shown in parentheses correspond to the amount of analyte trapped in the column.

ambient sampling (Ras et al., 2009), requiring additional water removal steps such as the utilization of chemical scrubbers, which can react with compounds of interest (Koppmann and Wildt, 2008; Roukos et al., 2009), or trapping at above optimal temperatures, which may result in the loss of more volatile compounds (Vairavamurthy et al., 1992; Roukos et al., 2009). These issues motivate our use of dilution and cryotrapping on the column to transmit a wider range of analytes through our system.

Trapping efficiency was assessed by cryofocusing a mixture of propene HN and IHN for varying amounts of time (and thus sample volumes) in order to test for linearity of the cryotrap. Results provided in the Supplement show that the GC peak area was linearly proportional to the volumes sampled, suggesting that compounds are preserved on the column during trapping (Fig. A.16). Analyte breakthrough has been monitored in the laboratory by directing the GC flow into the CIMS during trapping to monitor analyte signals. For most compounds of interest ($>C_3$), there has been no evidence of breakthrough under typical trapping conditions (-20 °C) when this procedure has been performed for a trapping period of up to 12 min, though we note chromatography can be significantly degraded prior to breakthrough, as the analytes spread to larger bands on the column.

Experiments were performed to determine if oxidants such as ozone and NO_2 can interfere with targeted compounds trapped on the column. We oxidized isoprene under high-NO_x conditions to produce IHN, as its isomer-specific reaction rate with ozone would make it apparent whether certain isomers were affected more than others. When we attempted to co-trap 100 ppb of NO_2 and 200 ppb of ozone, our results show no evidence that either oxidant affects the IHN trapped on the column, even at lower dilutions (15×) and lower trapping temperatures (-50 °C).

Trapping Temperature and Column Humidity

Our trapping temperature (-20 °C) was optimized on the original laboratory prototype and was chosen as a compromise between analyte retention and avoidance of water retention. We find that trapping above -20 °C results in degradation of the chromatography for several species, examples of which can be seen in the Supplement (Fig. A.17). However, at -20 °C some higher-volatility compounds are not trapped efficiently, resulting in irregular peak shapes (Fig. A.18). Further optimization of trapping conditions is needed in order to improve the chromatography for these species and further reduce the likelihood of water retention.

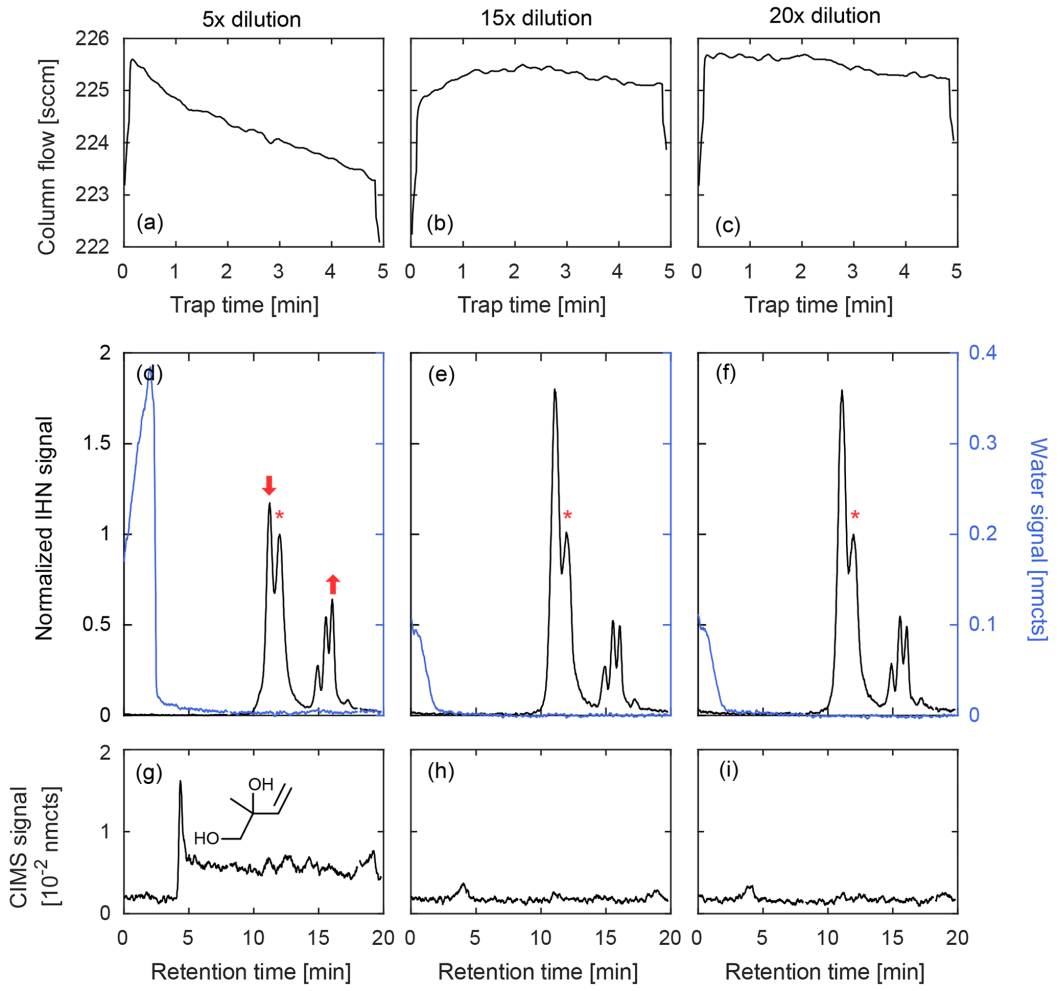

Figure A.7: Comparison of GC column flow (a–c) and three chromatograms (d–f) of IHN (m/z 232, black) and water (m/z 104, blue) at three different dilutions from a high-RH chamber experiment. The beginning of a chromatogram is marked when the temperature program initiates. When water is trapped during the lowest dilution (5×), column flow decreases (indicating an ice blockage) and the isomer distribution of IHN is dramatically altered as noted by a loss in the first peak (1,2-IHN) and increase in the last peak (E 1,4-IHN). These peak changes are marked by arrows and described relative to 4,3-IHN (starred). The 1,2-isoprene diol (m/z 187, g), an expected product of 1,2-IHN hydrolysis, is also observed in this scenario. However, when the sample is sufficiently diluted prior to trapping, the water signal quickly falls to background levels and isomer distribution is preserved with minimal diol formation. Column flow also remains relatively stable throughout the trapping period when minimal water is retained.

Because compounds are trapped at sub-ambient temperatures, unless special care is taken, relative humidity inside the column can easily reach 100% during ambient sampling. This is problematic because co-trapped water and ice clog the column, and many species of interest are highly soluble and reactive and readily hydrolyze (Koppmann and Wildt, 2008; Roukos et al., 2009; Lee et al., 2014; Teng et al., 2017). We address this issue by diluting the ambient air with dry N_2 prior to cryotrapping to reduce the RH below the ice point at −20 °C (1.3 hPa water vapor). This is illustrated in Fig. A.7 during GC analysis of IHN at high RH (~50%) with three different sample dilutions. When water is trapped during the lowest dilution (5×), the column flow is observed to decrease over time (Fig. A.7a), indicating the formation of an ice blockage. In addition, the isomer distribution of IHN is dramatically altered, as seen by the loss of 1,2-IHN (first peak, Fig. A.7d) and the corresponding formation of an isoprene diol, its hydrolysis product (Fig. A.7g). However, at the two higher dilutions (15× and 20×), the column flow remains stable throughout the trapping period (Fig. A.7b-c) — consistent with minimal ice formation — and the isomer distribution of IHN is preserved between the two runs (Fig. A.7e-f). Though some water is retained on the column even at these higher dilutions, it was likely trapped downstream of the analytes, limiting its interactions with IHN.

During sampling, the operating dilution is chosen based on ambient RH measurements. The effectiveness of the dilution is verified by monitoring the water signal ($[H_2O \cdot CF_3O]^-$, m/z 104), which should quickly fall to background levels during elution when minimal water is retained (as seen in Fig. A.7e-f). For the data shown here, we diluted the samples by a factor of 15 during laboratory studies and by a factor of 20 to 30 in the field studies. The high sample dilution demands a very high sensitivity to be able to adequately quantify many of the compounds of interest, which is achievable on this instrument when operating in IS mode. Even so, ambient mixing ratios of several of the targeted analytes described here pushed the detection limits of the instrumentation, leading to increased uncertainty, especially when deconvolution was required prior to integration of chromatographic peaks.

Analyte Transmission

In addition to rapid hydrolysis, many targeted OVOCs are highly susceptible to irreversible losses or chemical conversion upon contact with surfaces (Grossenbacher et al., 2001, 2004; Giacopelli et al., 2005; Rivera-Rios et al., 2014; Xiong et al., 2015; Mills et al., 2016; Hellén et al., 2017). We addressed this issue

through the utilization of metal-free LP-GC. As mentioned above, this technique holds several known advantages over traditional GC methods, including elution at lower temperatures (Table A.2), that make it possible to better preserve thermally labile species. In addition, all wetted instrument surfaces (with the exception of the ion source) are composed of inert materials such as PFA/PTFE Teflon, PEEK, and column-phase materials. This reduces unwanted reactions on surfaces, most notably the metal-catalyzed decomposition of compounds such as hydroxyperoxides and organic nitrates (Rivera-Rios et al., 2014; Mills et al., 2016).

Despite measures taken to improve analyte transmission, losses are still observed for some species such as hydroperoxides and epoxides. This highlights the importance of accurately quantifying analyte transmission through the GC column. Yet, for traditional GC-based measurements, transmission typically remains unknown, which can be detrimental when there is a lack of available standards and GC response factors must be based on another compound that has a similar chemical makeup but may interact differently with the column phase. However, the combination of our LP-GC system with the high sensitivity of the CIMS provides two sampling modes (direct CIMS and GC-CIMS) that automatically alternate between each other in half-hour increments. This allows us to compare individual chromatograms to CIMS measurements taken simultaneously with cryotrapping in order to assess GC transmission efficiency under field conditions, without the need for external standards. This is carried out by comparing mixing ratios calculated from direct CIMS sampling measurements and the sum of the entire chromatogram signal (normalized by the amount of air trapped), which is best performed when concentrations are high, and thus, measurement error is minimized. Using this method, we assess the transmission efficiency of IHN, which has been shown to have 100% transmission through a similar system (Lee et al., 2014). In the field, the percent difference of IHN mixing ratios calculated from these two measurement modes was typically less than 5%. We note that transmission less than unity can be the result of incomplete transmission of a single isomer (rather than the sum of all isomers). An example of this is in the case of ISOPOOH and IEPOX — IEPOX is transmitted more poorly through this column than ISOPOOH (Bates et al., 2014). In these cases, we use laboratory experiments to monitor discrepancies between mixing ratios obtained from direct CIMS sampling and GC-CIMS analysis and observe how these discrepancies change as we alter the isomer distribution (such as through additional oxidation of ISOPOOH). Using this method, we determine that ISOPOOH transmission is nearly 100%, while IEPOX has a transmission of about 67%.

A.5 Field Performance and Ambient Air Measurements

The GC-HRToF-CIMS has participated in two field studies that served as a test for this analytical method. Its first deployment occurred as part of the Program for Research on Oxidants, Photochemistry, Emissions and Transport (PROPHET) campaign that occurred between 1 and 31 July 2016, when it was placed on the top of a 30m research tower surrounded by the dense forests of rural northern Michigan. The following summer, the instrument underwent a second deployment at the California Institute of Technology (Caltech) campus in Pasadena, CA, where measurements were taken from the roof of the 44m tall Millikan Library between 15 July and 17 August 2017. In contrast to PROPHET, Pasadena is typically characterized as a high-NO_x urban environment due to its proximity to Los Angeles, though biogenic emissions have also been known to influence the area (Arey et al., 1995; Pollack et al., 2013). During both deployments, the instrument provided a near-continuous measure of OVOC concentrations, through either direct sampling or GC analysis. Interruptions in the GC measurements were primarily due to required maintenance of the cooling system (e.g., changing CO_2 tanks). When the GC was operational, data were captured during 1 h cycles in which the first half was dedicated to direct CIMS measurements and the latter half measured analytes after chromatographic separation, with the collection of ambient and dry zeros interlaced between operational modes. This sampling routine is shown in Fig. A.8 for a single mass (m/z 232) collected during the 2017 Caltech field study.

At PROPHET, the low-NO_x environment (Millet et al., 2018) provided ideal conditions for measuring several organic peroxides, such as ISOPOOH. However, because ISOPOOH and its oxidation product, IEPOX, are isobaric, other analytical techniques are either unable to separate these two species or rely on the relative abundances of fragment ions to determine the relative contribution of each to the observed signal (Paulot et al., 2009b). With the GC-CIMS, we were able to physically separate the isomers prior to quantification (Fig. A.6), allowing real-time information regarding the distribution of these two species (Fig. A.9). As such, we observed that IEPOX comprised about half of the total daytime signal (07:00–22:00 local time; Fig. A.9E), a fraction that is typically estimated through models when assessing IEPOX aerosol uptake (as in Budisulistiorini et al., 2017). In addition, we are also able to differentiate the isomers that make up ISOPOOH and IEPOX, which can serve to highlight the isomer-specific chemistry of these compounds. A prime example is the observed daytime ratio of 1,2-ISOPOOH to 4,3-ISOPOOH. This ratio (~7.6) is higher than expected when accounting only for the isomer-specific

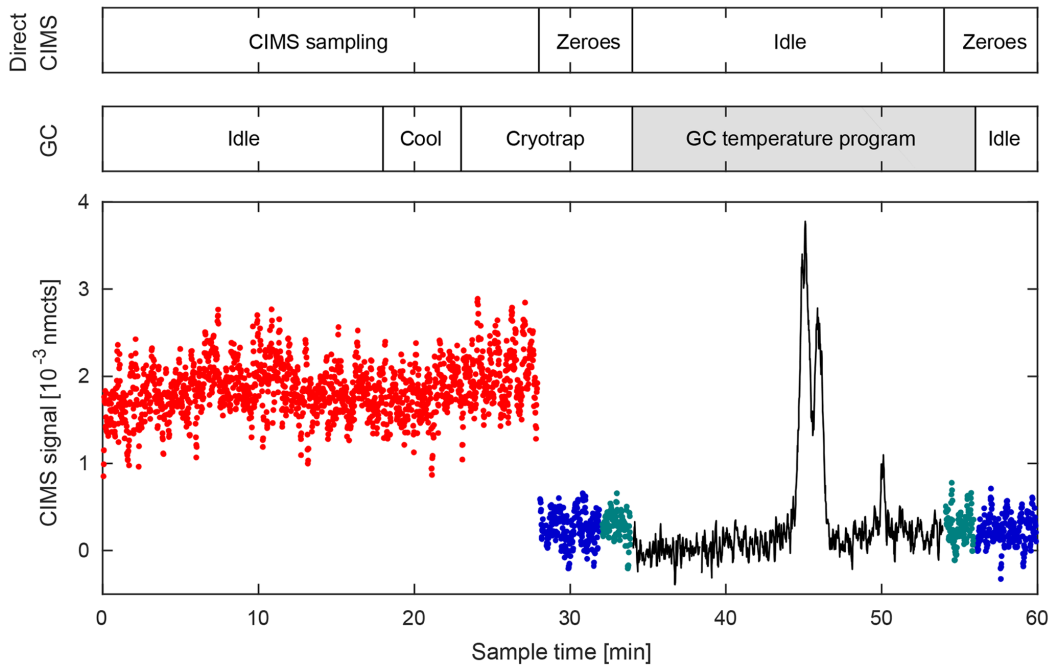

Figure A.8: Typical GC-CIMS sampling cycle during the 2017 field study in Pasadena, CA. Data shown for m/z 232. Cycle has a period of 1 h in which the first half is dedicated to direct CIMS measurements (red), and the latter half measures compound signals that have undergone chromatographic separation (black). The two sampling modes are separated by a zeroing period comprised of a 4 min ambient zero (blue) and a 2 min dry zero (green). Most GC processes occur in the background during direct sampling, so as not to interrupt data collection. Data shown here are a 2 s average. Changes in the amount of flow entering the ion source during direct CIMS and GC-CIMS sampling directly correlate with the signal-to-noise ratio seen during each operating mode. The increased flow rate through the ion source during the GC sampling mode results in higher ion counts and an increased signal-to-noise ratio.

bimolecular reaction rates of the isoprene peroxy radicals (Wennberg et al., 2018). Thus, these measurements allow us to conclude that there was competitive RO_2 isomerization of the 4-OH isoprene peroxy radicals (Peeters et al., 2009; Crounse et al., 2011; Teng et al., 2017) during the course of this campaign.

Other multifunctional organic peroxides were also observed during this campaign, such as those seen at m/z 201 (Fig. A.10). Though the CIMS signal at m/z 201 has previously been assigned to the HPALDs (Crounse et al., 2011), a product of isoprene RO_2 isomerization, laboratory GC studies have determined that this signal is actually composed of several compounds (Teng et al., 2017). This is consistent with field chromatograms obtained at PROPHET, which show up to five individual

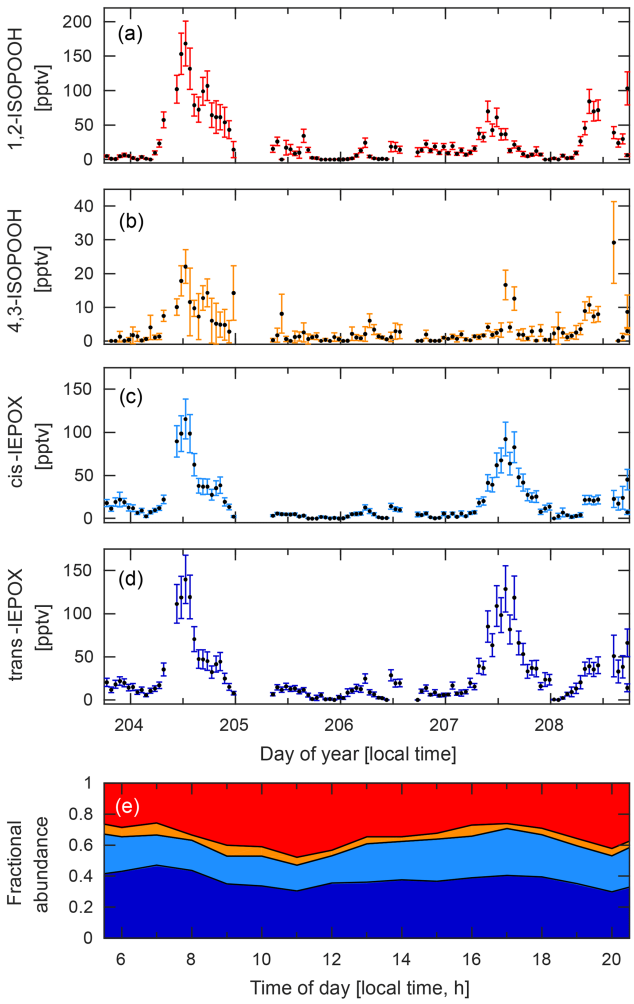

Figure A.9: Time series for the four isobaric species: (a) 1,2-ISOPOOH, (b) 4,3-ISOPOOH, (c) cis-IEPOX, and (d) trans-IEPOX. Data were collected during the PROPHET campaign between 22 and 27 July 2016. (e) Diurnal profile of the fractional abundance of each of these four isomers based on their hourly mean values calculated from the time series data shown here. Shaded areas correspond to 1,2-ISOPOOH (red), 4,3-ISOPOOH (orange), cis-IEPOX (light blue), and trans-IEPOX (dark blue).

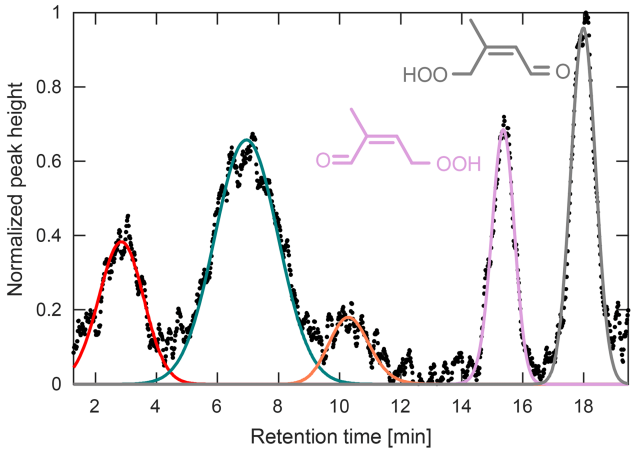

Figure A.10: Chromatogram obtained during the PROPHET campaign for m/z 201. The latter two peaks have been identified previously as the two HPALD isomers (Teng et al., 2017). The three early peaks remain unidentified. GC signal has been normalized to the largest peak height.

peaks at this mass-to-charge ratio. Using the peak assignment discussed in Teng et al. (2017), we assign the last two peaks in Fig. A.10 as the 1-HPALD (purple) and 4-HPALD (gray), which together compose ~38% of the total GC peak area. The second peak (green) is likely the same unidentified early eluting peak seen in the Teng et al. (2017) study (which also results from isoprene RO_2 isomerization). The two other peaks (red and orange) are unidentified and may result from different chemistry.

The GC-HRToF-CIMS has also demonstrated its ability to measure individual isomers of organic nitrates during its two deployments, as showcased by our IHN measurements. The two dominant isomers of IHN (1,2-IHN and 4,3-IHN) were observed at both PROPHET (with an average daytime ratio of ~2.6) and at Caltech (with an average daytime ratio of ~1.4). At Caltech, other IHN isomers (Fig. A.11), as well as an unidentified component that has been previously observed during laboratory studies, were also quantified (Teng et al., 2017). Comparison of isomer ratios obtained from each site was used to assess the isoprene RO2 chemistry and is consistent with competitive unimolecular reaction pathways at PROPHET. Interestingly, the IHN ratio at PROPHET differed significantly from the corresponding ISOPOOH ratio despite the similar formation pathways of each pair of oxidation products. We suspect this reflects differences in their loss pathways, which will be discussed further in an upcoming paper.

In addition to IHN, the GC-CIMS also observed other large (>C_3) organic nitrates.

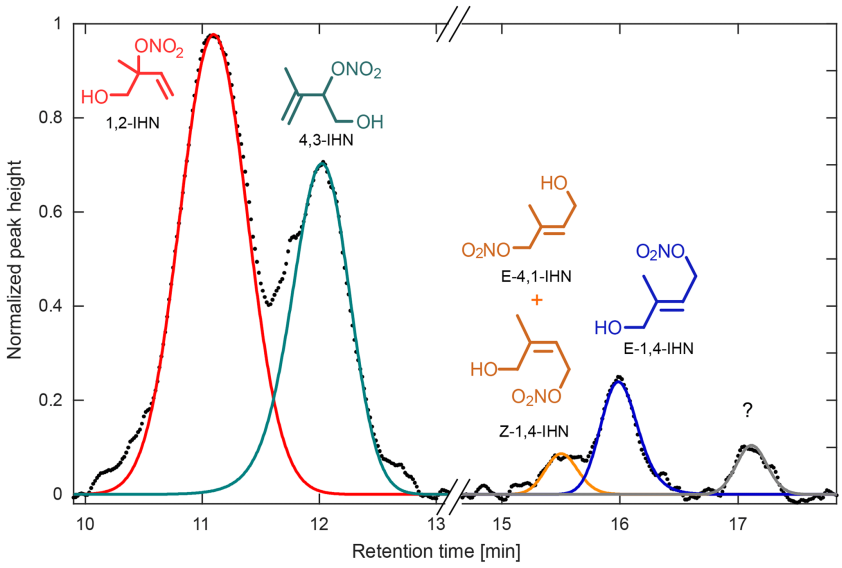

Figure A.11: Chromatogram obtained during the Caltech field study for m/z 232, attributed to the IHN isomers, normalized to the largest peak height. At least four isomers of IHN were observed: 1,2-IHN (red), 4,3-IHN (green), E-4,1- and Z-1,4-IHN (coelute, orange), and E-1,4-IHN (blue). Z-4,1-IHN was not present above the instrument detection limit. An unidentified component, which likely corresponds to a species observed in laboratory isoprene oxidation studies, is present near the end of the chromatogram (gray; see Teng et al., 2017).

For example, evidence of isoprene + NO_3 chemistry during the Caltech experiment is indicated by the nighttime increase in the signal at m/z 230, which is assigned to the ICNs (Schwantes et al., 2015). Though only two isomers were observed during this study (Fig. A.12), the distribution of these species (assigned as 4,1-ICN and 1,4-ICN) matches results from Schwantes et al. (2015) and may confirm the hypothesis that NO_3 addition to the C1 carbon of isoprene is favored (Suh et al., 2001). As the distribution of the isoprene nitroxy peroxy radical (INO_2) is less constrained than the OH-derived RO_2 counterpart, further observations of ambient ICN isomers with the GC-CIMS may lead to improved understanding of the impact of nighttime NO_3 chemistry (Schwantes et al., 2015). In addition, a suspected nitrogen-containing compound was observed at Caltech at m/z 236 (MW 151; Fig. 13). Data obtained from direct CIMS sampling showed at least two local maxima, one occurring before sunrise and the other shortly after noon. With the addition of the GC, we find that two distinct species contribute to this instrument signal with varying contributions over the course of a day. That is, the first compound (eluting at 9.8 min) is responsible for the majority of the signal in the early afternoon, possibly indicative of production via photooxidation, whereas the second compound (eluting

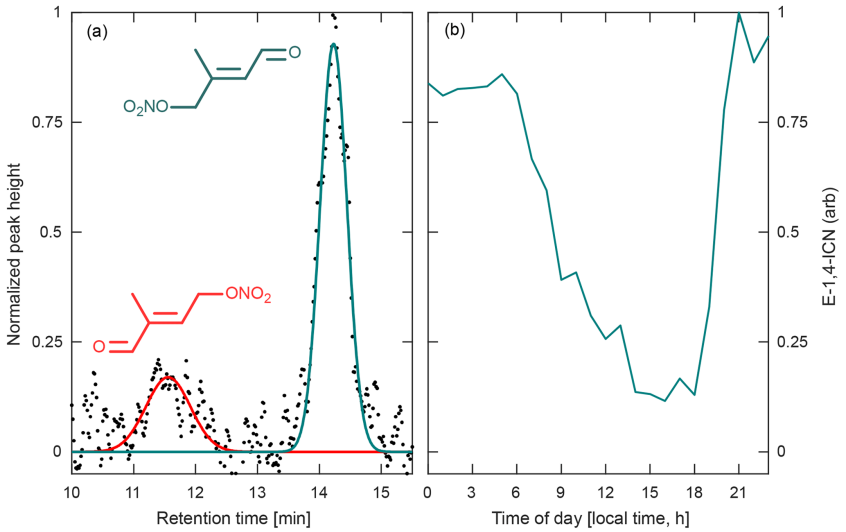

Figure A.12: Chromatogram obtained during the Caltech field study for the two isoprene carbonyl nitrate isomers (4,1-ICN in red and 1,4-ICN in green, m/z 230) produced by isoprene + NO_3 chemistry, normalized to the largest peak height. Peak assignment is based on results from Schwantes et al. (2015). (b) Average diurnal profile of the most abundant ICN isomer, 1,4-ICN, obtained from chromatograms collected between 1 and 16 August 2017 during the Caltech field study. This profile appears to correspond with the expected formation of ICN from NO3 oxidation of isoprene in dark/dim conditions and the rapid loss in light periods.

at 13.8 min) is most abundant between sunset and sunrise, possibly due to production from nighttime NO_3 chemistry, high photolability, a short lifetime against the OH radical, or some combination thereof.

A.6 Summary

We have developed an automated GC-CIMS system that captures diurnal changes in the isomer distributions of a wide range of important OVOCs. This novel method addresses common issues typically associated with ambient GC measurements, allowing observations of compounds that have previously proven difficult to measure. We use a combination of sample dilution and temperature control to avoid the adverse effects caused by high column humidity (e.g., hydrolysis of reactive compounds). This, along with the use of LP-GC methodology, cryotrapping directly on the column, and the creation of a near-metal-free GC design, reduces analyte degradation upon contact with the instrument surfaces.

Analytical performance was assessed through a combination of laboratory studies and field campaigns. GC-HR-ToF-CIMS has demonstrated its ability to provide

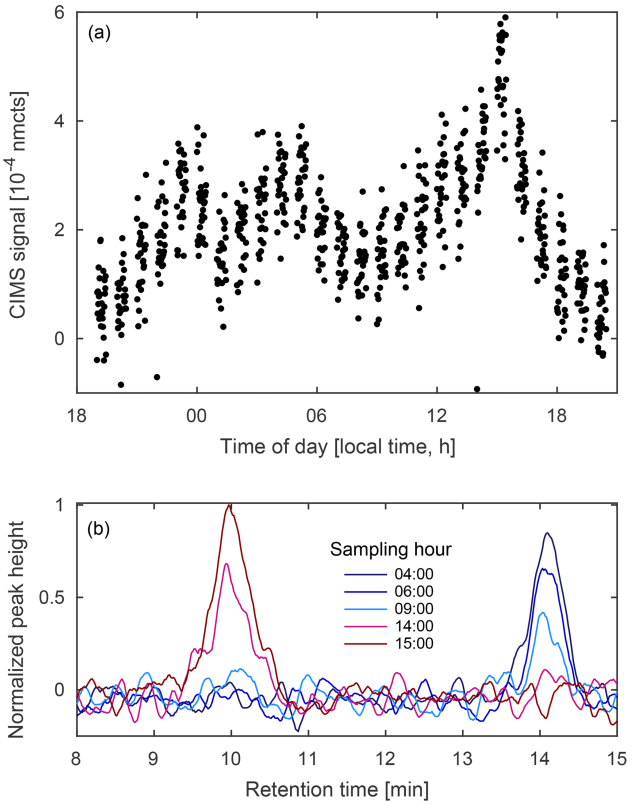

Figure A.13: (a) Diurnal profile of unidentified compounds observed at m/z 236 (MW151) from 11 to 12 August 2017 during the Caltech field study and (b) select field chromatograms from the same sampling period. The GC shows at least two compounds contribute to the signal, one more abundant at night (blue) and the other more abundant in the late afternoon (red).

continuous reproducible measurements, effectively trapping tested species with no observable breakthrough and providing a quantitative measurement of GC transmission by utilizing its two sampling modes (direct CIMS and GC-CIMS sampling). Though additional optimization is needed to expand the number of species that can be measured using this technique, its participation in future field studies will help enable the elucidation of the chemical mechanisms of a number of species, such as the isoprene oxidation products, by providing information that will help assess how compound structure impacts their formation or atmospheric fate and thereby their effect on the global atmosphere.

Acknowledgements

We would like to thank Steve Bertman, Phil Stevens, and the University of Michigan Biological Station (UMBS) for organizing the PROPHET 2016 campaign. We are indebted to the many PROPHET participants who helped us move the instrument

to and from the top of the tower safely. We also thank the Caltech campus and affiliated staff for accommodating the summer 2017 study. The construction of the GC-HRToF-CIMS instrument was supported by the National Science Foundation (AGS-1428482), with additional NSF support (AGS-1240604) provided for the instrument field deployments. Work performed by Krystal T. Vasquez and Hannah M. Allen was supported by the National Science Foundation Graduate Research Fellowship (NSF GRFP). Krystal T. Vasquez also acknowledges support from an Earl C. Anthony Fellowship in chemistry during an early portion of this study.

Data Availability

Data from the 2017 Caltech study are available at https://doi.org/10.22002/D1.971 (Vasquez et al., 2018). Additional data are available upon request to the corresponding authors.

A.7 Supplemental Information

Instrument Calibration

Instrument calibrations were performed using four authentic standards for hydrogen cyanide (HCN), sulfur dioxide (SO_2), hydroxyacetone (HAc) and glycolaldehyde (GLYC) with HRToF-CIMS. For HCN and SO_2, calibrations were performed using a standard gas mixture (300 ppmv in N_2 and 50 ppmv in N_2, respectively) which were individually diluted with N_2 using mass flow controllers prior to being sampled by the HRToF-CIMS. Cylinder concentrations of these two gases were verified using Fourier-transform infrared spectroscopy (FTIR) using cross section data archived in the Pacific Northwest National Lab (PNNL) IR database (Sharpe et al., 2004). Gas-phase HAc mixture was created by flowing dry N_2 over the commercially available compound (Aldrich, 90%) into a 0.1 m^3 bag made of fluorinated ethylene propylene (Teflon-FEP) to obtain several ppmv HAc. This mixture was then further diluted with N_2 after being measured by the FTIR before entering the instrument. Gas-phase GLYC was produced by flowing dry N_2 through a three-ported vial which contained the commercially available glycolaldehyde dimer (Aldrich). During this process, the three way vial was gently heated and cotton was inserted downstream of the vial to collect particles and low vapor pressure impurities before the gas was transferred to the 0.1 m^3 bag. The remainder of the procedure for GLYC mirrors that of HAc.

Though we were able to calibrate these four gases, many compounds of interest are not commercially available and difficult to synthesize and purify. Therefore, the above experiments were performed simultaneously on the cToF-CIMS in order to

directly compare the sensitivities of these two instruments. On average, the cToF-CIMS was 1.37 ± 0.22 times more sensitive than HRToF-CIMS under the same operating conditions of the field deployments. For the analysis described within the main text, we use this ratio between the two instrument sensitivities to convert previously determined cToF-CIMS sensitivities from calibrations or estimated from the ion-molecule collision rate which can be calculated using the dipole and polarizability of the analyte species (Paulot et al., 2009; Garden et al., 2009; Crounse et al., 2011).

Instrument Characterization

A number of chamber experiments were performed to properly characterize the GC-HRToF-CIMS both prior to and following field deployment. A list of experiments discussed in this study can be found in Table A.3.

Table A.3: Instrument characterization experiment list.

Expt	HO_x source[a]	NO[a]	VOC[b]	Objective
1	CH_3ONO, 50	100	Isoprene, 50	IonSrc Enhancement Ratio
2	CH3ONO, 100	500	Isoprene, 100	IHN Transmission
				IonSrc Enhancement Ratio
3	CH3ONO, 100	500	Isoprene, 100	IHN Peak Assignment
4	H2O2, 2000	0	Isoprene, 100	ISOPOOH + IEPOX Peak Assignment
				ISOPOOH + IEPOX Transmission
5	CH3ONO, 100	0	Isoprene, 100	HPALD Peak Assignment
6	CH3ONO, 100	500	Isoprene, 100	Column Humidity Effect
7	CH3ONO, 100	500	trans-2-Butene, 100	Butene HN Peak Assignment
8	CH3ONO, 100	500	2-methyl-Propene, 100	Butene HN Peak Assignment
9	CH3ONO, 100	500	1-Butene, 100	Butene HN Peak Assignment
10	CH3ONO, 100	500	cis-2-Butene, 100	Butene HN Peak Assignment
11	CH3ONO, 100	500	Propene, 100	Propene HN Peak Assignment
12	CH3ONO, 100	500	Propene, 100	Trap Linearity Test
				Isoprene, 100

[a] Mixing ratios given in ppbv

[b] Mixing ratios given in pptv.

Reagents

1-propene (propene) (>99%), 1-butene (>99%), cis-2-butene (>99%), trans-2-butene (>99%) 2-methyl-propene (>99%), isoprene (>98%) and hydrogen peroxide (H_2O_2; 30% by weight in water) were purchased from Sigma Aldrich and used without further purification in the amounts listed in Table S1. A nitric oxide standard

gas tank (NO; 1994 ppmv in high purity N_2) used for the majority of experiments was prepared by Matheson. Methyl nitrite (CH_3ONO) was synthesized, purified and stored in a glass trap submerged in liquid nitrogen using methods described in Taylor et al. (1980). In most cases, CH_3ONO served as the HO_x precursor.

Chamber Experiments

Instrument characterization experiments were conducted in either a 0.1 m^3 or 0.8 m^3 Teflon bag with a 6.35 mm PFA port used for the introduction and sampling of gases. During each experiment, the bag was filled with appropriate concentrations of reactants and placed inside a enclosure with UV reflective surfaces and eight UV lights ($\lambda_{peak} = 350$ nm). Addition of the alkene, CH_3ONO and NO was accomplished by filling a 500 cm^3 glass bulb with the compound to the desired pressure before filling with N_2 to reach approximately 993 hPa. If needed, the reagent gas was serially diluted up to two times by pumping down the bulb to the desired pressure and backfilling again with N_2. The contents of the bulb were then transferred to the chamber with the remaining bag volume filled with dry zero air. For experiment 4, H_2O_2 served as the HO_x source. Addition of H_2O_2 into the chamber was performed by flowing 20 L min^{-1} N_2 over 8 μL of H_2O_2 contained in a shallow glass vial for approximately 10 – 15 minutes to create a bag concentration of ~2 ppmv H_2O_2. In experiment 6, high RH conditions (~50%) were created by filling a portion of the bag volume with dry zero air that has passed through a water bubbler prior to entering the chamber.

Once all reagents were in the chamber bag, photochemistry was initiated upon illumination of 1–8 UV lights. Alkene oxidation occurred at approximately 298 K, with the exception of experiment 5 which was performed at an elevated temperature (315 K) to allow for increased rates of unimolecular isomerization. Experiment 5 also required longer peroxy radical lifetimes to produce a sufficient GC signal of these isomerization products. This was performed by using a single UV light in which all direct radiation was blocked, allowing only the photons scattered off the walls to contribute to the chemistry.

For the majority of experiments, photochemistry was stopped when approximately 10% of the alkene had reacted, to minimize secondary chemistry of products. Chamber air was then sampled by the GC-HRToF-CIMS at approximately 2-3 L min^{-1} through ~2.4 m of 5.84 mm ID tubing to reduce residence time in and speed equilibration of the sampling line. Chamber analysis typically alternated between

the direct CIMS and GC-CIMS sampling to assess any changes in concentration or transmission that may occur throughout the experiment. In most cases, GC effluent was directed into the ion source to allow for enhanced signal to noise (IS mode, see main text). Divergence from this procedure occurred during experiments 1 and 2 when determining the ion source enhancement ratio. During this time, each GC cycle alternated between IS mode and FT mode and the ratio of these two types of GC signals which were used to determine the signal enhancement. A similar procedure was followed when assessing the GC transmission of targeted analytes. In addition, output from the GC during trapping was also occasionally directed into the mass spectrometer to monitor potential breakthrough.

Previous Design of GC Assembly

Instrument upgrades occurred between the PROPHET and Caltech field studies to improve the chromatography and significantly reduce the need for GC downtime due to cooling system maintenance. These upgrades included a redesign of the GC assembly, which was necessary to fix some key issues experienced at PROPHET, such as large temperature gradients across the column and poor temperature control as a whole. The previous version of the field deployable GC assembly can be seen in Fig. A.14. Rather than two aluminum plates, this assembly consisted of a thin copper band. The column rested along the inner diameter of this band and was held within a 1.59 mm O.D. copper tube. The GC was cooled as liquid CO_2 expanded and flowed along 3.18 mm tubing that was soldered onto the inside of the band (to increase thermal contact). The CO_2 liquid entered at one location in the ring positioned near the two ends of the column and its flow was split at a stainless steel tee to allow both sides of the ring to cool evenly. CO_2 flow and temperature were regulated as described in the main text, however GC temperature was measured at only one location on the ring, near the CO_2 inlet (Fig. A.14, red star).

Unfortunately, by having the CO_2 flow enter through only one location in the ring, we found that the temperature gradient of opposite sides of the ring could exceed several degrees. In addition, because temperature was only monitored in one location near the coldest point of the column, it is difficult to assess the quality of the GC trapping conditions. In contrast, the redesigned GC allows CO2 to enter from the center of the plates and move outward to the diameter of the column ring. This ensures that the entire GC column is cooled at approximately the same rate. Furthermore, the addition of two more RTDs along the column also allows us to monitor the temperature gradient in real time and provides finer temperature control overall.

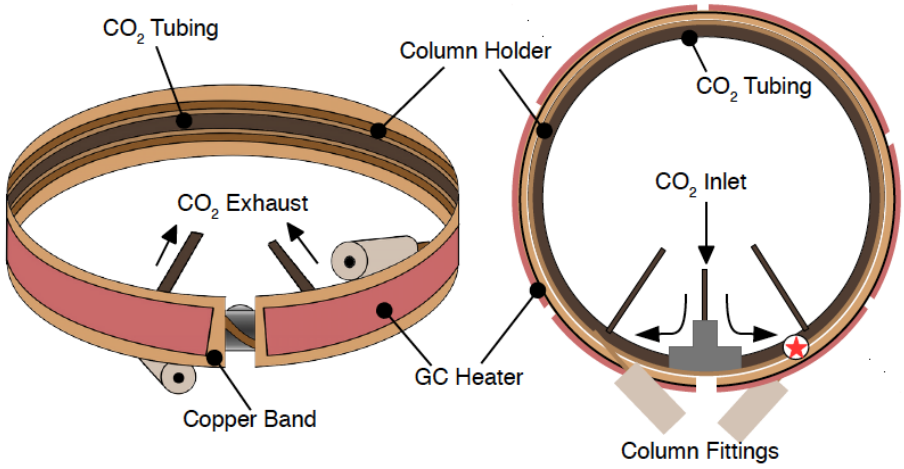

Figure A.14: Original design of the GC cryotrapping and heating assembly used during the PROPHET campaign. Here, the GC assembly consists of a thin copper band. The GC column is held within a 1.59 mm O.D. copper tube which makes thermal contact along the inner diameter of the outer band. To cool the column, the CO2 enters through a short pieces of 3.18 mm O.D. copper tubing and its flow is split at a stainless steel tee (as shown in the right diagram) so both sides of the ring can cool evenly. Heaters are adhered to the outside of the copper band (red) and GC temperature was monitored at one location, marked by a red star.

GC Cryotrap Performance

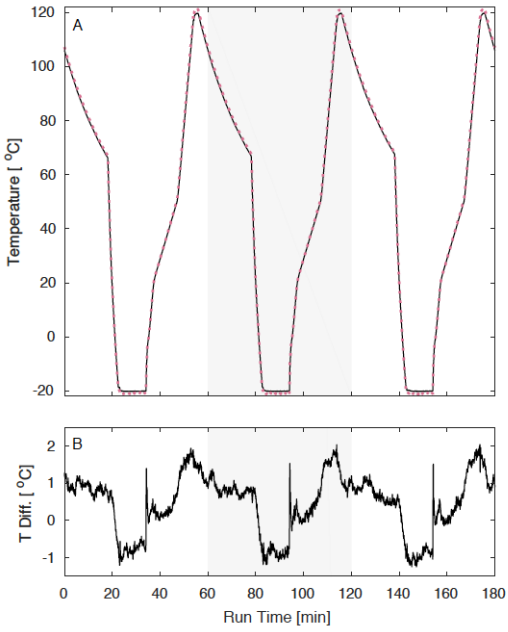

Figure A.15: (A) Temperature profiles for three consecutive GC runs demonstrating the reproducibility of GC temperature despite frequent thermal cycling. (B) Temperature difference between locations (1) and (2) on the GC (see Fig. 2, main text) show a consistently small temperature gradient (<2°C) across the column during the temperature program. Ambient temperatures during these GC cycles ranged between 27.8 – 33.2 °C.

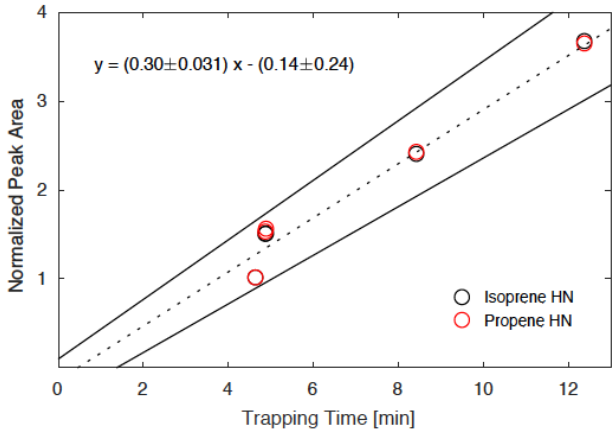

Figure A.16: Chromatogram peak areas as a function of trapping time (and, as a result, trapping volume). Analytes were cryofocused on the GC column held at −20 °C. Circles represent the sum of the peak areas of the two dominant IHN isomers (black) and the two isomers of propene HN (red) normalized to samples trapped at 4 minutes.

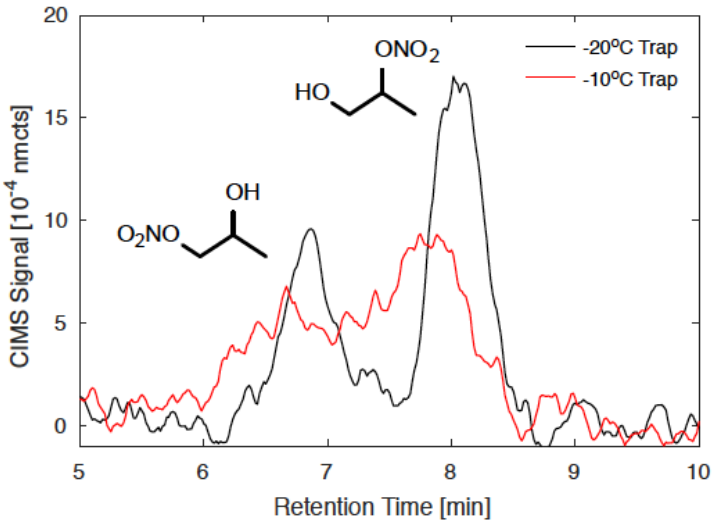

Figure A.17: Comparison of consecutive chromatograms obtained during the Caltech field study of propene HN trapped at −20 °C (black) and −10 °C (red), demonstrating the effect trapping temperature can have on the chromatography of higher volatile species.

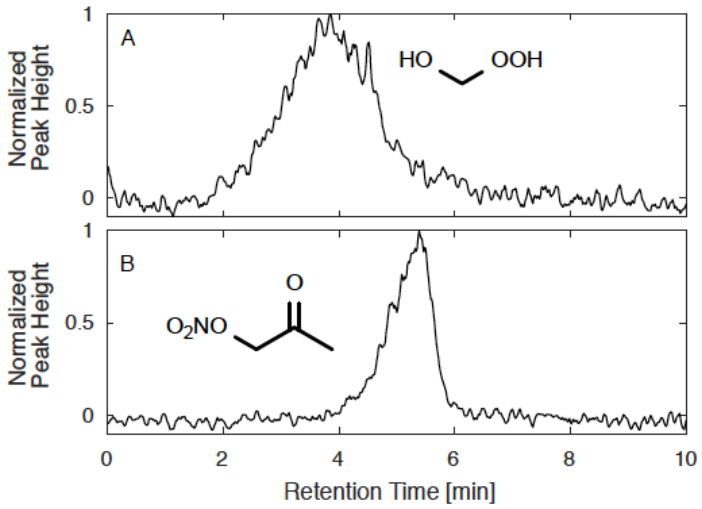

Figure A.18: Chromatograms obtained during the Caltech field study field data for (A) hydroxymethyl hydroperoxide (HMHP) and (B) propanone nitrate (PROPNN) demonstrating irregular peak shapes that can result for higher volatility species during typical trapping conditions used in this study. Further optimization of GC cryotrapping is needed in order to better quantify these compounds through GC analysis. GC signal shown here has been normalized to the largest peak in the displayed window.

Ion Fragmentation

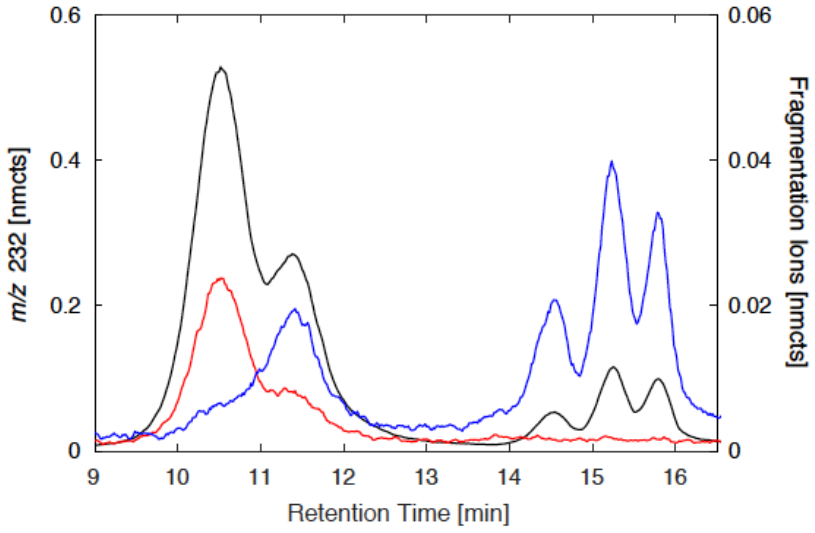

Figure A.19: Examples of fragmentation ions of IHN resulting from direct electron attachment to IHN. The primary product ion from IHN clustering with CF_3O^- (m/z 232, black) is compared with fragmentation ions resulting from electron attachment (m/z 99, blue and m/z 146, red) These fragment ions can provide additional structural information. For example m/z 99 has high yields from primary and secondary IHN structures while m/z 146 has high yields from β-hydroxy nitrates.

A.8 References

Amelynck, C., Schoon, N., and Arijs, E.: Gas phase reactions of CF_3O^- and $CF_3O-.H_2O$ with nitric, formic, and acetic acid, Int. J. Mass. Spectrom., 203, 165-175, https://doi.org/10.1016/S1387-3806(00)00321-3, 2000a.

Amelynck, C., Van, A.-M., Schoon, B. N., and Arijs, E.: Gas phase reactions of CF_3O^- and $CF_3O^- \cdot H_2O$ and their relevance to the detection of stratospheric HCl, Int. J. Mass. Spectrom., 202, 207-216, https://doi.org/10.1016/S1387-3806(00)00244-X, 2000b.

Apel, E. C., Hills, A. J., Lueb, R., Zindel, S., Eisele, S., and Riemer, D. D.: A fast-GC/MS system to measure C_2 to C_4 carbonyls and methanol aboard aircraft, J. Geophys. Res.-Atmos., 108, 8794, https://doi.org/10.1029/2002JD003199, 2003.

Apel, E. C., Brauers, T., Koppmann, R., Bandowe, B., Boßmeyer, J., Holzke, C., Tillmann, R., Wahner, A., Wegener, R., Brunner, A., Jocher, M., Ruuskanen, T., Spirig, C., Steigner, D., Steinbrecher, R., Gomez Alvarez, E., Müller, K., Burrows, J. P., Schade, G., Solomon, S. J., Ladstätter-Weißenmayer, A., Simmonds, P., Young, D., Hopkins, J. R., Lewis, A. C., Legreid, G., Reimann, S., Hansel, A., Wisthaler, A., Blake, R. S., Ellis, A. M., Monks, P. S., and Wyche, K. P.:

Intercomparison of oxygenated volatile organic compound measurements at the SAPHIR atmosphere simulation chamber, J. Geophys. Res.-Atmos., 113, D20307, https://doi.org/10.1029/2008JD009865, 2008.

Arey, J., Crowley, D. E., Crowley, M., Resketo, M., and Lester, J.: Hydrocarbon emissions from natural vegetation in California's South Coast Air Basin, Atmos. Environ., 29, 2977-2988, https://doi.org/10.1016/1352-2310(95)00137-N, 1995.

Atkinson, R. and Arey, J.: Atmospheric Degradation of Volatile Organic Compounds, Chem. Rev., 103, 4605-4638, https://doi.org/10.1021/cr0206420, 2003.

Bates, K. H., Crounse, J. D., St Clair, J.M., Bennett, N. B., Nguyen, T. B., Seinfeld, J. H., Stoltz, B. M., and Wennberg, P. O.: Gas phase production and loss of isoprene epoxydiols, J. Phys. Chem. A, 118, 1237-46, https://doi.org/10.1021/jp4107958, 2014.

Bates, K. H., Nguyen, T. B., Teng, A. P., Crounse, J. D., Kjaergaard, H. G., Stoltz, B. M., Seinfeld, J. H., and Wennberg, P. O.: Production and Fate of C_4 Dihydroxycarbonyl Compounds from Isoprene Oxidation, J. Phys. Chem. A, 120, 106-117, https://doi.org/10.1021/acs.jpca.5b10335, 2016.

Budisulistiorini, S. H., Nenes, A., Carlton, A. G., Surratt, J. D., McNeill, V. F., and Pye, H. O. T.: Simulating Aqueous-Phase Isoprene-Epoxydiol (IEPOX) Secondary Organic Aerosol Production During the 2013 Southern Oxidant and Aerosol Study (SOAS), Enviro. Sci. Technol., 51, 5026-5034, https://doi.org/10.1021/acs.est.6b05750, 2017.

Clemitshaw, K.: A Review of Instrumentation and Measurement Techniques for Ground-Based and Airborne Field Studies of Gas-Phase Tropospheric Chemistry, Crit. Rev. Env. Sci. Tec., 34, 1-108, https://doi.org/10.1080/10643380490265117, 2004.

Crounse, J. D., McKinney, K. A., Kwan, A. J., and Wennberg, P. O.: Measurement of Gas-Phase Hydroperoxides by Chemical Ionization Mass Spectrometry, Anal. Chem., 78, 6726-6732, https://doi.org/10.1021/ac0604235, 2006.

Crounse, J. D., Paulot, F., Kjaergaard, H. G., and Wennberg, P. O.: Peroxy radical isomerization in the oxidation of isoprene, Phys. Chem. Chem. Phys., 13, 13607-13613, https://doi.org/10.1039/C1CP21330J, 2011.

Demeestere, K., Dewulf, J., De Witte, B., and Van Langenhove, H.: Sample preparation for the analysis of volatile organic compounds in air and water matrices,

J. Chromatogr. A, 1153, 130-144, https://doi.org/10.1016/j.chroma.2007.01.012, 2007.

Garden, A. L., Paulot, F., Crounse, J. D., Maxwell-Cameron, I. J., Wennberg, P. O., and Kjaergaard, H. G.: Calculation of conformationally weighted dipole moments useful in ion-molecule collision rate estimates, Chem. Phys. Lett., 474, 45-50, https://doi.org/10.1016/j.cplett.2009.04.038, 2009.

Giacopelli, P., Ford, K., Espada, C., and Shepson, P. B.: Comparison of the measured and simulated isoprene nitrate distributions above a forest canopy, J. Geophys. Res.-Atmos., 110, D01304, https://doi.org/10.1029/2004JD005123, 2005.

Goldan, P. D., Kuster, W. C., Williams, E., Murphy, P. C., Fehsenfeld, F. C., and Meagher, J.: Nonmethane hydrocarbon and oxy hydrocarbon measurements during the 2002 New England Air Quality Study, J. Geosphys. Res.-Atmos., 109, D21309, https://doi.org/10.1029/2003JD004455, 2004.

Grossenbacher, J. W., Couch, T., Shepson, P. B., Thornberry, T., Witmer-Rich, M., Carroll, M. A., Faloona, I., Tan, D., Brune,W., Ostling, K., and Bertman, S.: Measurements of isoprene nitrates above a forest canopy, J. Geophys. Res.-Atmos., 106, 24429-24438, https://doi.org/10.1029/2001JD900029, 2001.

Grossenbacher, J. W., Barket Jr., D. J., Shepson, P. B., Carroll, M. A., Olszyna, K., and Apel, E.: A comparison of isoprene nitrate concentrations at two forest-impacted sites, J. Geophys. Res.-Atmos., 109, D11311, https://doi.org/10.1029/2003JD003966, 2004.

Hellén, H., Schallhart, S., Praplan, A. P., Petäjä, T., and Hakola, H.: Using in situ GC-MS for analysis of C2-C7 volatile organic acids in ambient air of a boreal forest site, Atmos. Meas. Tech., 10, 281-289, https://doi.org/10.5194/amt-10-281-2017, 2017.

Huey, L. G., Villalta, P. W., Dunlea, E. J., Hanson, D. R., and Howard, C. J.: Reactions of CF_3O^- with Atmospheric Trace Gases, J. Phys. Chem., 100, 190-194, https://doi.org/10.1021/jp951928u, 1996.

Hyttinen, N., Otkjær, R. V., Iyer, S., Kjaergaard, H. G., Rissanen, M. P., Wennberg, P. O., and Kurtén, T.: Computational Comparison of Different Reagent Ions in the Chemical Ionization of Oxidized Multifunctional Compounds, J. Phys. Chem. A, 122, 269-279, https://doi.org/10.1021/acs.jpca.7b10015, 2018.

Klenø, J. G., Wolkoff, P., Clausen, P. A., Wilkins, C. K., and Pedersen, T.: Degradation of the Adsorbent Tenax TA by Nitrogen Oxides, Ozone, Hydrogen Peroxide, OH Radical, and Limonene Oxidation Products, Environ. Sci. Technol., 36, 4121-4126, https://doi.org/10.1021/es025680f, 2002.

Koppmann, R. and Wildt, J.: Oxygenated Volatile Organic Compounds, John Wiley & Sons, 129-172, 2008.

Lee, L., Teng, A. P., Wennberg, P. O., Crounse, J. D., and Cohen, R. C.: On rates and mechanisms of OH and O_3 reactions with isoprene-derived hydroxy nitrates, J. Phys. Chem. A, 118, 1622-1637, https://doi.org/10.1021/jp4107603, 2014.

Lerner, B. M., Gilman, J. B., Aikin, K. C., Atlas, E. L., Goldan, P. D., Graus, M., Hendershot, R., Isaacman-VanWertz, G. A., Koss, A., Kuster, W. C., Lueb, R. A., McLaughlin, R. J., Peischl, J., Sueper, D., Ryerson, T. B., Tokarek, T. W., Warneke, C., Yuan, B., and de Gouw, J. A.: An improved, automated whole air sampler and gas chromatography mass spectrometry analysis system for volatile organic compounds in the atmosphere, Atmos. Meas. Tech., 10, 291-313, https://doi.org/10.5194/amt-10-291-2017, 2017.

Mellouki, A., Le Bras, G., and Sidebottom, H.: Kinetics and Mechanisms of the Oxidation of Oxygenated Organic Compounds in the Gas Phase, Chem. Rev., 103, 5077-5096, https://doi.org/10.1021/cr020526x, 2003.

Mellouki, A., Wallington, T. J., and Chen, J.: Atmospheric Chemistry of Oxygenated Volatile Organic Compounds: Impacts on Air Quality and Climate, Chem. Rev., 115, 3984-4014, https://doi.org/10.1021/cr500549n, 2015.

Millet, D. B., Donahue, N. M., Pandis, S. N., Polidori, A., Stanier, C. O., Turpin, B. J., and Goldstein, A. H.: Atmospheric volatile organic compound measurements during the Pittsburgh Air Quality Study: Results, interpretation, and quantification of primary and secondary contributions, J. Geophys. Res.-Atmos., 110, D07S07, https://doi.org/10.1029/2004JD004601, 2005.

Millet, D. B., Alwe, H. D., Chen, X., Deventer, M. J., Griffis, T. J., Holzinger, R., Bertman, S. B., Rickly, P. S., Stevens, P. S., Léonardis, T., Locoge, N., Dusanter, S., Tyndall, G. S., Alvarez, S. L., Erickson, M. H., and Flynn, J. H.: Bidirectional Ecosystem-Atmosphere Fluxes of Volatile Organic Compounds Across the Mass Spectrum: How Many Matter?, ACS Earth Space Chem., 2, 764-777, https://doi.org/10.1021/acsearthspacechem.8b00061, 2018.

Mills, G. P., Hiatt-Gipson, G. D., Bew, S. P., and Reeves, C. E.: Measurement of isoprene nitrates by GCMS, Atmos. Meas. Tech., 9, 4533-4545, https://doi.org/10.5194/amt-9-4533-2016, 2016.

Nguyen, T. B., Crounse, J. D., Schwantes, R. H., Teng, A. P., Bates, K. H., Zhang, X., St. Clair, J. M., Brune, W. H., Tyndall, G. S., Keutsch, F. N., Seinfeld, J. H., and Wennberg, P. O.: Overview of the Focused Isoprene eXperiment at the California Institute of Technology (FIXCIT): mechanistic chamber studies on the oxidation of biogenic compounds, Atmos. Chem. Phys., 14, 13531-13549, https://doi.org/10.5194/acp-14-13531-2014, 2014.

Nguyen, T. B., Crounse, J. D., Teng, A. P., St. Clair, J. M., Paulot, F., Wolfe, G. M., and Wennberg, P. O.: Rapid deposition of oxidized biogenic compounds to a temperate forest, P. Natl. Acad. Sci. USA, 112, E392-E401, https://doi.org/10.1073/pnas.1418702112, 2015.

Nozière, B., Kalberer, M., Claeys, M., Allan, J., D'Anna, B., Decesari, S., Finessi, E., Glasius, M., Grgić, I., Hamilton, J. F., Hoffmann, T., Iinuma, Y., Jaoui, M., Kahnt, A., Kampf, C. J., Kourtchev, I., Maenhaut, W., Marsden, N., Saarikoski, S., Schnelle-Kreis, J., Surratt, J. D., Szidat, S., Szmigielski, R., and Wisthaler, A.: The Molecular Identification of Organic Compounds in the Atmosphere: State of the Art and Challenges, Chem. Rev., 115, 3919-3983, https://doi.org/10.1021/cr5003485, 2015.

O'Haver, T.: Peak Fitters, available at: https://terpconnect.umd.edu/ toh/spectrum/ InteractivePeakFitter.htm (last access: 30 June 2018), 2017.

Orlando, J. J. and Tyndall, G. S.: Laboratory studies of organic peroxy radical chemistry: an overview with emphasis on recent issues of atmospheric significance, Chem. Soc. Rev., 41, 6294-6317, https://doi.org/10.1039/C2CS35166H, 2012.

Paulot, F., Crounse, J. D., Kjaergaard, H. G., Kroll, J. H., Seinfeld, J. H., and Wennberg, P. O.: Isoprene photooxidation: new insights into the production of acids and organic nitrates, Atmos. Chem. Phys., 9, 1479-1501, https://doi.org/10.5194/acp-9-1479-2009, 2009a.

Paulot, F., Crounse, J. D., Kjaergaard, H. G., Kürten, A., St. Clair, J. M., Seinfeld, J. H., and Wennberg, P. O.: Unexpected Epoxide Formation in the Gas-Phase Photooxidation of Isoprene, Science, 325, 730-733, https://doi.org/10.1126/science.1172910, 2009b.

Peeters, J., Nguyen, T. L., and Vereecken, L.: HO_x radical regeneration in the oxidation of isoprene, Phys. Chem. Chem. Phys., 11, 5935-5939, https://doi.org/10.1039/B908511D, 2009.

Peeters, J., Müller, J.-F., Stavrakou, T., and Nguyen, V. S.: Hydroxyl Radical Recycling in Isoprene Oxidation Driven by Hydrogen Bonding and Hydrogen Tunneling: The Upgraded LIM1 Mechanism, J. Phys. Chem. A, 118, 8625-8643, https://doi.org/10.1021/jp5033146, pMID: 25010574, 2014.

Pollack, I. B., Ryerson, T. B., Trainer, M., Neuman, J. A., Roberts, J. M., and Parrish, D. D.: Trends in ozone, its precursors, and related secondary oxidation products in Los Angeles, California: A synthesis of measurements from 1960 to 2010, J. Geophys. Res.-Atmos., 118, 5893-5911, https://doi.org/10.1002/jgrd.50472, 2013.

Praske, E., Crounse, J. D., Bates, K. H., Kurten, T., Kjaergaard, H. G., and Wennberg, P. O.: Atmospheric Fate of Methyl Vinyl Ketone: Peroxy Radical Reactions with NO and HO_2, J. Phys. Chem. A, 119, 4562-4572, https://doi.org/10.1021/jp5107058, 2015.

Praske, E., Otkjær, R. V., Crounse, J. D., Hethcox, J. C., Stoltz, B. M., Kjaergaard, H. G., and Wennberg, P. O.: Atmospheric autoxidation is increasingly important in urban and suburban North America, P. Natl. Acad. Sci. USA, 115, 64-69, https://doi.org/10.1073/pnas.1715540115, 2018.

Ras, M. R., Borrull, F., and Marcé, R. M.: Sampling and preconcentration techniques for determination of volatile organic compounds in air samples, Trends Anal. Chem., 28, 347-361, https://doi.org/10.1016/j.trac.2008.10.009, 2009.

Rivera-Rios, J. C., Nguyen, T. B., Crounse, J. D., Jud, W., St. Clair, J. M., Mikoviny, T., Gilman, J. B., Lerner, B. M., Kaiser, J. B., de Gouw, J., Wisthaler, A., Hansel, A., Wennberg, P. O., Seinfeld, J. H., and Keutsch, F. N.: Conversion of hydroperoxides to carbonyls in field and laboratory instrumentation: Observational bias in diagnosing pristine versus anthropogenically controlled atmospheric chemistry, Geophys. Res. Lett., 41, 8645-8651, https://doi.org/10.1002/2014GL061919, 2014.

Roukos, J., Plaisance, H., Leonardis, T., Bates, M., and Locoge, N.: Development and validation of an automated monitoring system for oxygenated volatile organic compounds and nitrile compounds in ambient air, J. Chromatogr. A, 1216, 8642-8651, https://doi.org/10.1016/j.chroma.2009.10.018, 2009.

Sapozhnikova, Y. and Lehotay, S. J.: Review of recent developments and applica-

tions in low-pressure (vacuum outlet) gas chromatography, Anal. Chim. Acta, 899, 13-22, https://doi.org/10.1016/j.aca.2015.10.003, 2015.

Schwantes, R. H., Teng, A. P., Nguyen, T. B., Coggon, M. M., Crounse, J. D., St Clair, J. M., Zhang, X., Schilling, K. A., Seinfeld, J. H., and Wennberg, P. O.: Isoprene NO_3 Oxidation Products from the RO_2 + HO_2 Pathway, J. Phys. Chem. A, 119, 10158-10171, https://doi.org/10.1021/acs.jpca.5b06355, 2015.

Sharpe, S. W., Johnson, T. J., Sams, R. L., Chu, P. M., Rhoderick, G. C., and Johnson, P. A.: Gas-Phase Databases for Quantitative Infrared Spectroscopy, Appl Spectrosc, 58, 1452-1461, https://doi.org/10.1366/0003702042641281, https://doi.org/10.1366/0003702042641281, pMID: 15606959, 2004.

Squire, O. J., Archibald, A. T., Griffiths, P. T., Jenkin, M. E., Smith, D., and Pyle, J. A.: Influence of isoprene chemical mechanism on modelled changes in tropospheric ozone due to climate and land use over the 21st century, Atmos. Chem. Phys., 15, 5123-5143, https://doi.org/10.5194/acp-15-5123-2015, 2015.

St. Clair, J. M., McCabe, D. C., Crounse, J. D., Steiner, U., and Wennberg, P. O.: Chemical ionization tandem mass spectrometer for the in situ measurement of methyl hydrogen peroxide, Rev. Sci. Instrum., 81, 095102, https://doi.org/10.1063/1.3480552, 2010.

St. Clair, J. M., Rivera-Rios, J. C., Crounse, J. D., Knap, H. C., Bates, K. H., Teng, A. P., Jorgensen, S., Kjaergaard, H. G., Keutsch, F. N., andWennberg, P. O.: Kinetics and Products of the Reaction of the First-Generation Isoprene Hydroxy Hydroperoxide (ISOPOOH) with OH, J. Phys. Chem. A, 120, 1441-1451, https://doi.org/10.1021/acs.jpca.5b06532, 2016.

Suh, I., Lei,W., and Zhang, R.: Experimental and Theoretical Studies of Isoprene Reaction with NO3, J. Phys. Chem. A, 105, 6471-6478, https://doi.org/10.1021/jp0105950, 2001.

Taylor, W. D., Allston, T. D., Moscato, M. J., Fazekas, G. B., Kozlowski, R., and Takacs, G. A.: Atmospheric photodissociation lifetimes for nitromethane, methyl nitrite, and methyl nitrate, Int J Chem Kinet, 12, 231-240, https://doi.org/10.1002/kin.550120404, 1980.

Teng, A. P., Crounse, J. D., Lee, L., St. Clair, J. M., Cohen, R. C., and Wennberg, P. O.: Hydroxy nitrate production in the OH-initiated oxidation of alkenes, Atmos. Chem. Phys., 15, 4297-4316, https://doi.org/10.5194/acp-15-4297-2015, 2015.

Teng, A. P., Crounse, J. D., and Wennberg, P. O.: Isoprene Peroxy Radical Dynamics, J. Am. Chem. Soc., 139, 5367-5377, https://doi.org/10.1021/jacs.6b12838, 2017.

Vairavamurthy, A., Roberts, J. M., and Newman, L.: Methods for determination of low molecular weight carbonyl compounds in the atmosphere: A review, Atmos. Environ. Pt. A, 26, 1965-1993, https://doi.org/10.1016/0960-1686(92)90083-W, 1992.

Vasquez, K. T., Xu, L., Allen, H. M., Praske, E., Crounse, J. D., and Wennberg, P. O.: GCHRToFCIMS – IHN GC Data from 2017 Caltech Roof Study, Version R0, https://doi.org/10.22002/D1.971, last access: 4 July 2018.

Wennberg, P. O., Bates, K. H., Crounse, J. D., Dodson, L. G., McVay, R. C., Mertens, L. A., Nguyen, T. B., Praske, E., Schwantes, R. H., Smarte, M. D., St Clair, J. M., Teng, A. P., Zhang, X., and Seinfeld, J. H.: Gas-Phase Reactions of Isoprene and Its Major Oxidation Products, Chem. Rev., 118, 3337-3390, https://doi.org/10.1021/acs.chemrev.7b00439, 2018.

Xiong, F., McAvey, K. M., Pratt, K. A., Groff, C. J., Hostetler, M. A., Lipton, M. A., Starn, T. K., Seeley, J. V., Bertman, S. B., Teng, A. P., Crounse, J. D., Nguyen, T. B.,Wennberg, P. O., Misztal, P. K., Goldstein, A. H., Guenther, A. B., Koss, A. R., Olson, K. F., de Gouw, J. A., Baumann, K., Edgerton, E. S., Feiner, P. A., Zhang, L., Miller, D. O., Brune, W. H., and Shepson, P. B.: Observation of isoprene hydroxynitrates in the southeastern United States and implications for the fate of NO_x , Atmos. Chem. Phys., 15, 11257-11272, https://doi.org/10.5194/acp-15-11257-2015, 2015.

Zhao, Y., Kreisberg, N. M., Worton, D. R., Teng, A. P., Hering, S. V., and Goldstein, A. H.: Development of an In Situ Thermal Desorption Gas Chromatography Instrument for Quantifying Atmospheric Semi-Volatile Organic Compounds, Aerosol. Sci. Technol., 47, 258-266, https://doi.org/10.1080/02786826.2012.747673, 2013.